Forschungsbericht 2019-23

Validation of Damage Parameter Based Finite Element Fatigue Life Analysis Results to Combustion Chamber Type Thermomechanical Fatigue Panel Tests

Ray Gordan Thiede

Deutsches Zentrum für Luft- und Raumfahrt
Institut für Raumfahrtantriebe
Lampoldshausen

132 Seiten
66 Bilder
12 Tabellen
161 Literaturstellen

Deutsches Zentrum
DLR für Luft- und Raumfahrt

Institut für Angewandte Mechanik

RWTH AACHEN UNIVERSITY

Validation of Damage Parameter Based Finite Element Fatigue Life Analysis Results to Combustion Chamber Type Thermomechanical Fatigue Panel Tests

Fakultät für Bauingenieurwesen
Rheinisch-Westfälische Technische Hochschule Aachen

zur Erlangung des Grades

Doktor-Ingenieur
(Dr.-Ing.)

vorgelegt von

Ray Gordan Thiede
geboren in Hoyerswerda

Aachen - 2019

Als Dissertation genehmigt von der
Fakultät für Bauingenieurwesen
Rheinisch-Westfälische Technische Hochschule Aachen

Tag der Einreichung:	13.03.2019
Tag der mündlichen Prüfung:	11.07.2019
Vorsitzender:	Univ.-Prof. Dr.-Ing. Markus Feldmann
Berichter:	Univ.-Prof. Dr.-Ing. Stefanie Reese
Berichter:	Univ.-Prof. Dr. rer. nat. Michael Oschwald

"True heroism is minutes, hours, weeks, year upon year of the quiet, precise, judicious exercise of probity and care - with no one there to see or cheer. This is the world."

The Pale King by David Foster Wallace

Acknowledgments

This thesis is carried out within collaboration between the Institute of Applied Mechanics of the RWTH Aachen University and the structure group of the DLR Institute of Space Propulsion in Lampoldshausen. To work on the topic of *Fatigue Life Prediction of Actively Cooled Wall Structures Under Cyclic Thermomechanical Loading* gave me the opportunity to combine numerical work with experimental work at once. It was an extremely exciting task but also very challenging. This experience will accompany me throughout my upcoming professional career as well as throughout my future life.

First of all, I would like to thank Prof. Dr.-Ing. Stefanie Reese for mentoring and excellent support. I feel very lucky that she gave me the opportunity for writing this thesis in her magnificent institute. Likewise I would like to thank all members of the IFAM and Marek Fassin for the every warm welcome of each visit in Aachen as well as for numerous of helpful advice regarding the theory of material modeling and continuum mechanics.

I also would like to thank Prof. Dr. rer. nat. Michael Oschwald for his willingness to be an examiner of this work, for the department's quarterly status meetings which helped me to focus on the thesis and for his personal advice to keep going - particularly in tough times.

In addition, I would like to thank Prof. Dr.-Ing. Markus Feldmann to act as the chairman of the oral defense committee.

With regard to the development of my professional skills, I would like to express my gratitude to Dr.-Ing. Jörg Riccius who guided me through the thesis. His profound knowledge combined with a great wealth of ideas is what will keep in my mind. I will never forget Jörg's selfless dedication to this research topic and his tireless efforts to make steady progress.

Furthermore, I would like to thank all colleagues from the Institute of Space Propulsion who accompanied me the long way. In particular, I would like to mention Dr.-Ing. Wissam Bouajila, Evgeny Zametaev for myriad of fruitful discussions, Philip Kron for being the technician who kept the test bench going, Dr.-Ing. Dmitry Suslov for the delicious coffee breaks, Jan Haemisch for being a precious running partner during the lunch breaks, Dr.-Ing. Andreas Gernoth and Ingo Dörr for having developed the TMF test bench M51, the M11 crew for being the coolest guys at the site and for pushing the social interaction among the DLR colleagues forward, the Italians for excellent handmade coffee and for sharing the joy of living, Stuart Blake for having improved my English enormously, Pascal Kringe for his precious support during the examination period and for excellent proofreading, and all the others who supported and encouraged me all the time.

Not to forget to acknowledge the contributions of Prof. Dr.-Ing. Marion Bartsch, Dr.-Ing. Klemens Kelm and Philip Watermeyer from the DLR Institute of Material Research for performing the SEM investigations as well as the contributions of Dr.-Ing. Otmar Zimmer and Ute Nimsch from the Fraunhofer Institute of Material and Beam Technology for excellent work concerning the PVD coating technology. In addition, I would like to express my respect to Andreas Märklen and Alfredo Rohatschek for their outstanding work and their profound

knowledge without the TMF panel could not have been realized. Your contribution prevented ourselves from a lot of mistakes.

My special thanks go to Dr.-Ing. Tadashi Masuoka who was delegated as a guest scientist from the Japan Aerospace Exploration Agency (JAXA) to our structure group for one year. He broadened my personal horizon and I am glad to have met him and his lovely family.

Last but not least, I would like to acknowledge my wife Elena, my family and my close friends who supported and motivated me all the time to get through this period. Especially to my wife, thank you very much for being my anchor in calm and turbulent seas. You were the person who suffered the most. Thank you!

Abstract

Liquid rocket engine technology still maintains our access to space by providing thrust for transporting satellites and humans precisely into orbit. One of the most critical parts of such an engine is the combustion chamber that has to withstand extreme temperature and pressure gradients during operation. By applying alternative inexpensive combustion chamber materials as well as reusing the engines for several rocket launches, the costs of development, production and operation would decrease significantly. But numerical prediction of the engine's fatigue life as well as numerical modeling of the engine's major structural failure mode with respect to material deformation and degradation (the so-called doghouse effect) is still a difficult task for engineers. Therefore, a combustion-chamber-type thermomechanical fatigue (TMF) panel experiment has been developed at the German Aerospace Center (DLR) to improve and validate such numerical analyses for research purposes.

By performing a test campaign with a combustion-chamber-type thermomechanical fatigue panel, experimental results are used to validate a one-way fluid-structure-interaction analysis with a viscoplastic damage model. This material model is implemented into the commercial finite element program Ansys and takes into account ductile isotropic damage, kinematic hardening, combined isotropic hardening and isotropic softening, microdefect closure effect and thermal ageing. Uniaxial material tests at ambient and elevated temperatures are conducted to determine the structural material parameters of the applied copper-base alloy (CuCrZr) that is assumed to be an appropriate inexpensive inner liner material candidate for future rocket engines. Following the validation, numerical results are compared to experimental results and the material model is applied to a simplified rocket combustion chamber segment.

The predicted fatigue life of the combustion-chamber-type thermomechanical fatigue panel shows a very good agreement with experimental data and is underestimated by only 3.5 %. In addition, the origin of the crack that leads to structural failure of the laser loaded wall ligament is predicted correctly. With regard to the simplified combustion chamber segment analysis, bulging and necking of the hot wall could be reproduced very well. It is therefore concluded that the presented fatigue life analysis with the proposed damage model is suitable for fatigue life prediction of the combustion-chamber-type thermomechanical fatigue panel experiment. To draw a conclusion to a rocket combustion chamber, the thermomechanical panel experiment needs to be modified to ensure tensile rupture of the laser loaded wall ligament. Application of an alternative material with decreased strength (such as pure copper) as well as a different TMF panel geometry could help to address this issue in the future. Combining ductile damage with fatigue and creep damage could also improve the reproduction of the structural material degradation behavior leading to a decreased engine's life time.

Zusammenfassung

Raketentriebwerke sind während des Betriebes hohen thermischen und mechanischen Lasten ausgesetzt. Bei geplanter mehrfacher Verwendung solcher Triebwerke tritt ein zyklisches Ausdünnen und Ausbeulen der Brennkammerwand auf, welches zu Rissen entlang der Kühlkanäle führt und damit die Lebensdauer des Triebwerks limitiert. Dieser Schädigungsmechanismus ist aufgrund des Deformationsbildes als *Doghouse*-Effekt bekannt. Er wurde erstmals von Wissenschaftlern der *National Aeronautics and Space Administration* (kurz: NASA) bei der Entwicklung des *Space Shuttle Main Engine* experimentell und numerisch untersucht. Da experimentelle Raketentriebwerkstests sehr aufwändig und sehr kostenintensiv sind, wurde ein Experiment entwickelt (das sogenannte TMF-Panel-Experiment), welches strukturelle Lebensdaueruntersuchungen an einem aktiv-gekühlten Kühlkanalprobekörper unter thermomechanischen Lastbedingungen ermöglicht. Die experimentellen Ergebnisse werden verwendet, um aktuelle numerische Lebensdauerberechnungen zu validieren und die Erkenntnisse auf die Entwicklung von flüssigkeitsgekühlten Raketenbrennkammern zu übertragen. Umso zuverlässiger eine solche komplexe Lebensdaueranalyse ist, umso höher ist die Kostenersparnis in der Vorentwicklung mit Hinblick auf die Anwendung von alternativen und kostengünstigeren Brennkammerwandmaterialen und mit Hinblick auf die Untersuchung des Einflusses unterschiedlicher Kühlkanalgeometrien (Parameterstudien).

In dieser Arbeit wird eine numerische Berechnung zur Ermittlung der Lebensdauer eines solchen TMF-Panel-Experiments vorgestellt. Die Validierung dieses Modells erfolgt anhand von experimentellen Ergebnissen. Dabei wird detailliert der Versuchsaufbau, die Durchführung sowie die experimentellen Ergebnisse beschrieben. Um diesen Ermüdungsversuch numerisch nachzubilden, wurde eine serielle Fluid-Struktur-Interaktionsanalyse durchgeführt. Dafür wird zunächst das dreidimensionale Temperaturfeld des TMF-Panel-Probekörpers während aktiver Laserbelastung und aktiver Stickstoffkühlung mittels einer stationären Thermal-und Strömungsanalyse berechnet. Das Temperaturfeld wird an die quasistationäre Strukturanalyse übergeben und mit Berücksichtigung des Kühlkanaldrucks als zyklische Belastungsrandbedingung aufgebracht. Um die Schädigung und somit die Lebensdauer des TMF-Panels während zyklisch aufgebrachter Laserapplikation zu berechnen, wurde ein viskoplastisches Schädigungsmodell implementiert und angewendet. Komplettiert wurde das Modell durch das Hinzufügen von weiteren Effekten, wie zum Beispiel der Rissschließungseffekt während Druckbelastung und die thermische Alterung des Materials bei hohen Temperaturen und zunehmender Auslagerungszeit. Die dafür benötigen thermophysikalischen Stoffeigenschaften und mechanischen Materialparameter wurden durch spezielle Messverfahren und durch uniaxiale Materialversuche bestimmt.

Die berechnete Lebensdauer und das berechnete Verformungsbild des untersuchten TMF-Panels wurden mit den experimentellen Ergebnissen verglichen. Es konnte gezeigt werden, dass sowohl die Lebensdauerabschätzung als auch der Ursprung des Risses, welcher zum Versagen führt, sehr gut übereinstimmen. Auch der Temperaturgradient quer zu den Kühlkanälen konnte sehr gut reproduziert werden. Jedoch ist die berechnete Strukturdeformation unverhältnismäßig

stark ausgeprägt, was auf viskoplastische Effekte (Kriechen) in den Seitenwänden der Kühlkanäle bei Temperaturen unter 800 K zurückzuführen ist. Zwar konnte ein solches Kriech-Verhalten bei uniaxialen Materialtests schon ab einer Temperatur von 700 K beobachtet werden, sollte aber bei weiteren Berechnungen vernachlässigt werden. Außerdem haben mikrographische Untersuchungen gezeigt, dass der Bruch durch ein zyklisches Risswachstum infolge thermischer Lastwechsel erfolgt sein muss. Das hier verwendete phänomenologische Schädigungsmodell ist jedoch nur bis zur Entstehung eines Risses gültig. Ein zyklisches Risswachstum könnte demnach mit einem Modell aus der Bruchmechanik präziser bestimmt werden.

Der letzte Teil dieser Arbeit besteht aus der Anwendung des validierten Materialmodells auf den realen Anwendungsfall. Als Grundlage für das Modell wurde eine vereinfachte quasi zwei-dimensionale Geometrie einer Raketenbrennkammerwand gewählt, die aus der Kupferbasislegierung CuCrZr bestand. Mittels einer transienten Thermalanalyse und einer quasi-statischen Strukturanalyse wurde das transiente Temperaturfeld während eines Heißlaufs, die Anzahl der Zyklen und das Verformungsbild des vereinfachten Kühlkanals berechnet. Obwohl die ermittelte Lebensdauer von 36 Zyklen bis zum strukturellen Versagen unerwartet hoch ist, konnte eine Einschnürung und eine Ausbeulung der Kühlkanalwand nachgebildet werden. Eine bessere Übereinstimmung mit der Realität wird durch Anwendung einer zweiseitig gekoppelten Fluid-Struktur-Interaktionsanalyse sowie durch Berücksichtigung von *Blanching* (zyklische Erhöhung der Rauheit der Heißgaswandoberfläche), Wasserstoffversprödung (reduzierte Duktilität in der Heißgaswand und Rissbildung), Abtragung des Wandmaterials durch abrasiven Verschleiß (erhöhte Wandausdünnung nach mehreren Zyklen) und Kopplung von duktiler- und ermüdungsbasierter Schädigung (Reduzierung der Lebensdauer) erwartet.

Contents

List of Figures

List of Tables

Nomenclature

Symbol	Unit	Description
$\mathbf{1}$	[-]	Second-order unity tensor
a	[m s^{-1}]	Thermal diffusivity
A	[m^2]	Area
A_R	[m^2]	Rupture area
A_x	[-]	Static recovery coefficient for kinematic hardening
α	[K^{-1}]	Thermal expansion coefficient
α_θ	[Pa s]	Thermal ageing material parameter
$b_{1,2}$	[Pa]	Drag stress material parameters
b_{kin}	[-]	Back stress material parameter
β_θ	[s]	Thermal ageing material parameter
c_p	[J kg^{-1} K^{-1}]	Specific heat capacity
C	[-]	Wall roughness constant by using natural logarithm
$\boldsymbol{\mathcal{C}}_1, \boldsymbol{\mathcal{C}}_2$	[-]	Fourth-order elasticity tensors depending on $E_1(\nu_1)$ and $E_2(\nu_2)$
d_{H}	[m]	Hydraulic diameter
D	[-]	Damage state variable
D_c	[-]	Critical damage material parameter
δ, δ_{ij}	[-]	KRONECKER delta
E_i	[Pa]	YOUNG's modulus
$\boldsymbol{\varepsilon}$	[-]	Second-order GREEN strain tensor
$\boldsymbol{\varepsilon^e}$	[-]	Elastic part of the strain tensor
$\boldsymbol{\varepsilon^p}$	[-]	Plastic part of the strain tensor
$\boldsymbol{\varepsilon^{pe}}$	[-]	Reversible plastic part of the plastic strain tensor
$\boldsymbol{\varepsilon^{pi}}$	[-]	Irreversible plastic part of the plastic strain tensor
ε_{eng}	[-]	Engineering strain
$\varepsilon_{\text{true}}$	[-]	True (logarithmic) strain
ε_α	[-]	Emissivity coefficient
η	[Pa s]	Viscosity material parameter
F	[N]	Force
$\boldsymbol{f}_E, \boldsymbol{f}_M$	[-]	Energy source, momentum body forces
γ_t	[m^2 s^{-1}]	Eddy diffusivity
γ_θ	[Pa]	Thermal ageing material parameter
Γ_i	[-]	Surface of Domain i
h	[-]	Microdefect closure material parameter
h_c	[-]	Heat transfer coefficient

Symbol	Unit	Description
$H, H_\mathrm{T}, H_\mathrm{S}$	[J]	Enthalpy, total enthalpy, static enthalpy
I	[A]	Electric current
$I_{x,y}$	[m^4]	Second moment of area
$\boldsymbol{\mathcal{I}}^\mathrm{Sym}$	[-]	Symmetric fourth-order unity tensor
k_B	[J K^{-1}]	Boltzmann constant
k_D	[-]	Ductile damage material parameter
k_t	[J kg^{-1}]	Turbulent kinetic energy
k_θ	[W m^{-1} K^{-1}]	Thermal conductivity
K_A, K_C	[-]	Correlation factors
κ	[-]	von Karman constant
l_i	[m]	Distance of i, e.g. Laser
λ	[m]	Wave length
λ_L	[Pa]	Lamé parameter
$\dot{\lambda}$	[-]	Plastic multiplier
m	[kg]	Mass
m_η	[-]	Viscosity material parameter
$\dot{m}$	[kg s^{-1}]	Mass flow rate
μ_L	[Pa]	Lamé parameter
μ, μ_t	[Pa s]	Dynamic viscosity, dynamic turbulent viscosity
$\boldsymbol{n}$	[-]	Normal vector
$\boldsymbol{n}_i$	[-]	Eigenvectors
ν_i	[-]	Poisson's ratio
ω	[s^{-1}]	Rotational speed
Ω_i	[-]	Domain i
p	[Pa]	Pressure
p_α	[-]	Accumulated plastic strain
p_D	[-]	Damage threshold material parameter
P	[W]	Power
Pr, Pr$_t$	[-]	Prandtl number, turbulent Prandtl number
ψ	[J]	Helmholtz free energy
ψ^*	[J]	Gibbs free enthalpy
Φ_Mises	[Pa]	von Mises yield criterion
$q, \boldsymbol{q}$	[W m^{-2}]	Heat flux
Q	[W]	Heat
$Q_{0,1,2}$	[Pa]	Drag stress material parameters
R	[Pa]	Drag stress
R_i	[m]	Radius
R_s	[m]	Sand-grain surface roughness
R_z	[m]	Peak-to-valley surface roughness
R_ε	[-]	Strain ratio
Re	[-]	Reynolds number
ρ	[kg m^{-3}]	Density

Symbol	Unit	Description
S	[J K^{-1}]	Entropy
S_D	[Pa]	Ductile damage material parameter
S_ϑ	[Pa]	Damage reduction material parameter
$\boldsymbol{\sigma}$	[Pa]	Second-order CAUCHY stress tensor
$\boldsymbol{\sigma}^D$	[Pa]	Deviatoric part of the stress tensor
σ_{eng}	[Pa]	Engineering stress
σ_{true}	[Pa]	True (logarithmic) stress
σ_θ	[Pa]	Thermal ageing stress
σ_v	[Pa]	Viscous stress
σ_y	[Pa]	Yield stress
t	[s]	Time
t_θ	[s]	Ageing time
t_ϑ	[s]	Damage reduction material parameter
$\boldsymbol{\tau}^R$	[Pa]	Second-order REYNOLDS shear stress tensor
τ_w	[Pa]	Wall shear stress
θ	[K]	Temperature
$\dot{u}$	[m s^{-1}]	Velocity
$\dot{u}_t$	[m s^{-1}]	Velocity tangential to the wall
$\dot{u}_\tau$	[m s^{-1}]	Friction velocity near the wall
$\dot{u}^+$	[m s^{-1}]	Velocity near the wall
U	[V]	Electric voltage
V	[m^3]	Volume
$\dot{V}$	[m^3 s^{-1}]	Volumetric flow rate
x, y, z	[m]	CARTESIAN coordinates
$\boldsymbol{X}$	[Pa]	Second-order back stress tensor
Y	[Pa]	Damage driving force (strain energy density release rate)
Z	[-]	Necking factor

Function	Description
$\dot{x}$	Derivative value
$\hat{x}, \hat{\boldsymbol{x}}$	Maximum value, principal values of $\boldsymbol{x}$
$\tilde{x}$	Effective value
$\bar{x}$	Mean value
$\overline{x_i x_j}$	Mean scalar gradient of $\boldsymbol{x}$
Δx	Difference of two values
$\langle x \rangle$	MACAULEY brackets
$\nabla \boldsymbol{x}$	Gradient of $\boldsymbol{x}$
$\boldsymbol{x}^T$	Transpose matrix of $\boldsymbol{x}$
$\lvert x \rvert, \lvert \boldsymbol{x} \rvert$	Absolute value, scalar product of $\boldsymbol{x}$
$\lvert\lvert \boldsymbol{x} \rvert\rvert$	Tensor product of $\boldsymbol{x}$
$\text{tr}^+(\boldsymbol{x}) = \langle \text{tr}(\boldsymbol{x}) \rangle$, $\text{tr}^-(\boldsymbol{x}) = -\langle -\text{tr}(\boldsymbol{x}) \rangle$	Trace of $\boldsymbol{x}$
$\boldsymbol{x} \otimes \boldsymbol{y}$	Dyadic product of $\boldsymbol{x}$ and $\boldsymbol{y}$

1 Introduction

1.1 Motivation

In recent years the cost aspect of the development, production and operation of liquid rocket engines has become more and more important with respect to the competitiveness on the commercial satellite launch market. One aspect of the development is focused on the ability of reusing the entire launch system and its engines. The other aspect is focused on the development of novel inexpensive hot gas wall materials for inner liners of rocket combustion chambers that can withstand the extreme operational conditions. Actively cooled inner liners are usually made of high thermal conductivity copper-base alloys and their structural behavior is mainly governed by low-cycle fatigue, ratcheting, and creep at elevated temperatures. Due to a combination of ratcheting-caused tensile rupture and thermomechanical fatigue, the thickness of the cooling channel wall between the hot gas and the coolant decreases at every loading cycle until a doghouse deformation shape becomes apparent. This effect is primarily responsible for inducing cracks into the hot gas wall and limiting the fatigue life of rocket combustion chambers. In order to improve numerical life prediction analyses of regeneratively cooled combustion chambers, this demanding task is downsized to the experimental level by using inexpensive combustion-chamber-type thermomechanical fatigue (TMF) panel experiments. These TMF panel experiments are used to investigate the fatigue life of a full-scale rocket engine's single cooling channel experimentally, and to validate numerical analyses with state-of-the-art damage models.

This thesis describes an approach of validating a numerical fatigue life analysis to experimental results from a combustion-chamber-type TMF panel experiment. With regard to the numerical fatigue life analysis, a viscoplastic damage model basing on the work of Tini is extended by several effects (such as combined isotropic hardening and softening, microdefect closure, and thermal ageing) and implemented into a commercial finite element program. A one-way coupled fluid-structure interaction (FSI) analysis is carried out to compute the TMF panel's structural deformation and its fatigue life. Because the copper-base alloy CuCrZr is assumed to be a potential inexpensive material candidate for inner liners of future rocket combustion chambers, it is applied for both the TMF panel experiment and the rocket engine's inner liner. Finally, the difficult task of predicting the fatigue life of a combustion-chamber-type TMF panel experiment and, moreover, a rocket engine's combustion chamber is examined in this work.

1.2 State of the Art

The very first experimental study on low cycle thermal fatigue failure of cooling tubes for the application in a regeneratively cooled nuclear rocket nozzle was presented by Carden [1] in

1966. The authors demonstrated that thermal fatigue and increased high-temperatures holding times can be a serious problem and has to be considered in combination with low-cycle fatigue (LCF) for the fatigue life analysis of such complex structures.

Since the 1970s, numerical life prediction of thrust chambers was strongly encouraged by the National Aeronautics and Space Administration (NASA) for the development of the Space Shuttle Main Engine (SSME). From that point on, reusability became one of the most critical aspects of such complex fatigue life analyses.

In 1974, Miller [2] performed the first isothermal strain analysis of a regeneratively cooled rocket combustion chamber made of an oxygen-free, high conductivity (OFHC) copper inner liner and a electroformed nickel alloy structural jacket. A bi-linear approach was used to model the elastoplastic material behavior. The finite element model consisted of 34 elements using generalized plane strain formulation and taking into account thermal and pressure loads as well as temperature dependent material properties. As depicted on the left-hand side of Fig. 1.1, the analysis was carried out for chamber configuration and operation conditions corresponding to an experimental full-scale test. As a result of the analysis, the predicted fatigue life was overestimated by a factor of two. Based on Miller's structural model, Kasper [3] developed a simple graphical method to estimate the fatigue life in dependency on the total mechanical strain. Although Kasper's graphical approach was conservative because a larger strain range resulted in a shorter expected fatigue life, the authors showed that fatigue life was more dependent on thermally induced mechanical strain at high temperatures than to the pressure either in the chamber or in the coolant inlet. Another important aspect of Miller's work is that cyclic creep was identified to play a major role in accelerated failure of such structures due to cyclic mean stress and thermal ratcheting at high temperatures.

In accordance to the requirement of high performance and reusability of the SSME, the mechanical and physical properties of six candidate high performance rocket nozzle materials were investigated and presented by Esposito and Zabora [4]. The three candidates OFHC copper, the copper-zirconium alloy Amzirc and the copper-zirconium-silver alloy NARloy-Z were selected to be sufficient being applied in such reusable thrust chambers. Basing on Esposito and Zabora's work, Armstrong and Brogren [5] investigated the thermomechanical behavior and the fatigue life of a full-scale Plug Nozzle Thrust Chamber (see right-hand side of Fig. 1.1). The structural closeout wall and the inner liner wall of the Plug Nozzle Thrust Chamber was composed of electroformed copper (EFCU) and three potential copper alloys (i.e. OFHC copper, Amzirc, NARloy-Z), respectively. A two-dimensional finite element analysis was performed by using a plane-strain model with 281 elements taking into account elasticity, plasticity and creep effects as well as thermal strains. The authors concluded that fatigue life was strongly dependent on the operation conditions, the material selection and the applied thermal field. As a follow-up investigation, Armstrong and Brogren [6] performed a three-dimensional structural finite element analysis with a cylindrical model consisting of 72 elements. The same material parameters and loading history was applied. By comparing two-dimensional and three-dimensional results, the authors demonstrated that the two-dimensional analysis was able to capture the thermal strains but not the thermomechanical strains for which the three-dimensional analysis was necessary.

Further experimental investigations for a better understanding of the primary failure mechanisms in cylindrical rocket thrust chambers were strongly encouraged by Quentmeyer [7] in 1977. Cylinder liners made of OFHC copper, Amzirc and NARloy-Z were tested under similar cyclic conditions similar to Armstrong and Brogren. Quentmeyer showed that NARloy-Z and aged Amzirc had the best cyclic life characteristics. The left-hand side of Fig.

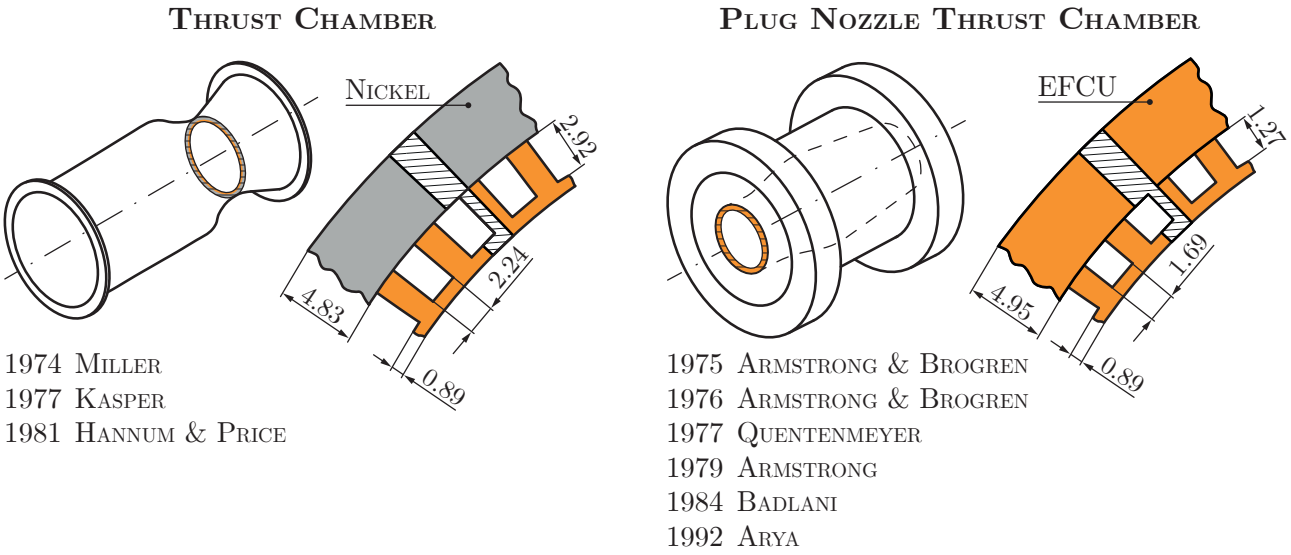

Figure 1.1: Investigations of thrust chamber configurations at the NASA Lewis Research Center with dimensions in mm.

1.2 depicts the experimentally obtained fatigue failure. Thinning and bulging of the cooling channel wall characterizes each failure mechanism with a remarkable deformation of the cooling channel's wall ligament. From that point on, this failure mechanism has become known as the doghouse effect. Quentmeyer concluded that every life prediction analysis has to take into account the deformation of the cooling channel's cross-section, the transient thermal field in the cooling channel wall, and the change of material properties during cyclic loading of the thrust chamber.

In addition to Quentmeyer's experimental work, Armstrong [9] demonstrated in 1979 that failure of regeneratively cooled rocket combustion chambers was not entirely governed by material fatigue but also by the plastic flow in the failed areas. Therefore, a thermal history of cyclic firings was applied to a finite element model with generalized plane-strain elements. The structural analysis of an OFHC copper liner showed that the inclusion of cumulative cyclic plastic effects enables the observed cooling channel wall thinning.

In 1981, Hannum and Price [8] conducted an experimental test setup on a cyclically loaded thrust chamber based on the work of Miller and Kasper with liners made of OFHC copper, aged Amzirc and NARloy-Z. On the one hand, the authors found that ratcheting was present in all fabricated thrust chambers until a crack was produced in the hot-gas-side wall. Only the failure mechanism observed with OFHC copper thrust chambers was consistent with the stress rupture type of the mechanism described by Quentmeyer related to the Plug Nozzle Thrust Chamber (see Fig. 1.2). On the other hand, the authors assumed that the previously observed bulging and thinning deformation of the cooling channel wall was supported by the roughening of the hot-gas-side wall surface due to an increase of the heat transfer coefficient at the inner radius of the thrust cell liner. Polishing of the liners after each cycle would increase fatigue life due to the reduction of the temperatures at the hot-gas-side surface. In the end, the number of cycles to failure of a polished liner was approximately similar as for an unpolished liner.

In continuation of Armstrong's work, a simplified analytical method for predicting the rocket engine thrust chamber life was developed by Badlani [10] in 1984. High pressure differences and time-dependent creep effects were taken into account. The author classified

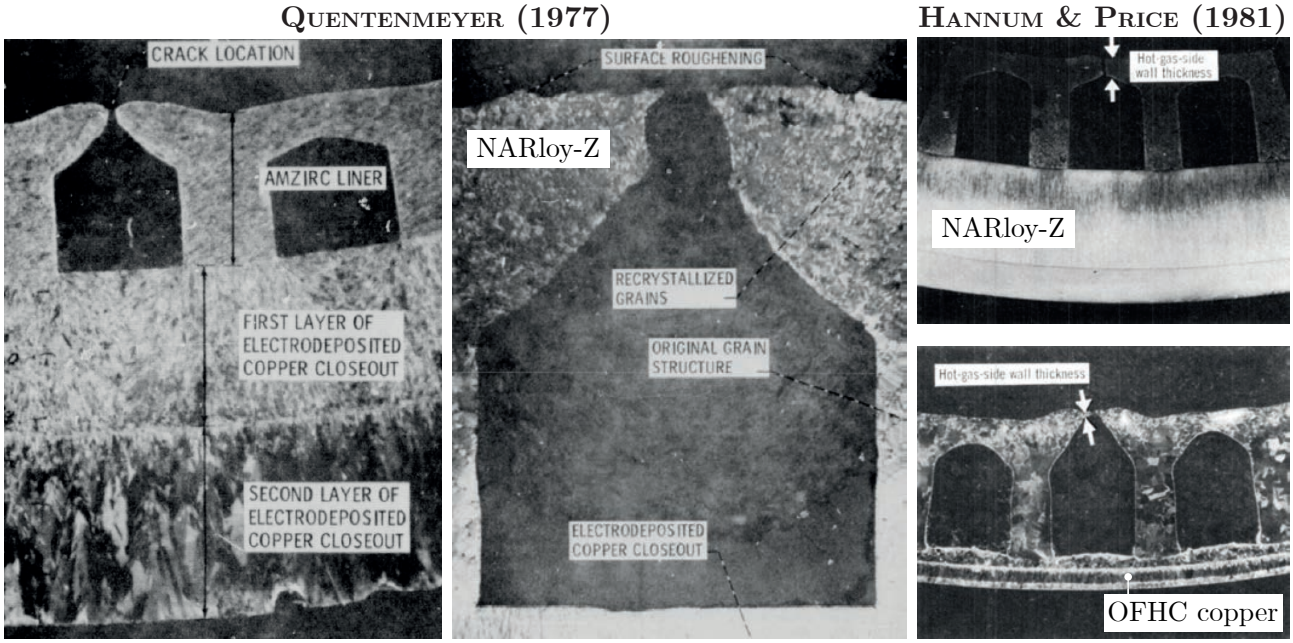

Figure 1.2: Cooling channel failure of different thrust chamber configurations made of OFHC copper, Amzirc and NARloy-Z [7, 8].

fatigue, creep rupture damage and plastic instability as possible failure modes and limiting criteria for the life of a thrust chamber. This simplified method was able to capture the number of firing cycles until plastic tensile instability failure; however, plasticity and creep effects of materials were not taken into account. In 1992, a viscoplastic stress-strain analysis with kinematic hardening (represented as a single internal state variable) was presented by Arya and Arnold. A nonlinear thermo-structural analysis was carried out to a finite element model consisting of 35 elements and 54 nodes to be compared to experimental results of the Plug Nozzle Thrust Chamber (see Fig. 1.1). In the end, this analysis was able to predict the doghouse effect and the thinning of the cooling channel wall. The authors concluded that such viscoplastic models were required to perform realistic nonlinear structural analyses of components related to complex thermomechanical loading conditions. In 1995, Dai [11] presented a continuous-time damage and life prediction model of the thrust chamber under steady-state and transient conditions based on a sandwich beam approximation. The authors concluded that the predicted life mainly depends on the applied material, the channel design, the pressure difference between chamber and channel, the wall temperature and the loading cycle duration. These results were confirmed by Butler and Pindera [12] in 2004. By variation of the secondary creep exponent of the employed Robinson [13] and Norton power-law [14] models (see Fig. 1.3), the authors demonstrated that the principal mechanism of the doghouse failure mode was related to the pressure difference between the cooling channel and the hot gas wall, the thickness of the cooling channel wall as well as creep and relaxation effects of the applied material. Butler and Pindera concluded that the effect of primary or transient creep needs to be addressed for short-term creep and relaxation response in combustion chamber liners.

During the last 40 years fundamental experimental and numerical work has been performed by NASA within the Space Shuttle program to aim for both, improving the prediction of a rocket combustion chamber's life and obtaining a better understanding of the governing hot gas wall failure mechanism caused by thermomechanical fatigue. Similar research activities

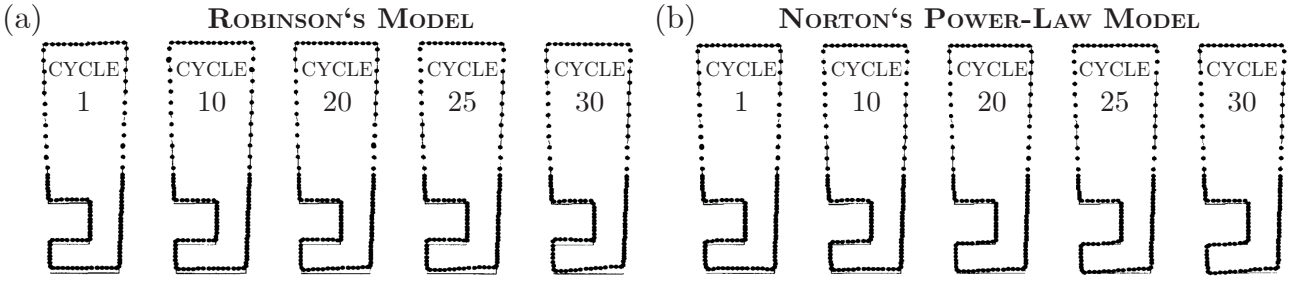

Figure 1.3: Predicted deformation of a NARloy-Z thrust cell liner for a 3.5-second loading cycle using creep models of Robinson (a) and Norton (b) [12].

were strongly encouraged in Europe after the structural failure of the main engine Vulcain of the European space transportation system Ariane 5 ECA.

In 2002, a coupled thermomechanical finite element fluid-structure interaction (FSI) analysis of a combustion chamber was developed by Kuhl [15] at the German Aerospace Center (DLR) in Lampoldshausen. A three-dimensional thermal fluid analysis was carried out and the results were applied to a two-dimensional nonlinear structure analysis to compute the cooling channel's flow, the heat transfer in the hot gas wall and the deformation of the hot gas wall ligament with regard to the local wall temperature distribution. A nonlinear elastoplastic material model with linear kinematic hardening was applied and bilinear plane stress finite elements were used. Kuhl's structural results showed that an analysis of a single loading process was not sufficient to predict the fatigue life of such combustion chambers. In contrary to the experimental results of Quentmeyer [7, 16] and Popp and Schmidt [17], the failure was then predicted on the hot gas side in the symmetry plane of the cooling channel fins where the highest plastic strains were observed. Therefore, Kuhl extended the analysis to cyclic loading and unloading. The cyclic repetition leads to an increase of accumulated plastic strains within every loading and unloading process resulting in thinning of the chamber wall, initiation of microcracks and finally to the doghouse deformation mode.

Later in 2006, Riccius [18] compared the influence of three different finite element analyses on the fatigue life of a typically rocket combustion chamber hot wall. He carried out two-dimensional plane strain, two-dimensional generalized plane strain and three-dimensional finite elements to a coupled thermal and structural analysis. The fatigue life was computed by the means of post-processing considering cyclic fatigue, quasi static (or ratcheting) fatigue and thermal ageing. By applying elastoplastic material behavior with isotropic hardening, the two-dimensional generalized plane strain analysis and the three-dimensional analysis resulted in a better coincidence with the real deformation of such a combustion chamber. However, the fatigue life was overestimated in all analyses.

Over the last years, computing capacities have been increased significantly; so that it is now possible to use complex damage models with coupled three-dimensional finite element analyses. In 2011, different model variants based on continuum damage mechanics (CDM) were implemented and compared by Schwarz [19]. For evaluating the damage distribution and the number of cycles to failure of a typical combustion chamber, the authors applied an anisotropic and an isotropic damage model with and without microdefect closure effect. It was concluded that the anisotropic damage model with microdefect closure effect fits best to model the doghouse failure of a combustion chamber's hot gas wall (see Fig. 1.4). According to further research of Schwarz [20, 21], it was shown that the main failure mechanism of the hot gas wall made of NARloy-Z was more related to tensile rupture than to fatigue. Macro-cracks

at the tip of the hot wall crack were characterized by irregular porous ductile fracture surfaces. On the right-hand side of Fig. 1.4, the final deformation of the applied mechanism-orientated model and the phenomenological model based on anisotropic damage with microdefect closure effect are compared to a scanning electron microscopy (SEM) recording. It can be seen that the doghouse effect could be reproduced very well with these models. However, the authors found that fatigue life of the regarded combustion chamber is overestimated by 25 %.

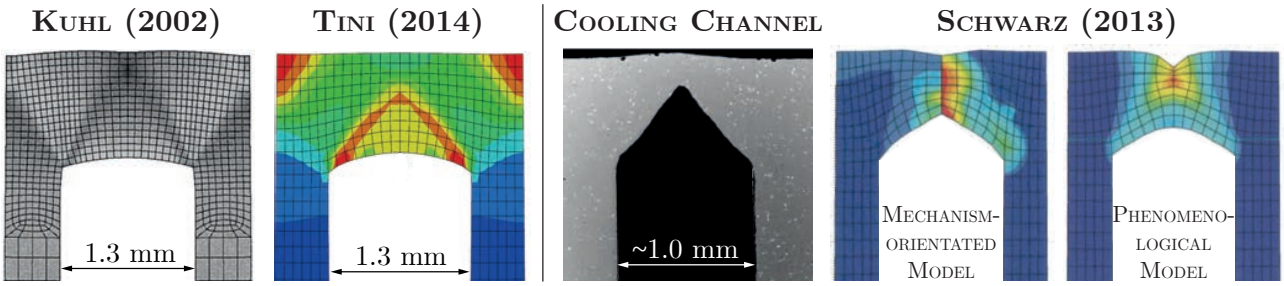

Figure 1.4: Comparison of numerical results from finite element analyses related to rocket combustion chambers [15, 21–23].

In 2012, alternative viscoplastic models coupled with damage and isotropic and kinematic hardening effects were presented by Tini [22, 24, 25]. By using isotropic ductile damage, a conservative fatigue life prediction of a rocket combustion chamber could be achieved. As depicted on the left-hand side of Fig. 1.4, more realistic numerical results regarding fatigue life and final deformation were obtained taking into account anisotropic damage and microdefect closure effect [26]. Tini concluded that the microdefect closure effect plays an important role for determining the evolution of damage.

One year later, Riccius [27] presented a fatigue life analysis of a simplified cut-out model of an actively cooled combustion chamber wall (the so-called TMF panel). The estimation of the life was carried out by using both an elastoplastic material model with kinematic hardening and isotropic softening and a post-processed cyclic mechanical strain difference (the so-called Manson-Coffin relation). In the end, the fatigue life was underestimated by 32 %.

On the basis of the work of Tini and Riccius, the viscoplastic material model including isotropic ductile damage is extended and applied to improve the prediction of the combustion-chamber-type TMF panel's fatigue life. Experimental test results are used to validate this fatigue life analysis. The knowledge obtained there is then transferred to a simplified rocket combustion chamber model that considers the copper-base alloy CuCrZr being a potential inexpensive material candidate for inner liners of future rocket combustion chambers.

2 Experimental Setup

2.1 Thermomechanical Fatigue Panel

TMF panels are small actively cooled sections of the hot-gas combustion-chamber wall that are subjected to cyclic laser heating. These inexpensive TMF panel experiments are used to study the fatigue life and the failure mode of novel materials without the need for testing a full-scale rocket engine. Although the TMF panel is a simplified representation of flight hardware, these fatigue life validation experiments are conducted as close as possible to realistic combustion chamber conditions [28].

2.1.1 Design

The second generation (2G) and the third generation (3G) combustion-chamber-type TMF panels are examined in this thesis (see Fig. 2.1). The two TMF panels are made out of the same raw material that has been already used for the first generation TMF panel designed by Riccius [27]. In contrary to the nickel and copper-base alloy sandwich structure of the first generation TMF panel, the galvanic nickel layer is omitted due to economical and manufacturing reasons. In particular, it avoids delamination of the nickel layer from the CuCrZr as observed during the test of the High Aspect Ratio Cooling Channel (HARCC) panel.

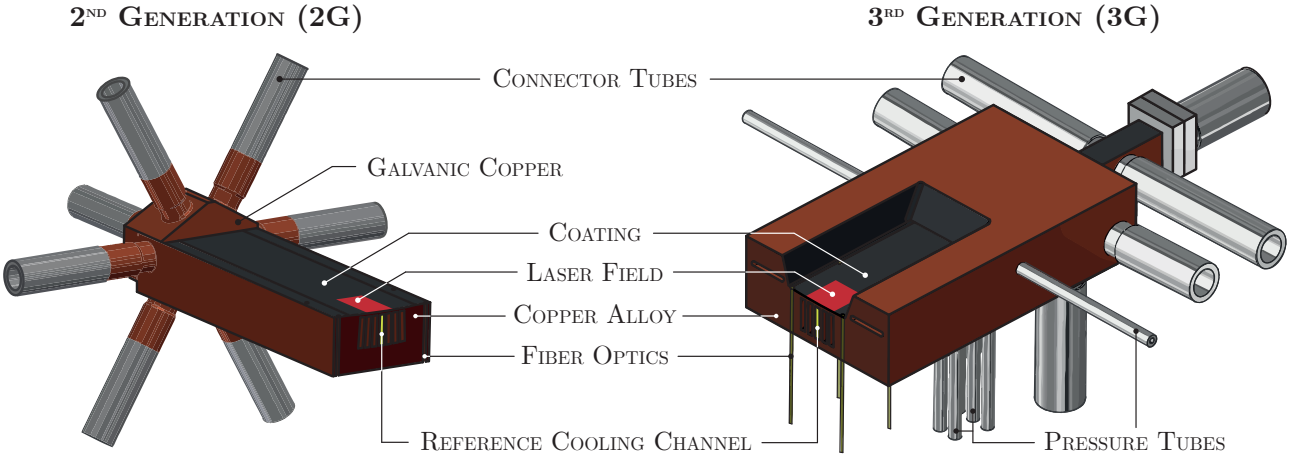

Figure 2.1: Schematics of the 2G and 3G TMF panel's half with cooling channels, connector tubes and illustrated laser field.

As depicted in Fig. 2.1, the copper-base alloy CuCrZr encloses all seven rectangular cooling channels of the two TMF panels entirely. The length of the copper part is 200 and 230 mm for the 2G TMF panel and the 3G TMF panel, respectively. Basing on the work of Kuhl [15], the

dimensions of the cooling channels in the cross-section is $l_{\text{Height}} = 9$ mm in height direction and $l_{\text{Width}} = 1.3$ mm in width direction. In combination with a hot wall thickness of $l_{\text{Thickness}} = 1$ mm around the laser loaded area, either the seven (2G) or the five (3G) cooling channels are radially arranged with a radius of $R = 130$ mm at an angle of 1°. Note that only the TMF panel's center cooling channel represents one cooling channel in a real combustion chamber's throat. The surrounding cooling channels are needed to minimize the heat flux in transversal direction. The outer cooling channels of the 3G TMF panel are rotated and moved outwards to decrease the temperature in this part (see right-hand side of Fig. 2.1). This modification should help to induce a hoop stress replacement compressive loading into the TMF panel hot wall which encourages both an accumulated tensile deformation of the laser-loaded surface and a doghouse failure of the center cooling channel wall. With regard to real combustion chambers, this hoop-stress-effect is induced by the surrounding super-cooled nickel jacket that carries the rocket's thrust load. To connect the TMF panel with the cooling fluid feed system of the TMF test bench, SWAGELOK connector tubes and SWAGELOK tube fittings are used. The connector tubes are made of a nickel-base alloy. The open endings of the wire-cut cooling channels are sealed with inlays made of the same nickel-base alloy by using laser welding again. The temperature and pressure of the 2G TMF panel is measured within the connector tubes before the inlet and behind the outlet. In contrast, the static pressure of the 3G TMF panel as well as the pressure drop in the cooling channels are measured directly in the cooling channels at a length of 88 mm ($2^{\text{nd}}, 4^{\text{th}}$ and 6^{th} channel) and 105 mm ($1^{\text{st}}, 3^{\text{rd}}, 5^{\text{th}}$ and 7^{th} channel).

Roughness along the cooling channel wall is measured with a KEYENCE VHX-5000 [29] digital microscope in combination with a KEYENCE VH-Z500R [30] high-resolution zoom lens that allows a magnification of 500 to 5000x. An area of approximately 6.5 x 6.5 mm is recorded by using the automatic three-dimensional stitching function that is provided by the microscope's software. In fact, 400 images are depth-focused and then assembled to one single image with an optical zoom of 500x. The left-hand side of Fig. 2.2 shows the averaged R_z-value (distance between highest peak and lowest valley) in wire direction and in wire movement direction of the 2G TMF panel's center cooling channel wall after testing. The profile line is averaged over 30 lines at a distance of 70 µm each ($\bar{R}_z$). One can see that the roughness in both direction is almost equal with a total averaged value of $\bar{R}_{z,2\text{G}} \approx 1.5$ µm. The right-hand side of Fig. 2.2 depicts the averaged R_z-value of the 3G TMF panel before testing. The profile line is averaged over 30 lines at a distance of 90 µm each. The roughness in wire direction differs from the roughness in wire movement direction by a factor of 1.6 to 2.16, respectively. Therefore, an averaged roughness value of $\bar{R}_{z,3\text{G}} \approx 1.16$ µm for 3G TMF panel's cooling channel surface can be assumed.

In addition, a high-emissivity coating is applied by means of physical vapor deposition (PVD) on the concave laser-loaded surface of the 2G TMF panel and the 3G TMF panel. The coating is composed of three layers. It increases the absorption of the infrared laser radiation into the TMF panel wall (leading to a higher temperature gradient along the laser-loaded wall) and it prevents oxidation of the copper surface. A stochastic speckle pattern made of aluminum oxide (Al_2O_3) with high contrast to the coating is applied on the coated surface. The speckle pattern allows the measurement of the surface deformation by using a stereo-camera system with digital image correlation (DIC) software. Finally, fiber optics with a diameter of 0.75 mm are used to adjust the laser beam onto the TMF panel's surface accurately and to define the coordinate system origin and the longitudinal direction within the DIC software.

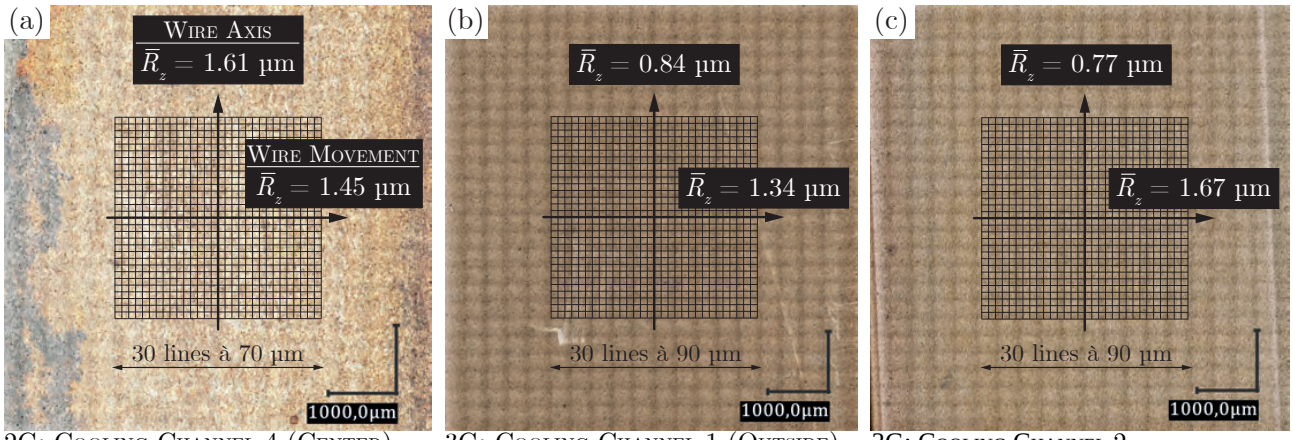

2G: Cooling Channel 4 (Center) 3G: Cooling Channel 1 (Outside) 3G: Cooling Channel 2

Figure 2.2: Illustration of the measurement area on different cooling channel walls with averaged roughness values in wire length and wire movement direction of the 2G's center cooling channel (a), the 3G's outer cooling channel (b) and its neighboring cooling channel (c).

2.1.2 Material Selection

As mentioned in Sec. 2.1.1, the copper-base alloy CuCrZr with components of chromium and zirconium is applied to represent the inner liner material of a thrust chamber. The high-conductivity CuCrZr alloy with moderate strength is procured as a rolled cold-worked plate of Elbrodur N provided by KME. This copper alloy is usually used as electrode material for welding [31]. It is assumed to be an inexpensive substitute compared to other copper-base alloys, such as NARloy-Z that has been already used as inner liner materials of the SSME and Vulcain as well as the copper-chromium-niobium alloy (GRCop-84) has been selected for application in the Reusable Launch Vehicle program [32]. In Tab. 2.1, chemical composition of the procured low-alloyed CuCrZr is depicted.

Table 2.1: Chemical composition of CuCrZr.

	Cu	**Cr**	**Zr**	**Ag**	**Fe**	**Al**	**Sn**	Other elements (max.)
wt.%	99.425	0.500	0.054	0.005	0.003	0.001	0.0008	0.012
at.%	99.326	0.604	0.039	0.003	0.003	0.002	0.0004	0.023*

*calculated with an assumed averaged atomic weight of 15 g/mol

For determination of the chemical composition, two specimens out of the procured material batch are cut into two parts. One part is solved in a mixture of nitric (HNO_3) and hydrochloric (HCl) acid. The other part is dissolved in a mixture of nitric (HNO_3) and hydrofluoric (HF) acid. Then, the elements of two solved specimens are determined by Inductively Coupled Plasma - Mass Spectrometry (ICP-MS) with a Thermo Scientific ICAP 6500 spectrometer, Inductively Coupled Plasma - Atomic Emission Spectroscopy (ICP-AES) with a Thermo Scientific ICAP Q mass spectrometer and Atomic Absorption Spectrometry (AAS) with an Elmer Perkin 2380 photometer. The relative measurement error of the semi-quantitative analysis is determined to be approximately 20 % of the measured value. Regarding Tab. 2.1, the procured copper alloy consists of a copper matrix including 0.5 ± 0.1-wt.% chromium, 0.054 ± 0.011-wt.% zirconium and other elements. The alloying component chromium prevents extensive grain growth after recrystallization at high temperatures [33, 34]. Zirconium refines

the grains and ties the oxygen within the structure [34]. It also enhances the strength by the decrease of inter-precipitate spacing of chromium precipitates and the precipitation of Cu_5Zr phase. Stress relaxation resistance is increased by the precipitation of the Cu_5Zr phase and the preferentially forming of Cu_5Zr precipitates on dislocations (see Fig. 2.3) [35]. Furthermore, Cu_5Zr particles suppress the grain growth more effectively than the chromium particles and provide additional hardening during aging [36]. Note that age hardening is limited by the solubility of chromium and zirconium in the copper matrix. The solubility of chromium and zirconium is 0.36 at.% and 0.11 at.% at the eutectic temperature of 963 °C (1236.15 K) [37] as well as 0.037 at.% and lower than 0.007 at.% at ambient conditions [38], respectively (see Tab. 2.2). Therefore, the solubility of chromium and zirconium in the copper matrix decreases with decreasing temperature.

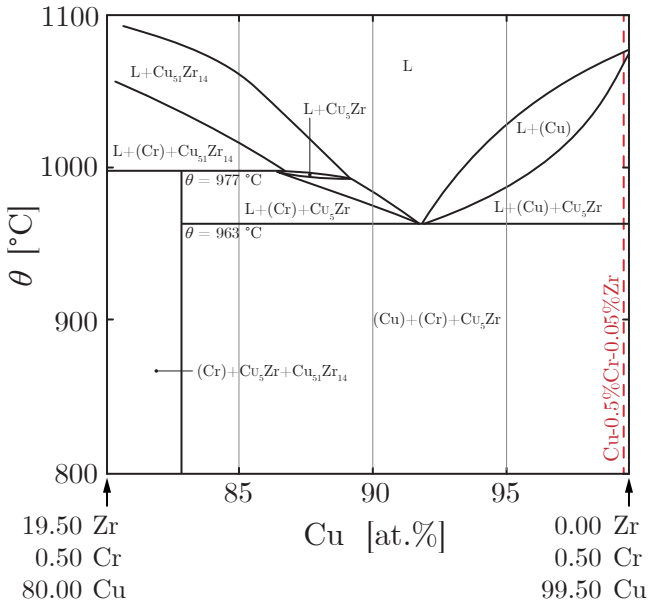

Figure 2.3: Binary phase diagram of CuCrZr with a constant Cr content of 0.5 at.% [37].

Table 2.2: Crystal structure data of CuCrZr at 963 °C [37].

Phase	**Composition (at.%)**		
	Zr	Cr	Cu
Cu_5Zr	16.7	0	83.3
(Cu)	0.11	0.36	99.53
(Cr)	≈ 0	≈ 100	≈ 0

Regarding the binary phase diagram of CuCrZr with a constant chromium content of 0.5 at.% depicted in Fig. 2.3, it can be assumed that this alloy consists of pure copper (Cu) with dissolved pure chromium (Cr) and Cu_5Zr phases - even if it gets heated up to 1000 K during TMF tests (hypoeutectic microstructure). To validate the components of the microstructure, two test samples with different heat treatments are analyzed with scanning electron microscopy (SEM) together with energy dispersive X-ray spectroscopy (EDX). SEM imaging is performed with a Zeiss Ultra 55 and secondary electrons. EDX imaging is performed with an Oxford Aztec. The minimal detection limit of the EDX is 0.1 wt.%. Please note that the weight content of zirconium (0.05 wt.%) is lower than the detection limit; therefore, zirconium can be only

detected in the presence of concentrated precipitations. The magnified section of the procured material shows a grey matrix and pits (see Fig. 2.4a). In accordance to Holzwarth [39], the typical size of the circular pits ranges between 0.2 and 2 µm (magnification of 2000x). However, two pits with a maximum diameter of approximately 10 µm could be detected by using lower magnification of 100x. The EDX analysis revealed a chromium contest between 60.83 to 88.15 at.% of the examined pits (see Attmt. A.1). Usually the chromium content should be dissolved completely (100 at.%) within the copper matrix [37, 39–41]. The reason is that the EDX-resolution of the region from which the characteristic X-rays are generated (interacting volume) is 1.5 µm^3. Therefore, the three-dimensional surrounding matrix is also analyzed due to the penetration depth of the X-rays [42, 43]. The EDX analysis of the grey matrix shows a copper content between 99.36 to 99.52 at.% with remaining traces of chromium (see Attmt. A.1). White particles of Cu_5Zr could not be detected because of the low zirconium content in combination with the EDX detection limit. But traces of Cu_5Zr are found near the borders of the pits (see Fig. 2.4a). This accords to observations of Holzwarth [39] who associated the white particles with the detection of zirconium. The authors also assumed that chromium precipitates around a core of Cu_5Zr are embedded in a pure copper matrix. Figure 2.4b depicts a test sample after ageing at 1000 K for 10 h. This test sample is cooled down in air without any quenching. In contrary to the procured material, distributed concentrations of white particles could be observed. Depending on the size of the particles, the EDX analysis examined a zirconium content between 4.78 and 11.74 at.% together with a copper content between 83.78 and 93.27 at.% (see Attmt. A.1). According to Zeng [40, 44], these white particles indicate phases of Cu_5Zr that exist in this system. Ageing at high temperatures leads to distributed spots of concentrated Cu_5Zr particles that would decrease strength and ductility of the aged material considerably.

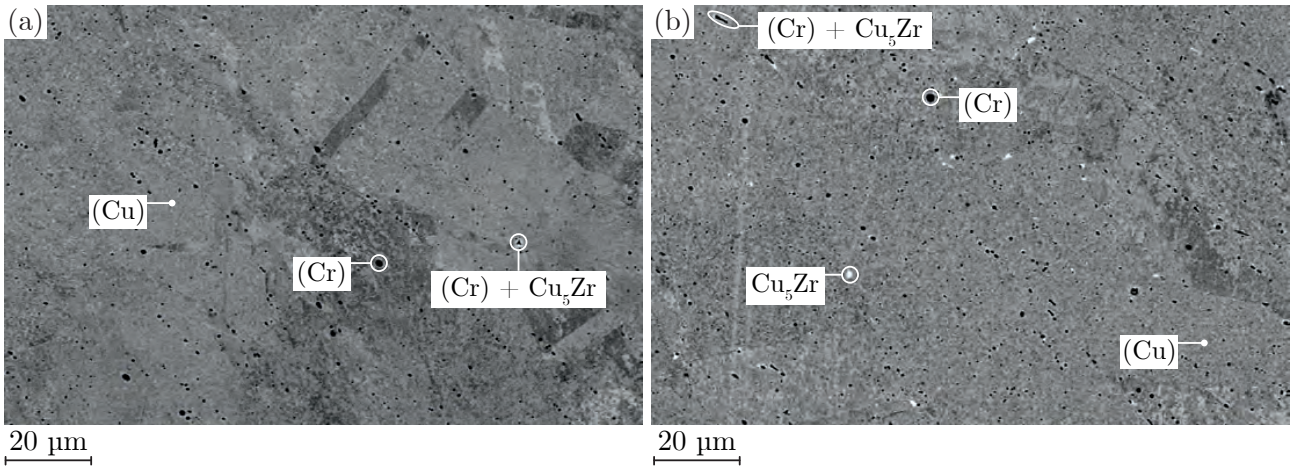

Figure 2.4: SEM images of samples taken out of the procured raw material (a) and after ageing up to 1000 K for 10 h (b).

Because the procured material is taken out of a rolled cold-worked plate, the grain structure is investigated by using a laser scanning microscope (LSM) Zeiss LSM 700. The examined surfaces have been polished with silicon dioxide (SiO_2, 0.05 µm) and milled chemically with potassium metabisulfite ($K_2S_2O_5$) dissolved in water. Note that these surfaces are directed towards the transverse rolling direction. The grain color indicates different grain orientations and the averaged grain size is determined by using ASTM E112 standard. The higher the averaged grain size number, the smaller the grains. Figure 2.5 (a-c) depict micrographs of the

procured, annealed (up to 1000 K) and aged material (20 h at 1000 K), respectively. The microstructure of the procured material is homogenous with fine and partly distributed coarse copper grains. The average grain size number within the finest structure region is 7.0 (A). A similar structure can be observed for the annealed material without any ageing. The average grain size number within the finest and coarsest structure region is 7.0 (C) and 6.0 (B). In contrary, the grains of the aged material are larger compared to the procured and annealed material. The average grain size is 6.0 (D) within the finest and 4.5 (E) within the coarsest structure region. Therefore, the structural change due to thermal ageing is an important factor and has to be taken into account with reference to the application of CuCrZr as an inner liner material in rocket engines. Note that both adjustment of temperature and time during heat treatment after casting and definition of the cold-forming degree need to be defined precisely.

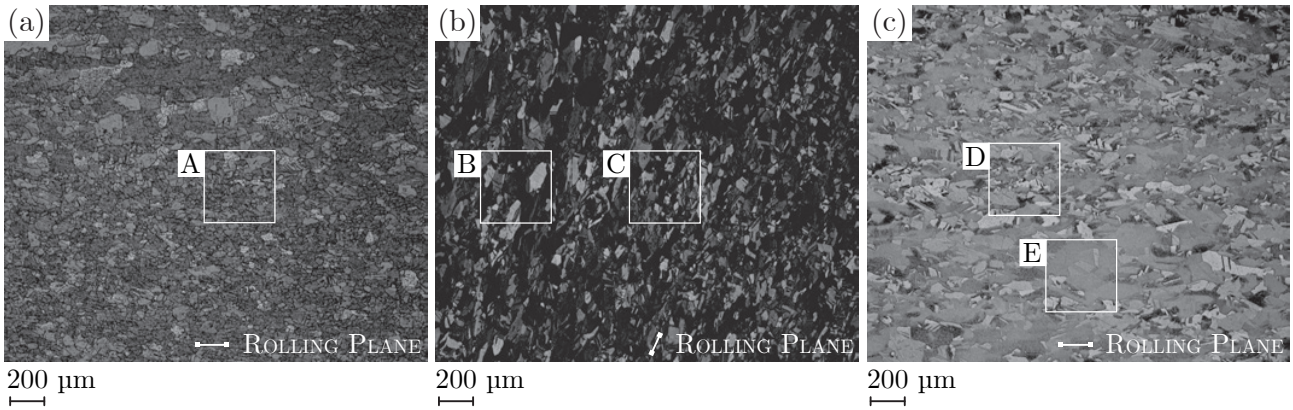

Figure 2.5: LSM images from material test samples of procured material batch (a), annealed up to 1000 K (b) and aged at 1000 K for 20 h (c).

2.1.3 Manufacturing

Wire-cut electric discharge machining (EDM) allows cutting without any forces between the tool and the structure. At first, it is used to separate a rectangular block with rough dimensions of the TMF panel out of the cold-worked raw material. To cut out the cooling channels, EDM pilot-hole drilling with a diameter of 0.5 mm is conducted through the entire block's length where the rolling plane is located. These drilling holes represent the starting points from where the radially oriented cooling channel contour is cut by EDM. In the next step, EDM is also used to cut the concave surface where the laser beam is applied. The diameter of the concave surface corresponds to the throat diameter of a 1000 kN liquid rocket engine's combustion chamber at a pressure of 100 bar. Regarding the 3G TMF panel, the upper part (the so-called pit) is removed by milling and holes for the connector tubes, sensors and fiber optics are drilled into the structure. After having machined the outer dimensions of the TMF panel as well as the cooling channels, a tube retainer made of pure copper is connected to each side of the TMF panel by using galvanic deposition. After having completed the two galvanic deposition processes, the holes for the connector tubes are drilled into the connector tube retainer precisely. Then, a thin layer of pure copper is deposited onto the surface of one half of the connector tubes that are made of stainless steel. The copper side of the connector tubes are then inserted into the retainers to get prepared for the follow-on galvanic deposition process of the entire 2G TMF panel assembly. In total, four galvanic deposition processes are needed to realize a non-leaking connection between the TMF panel and the TMF test bench's feeding lines.

2.1.4 Coating

As depicted in Fig. 2.1, a coating with high emissivity is applied on the wire-cut concave copper surface and the upper-side of the TMF panel by the means of vacuum arc deposition (Arc-PVD). Arc-PVD is a physical vapor deposition (PVD) process that is usually used to prepare hard nitride coatings on tools for industrial high temperature application. The main components of a vacuum arc coating system are a vacuum chamber, arc sources (anode and cathode), and a rotating substrate holder within the chamber [45]. To apply a coating layer on the TMF panel, the TMF panel is placed on the substrate holder and then connected to a current source that represents the anode. An arc discharge at high current and low voltage between the cathode and the anode generates a supersonic stream of fully ionized plasma that originates from the cathode material with a very high power density (up to 10^7 W m^{-2}) [46,47]. Depending on the cathode material, multiple layers with different properties can be applied successively. The coating of the TMF panel surface consists of three different layers: Titanium (Ti), nickel and chromium (Ni/Cr), and the high emissivity layer (HE). At first, the Ti-layer is applied on the TMF panel surface with a thickness of $s_{\mathrm{Ti}} \approx 0.1$ µm to increase the adhesion of the entire coating system. The intermediate Ni/Cr-layer is applied on the Ti- layer with a thickness of $s_{\mathrm{NiCr}} \approx 2$ µm. The Ni/Cr-layer acts as a barrier for oxygen and prevents oxidation of the copper surface. The high emissivity layer is applied with a thickness of $s_{\mathrm{HE}} \approx 6$ µm on top of the intermediate Ni/Cr-layer and determines the optical properties of the entire coating system. A PerkinElmer Lambda 950 UV/VIS spectrophotometer is used to measure the directed reflection of three coated specimens at a wave length range from 900 to 1000 nm at ambient temperature (see Fig. 2.6a). An averaged directed reflection of approximately 0.25 % is obtained at a laser wave length of 940 nm. Figure 2.6b shows measurements of the directed reflection at 10° with a PerkinElmer Spectrum 2000 FT/IR spectrometer at a wave length range from 1300 to 6000 nm at ambient temperature. The measured directed reflection at the narrow band pass filter wave length of 3990 nm is approximately 6 % at ambient temperature. The reflection properties of the coating system are important to specify the amount of laser power that is induced as a heat flux into the TMF panel's laser loaded wall. Note that the heat flux affects mainly the temperature gradient of the TMF panel's hot wall and, consequently, the temperature distribution of the entire TMF panel. Finally, a random speckle pattern made of aluminum oxide (Al_2O_3) is applied onto the coated surface to determine the displacement field by the means of digital image correlation (see Sec. 2.2.4).

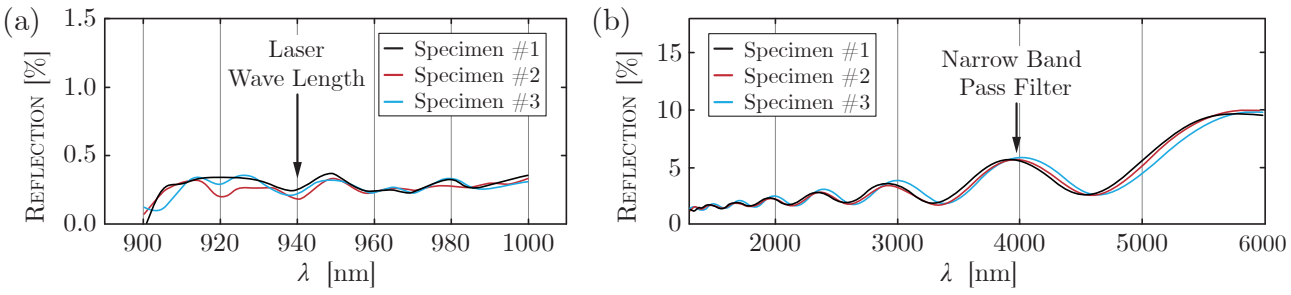

Figure 2.6: Measurement of the coating's directed reflection in a wave length range of 900 to 1000 nm (a) and 1300 to 6000 nm (b).

2.2 Test Bench

As mentioned already in Sec. 1.2, the very first thermomechanical test bench to study the thermal fatigue of cryogenically cooled rocket nozzles was presented by Carden [1] in 1966. The authors applied a heat flux of $q_{\text{Quartz}} \approx 1.1$ MW m^{-2} generated by a quartz lamp onto a thermal cycle specimen that consists of six coolant tubes bonded to each other onto a base plate. The tubes as well as the base plate are made out of the nickel-chromium-iron-molybdenum alloy Hastelloy X. During the cyclic heating tests over a period of either 15 s or 5 min, the tubes are constantly cooled with liquid nitrogen at cryogenic temperatures of $\theta_{\text{LN2}} = -200$ °F (128.89 K) to prevent the structure from melting. The maximum obtained temperature on the surface is $\hat{\theta}_{\text{tubes}} = 1900$ °F (1037.78 K) measured with numerous thermocouples. Carden concluded that thermal fatigue can be a serious problem for the coolant tubes of regeneratively cooled rocket nozzles and increasing the holding times at high temperatures can decrease the fatigue life significantly.

In Europe, the first test setup for investigating subscale structure components related to a liquid rocket engine was developed within the Flight Recovery Program of the Ariane 5 ECA launcher. Dump-cooled nozzle structures (the so-called tube wall panels) were tested under relevant thermomechanical loading conditions [48]. A laser system consisting of a diode laser and a Nd:YAG (Neodymium-doped Yttrium Aluminum Garnet) laser are used to apply a heat flux onto the tube wall panel's surface with a laser power of $P_{\text{Nd:YAG}} = 10$ kW at an area of 30 x 70 mm. In addition, pressurized supercritical nitrogen with a defined mass flow rate is used as a coolant representing the full-scale engine's nozzle extension dump cooling with supercritical cryogenic hydrogen. The panel structure is then cyclically loaded until failure. The experimental data obtained by these novel inexpensive thermomechanical panel tests could be used to validate finite element models with respect to life prediction of liquid rocket engine components [48–50]. In 2007, a concept for an improved test bench is presented by Riccius [49]. On the basis of this concept, Gernoth developed a thermomechanical fatigue test bench at the German Aerospace Center (DLR) in Lampoldshausen [51, 52]. Several TMF panels including a redesigned nozzle-extension-type TMF panel and the first generation combustion-chamber-type TMF panel (1G) were successfully tested at the TMF test bench M51. By using this test bench, Gernoth was able to create validation data for the verification of computational fluid dynamic (CFD) models and thermal finite element (FE) models as well as for the pre-qualification of newly developed hot gas wall structures and materials [27, 53, 54].

The main components of the test bench are a laser unit to generate the heat flux into the TMF panel structure, a fluid system to provide a mixture of liquid nitrogen (LN2) and gaseous nitrogen (GN2) as a coolant for the heated TMF panel structure, an infrared camera (IRC) to measure the maximum temperature on the TMF panel's surface, a stereo-camera-system (SCS) to record images of the TMF panel surface, a measurement unit to capture temperature, pressure and mass flow data, and a controlling unit to operate the TMF test bench. But before testing the combustion-chamber-type 2G TMF panel with seven cooling channels, two additional cooling channel feeding lines had to be added to the existing test bench (instead of only five feeding lines for the 1G TMF panel test in 2013) [28].

2.2.1 Diode Laser System

The diode laser system Dilas DL 100 consists of a laser head with a defined maximum optical output power of $\hat{P}_{\text{Laser}} = 11$ kW at a single wave length of $\lambda_{\text{Laser}} = 940 \pm 10$ nm, a

combined five-stack power supply with an integrated control unit, and a water cooling unit for the laser head and the power supplies. In particular, the laser head is composed of five diode laser units including 400 diodes each (2000 diodes in total) that are soldered to stacked copper bars and cooled with water at ambient temperature. On the targeted surface of the TMF panel a homogenized intensity distribution with an accuracy of better than ± 5 % is achieved. The homogenized intensity distribution of the laser beam leads to a top-hat intensity profile at an area of $A_{\text{Laser}} \approx 10$ x 32 mm at a working distance of $l_{\text{Laser}} = 415$ mm. Note that the laser optics within the laser head needs to be connected to a gaseous nitrogen supply for cooling and cleaning purpose during operation [55, 56].

To determine the output power of the laser system, the highly accurate power meter PRIMES POWERMONITOR PM DIODE is used. The laser beam enters the PRIMES PM DIODE and is then guided with a focusing mirror into a water-cooled cylindrical absorber. The cylindrical absorber enables very high absorption levels at very low back reflection. By measuring the cooling water flow rate and the respective temperature difference between the inflowing and the outflowing water, the absorbed laser power is determined with respect to the change of the water's enthalpy [57, 58]. Figure 2.7 shows results of the laser power measurements that have been performed after the TMF panel test. A maximum laser power of $\hat{P}_{\text{Laser}} = 11175$ W is measured at a maximum laser control voltage of $\hat{U}_{\text{Laser}} = 6.4$ V (corresponding to a maximum laser diode supply current of 64 A). The PM DIODE is specified with an accuracy of better than ± 3 % (± 335.25 W) and a reproducibility of ± 1 %. The slope of the laser power as a function of the laser output voltage shows a nonlinear behavior at low output voltages (A) and a linear behavior from low to high voltages (B) [54, 55]. By performing a regression, the resulting polynomial fit ($R^2 = 0.99$) for the laser power [W] as a function of the voltage [V ∼ 10 A] is

$$P_{\text{Laser}}(U) = -13.88074\ U^3 + 167.54108\ U^2 + 1631.07334\ U - 1845.1414 \tag{2.1}$$

with a linear constant slope of 2262.034 W V^{-1} between 2 and 6 V.

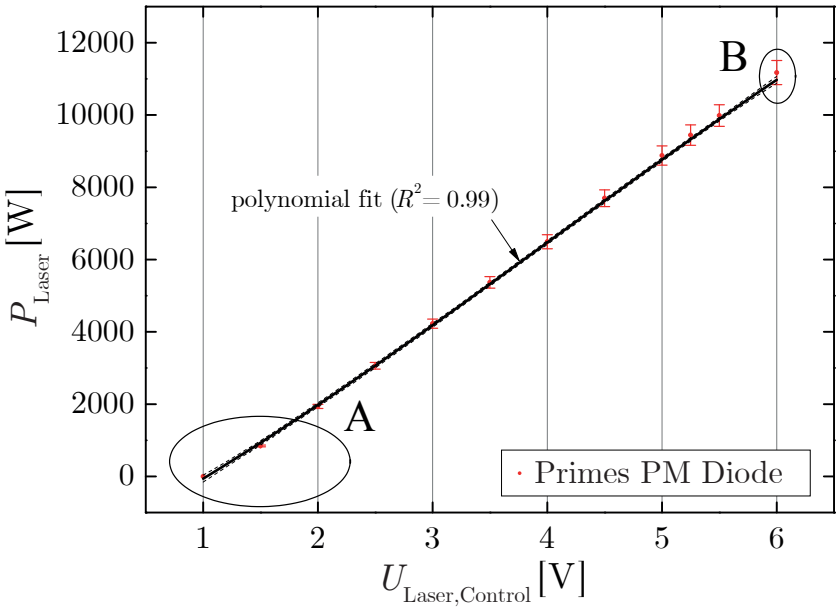

Figure 2.7: Laser power measured with a laser power meter PRIMES PM DIODE.

Furthermore, the beam profiler PRIMES BEAMMONITOR BM 100 is used to characterize the laser beam's profile and the laser beam's intensity distribution in the focal plane. The

BM 100 scans the laser beam with a rotation measurement tip and a linear moving mirror carrier. The partial laser beam is then deflected and guided towards the detector. During the measurement, the laser beam exits the BM 100 and needs to be absorbed by the water-cooled PM Diode [59, 60]. Figure 2.8 shows the two-dimensional results of the laser beam intensity distribution at an angle of 0° and 5°. An incline of 5° corresponds to the angle at which the TMF panel is mounted in front of the laser. It prevents the laser from damage due to reflecting laser light back into the laser optics. On the one hand, a rotation by 5° influences slightly the length of the top hat profile in longitudinal direction by approximately 0.3 mm (see left-hand side of Fig. 2.8). However, the difference between the two measurements in longitudinal direction is negligible. On the other hand, the top hat's width in lateral direction is decreased by 2.3 mm and its flank's angle is also lower compared to 0° (see right-hand side of Fig. 2.8). In the end, the total spot size can be estimated by 35.5 x 16.5 mm with an accuracy of better than ± 5 % (± 1.78 x 0.83 mm) of the beam diameter at an angle of 0°, and 35.5 x 18.1 mm (± 1.78 x 0.91 mm) with the similar accuracy at an angle of 5°. The spot size at the top-hat intensity can be estimated at 30.1 x 9.4 mm and at 29.8 x 7.1 mm, respectively. The resulting laser beam intensity is $\bar{I}_{\text{Laser}} \approx 29$ MW m^{-2} at a output voltage of $U_{\text{Laser}} = 6$ V taking into account an accuracy of better than ± 5 % (± 1450 W m^{-2}) for the two measurements.

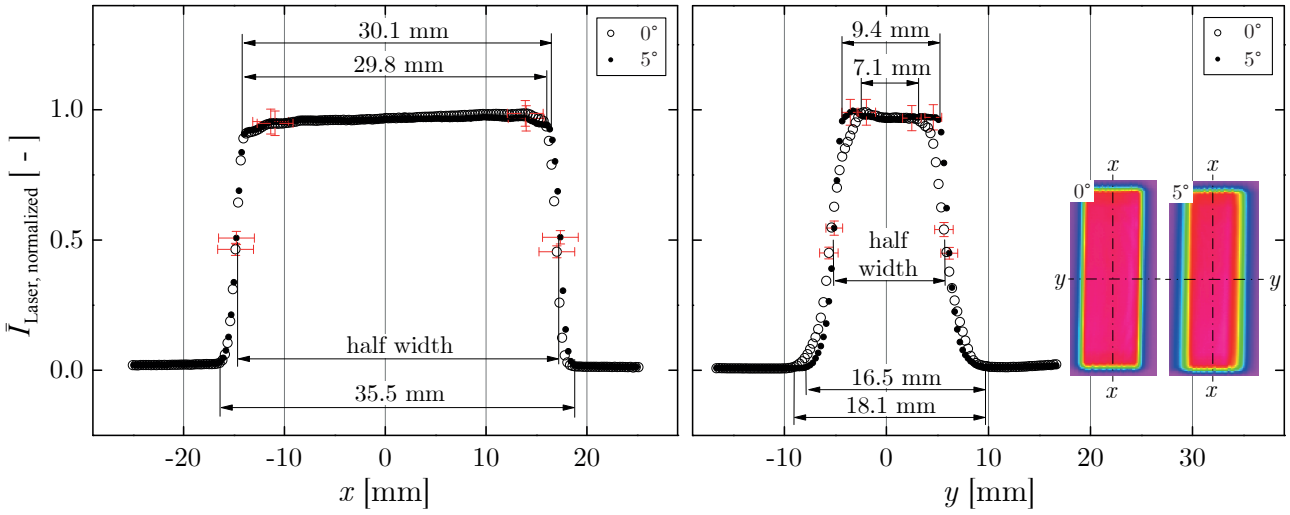

Figure 2.8: Intensity distributions in the focal plane of the laser with a normalized intensity profile along the symmetry axes x and y.

2.2.2 Fluid System

The cooling fluid feed system of the TMF test bench M51 provides nitrogen as a coolant for the laser loaded TMF panel. Although the combustion chamber is regeneratively cooled with liquid hydrogen, nitrogen is used for safety reasons instead. Figure 2.9 shows the flow chart of the test bench. The centralized nitrogen supply of the Lampoldshausen site of DLR provides gaseous nitrogen (GN2) at ambient temperature and a pressure of $p_{\text{GN2}} = 200$ bar (with two cryogenic reciprocating pumps operating simultaneously). The pressurized GN2 is then buffered by the means of two tanks with a volume of $V_{\text{GN2}} = 1$ m^3 each (in total 2 m^3). On the one hand, the GN2 is forwarded to the TMF test bench where a Swagelok magnetic pressure regulator (MPR) is used to flood the test area with depressurized GN2. This prevents condensation of air moisture on the tubes and on the TMF panel surfaces during cryogenic cooling. On the other

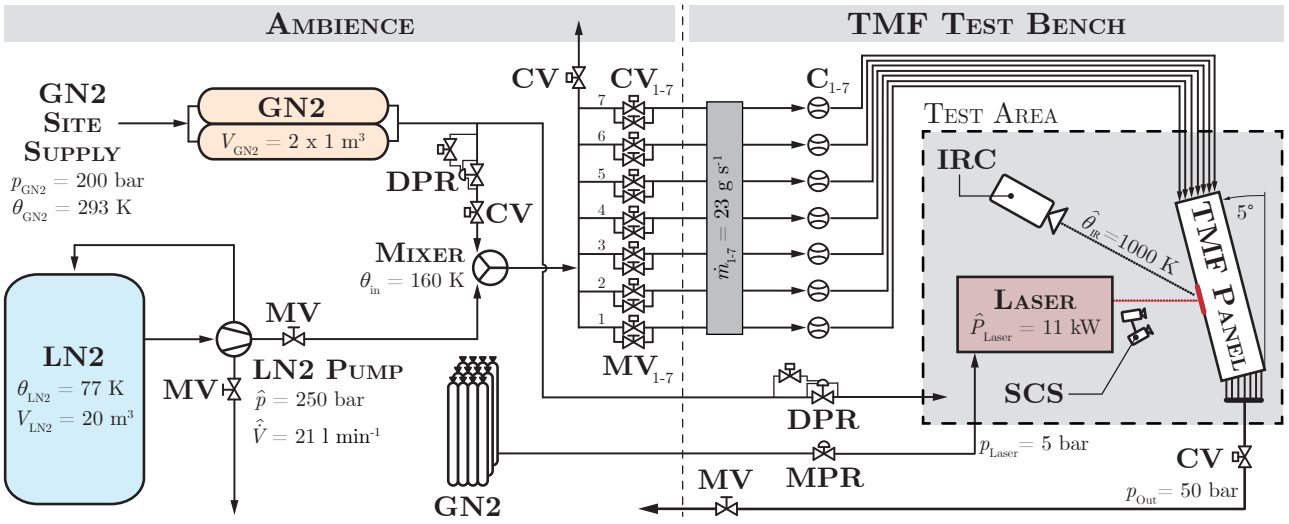

Figure 2.9: Flow chart of the TMF test bench M51 with pressure regulators (PR), control valves (CV), manual valves (MV), Coriolis flow meter, infrared camera (IRC) and stereo camera system (SCS).

hand, the GN2 is forwarded to the TMF feeding line system. The pressure and the mass flow of GN2 in the TMF feeding line is adjusted by a dome loaded pressure regulator (DPR). The specified coolant temperature of $\theta_{in} = 160$ K is obtained by mixing GN2 at ambient temperature with liquid nitrogen (LN2) at cryogenic temperature. LN2 is stored in a separate tank with a volume of $V_{LN2} = 20$ m^3 at a boiling temperature of θ_{LN2} (at a pressure of ≈ 5 bar). A cryogenic reciprocating pump provides LN2 with a maximum volume flow of $\hat{V} = 21$ l min^{-1} (0.00035 m^3 s^{-1}) and a maximum pressure of $\hat{p} = 250$ bar [61]. Vibrations of the LN2 system are decreased by using a pulsation damper together with several orifices [54, 62]. Behind the LN2-GN2-mixer, the single feeding line is split into seven separate feeding lines representing one cooling channel of the TMF panel each. For speeding up the chill-down process of the mixer, an additional control valve is used there to dump the premixed coolant into ambience before entering the testing area during chill-down of the fluid system. The mass flow of each cooling channel feeding line is adjusted roughly with manual valves (MV_{1-7}) and fine tuned with control valves (CV_{1-7}). Because each manual valve is critically flowed (corresponds to supersonic flow there), the coolant's mass flow can be adjusted independently from the fluid pressure in the TMF panel [54]. Note that due to the shape of the fluid duct of the manual valves, the valves have to be mounted against the given flow direction. To measure the mass flow in the cooling channels, Emerson Coriolis flow meters are used with a maximum possible mass flow of $\hat{\dot{m}}_{Coriolis} = 605$ g s^{-1} and a zero point stability of 0.0075 g s^{-1}. At ambient temperature, the relative accuracy of a Coriolis flow meter is $\pm$ 0.10 % and the reproducibility is $\pm$ 0.05 % of the measured mass flow value [63]. However, at LN2 boiling temperature, this accuracy is reduced to 0.5 % of the measured mass flow rate. The cryogenic supercritical nitrogen (acting as a gas) is then directed into the test area by a separate piping system to connect the mounted TMF panel with the test bench's feeding system. The diode laser, an infrared camera (IRC) and a stereo camera system (SCS) are installed next to the TMF panel in the test area. As mentioned already, the laser head of the diode laser needs to be cooled and cleaned with pure GN2. Therefore, bundled GN2 gas bottles are connected directly to the laser head. A manual pressure regulator is used to control the pressure of that separate GN2 flow. At the outlet of the

TMF panel, the separate cooling channels are merged to a single exit line. By using a control valve at the exit line, the pressure in the entire TMF feeding line system can be regulated to the desired outlet pressure of $p_{\text{out}} = 50$ bar. Finally, the nitrogen is released to ambience.

2.2.3 Infrared Camera

A FLIR SC7600 infrared camera (IRC) with a resolution of 640 x 512 pixels, a pixel pitch of 15 µm, a spectral range of 1.5 to 5.1 µm and a maximum acquisition rate up to 25 Hz is applied in the test area to measure the two-dimensional thermal field as well as the maximum temperature on the laser loaded side of the TMF panel (see Fig. 2.9) [64]. With regard to the laser's wave length ($\lambda_{\text{Laser}} = 940$ nm), the infrared camera contains an InSb (Indium Antimonide) detector with high sensitivity and noise levels better than 20 mK. A narrow band pass filter with a center wave length of $\lambda_{\text{N-Filter}} = 3.99$ µm is used to obtain a measurement range of 573.15 to 1773.15 K. This narrow band pass filter is mounted on a motorized four position filter wheel in the camera [64]. The manufacturer tolerance is lower than ± 1 % or ± 1 K above 373.15 K (emissivity coefficient of 1.0) of the measured temperature value proved by the calibration report of the infrared camera. In addition, a Spectrogon filter made of Germanium (Ge) with dimensions of 120 x 120 x 5 mm is used to block radiation in a range from ultraviolet (UV) to 2300 nm. Local cracks in the coating of the TMF panel would lead to a reflection of laser radiation from the pure copper surface and without the above mentioned long way pass filter, this reflected laser light would lead to a falsification of the temperature measurement. The 5-%-Cut-On of this filter is defined at 2500 ± 100 nm with a transmission of higher than 70 % up to 12 µm [65]. Finally, the infrared imaging software FLIR Altair is used to determine the two-dimensional distribution of the wall temperature on the laser-loaded surface of the TMF panel. To adjust the surface temperature during a hot run directly, either the laser power or the coolant's mass flow rate are tuned. After an initial mass flow rate determination phase, only the laser power is adjusted and the mass flow rate remains constant. Note that during laser heating, the outlet pressure increases by $\Delta p_{\text{out}} \approx 10$ %. The two-dimensional thermal field determined by the IR camera is then used to validate the thermal field that has been determined by a thermal finite element analysis (either by fitting film coefficients manually or by a thermal fluid flow analysis of the TMF panel). Note that the emissivity of the targeted material (coating with speckle marks) is dependent on temperature and needs to be determined experimentally before testing. In the TMF test, a constant emissivity coefficient of $\varepsilon_\alpha = 0.92$ is used to account for reflection of the PVD coating and applied speckle pattern.

2.2.4 Stereo-Camera-System

During the experiments, the TMF panel surface bulges towards the laser because of the pressure in the cooling channels and the extreme temperature gradient in the hot wall ligament. To evaluate the three-component displacement field of the TMF panel surface during cyclic laser loading, an optical (non-contact) stereo-camera system Limess Q-400 in combination with the digital image correlation (DIC) software Istra 4D (Dantec Dynamics) is used. This system comprises of two monochrome Prosilica GE4900 cameras, each contains a ON Semiconductor KAI-16000 progressive charge-coupled device (CCD) sensor. By using these cameras, images are acquired with a resolution of 4872 x 3248 pixels, an acquisition rate up to 3 Hz and a full optical sensor size of 35 mm. Both cameras are connected to the computer separately with gigabit Ethernet (IEEE 802.3 standard) to transfer the acquired data [66, 67].

In the TMF test, the acquisition rate is set to 1 Hz. In addition, two NIKON objectives with a magnification of 2.8x are mounted together with three serially mounted B+W infrared cut filter 489 (SCHNEIDER-KREUZNACH) on each camera. The infrared filters are needed to protect the cameras from reflected laser radiation within the self-contained test area. Synchronization of the cameras is ensured by a TU-4XB timing hub. The timing hub is connected to each camera with a coaxial cable and to the computer with an USB cable. Note that the timing hub is powered and controlled by the computer using NATIONAL INSTRUMENTS DAQMX software.

As mentioned already, the system performs high-precision measurements of three-dimensional coordinates and evaluates three-dimensional surfaces, motion, deformation and strain. A stochastic pattern of speckle marks made of aluminum oxide (Al_2O_3) particles is applied on the coated surface that increases reflection properties of the coating. The higher the contrast between the pattern and the coating, the lower the correlation residuum and the higher the accuracy of the correlation [68]. To overpower thermal emission of the TMF panel's hot surface, three MAGNUM-X LED lamps are used for lightning. In order to evaluate the object geometry from captured digital images, the imaging parameters of each camera (intrinsic parameters) have to be determined as well as the relative position and orientation of one camera with respect to the other one (extrinsic parameters) [69]. Therefore, a calibration is required before each test by using a calibration plate that is placed from different perspectives until matching accuracy is better than 0.01 pixels [68]. Basing on the calibrated camera settings, the three-dimensional coordinates of the object contour for each measurement step (that depends on the acquisition rate) can be evaluated. The displacement field on a surface is obtained by using a pseudo-affine coordinate transformation of points from two speckle images acquired from the stereo camera system at different loading stages [70,71]. By using the interconnections between the six light spots that are generated with the fiber optics onto the coated surface, a global coordinate system can be defined as a reference for the correlated values, e.g. displacement and strain.

2.2.5 Measurement and Control System

As depicted in Fig. 2.10, the entire measurement and control system is composed of three computers (measurement unit, control unit and laser measurement unit), two sets of amplifiers (AS4 and DEWETRON), a thermocouple reference unit (TRU), a watchdog counter (WDC) including a SIEMENS SIMATIC S7-1200 controller, an analog-digital converter (ADC), a cryogenic reciprocating pump control unit, a laser control unit, ten control valves, seven CORIOLIS flow meters, two powered magnetic valves, a dome loaded pressure regulator (GHR), several thermocouples and several absolute and differential pressure sensors. The construction of the measurement unit and the control unit is identical. LABVIEW software from NATIONAL INSTRUMENTS (NI) is used to acquire measurement data as well as to monitor and to control TMF test bench activities. Each unit is composed of multifunctional input and output (I/O) NI devices for attaching I/O signals of sensors and devices to each computer unit via PCI interfaces. The NI devices in the measurement and control unit operate at a nominal range of 0 to 10 V with an absolute accuracy of 1.077 µV (NI 6031E) to 3.100 µV (NI 6221). To measure the temperature values (θ) at inlet, outlet and the sidewalls of the TMF panel as well as before and after the mixer, ELECTRIC SENSOR thermocouples type K (Class 1) are used with a determined uncertainty of 1.35 K at 77.2 K (LN2) and a standard tolerance of ±1.5 K up to 375 K and $\pm\ 0.004 \cdot \theta$ up to 1000 K. The errors introduced by thermocouple loading are

removed by adjusting controller offset at 273.15 ± 0.03 K with an Isothermal Technology Limited TRUrac Model 847 (TRU) [72]. Then, the copper output wires of the TRU are connected to the AS4 amplifiers and thermocouple voltage values are amplified by a factor of 1000. The AS4 amplifiers are connected directly to the NI devices of the measurement unit. Note that the AS4 amplifiers with an accuracy of $^{+0.2}_{-0.5}$ % of the measured value was originally developed at the DLR Lampoldshausen [73]. Absolute pressure sensors are used to measure the pressure (p) at the outlet of all cooling channels, at the inlet of the center cooling channel and before and after the mixer. Furthermore, differential pressure sensors between inlet and outlet of each cooling channel are employed to measure the pressure drop. A constant supply voltage of $U = 10$ V is provided to the strain gauge based pressure sensors by the AS4 amplifiers and the Dewetron DEWE-30-32 amplifiers. By using the calibration coefficients of a quadratic polynomial function obtained from calibration reports, the pressure values are computed by the LabView program depending on their amplified input voltage. The mass flow ($\dot{m}$) is measured by a Coriolis flow meter in each cooling channel and it is acquired in the measurement unit with a NI serial interface device PCI-8431/8 and an eight-port serial adapter (COM). By using the COM interface, each Coriolis flow meter is adjusted to zero point with ProLink-III software before each test. The mass flow in each cooling channel is adjusted separately with the control unit. A watchdog counter is used to put the entire TMF test facility in a safe mode in case of interruption between either watchdog to measurement unit or watchdog to control unit. Examples of safe mode actions are full-opening of the control valves as well as sudden shut down of the cryogenic reciprocating pump and the laser. Furthermore, the rotational speed of the cryogenic reciprocating pump (n) and the laser voltage (U_{Laser}) between 0 and 6.4 V (V $\sim$ 10 A) can be set by the control unit and monitored by the watchdog counter. The laser power is then logged with respect to time in the laser measurement unit that is connected via Ethernet to the laser control unit. Finally, the watchdog counter provides power with a constant voltage of 5 V to the two Swagelok magnetic pressure regulators (MPR) and the GHR dome pressure regulator (DPR). The pressure of the DPR is also set by the control unit.

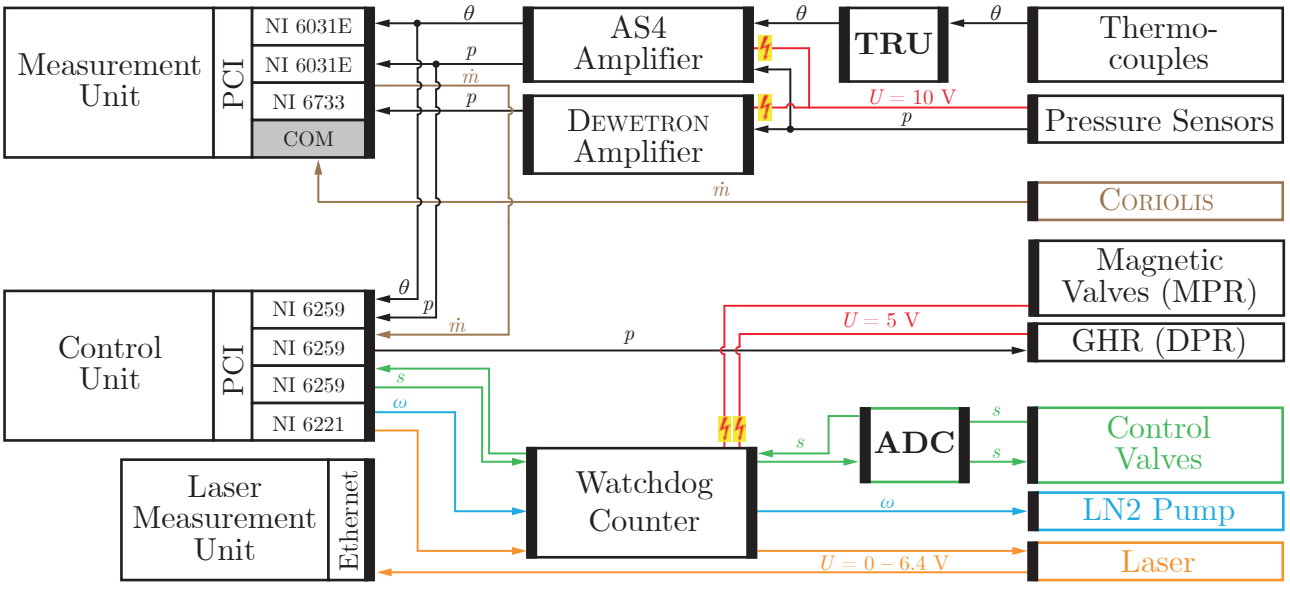

Figure 2.10: Measurement plan of the TMF test bench M51.

2.2.6 Holding System

Within the test area, each TMF panel is mounted in a separate holding system to ensure both, accurate positioning of the laser beam onto the TMF panel's surface and connection of the TMF panel without bending moments to the TMF test bench's feeding system. As depicted in Fig. 2.11, these holding systems consist of a main structure made of steel (2G) or Aluminum (3G), ball bearings (2G: 14x and 3G: 7x), pipe expansion joints (2G: 14x and 3G: 4x), SWAGELOK connectors with thermocouples (14x) and SWAGELOK connectors with pressure tubes (2G only: 14x). The main structure is mounted in the testing area and carries the TMF panel with its connectors. The ball bearings are also mounted at the holding system to allow movement of the TMF panel via pipe expansion joints due to thermal expansion or thermal contraction of the TMF panel. Regarding the 3G holding system, bending of the TMF panel in flow direction is also allowed with ball bearings at the back side of the main structure. SWAGELOK connectors with integrated pressure tubes are only used with the 2G holding system. The connectors are mounted in between the 2G TMF panel connectors and the pipe expansion joints feed the pressure sensors outside the testing area. The pressure tubes of the 3G TMF panel are laser welded on the structure; therefore, SWAGELOK connectors with pressure tubes are omitted for the 3G holding system.

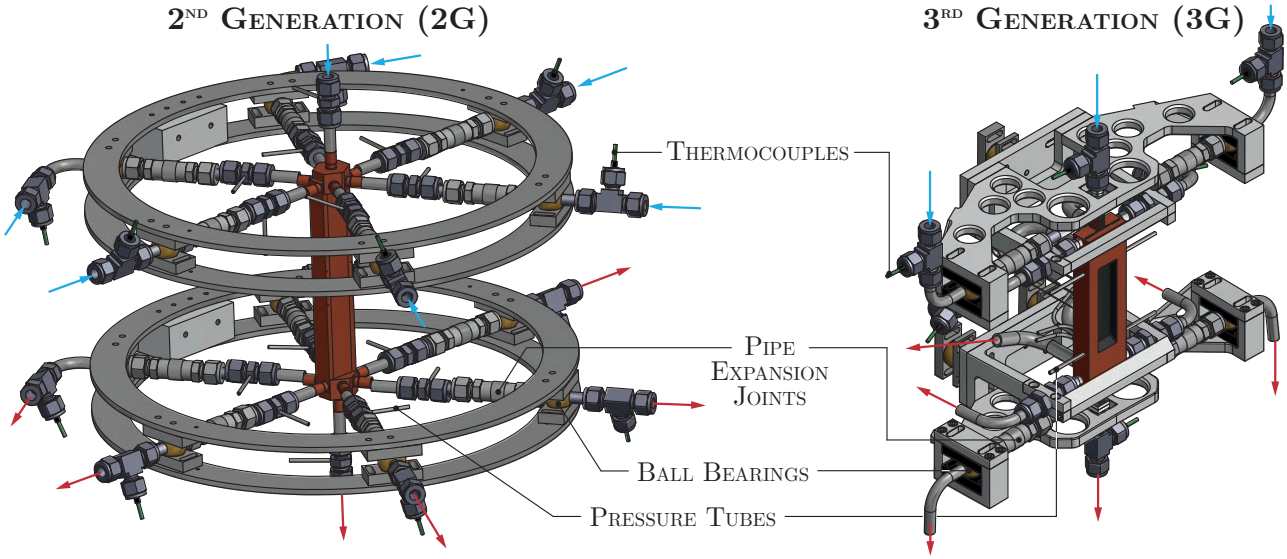

Figure 2.11: Schematics of the 2G and 3G TMF panel's holding system with pipes and connectors.

2.3 Experimental Results

An experimental test of the second generation (2G) combustion-chamber-type TMF panel made of CuCrZr is conducted to study the fatigue life and the failure mode under realistic combustion chamber conditions. In Tab. 2.3, the applied test conditions with tolerances and sensor accuracies of the TMF test setup are summarized.

As depicted in Tab. 2.3, a total mass flow rate of $\dot{m}_{\text{total}} = 161 \pm 3.5$ g s^{-1} , an absolute outlet pressure in the center cooling channel of $p_{\text{out,CCH4}} = 50 \pm 0.5$ bar and an inlet temperature in the center cooling channel of $\theta_{\text{in,CCH4}} = 160 \pm 2.0$ K are adjusted during steady state cooling of the

Table 2.3: Experimental test conditions of the 2G TMF panel test.

Parameter	Unit	Value	Tolerance	Sensor Accuracy	Sensor Type
$\dot{m}_{\mathrm{CCH}}$	[g s^{-1}]	23	± 0.5	± 0.115 (0.5 % at θ_{LN2})	Flow Meter
$p_{\mathrm{out,CCH4}}$	[bar]	50	± 0.5	± 0.1	Absolute Pressure Sensor
$\theta_{\mathrm{in,CCH4}}$	[K]	160	± 2.0	± 2.0	Thermocouple Type K
$\theta_{\mathrm{IR,max}}$	[K]	1000	± 1.0	± 10 (±1 %)	Infrared Camera

TMF panel. A wall heat flux of approximately $20 \cdot 10^6$ W m^{-2} is envisaged in this test. Taking into account a relative error of the Coriolis flow meter of 0.5 % for each cooling channel separately, the accuracy of the total mass flow is approximately ± 0.79 g s^{-1}. The absolute outlet pressure is measured in the outlet tube of the TMF panel's reference cooling channel at an accuracy of approximately ± 0.1 bar. In the same way, the inlet temperature is measured in the center of the inlet tube of the TMF panel's reference cooling channel with an accuracy of ± 2 K. During laser heating, all control valve positions are kept constant to ensure a steady state mass flow rate in the cooling channels. However, due to the heating of the coolant, the density of the coolant and its velocity is increased. This leads to an increased pressure drop in the pressure control valve downstream of the TMF panel and, therefore, the pressure in the cooling channels rise by ≈ 10% during the laser-on periods of the TMF panel test. The laser power is adjusted stepwise during laser loading to obtain an envisaged maximum surface temperature of $\hat{\theta}$ = 1000 K on the laser loaded surface. As mentioned previously, the two-dimensional surface temperature is captured with an infrared camera and an applied emissivity coefficient of ε_α = 0.92. Due to the fact that the emissivity coefficient and the laser area is constant, the laser power is proportional to the applied heat flux (see Eq. 3.19). To determine the total amount of heat that is absorbed from the coated TMF panel surface, the heating $Q_{\mathrm{N_2}}$ of the coolant is calculated by using the enthalpy difference $\mathrm{d}H_{\mathrm{N_2}}$ between the inlet and the outlet in each cooling channel

$$Q_{\mathrm{N_2}} = \sum_{i=1}^{7} \dot{m}_{\mathrm{CCH},i}\, \mathrm{d}H_{\mathrm{N_2},i} \tag{2.2}$$

leading to a calorically determined heat flux

$$\dot{q}_{\mathrm{caloric}} = \frac{Q_{\mathrm{N_2}}}{A_{\mathrm{Laser}}} \tag{2.3}$$

By using Eqs. 2.2 and 2.3, a caloric heat flux of $\dot{q}_{\mathrm{caloric}} = 19.29$ MW m^{-2} $^{+19.27}_{-23.02}$ % is calculated at the end of cycle 140 (randomly selected) where steady state heating conditions are assumed. The accuracy of this calculated heat flux includes maximum measurement uncertainties acquired from two Electric Sensor thermocouples to compute the temperature difference between inlet and outlet (± 4 K), from Schaevitz absolute pressure sensors at the cooling channel's outlet (± 0.022 to ± 0.1 bar), from Honeywell differential pressure sensors between the cooling channel's inlets and outlets (± 0.16 mbar), from Coriolis flow meters to obtain the total mass flow rate (0.7 %), and from the Primes BM 100 beam profiler to obtain the applied laser area (± 5 % per two-dimensional side length) (see Attmt. A.2). The temperature and pressure dependent enthalpy value is linearly interpolated from NIST RefProp database. Neglecting the uncertainty of the laser area measured by the beam profiler, the heat flux'

uncertainty decreases to ± 2.12 MW m^{-2} (± 11 %). Note that heat conduction through the feeding line tubes to the faraway fluid system is not taken into account. Therefore, it is assumed that the heat is entirely absorbed by the coolant in the cooling channels. Consideration of the heat conduction in axial direction of the tubes would increase the heat flux of the laser beam into the TMF panel surface.

2.3.1 Thermal Field

As mentioned previously, the thermal field is acquired in-situ during a TMF test with an infrared camera and a constant emissivity coefficient of $\varepsilon_\alpha = 0.92$. This emissivity coefficient takes into account reflection properties of the PVD coating. Additional longwave-pass filters are used to prevent misinterpretation of reflected laser light as radiation emission of the TMF panel surface in areas where the PVD coating has been delaminated and blank copper surface appeared (see Sec. 2.2.3). The temperature measurement is used for both, to monitor and to control the maximum surface temperature $\hat{\theta}_{\mathrm{IR}}$ and to validate the temperature gradient of the numerical analyses. Figure 2.12a shows the thermal loading history of a selective point taken out of the center of the acquired two-dimensional temperature field. A transient heating slope up to 18 s is observed there after the laser has been switched on instantaneously. Then, the temperature remains constant until the laser holding period ends at 200 s. Finally, the laser is ramped down linearly within 10 s at the end of the loading cycle. Comparison of the 50^{th} and 350^{th} cycle's transient thermal loading on the selective point shows a similar behavior; so that the difference between the two slopes is negligible. This indicates a low variation of the heat transfer coefficient on the depicted measurement point during an entire TMF test. In addition, the two-dimensional temperature field of different cycles under steady state conditions is depicted in Fig. 2.12b. Due to the high thermal conductivity of CuCrZr, a smooth symmetric temperature distribution is obtained at the first 100 cycles. In other words, the structure is almost certainly undamaged until then. With regard to the 200^{th} cycle, the temperature distribution narrows by approximately 20 % towards the longitudinal symmetry axis and becomes more and more asymmetric on the interfaces between 850 and 950 K. A reason could be that the development of microcracks and voids during cyclic thermal loading affects the thermal conductivity of the TMF panel material and, therefore, also the heat flow throughout the structure. With regard to rupture cycle (369), two temperature spots with decreased temperature level are identified caused by permanent surface deformation and thinning of the laser loaded wall. Surface deformation leads to undirected reflection of the infrared laser light that is interpreted as temperature by the infrared camera. Assuming a constant heat flux, a constant thermal conductivity and a constant cooling channel wall temperature, wall thinning and macrocrack development lead to a decreased hot wall's temperature gradient and, as a result, the surface temperature decreases (see Eq. 3.16). Note that the maximum temperature of $\hat{\theta}_{\mathrm{IR}} = 1000.05$ K is located apart from the symmetry axis in longitudinal direction (see Fig. 2.12).

Figure 2.13 shows the temperature distribution that has been extracted along two lines passing through the maximum (a) and minimum (b) temperature points parallel to the x-symmetry axis and the y-symmetry axis, respectively. On the one hand, the maximum temperature peak (A) is slightly downstream of the laser beam intensity distribution's center (see Fig. 2.13a). This leads to an asymmetric heat loading profile in flow direction caused by the coolant's flow velocity. A dependency of the temperature distribution on the number of cycles could not be observed along the $x_{\max}$ line (in flow direction). On the other hand, the deformation of the

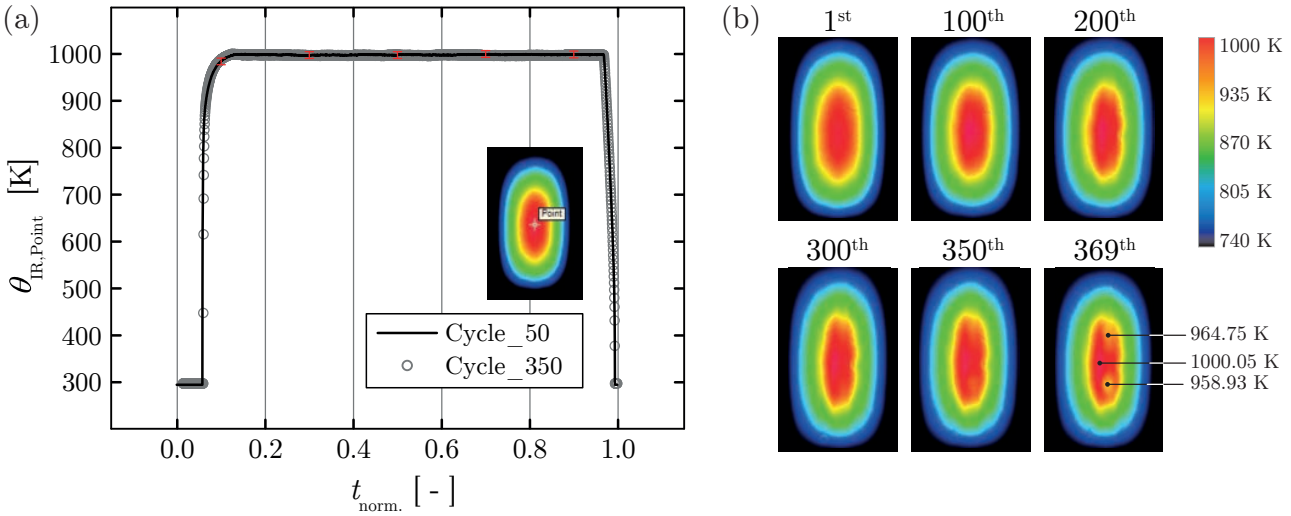

Figure 2.12: Results of temperature measurements by an infrared camera of a selected point during a laser loading cycle (a) and two-dimensional temperature distribution of different cycles (b).

laser loaded TMF panel wall due to cyclic thermal loading affects the temperature distribution perpendicular to the flow direction (see Fig. 2.13b). This can be observed at the rupture cycle 369 where a temperature drop occurs along the $y_{\min}$ line (B). The transversal temperature slope at the rupture cycle accords with optical deformation measurement results depicted in Fig. 2.20. Reasons for the temperature drop (B) could be variation of the emissivity coefficient coming from the copper surface radiating through the cracked coating. In addition, a decreasing temperature gradient with respect to increasing number of loading cycles (larger than 100 cycles) is determined at the beginning of the acquired temperature field in flow direction (C1) and at both sides in transversal direction (C2) as depicted in Fig. 2.13. One reason could be that cyclic thinning and bulging of the cooling channel walls affects the heat transfer between the TMF panel solid structure and the coolant; so that less heat is transferred into the coolant because of geometrical changes. Furthermore, successive surface deformation and corresponding coating delamination could also lead to a decreased absorption of the laser light into the coated TMF panel surface that would reduce the induced heat flux and temperature difference between coolant and hot wall, respectively. This accords with Gernoth [54] who performed TMF tests with nozzle-extension-type TMF panels. Note that the temperature's cut-off level at low temperatures (D) is caused by the narrow-band 3.99 m filter of the infrared camera.

2.3.2 Coolant Flow

The coolant flow throughout the TMF panel is mainly characterized by the mass flow rate per cooling channel ($\dot{m}_{CCH,1-7}$), the pressure at the TMF panel's outlet (p_{out}) and the temperature at the TMF panel's inlet (θ_{inlet}). During a TMF test, the mass flow rate is controlled by the positions of the control valves and the parallel connected manual valves for each cooling channel's feeding line before entering the TMF panel. The outlet pressure is controlled by the positions of the control valve and the serial connected manual valve at the outlet downstream of the TMF panel. The inlet temperature is controlled by the rotational speed of the cryogenic reciprocating pump. By operating with nitrogen under supercritical pressure and supercritical temperature conditions in combination with supersonic flow conditions within the manual

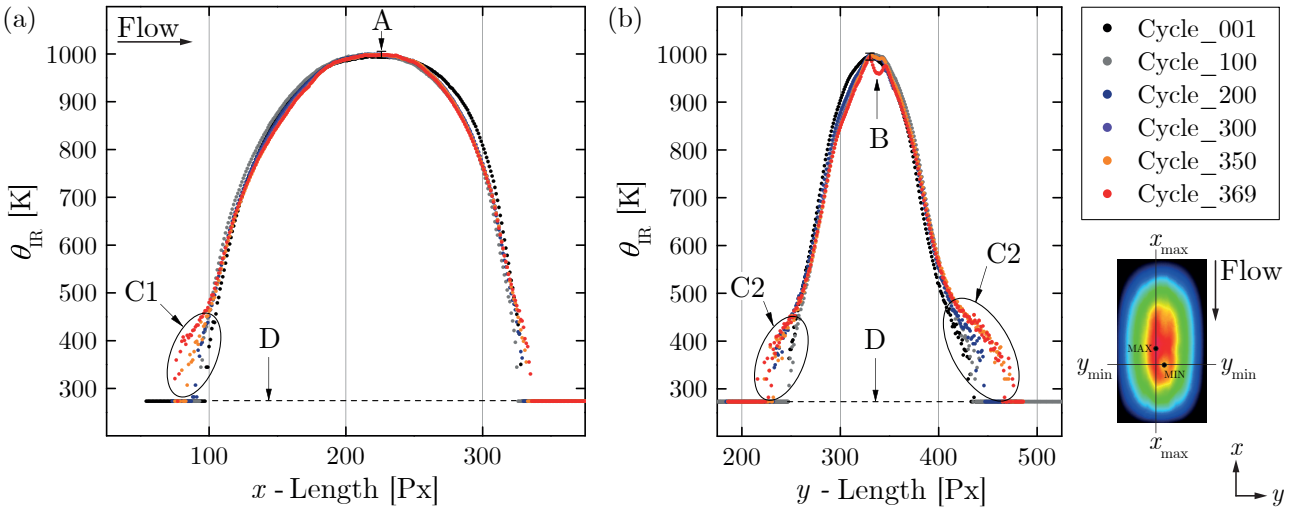

Figure 2.13: Temperature distribution along the $x_{\max}$ (a) and $y_{\min}$ (b) line for different cycles.

valves of the feeding lines, the mass flow rate and the outlet pressure can be controlled independently from each other. Note that only the outlet pressure and the inlet temperature in the reference cooling channel (CCH4) are considered in this section. As soon as steady state cooling conditions of coolant flow are reached within the given tolerances (see Tab. 2.3), the laser heating cycle is started. Figures 2.14 - 2.18 show the acquired data for the 1^{st}, 100^{th}, 200^{th}, 300^{th} and 369^{th} cycle of the 2G TMF panel test. Structural failure of the TMF panel occurred after completion of the 369^{th} cycle.

As depicted on the left-hand side of Fig. 2.14, the initial mass flow rate during the 1^{st} cycle is set to 42 g s^{-1} for each cooling channel with a total mass flow rate of $\dot{m}_{\text{total}} = 294$ g s^{-1}. This total mass flow rate based on results obtained from a preliminary CFD analysis. Stepwise ramping-up of the laser voltage from 2.3 up to 6.0 V lead to a maximum surface temperature of approximately 900 K in the first cycle ($\varepsilon_\alpha = 0.92$). In the following five cycles, the mass flow rate is decreased slightly down to 21 g s^{-1} until a maximum surface temperature of 1000 K is obtained with a laser voltage of $U_{\text{Laser},6^{\text{th}}} = 5.49$ V during the 6^{th} cycle. Therefore, the first cycles are used to adjust the mass flow rate with respect to a maximum surface temperature at an envisaged heat flux of approximately 20 MW m^{-2}. From the 10^{th} to the 95^{th} cycle, the mass flow rate is increased to 22 ± 0.5 g s^{-1} with an averaged laser voltage of approximately $\bar{U}_{\text{Laser},11-95^{\text{th}}} = 5.47$ V. Then, the mass flow rate is increased and held constant at 23 ± 0.5 g s^{-1} until the end of the TMF test. The right-hand side of Fig. 2.14 shows the mass flow rate for the 100^{th}, 200^{th}, 300^{th} and 369^{th} laser heating cycle measured with a Coriolis flow meter in each cooling channel feeding line separately. One can see that the cooling channel's mass flow rate decreases after switching-on the laser and increases after switching-off the laser. Unfortunately, the mass flow rate varies strongly in each cooling channel during laser heating. Usually, supersonic conditions are present in the manual valves that are parallel mounted to the control valves at each cooling channel feeding line. But the manual valves are mounted in the operational flow direction; so that the supersonic condition fluctuated within the feeding lines between control valves and TMF panel causing disturbances of the mass flow rate. In fact, the manual valves used here need to be mounted in opposite flow direction because of their structural construction in order to avoid this effect.

Figure 2.15 depicts two temperature measurements acquired with two Electric Sensor thermocouples type K. One thermocouple is mounted in the center of the inlet tube and the

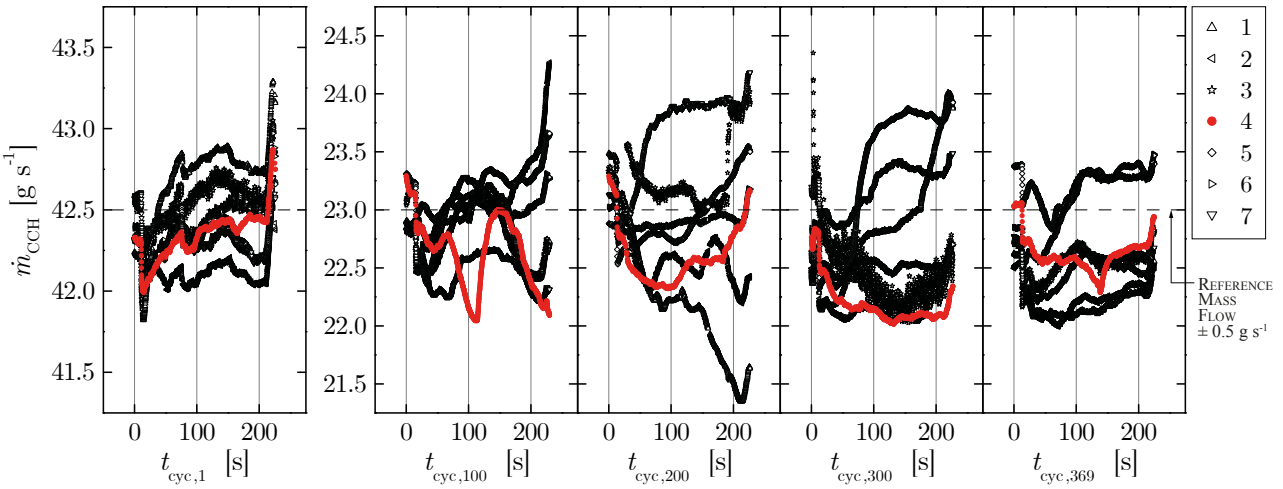

Figure 2.14: Mass flow rates of each cooling channel for different cycles.

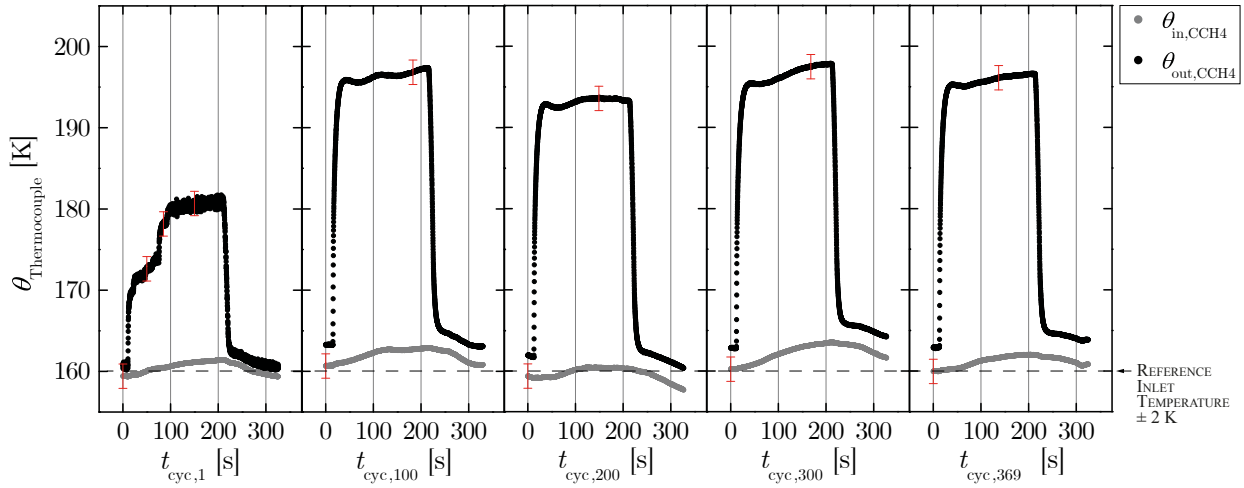

Figure 2.15: Inlet and outlet temperature of the reference cooling channel for different cycles.

other one is mounted in the center of the outlet tube of the TMF panel's reference cooling channel (CCH4). To ensure an exact mounting of each thermocouple in the center of the cross-flow within each tube, SWAGELOK fittings (T-piece) for pressures up to 250 bar are used. It is assumed that thermal stratification of the coolant in the outlet tube can be omitted due to mixture of the coolant when passing both the transition zone from rectangular cooling channel shape to the circular tube shape and the pressure sensor fitting as well as the pipe expansion joint. As already mentioned, the inlet temperature is adjusted to 160 ± 2 K. With respect to Fig. 2.15, the inlet temperature increases by approximately $\Delta\bar{\theta}_{in} = 2.16$ K due to pressure rise during laser heating. The outlet temperature of the first cycle is 12.44 K (≈ 181.71 K) lower compared to the average temperature rise of $\Delta\bar{\theta}_{out} = 33.99$ K (≈ 196.65 K) for the other cycles. In addition, the temperature offset between the inlet and the outlet thermocouple measurement is $\Delta\theta_{offset,1^{st}} = 1.26$ K for the first cycle. However, a relatively high scattering of temperature data (± 0.5 K) is observed during the pre-cooling period. The average offset for the other cycles is approximately $\Delta\bar{\theta}_{offset} = 2.72$ K with a 10-times lower scattering (± 0.05 K) compared to the first cycle.

The absolute pressure is measured with a SCHAEVITZ pressure sensor in the outlet tube of the TMF panel's reference cooling channel (see Fig. 2.16). By using a flow collector with all

outlet tubes connected together, the absolute pressure is equal at the end of each outlet tube. Only the pressure drop due to tube length, tube curvatures, SWAGELOK temperature fitting and pipe expansion joint from the flow collector to each pressure measurement position affect the outlet pressure in each cooling channel. As shown in Fig. 2.16, the laser heating leads to an averaged pressure rise of $\Delta\bar{p}_{\text{out}} = 5.66 \cdot 10^5$ Pa (5.66 bar) up to approximately $\bar{p}_{\text{out}} = 55.78 \cdot 10^5$ Pa (55.78 bar) in the reference cooling channel. While ramping-down the laser voltage, the outlet pressure decreases in a transient way; so that approximately 80 s are needed to reach initial conditions after switching-off the laser heating completely. One can see that a variation of the laser power directly affects the outlet pressure as well as the outlet temperature in the reference cooling channel. In the end, a constant cooling channel pressure of $55 \cdot 10^5$ Pa (55 bar) is employed at the cooling channel walls in structural analyses because the ambient pressure is omitted there.

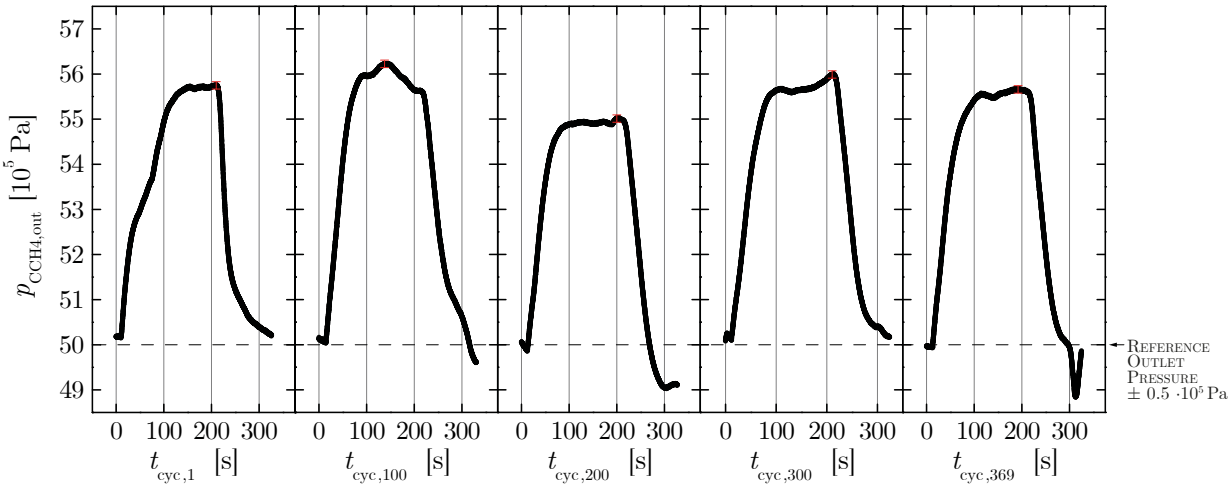

Figure 2.16: Absolute outlet pressure of the reference cooling channel for different cycles.

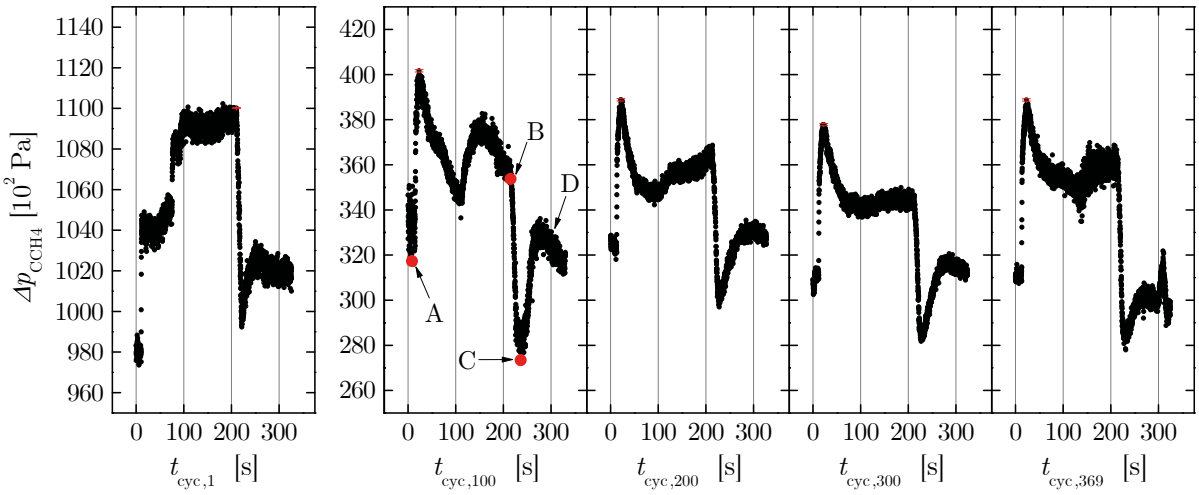

Figure 2.17: Differential pressure measured between the inlet and the outlet tube of the reference cooling channel for different cycles.

The differential pressure is measured with a HONEYWELL pressure sensor (see Fig. 2.17). The pressure sensor is mounted between the inlet tube and the outlet tube of the reference

cooling channel. A maximum differential pressure of $128.7 \cdot 10^2$ Pa (128.7 mbar) and $42.3 \cdot 10^2$ Pa (42.3 mbar) difference is measured in the 1^{st} and 10^{th} cycle due to variation of the mass flow rate, respectively. As soon as the laser is instantaneously switched on (A), the differential pressure rises. Then, the pressure decreases until stationary conditions depending on the cooling channel's mass flow rate. Ramping down of the laser (B) leads to a decrease of the differential pressure until the laser power is switched off (C). During post-cooling (D) the differential pressure is coupled to the mass flow rate again while the absolute pressure decreases transiently. Evaluation of the $100^{th}, 200^{th}, 300^{th}$ and 369^{th} cycle leads to a maximum average differential pressure rise between initial conditions and maximum peak of $\Delta \mathrm{d}\bar{p} = 78.3 \cdot 10^2$ Pa and to a averaged cooling channel's pressure drop of approximately $\Delta\bar{p} = 389.26 \cdot 10^2$ Pa. Because a pressure drop of approximately 0.78 % within the cooling channels of the TMF panel is relatively low, it is neglected in the structural analyses. So, only a constant pressure is applied on the cooling channel walls.

The adjusted laser power values are depicted for different cycles in Fig. 2.18. As already mentioned, the laser power is adjusted step by step during the first cycles to prevent thermal overloading (A) basing on results obtained from a preliminary CFD analysis. In the first cycle, a surface temperature of 900 K is obtained with a total mass flow rate of 294 g s^{-1} and a laser output voltage of $U_{\mathrm{Laser,1^{st}}} = 6.00$ V ($\approx$ 10974.54 W, see Eq. 2.1). Then, the laser output voltage is decreased as well as the cooling channel mass flow rate. At the beginning of cycle 95, the mass flow rate is set to 161 g s^{-1}. The average laser output voltage from the 95^{th} to the 369^{th} cycle is approximately $\bar{U}_{\mathrm{Laser,95-369}^{th}} = 5.49$ V ($\approx$ 9862.12 W according to Eq. 2.1). As shown in Fig. 2.18 the laser voltage is adjusted on-demand during laser heating (B) to ensure a maximum surface temperature of 1000 K that is measured with an infrared camera. Because of that, the heat flux could not be held completely constant during all heating cycles.

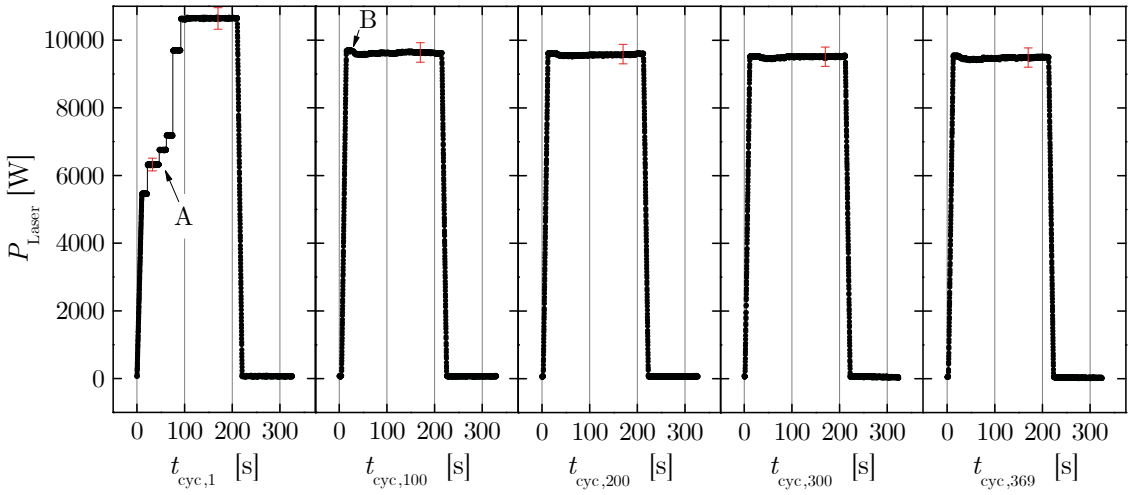

Figure 2.18: Laser power adjustment in LABVIEW for different cycles.

In the end, the operational conditions of the coolant are composed of three steps: Steady state cooling ($50 \cdot 10^5$ Pa, 160 K), heating of the coolant measured in the center of the outlet tube ($55 \cdot 10^5$ Pa, 195 K), and maximum heating within the thermal stratification of the coolant ($55.16 \cdot 10^5$ Pa, 951.3 K). With regard to the phase diagram of nitrogen illustrated in Fig. 2.19, the mixture of gaseous and liquid nitrogen operates at supercritical conditions but below the WIDOM line; so that the coolant is treated as gaseous single-phase nitrogen in fluid flow analyses. The WIDOM line (or pseudo-boiling line) represents a differentiation between liquid-

like and gas-like behavior of supercritical fluids [74]. According to Banuti [75], the Widom line can be calculated in the simplest case by

$$\ln\left(p_{\mathrm{r,pb}}\right) = 5.55\left(\theta_{\mathrm{r}} - 1\right) \tag{2.4}$$

where $p_{\mathrm{r,pb}}$ is the reduced pressure and θ_{r} is the reduced temperature of the Widom line. Note that the effect of pseudo-boiling reduces with growing pressure and becomes negligible for a pressure ratio of $p/p_{\mathrm{crit}} > 3$ [75].

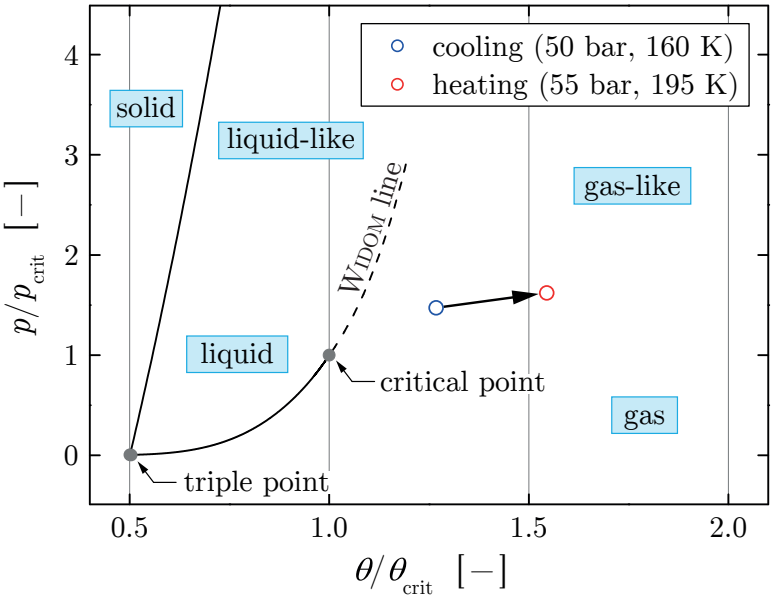

Figure 2.19: Phase diagram for nitrogen with Widom [75] line starting from the critical point at $p_{\mathrm{crit}} = 33.96$ bar and $\theta_{\mathrm{crit}} = 126.19$ K.

2.3.3 Deformation during Hot Run

The deformation during hot run is correlated from images that have been taken at the beginning of each test day at ambient temperature and pressure conditions. Unfortunately, the stereo camera system did not work properly from the 2$^{\mathrm{th}}$ to the 5$^{\mathrm{th}}$ day because of electric wiring issues related to the trigger cable connection between control unit and trigger box; therefore, only images at steady state conditions from the 1$^{\mathrm{st}}$ day and then continuously from the 6$^{\mathrm{th}}$ day to the 13$^{\mathrm{th}}$ day (test end) are available for correlation. As depicted on the right-hand side of Fig. 2.20, the coordinate system's origin is located in the center of the TMF panel surface where the two diagonals (coming from the four outer fiber optic endings) cross each other. Then, the x-axis is pointed through the intersection point of the diagonals coming from the four upper fiber optic endings. The z-axis points outwards of the TMF panel surface and follows the right-handed Cartesian coordinate system rule. However, a cylindrical coordinate system would be more appropriate for this case but it is not available in the used correlation software Istra 4D. To evaluate the out-of-plane deformation in z-direction, a y-z-cross-section is placed through the point where the correlated deformation is largest ($\hat{z}$). Then, the distance to the best fit x-y-plane is computed. Note that the best fit plane is generated automatically by the correlation software.

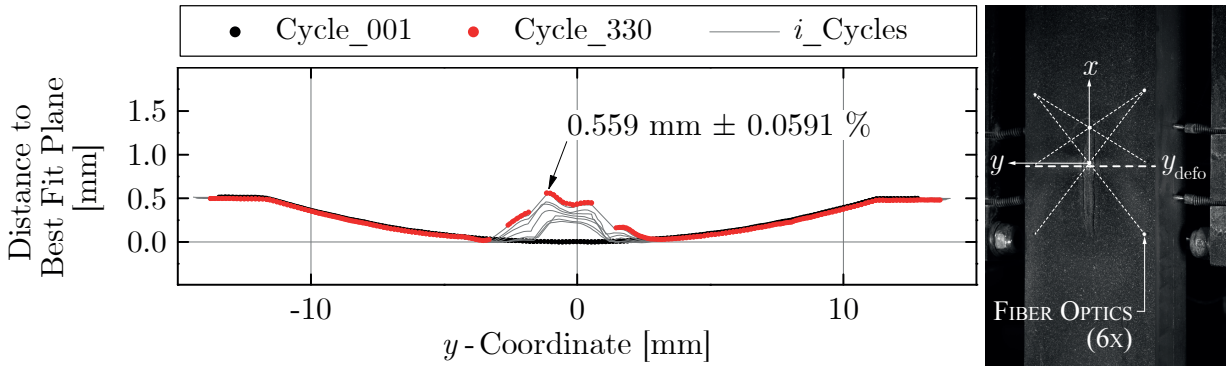

Figure 2.20: Cross-sectional out-of-plane displacement in z-direction of the laser loaded 2G TMF panel surface at different cycles (see Tab. 2.4).

The left-hand side of Fig. 2.20 shows the correlated out-of-plane deformation of the 2G TMF panel's surface along the y_{defo}-line. At the beginning of the last testing day, the maximum displacement in z-direction is approximately $\hat{z}_{330^{\text{th}}} = 0.559$ mm with a correlation error of $\pm$ 0.000591 mm. Correlation of the final deformation after rupture could not be conducted because of a smeared speckle pattern due to leaked nitrogen out of the crack. By performing a regression basing on correlated data depicted in Tab. 2.4, a resulting linear fit ($R^2 = 0.996$) of the maximum deformation $\hat{z}$ [mm] as a function of the number of cycles n_{cyc} [-] from the 1$^{\text{st}}$ to the 13$^{\text{th}}$ test day is obtained by

$$\hat{z} = 0.00139207\, n_{\text{cyc}} + 0.10423364 \tag{2.5}$$

On the basis of Eq. 2.5, the maximum assumed out-of-plane displacement after rupture can be estimated to $\hat{z}_{369^{\text{th}}} \approx 0.618$ mm.

Table 2.4: Correlated maximum out-of-plane displacement along the y_{defo}-line.

n_{day}	[-]	1	6	7	8	9	10	11	12	13
n_{cyc}	[-]	1	95	112	139	184	235	264	310	330
$\hat{z}$	[mm]	0	0.23491	0.26181	0.29995	0.36049	0.43312	0.45858	0.54916	0.55921

2.3.4 Fatigue Life after Cyclic Thermomechanical Loading

The successful TMF test was performed at 13 testing days until failure of the 2G TMF panel was reached after 369 cycles (including three short cycles) with an envisaged heat flux of $20 \cdot 10^6$ W m^{-2}. The failure is characterized by a crack that has been broken through the center cooling channel's laser loaded wall until coolant has been streamed out. On the one hand, the fatigue life of the 2G TMF panel is about 18.45 times higher than what we would expect from usual rocket engines. According to Haidn [76], this can be estimated to less than 20 cycles with a hot wall's plastic deformation of 3 to 4 %. On the other hand, the heat flux in common rocket engines is approximately four times higher compared to the TMF panel tests [77]. Therefore, the thermal gradient within the laser loaded TMF panel wall is four times lower compared to the thermal gradient in a rocket main engine's hot wall ligament.

Figure 2.21a shows the initial geometry in the cross section of the 2G TMF panel. Because the cooling channels are cut by EDM, an average radius of approximately $\bar{R}_{\mathrm{CCH}} = 0.22$ mm is obtained in the cooling channel's corners. In numerical analyses, idealized edges without radius (90°) are employed. By using an optical microscope with a digital measurement tool, the geometry of the two-dimensional TMF panel cut-out is measured at several positions (at least five measurements for each value) and then averaged. The average height and average width of the reference cooling channel are $\bar{l}_{\mathrm{Height}} = 8.73$ mm (initial value: 9.0 mm) and $\bar{l}_{\mathrm{Width}} = 1.28$ mm (initial value: 1.3 mm), respectively. The average thickness of the laser loaded wall is $\bar{l}_{\mathrm{Wall}} = 0.94$ mm (initial value: 1.0 mm) and the average thickness of the fins is $\bar{l}_{\mathrm{Fin}} = 0.94$ mm (initial value: 1.0 mm). In the end, the measured reference cooling channel's cross-section of $\bar{A} = 11.17$ mm^2 is approximately 4.49 % smaller compared to the idealized cooling channel's cross-section of $A_{\mathrm{Ideal}} = 11.7$ mm^2; so that the real cooling channel's flow velocity is increased by assuming incompressible stationary flow ($\dot{m} = Av\rho = \text{const.}$). A higher flow velocity would decrease the temperature at the cooling channel wall and, consequently, increase the heat flux applied onto the laser loaded wall to obtain a maximum surface temperature of 1000 K. The cross-section of a cut out from the ruptured 2G TMF panel after the TMF test is shown in Fig. 2.21b. As mentioned already, the crack occurred in the center where the reference cooling channel is located (A). The thickness of the laser loaded wall increased significantly at the fins next to the reference cooling channel (B). This observation accords with experimental results obtained from TMF tests performed with the 1G TMF panel that has been tested at 900 K and already presented by Riccius [27]. Finally, a doghouse failure could be observed in the center of the reference cooling channel as well as asymmetrically in the two adjacent cooling channels (C).

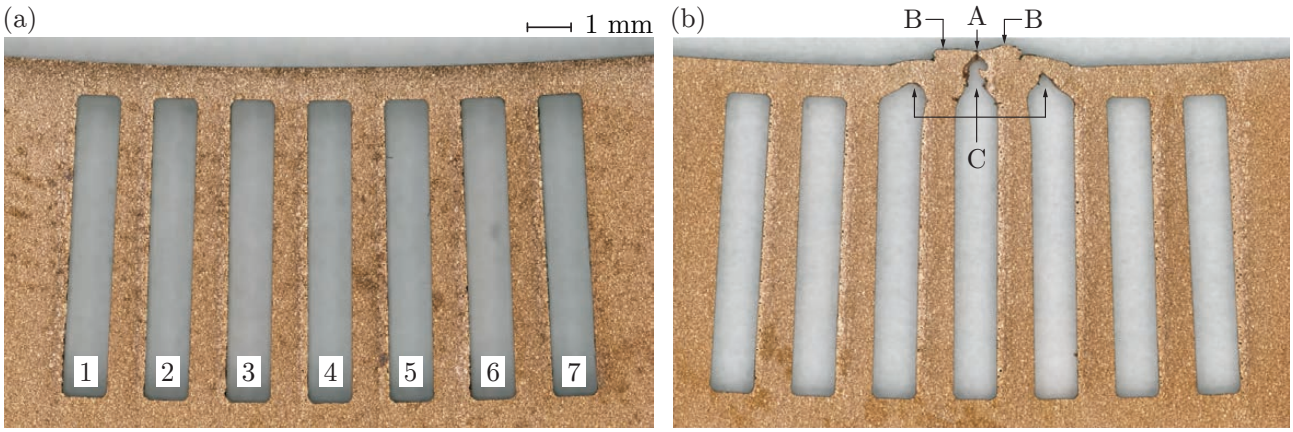

Figure 2.21: Optical microscope images from initial (a) and ruptured (b) 2G TMF panel cut out.

To draw a conclusion about the fatigue crack growth mechanism in the laser loaded wall of the 2G combustion-chamber-type TMF panel, several cross-sectional cut outs along the crack tip are investigated with a digital microscopy after the TMF test (see Figs. 2.22a-h). We assume that the failure mechanism can be divided into three stages: Firstly, the laser loaded wall bulges outwards because of the high wall temperature combined with the pressure in the cooling channels (A). The high wall temperature reduces stiffness significantly and accounts for creep effects during the laser-on holding period (200 s). In usual rocket engines, the protruding material would probably wipe off and surface roughness increases significantly due to blanching effect [78]. In the next stage, the doghouse deformation becomes apparent in the center of

the reference cooling channel (B). Finally, a macro crack starts to develop at the tip of the doghouse within the plastic zone (C). The macro crack evolves then vertically through the laser loaded wall. According to Donahue [79], the fatigue crack opens and closes in each cycle by a sliding off process during the tension stroke of each loading cycle (the so-called crack opening displacement). Similar to striations, the fatigue crack evolves cyclically until rupture of the TMF panel occurs (see Figs. 2.22e-h).

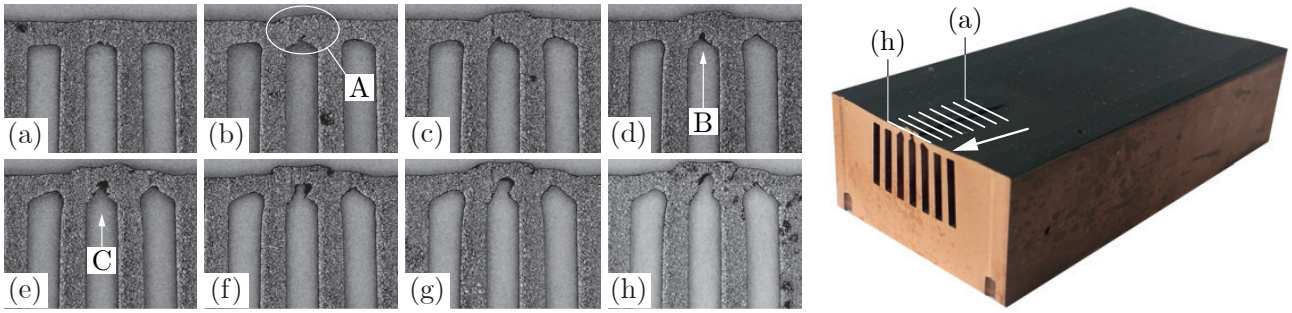

Figure 2.22: Cross-sectional cut outs along the crack of the ruptured 2G TMF panel.

2.3.5 Scanning Electron Microscopy of the TMF Panel

In addition to digital microscopy investigations of the 2G TMF panel described in Sec. 2.3.4, the main crack path and its fracture surface are examined in more detail by the means of scanning electron microscopy (SEM). The crack occurred in the center cooling channel from the channel's side straight through the wall to the bulged coated surface. In flow direction, a final crack length that's copper-color, contrasts the dark coated TMF panel surface and is determined to approximately 2.5 mm at the surface.

Before starting SEM investigations, the 2G TMF panel is cut in the cross section at the beginning of the crack and shortly behind the crack by EDM (see right-hand side of Fig. 2.23). Then, a cutting disc is used to cut out the damage region while the center cooling channel is split with a wedge to prevent the two fracture surfaces colliding together. The remaining part behind the crack is torn apart with a wedge; so that two parts of the center cooling channel are available for examination. The fracture surface of the one part is investigated with a Zeiss Discovery V12 stereo microscope and a Zeiss Ultra 55 scanning electron microscope combined with a FEI Helios 600i dual beam. Note that the SEM images are captured with detection of secondary electrons by Circular Backscattering (CBS) method. The other part is used to analyze the microstructure at the cooling channel's cross section with the Zeiss Axio Observer 7 light microscope [80].

Figure 2.23 depicts SEM images of the center cooling channel's crack in longitudinal direction. The length and width of the crack at the surface is 1.08 and 0.04 mm, respectively. Magnification shows a crack tip that is related to the first opening mode in fracture mechanics, i.e. the crack opens due to tensile stresses normal to the crack plane (A) [81]. This result accords to the mechanism of cyclic thermal expansion and contraction of the center TMF panel's laser loaded wall in transversal and longitudinal direction. Furthermore, a spiky profile along the thin crack edge is observed that indicates large plastic deformation (B) [80].

Fracture morphology is captured with a stereo microscope and it is depicted on the left-hand side of Fig. 2.24. Excessive plastic deformation of the center and the adjacent cooling channel is obtained after successful testing. Figure 2.24a shows a SEM image of the entire fracture surface

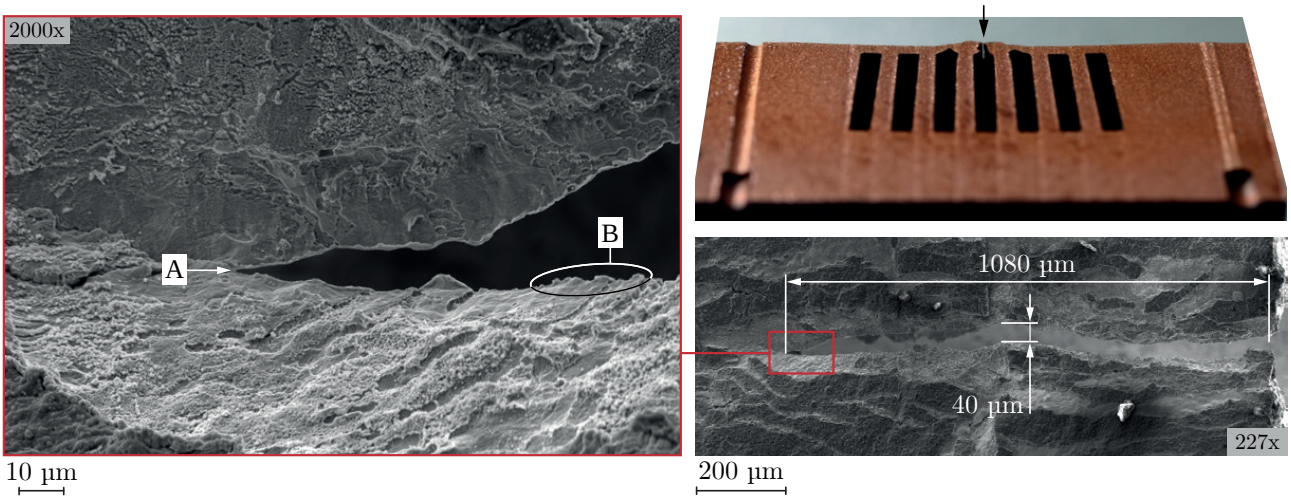

Figure 2.23: SEM images of the crack tip in longitudinal direction of the 2G TMF panel's center cut-out.

of at least one side of the longitudinal crack. One can see that the crack tip is shaped as a sharp edge with a smooth surface; so that the wall was joined together by a thin ligament with a thickness of 10 to 20 µm shortly before the failure (A). Diagonal striations on the ligament's smooth surface refer to a shear fracture. During the experiment, failure was recognized during post-cooling at 160 K and 50 bar. In other words, only the applied pressure caused final rupture of the cooling channel wall ligament until leaking of coolant through the crack is detected. In addition, the main fracture surface of the wall ligament is characterized by fatigue striations (B), grinding marks (C) and several microcracks. Fatigue striations are caused by cyclic crack growth. They are orientated perpendicular to the crack growth direction starting from the tip of the deformed cooling channel to the laser loaded surface. Unfortunately, a successive fatigue striation pattern is not observed due to both, material abrasion of collided fracture surfaces (grinding marks) during thermomechanical loading and strong oxidation of the crack's copper surface after the test. The distance between the existing striations is 3 to 10 µm though; so that an averaged crack growth of 5 µm per cycle is expected. With regard to a crack length of 1 mm and an experimental determined fatigue life of 369 cycles, the crack growth lasts approximately 200 cycles and could have started at the 169^{th} cycle (45.8 % of fatigue life time). Movement and collision of the crack surfaces are determined by regarding the grinding marks near the wall ligament and the arrangement of chromium precipitates within the fracture surface (see Fig. 2.25). Detected chromium particles have been grinded linear shaped and parallel arranged into the fracture surfaces; so that the movement of the crack surfaces during cyclic loading is assumed to be perpendicular to the laser loaded surface and perpendicular to the cooling channel's longitudinal direction [80].

A dimple structure (D) is observed at the upper side of the center cooling channel wall (see Fig. 2.24b). The diameter of the dimples is up to 5 µm. Such a dimple structure usually indicates a ductile failure due to micro void growth and micro void coalescence [81]. A similar structure with similar dimple diameter is observed by Schwarz [20] within the fracture surface of the hot wall crack that has been caused by a doghouse failure of a common rocket combustion chamber's cooling channel. However, only fatigue striations are observed at the fracture surface of the 2G TMF panel's crack; so that tensile rupture of the TMF panel may be excluded.

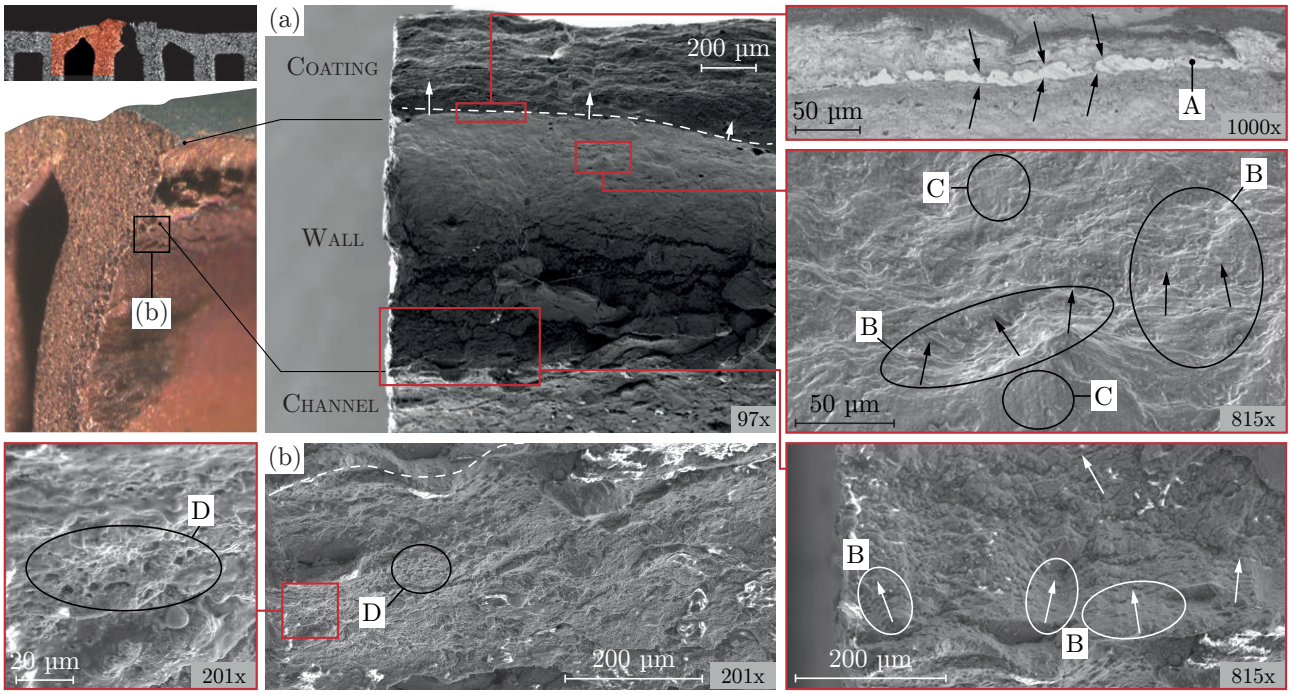

Figure 2.24: SEM images of the TMF panel's fracture surface (a) and upper cooling channel wall (b).

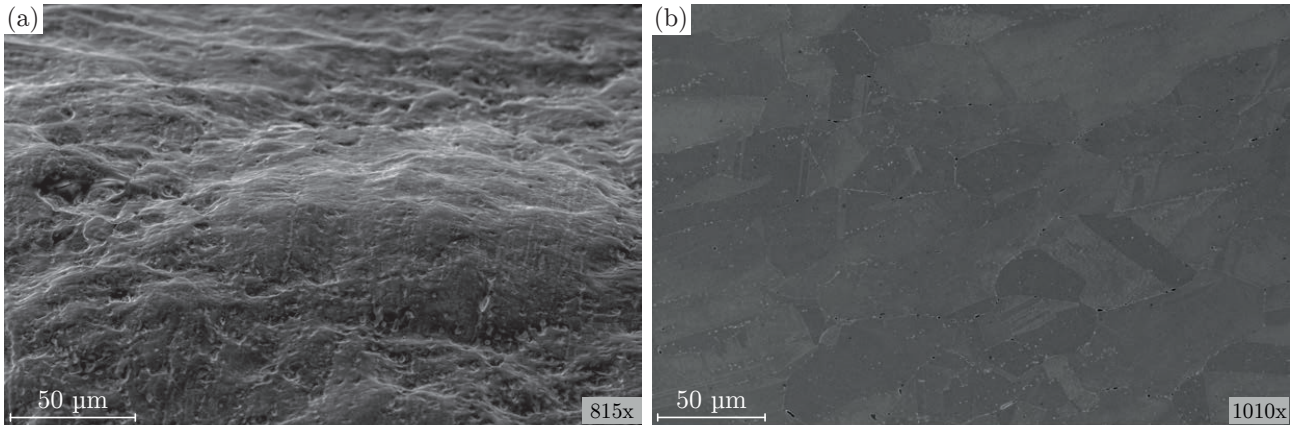

Figure 2.25: SEM images of the fracture surface with grinding marks and chromium precipitates (a) and the microstructure from a less deformed area (b).

3 Numerical Modeling

3.1 Fluid-Structure Interaction Equations

The following section describes the equations of the one-way coupled fluid-structure interaction (FSI) analysis that is carried out to simulate the TMF panel experiment. In this FSI analysis, several physical problems need to be addressed to reach agreement on experimental results. That is a computational fluid dynamics (CFD) analysis of the nitrogen flow throughout the cooling channels as well as a finite element (FE) analysis of the of the TMF panel's thermal and structural field taking into account cyclic laser heating and material degradation. Because the thermal field is one of the most important boundary conditions of the structural analysis computing material degradation and channel deformation correctly, the CFD analysis is coupled with the thermal FE analysis taking into account a steady state nitrogen flow under steady state laser heating. Finally, the temperature field is transferred to a quasi-static structural analysis applied there cyclically until structural damage reaches a critical value that corresponds to initiation of a macrocrack leading to failure.

3.1.1 Setup

Figure 3.1 depicts the modular setup of the TMF panel's one-way coupled FSI analysis in Ansys Workbench.

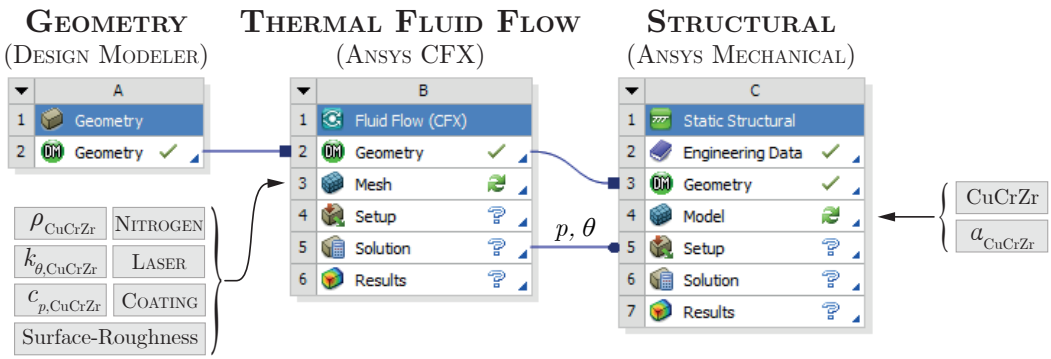

Figure 3.1: Approach of a TMF panels one-way coupled fluid-structure interaction (FSI) analysis in ANSYS Workbench.

First, the geometry is imported as a *.STEP file that is generated from computer-aided design (CAD) software and then divided into multiple parts. Division is needed to obtain a parameterized structured mesh of both the cooling channels throughout the TMF panel and the TMF panel structure itself. Ansys CFX is used to compute the pressure and the temperature distribution in the cooling channels and the temperature distribution in the TMF

panel during laser heating. The computed temperature distribution is then transferred to ANSYS MECHANICAL and applied cyclically as a nodal body force onto the structural mesh. Note that the deformation of the cooling channels due to cyclic laser heating has no effect on the CFD analysis results (e.g. heat transfer coefficient h_c) in this thesis. In fact, the time steps are not coupled among these two analyses. Even though a two-way coupled analysis is prepared, this analysis requires excessive numerical capacities that remain as a great challenge for future work. Finally, temperature dependent thermophysical material parameters of CuCrZr (density ρ, thermal conductivity k_θ, thermal expansion α, and specific heat capacity c_p), temperature dependent structural material parameters of CuCrZr (see Sec. 4.2.3), laser data (heat flux q, and laser beam power density distribution $\bar{I}$), coating property (emissivity ε_α), and real gas properties of the nitrogen coolant (density, enthalpy H, entropy S, specific heat capacity, thermal conductivity, and any other quantities) are applied in the present FSI analysis (see Fig. 3.1).

3.1.2 Fluid Dynamics Field

In ANSYS CFX, the fluid equations and the thermal equations are solved within the cooling channel domain (Ω_{CCH}) and the solid domain (Ω_{CuCrZr}), respectively. Formulation of the three-dimensional fluid equations (so-called NAVIER-STOKES equations) bases on the instantaneous balance of mass, momentum and energy conservation. According to the ANSYS MANUAL GUIDE [82], SCHLICHTING [83] and MUNSON [84], the stationary continuity equation for an compressible one-phase medium is

$$\frac{\partial \rho}{\partial t} + \nabla \cdot (\rho\, \dot{\boldsymbol{u}}) = 0 \tag{3.1}$$

where $\rho(\boldsymbol{x}, \theta, p)$ is the density, t is the time and $\dot{\boldsymbol{u}}(\boldsymbol{x}, \theta)$ is the three-dimensional flow field velocity vector. The momentum equation is defined as

$$\frac{\partial\,(\rho\, \dot{\boldsymbol{u}})}{\partial t} + \nabla \cdot (\rho\, \dot{\boldsymbol{u}} \otimes \dot{\boldsymbol{u}}) = \nabla \cdot \boldsymbol{\sigma} + \boldsymbol{f}_M \tag{3.2}$$

where $\boldsymbol{\sigma}(\boldsymbol{x}, \theta, \boldsymbol{\varepsilon}, \boldsymbol{\alpha})$ is the CAUCHY stress tensor (Eq. 3.20), and $\boldsymbol{f}_M(\boldsymbol{x})$ accounts for momentum body forces. The CAUCHY stress tensor can be divided into its hydrostatic part and deviatoric part by

$$\boldsymbol{\sigma} = -p\mathbf{1} + \boldsymbol{\sigma}^D \tag{3.3}$$

where p is the hydrostatic pressure, $\mathbf{1}$ is the unity tensor and $\boldsymbol{\sigma}^D$ is the deviatoric part of the CAUCHY stress tensor. By assuming that the fluid is isotropic, the stress tensor is a linear function of the strain rate tensor (that corresponds to the velocity gradient) and the viscous work term of the fluid $\nabla \cdot \left(\dot{\boldsymbol{u}} \cdot \boldsymbol{\sigma}^D\right)$ is omitted, the deviatoric CAUCHY stress tensor is then defined as

$$\boldsymbol{\sigma}^D = \mu \left(\nabla \dot{\boldsymbol{u}} + (\nabla \dot{\boldsymbol{u}})^{\mathrm{T}} - \frac{2}{3}\, \delta\, \nabla \cdot \dot{\boldsymbol{u}} \right) \tag{3.4}$$

where μ is a the dynamic viscosity constant, and δ depicts the KRONECKER delta function. The total energy equation is given as follows

$$\frac{\partial\,(\rho\, H_{\mathrm{T}})}{\partial t} - \frac{\partial p}{\partial t} + \nabla \cdot (\rho\, \dot{\boldsymbol{u}}\, H_{\mathrm{T}}) = \nabla \cdot \underbrace{(k_\theta \nabla \theta)}_{-\boldsymbol{q}} + \dot{\boldsymbol{u}} \cdot \boldsymbol{f}_M + \boldsymbol{f}_E \tag{3.5}$$

where $H_{\mathrm{T}}(\boldsymbol{x},\theta,p)$ is the total enthalpy, $k_\theta(\theta)$ and $\theta(\boldsymbol{x})$ are the thermal conductivity and the temperature related to the heat flux $\boldsymbol{q}(\boldsymbol{x},\theta)$, and $\boldsymbol{f}_E(\boldsymbol{x})$ is the energy source. The total enthalpy is related to the static enthalpy $H_{\mathrm{S}}(\boldsymbol{x},\theta,p)$ by

$$H_{\mathrm{T}} = H_{\mathrm{S}} + \frac{1}{2}\dot{\boldsymbol{u}}^2 \tag{3.6}$$

Taking into account real gas properties of the single-phase nitrogen fluid, the static enthalpy, the specific heat capacity, and the density are dependent on temperature and pressure. For the TMF panel analysis, this data is provided in Ansys CFX by using table data exported from the database Nist Refprop. Note that the CFX-solver computes the total enthalpy and derives the static enthalpy from Eq. 3.6 directly because a total energy model including the viscous work term is used in this CFD analysis. According to Kuhl [15], following Dirichlet boundary conditions[1] are applied at the cooling channel boundaries (Γ_{CCH}): Temperature at each cooling channel's inlet θ_{in}, pressure at each cooling channel's outlet p_{out}, the mass flow $\dot{m}_{\mathrm{CCH}}$ in the cooling channels, and symmetry conditions in the center of the center cooling channel boundaries ($\Gamma_{\mathrm{Sym,CCH4}}$).

$$\begin{aligned}
\theta &= \theta_{\mathrm{in}} \quad && \forall \quad \boldsymbol{x} \in \{\Gamma_{\mathrm{CCH}}\} \\
p &= p_{\mathrm{out}} \quad && \forall \quad \boldsymbol{x} \in \{\Gamma_{\mathrm{CCH}}\} \\
\rho\ A_{\mathrm{CCH}}\ \dot{\boldsymbol{u}}\cdot\boldsymbol{n} = \dot{m}_{\mathrm{CCH}},\ \dot{\boldsymbol{u}}\times\boldsymbol{n} &= 0 \quad && \forall \quad \boldsymbol{x} \in \{\Gamma_{\mathrm{CCH}}\} \\
\dot{\boldsymbol{u}}\cdot\boldsymbol{n} &= 0 \quad && \forall \quad \boldsymbol{x} \in \{\Gamma_{\mathrm{Sym,CCH4}}\}
\end{aligned} \tag{3.7}$$

To consider fluctuations along the cooling channel wall, we use Menter's Shear-Stress-Turbulence (SST) model with automatic wall treatment [87]. The SST model belongs to the two-equation eddy-viscosity turbulence models. This model combines the k-ω model of Wilcox [88] in the inner region of the boundary layer and switches to the baseline k-ε model in the outer region and in the free shear flow [87]. The Reynolds shear stress tensor in within the boundary layer is modeled by using the eddy-viscosity hypothesis and is given in tensor notation as follows

$$\boldsymbol{\tau}^{\mathrm{R}} = -\rho\overline{\dot{u}_i\dot{u}_j} = \mu_t\left(\frac{\partial\dot{u}_i}{\partial x_j}+\frac{\partial\dot{u}_j}{\partial x_i}\right) - \frac{2}{3}\,\delta_{ij}\left(\rho\ k_t + \mu_t\frac{\partial\dot{u}_k}{\partial x_k}\right) \tag{3.8}$$

where u_i, u_j and u_k are three-dimensional velocity components of $\dot{\boldsymbol{u}}(\boldsymbol{x},t)$ related to $\boldsymbol{x} = \{x;y;z\}$, μ_t is the turbulent viscosity, $k_t = \frac{1}{2}\dot{\boldsymbol{u}}^2$ is the dynamic turbulent kinetic energy and the symbol $\overline{x_i x_j}$ denotes the mean scalar gradient of $\boldsymbol{x}$. To model the heat transfer in the boundary layer more accurate, eddy diffusivity option with a turbulent Prandtl number is used. The eddy (turbulent) diffusivity hypothesis states that the Reynolds flux ($\rho\overline{u_i\varphi}$) of a scalar is linearly related to the mean scalar gradient

$$-\rho\overline{\dot{u}_i\varphi} = \gamma_t\ \frac{\partial\zeta}{\partial x_i} \tag{3.9}$$

where ζ is a variable depending on the total flux and γ_t is the eddy diffusivity [82]. The eddy diffusivity becomes

$$\gamma_t = \frac{\mu_t}{\mathrm{Pr}_t} \tag{3.10}$$

with Pr_t as the turbulent Prandtl number. According to the Ansys Manual Guide [82], the thermal boundary layer is modeled on the basis of Kader's logarithmic law of the wall

[1] Value of a variable is defined [85, 86].

function [89]. Due to the fact that the cooling channel surface roughness has an important influence on the heat transfer coefficient and the wall shear stress in this layer, an equivalent sand-grain roughness is applied. Following the work of ADAMS [90], peak-to-valley surface roughness (R_z, Fig. 2.2) is converted to equivalent sand-grain surface roughness (R_s) by

$$R_s = 0.978 R_z \tag{3.11}$$

The heat transfer between the boundaries of fluid domain (Γ_{CCH}) and solid domain (Γ_{CuCrZr}) are computed and interpolated at the interfaces by using conservative interface flux option and automatic mesh connection method, respectively. In fact, the heat flux vector $\boldsymbol{q}(\boldsymbol{x}, \theta)$ (Eq. 3.16) is then projected along the normal direction of the interface between cooling channel wall and the solid wall facing each other

$$-k_\theta \frac{\partial \theta}{\partial n}\bigg|_{\Gamma_{\mathrm{CCH}}} = -k_\theta \frac{\partial \theta}{\partial n}\bigg|_{\Gamma_{\mathrm{CuCrZr}}} \tag{3.12}$$

The shear stress in the viscous layer of the turbulent flow is also affected by applying an equivalent surface roughness (see Eq. 3.11). So, a logarithmic relation basing on the method of LAUNDER AND SPALDING [91] is used in ANSYS CFX to model the velocity near the wall ($\dot{u}^+$) that is directly coupled to the wall-shear stress (τ_w) by using

$$\dot{u}^+ = \frac{\dot{u}_t}{\dot{u}_\tau} = \frac{1}{\kappa} \ln\left(y^+\right) + C \tag{3.13}$$

with

$$y^+ = \frac{\rho \, \Delta y \, \dot{u}_\tau}{\mu} \tag{3.14}$$

and

$$\dot{u}_\tau = \sqrt{\frac{\tau_w}{\rho}} \tag{3.15}$$

where $\dot{u}_\tau$ is the friction velocity, $\dot{u}_t$ is the velocity tangent at a distance of Δy to the wall, y^+ is the dimensionless wall distance, κ is the VON KARMAN constant, and C is a constant depending on wall roughness by using natural logarithm [82].

Within the solid domain, thermal energy option is used for heat transfer and MONTE CARLO option is used for thermal radiation to ambience.

3.1.3 Thermal Field

Steady state heat transfer equations are solved in the solid domain Ω_{CuCrZr} to obtain a stationary temperature field $\theta(\boldsymbol{x})$. According to BATHE [92], FOURIER's law of heat conduction defines the heat flow through the surface of the structural domain

$$\boldsymbol{q} = -k_\theta \nabla \theta \tag{3.16}$$

where $\boldsymbol{q}(\boldsymbol{x}, \theta)$ is the heat flux, k_θ is the thermal conductivity, and $\nabla\theta$ denotes the gradient of the temperature field. Considering the heat flow equilibrium and energy balance law in the structural domain, we obtain

$$\nabla \boldsymbol{q} = -\boldsymbol{q}_B \qquad \forall \qquad \boldsymbol{x} \in \{\Omega_{\mathrm{CuCrZr}}\} \tag{3.17}$$

where $\boldsymbol{q}_B(\boldsymbol{x}, \boldsymbol{u}, \theta)$ is the rate of heat generated per volume (including the rate of dissipated heat). All boundary conditions of the thermal field are NEUMANN boundary conditions[2]. Examples are the heat flux on the laser loaded surface of the TMF panel (Γ_{Laser}) and at the cooling channel walls (Γ_{CCH}), symmetry conditions at the symmetry plane of the TMF panel (Γ_{Sym}), and radiation conditions at the outer uncoated surfaces of the TMF panel (Γ_{Out})

$$\begin{aligned} \boldsymbol{q} \cdot \boldsymbol{n} &= q_{\text{Laser}} && \forall && \boldsymbol{x} \in \{\Gamma_{\text{Laser}}\} \\ \boldsymbol{q} \cdot \boldsymbol{n} &= 0 && \forall && \boldsymbol{x} \in \{\Gamma_{\text{Sym}}; \Gamma_{\text{Out}}\} \\ \boldsymbol{q} \cdot \boldsymbol{n} &= q_S = \kappa \left(\theta_{\text{Out}} - \theta_S\right) && \forall && \boldsymbol{x} \in \{\Gamma_{\text{CCH}}\} \end{aligned} \tag{3.18}$$

where $\boldsymbol{n}$ denotes the coordinate axis in the direction of the unit normal vector $\boldsymbol{n}$ (pointing outward), q_S is the heat flux on the surface, θ^S is the known temperature on the surface (so-called bulk temperature), θ_{Out} is the ambient temperature, and $\kappa_B = k_B\big((\theta_r)^2+(\theta_S)^2\big)(\theta_r-\theta_S)$ is a coefficient with k_B determined from the BOLTZMANN constant, the emissivity of the radiant and absorbing materials and the geometric view factors [92]. The emissivity coefficients of the coated surface and the outer surfaces (non-polished copper) are set to $\varepsilon_\alpha = 1.0$ and 0.7, respectively. While neglecting reflection of the coated surface with speckle marks where the laser is applied, the resulting heat flux into the TMF panel surface is calculated by

$$q_{\text{TMF}} = \frac{P_{\text{Laser}}}{A_{\text{Laser}}}\, \varepsilon_\alpha = q_{\text{Laser}}\, \varepsilon_\alpha \tag{3.19}$$

where P_{Laser} is the optical laser power, A_{Laser} is the two-dimensional area of the laser beam's focal plane, and ε_α is the emissivity coefficient of the coating at a laser wave length of $\lambda_{\text{Laser}} = 940$ nm (see Fig. 2.6). The heat flux is determined by taking into account the two-dimensional distribution of the laser beam (measured with a laser beam profiler before the test), the total laser power (measured by a laser power meter), and the emissivity of the coating (determined by a laser wave length pyrometer) [27].

3.1.4 Mechanical Structural Field

For the quasi-static structural analysis, we assume that the system does not change in time. The deformation of the structural domain is described by the displacement field $\boldsymbol{u}(\boldsymbol{x}, \theta)$ which is governed by the balance of linear momentum

$$\nabla \cdot \boldsymbol{\sigma} = 0 \qquad \forall \qquad \boldsymbol{x} \in \{\Omega_{\text{CuCrZr}}\} \tag{3.20}$$

where $\boldsymbol{\sigma}(\boldsymbol{x}, \theta, \boldsymbol{\varepsilon}, \boldsymbol{\alpha})$ represents the temperature dependent CAUCHY stress tensor given as a function of the temperature, the GREEN strain tensor $\boldsymbol{\varepsilon}(\boldsymbol{u}, \boldsymbol{x})$ and the internal variables $\boldsymbol{\alpha}(\boldsymbol{x}, \boldsymbol{u}, \theta)$. Assuming small strains, the GREEN strain tensor is related to the displacement $\boldsymbol{u}(\boldsymbol{x}, \theta)$ by

$$\boldsymbol{\varepsilon} = \nabla^{\text{Sym}} \boldsymbol{u} = \frac{\left(\nabla \boldsymbol{u} + \nabla^{\text{T}} \boldsymbol{u}\right)}{2} \tag{3.21}$$

The applied NEUMANN boundary conditions are symmetry at the symmetry plane of the TMF panel (Γ_{Sym}), the pressure-free environment at all surfaces except the cooling channel walls (Γ_{Out}) and the cooling channel pressure p_{CCH} at the cooling channel walls (Γ_{CCH})

$$\begin{aligned} \boldsymbol{u} \cdot \boldsymbol{n} &= 0 && \forall && \boldsymbol{x} \in \{\Gamma_{\text{Sym}}\} \\ \boldsymbol{u} \cdot \boldsymbol{\sigma} \cdot \boldsymbol{n} &= 0 && \forall && \boldsymbol{x} \in \{\Gamma_{\text{Out}}\} \\ \boldsymbol{u} \cdot \boldsymbol{\sigma} \cdot \boldsymbol{n} &= p_{\text{CCH}} && \forall && \boldsymbol{x} \in \{\Gamma_{\text{CCH}}\} \end{aligned}$$

[2] Gradient normal to the boundary of a variable is defined [85, 86].

Note that the ambient pressure of the outer surfaces is neglected as well as the pressure loss from inlet to outlet ($\Delta p \approx 350$ mbar $\equiv 0.62$ % at $\Delta\bar{p}_{\mathrm{out}} = 5.66$ bar). Therefore, a static pressure of $p_{\mathrm{CCH}} = 55$ bar is applied on the cooling channel walls instead. DIRICHLET boundary conditions are applied at two nodes at the inlet surface of the solid domain for structural statically determination. In fact, the displacement field of the node in the symmetry plane is fixed in space $\boldsymbol{u}(\boldsymbol{x}) = 0$ as well as the displacement in axial direction (height) of the outside node $u(z) = 0$. A remote displacement boundary condition is used to couple the nodes on the outlet surface of the solid domain; hence, the rotational degrees are suppressed there $\varphi_{\mathrm{Out}}(\boldsymbol{x}) = 0$. This accords to the mounting of the TMF panel described in Sec. 2.2. Finally, the stress-strain relationship is defined by the viscoplastic damage model which is implemented in ANSYS (see Sec. 3.2).

3.2 Material Modeling

A viscoplastic damage model incorporating nonlinear kinematic hardening, combined isotropic hardening and isotropic softening, ductile isotropic damage, microdefect closure effect, and thermal ageing is carried out to the fatigue life analysis of the TMF panel. This model is motivated by the classical rheological model for elastoplasticity developed by FREDERICK AND ARMSTRONG [93, 94] and extended by TINI [24, 26] to consider viscoplasticity and damage. In this section, the extended one-dimensional rheological model and the resulting three-dimensional continuum mechanical equations are described within the small strain regime.

3.2.1 One-Dimensional Rheological Model

A rheological model is a simple tool for formulating physically based and thermodynamically consistent constitutive equations for describing inelastic material behavior [95]. Superposition of elastic springs, viscous dashpots and friction slips corresponds to a mathematical description of the one-dimensional rheological behavior [96].

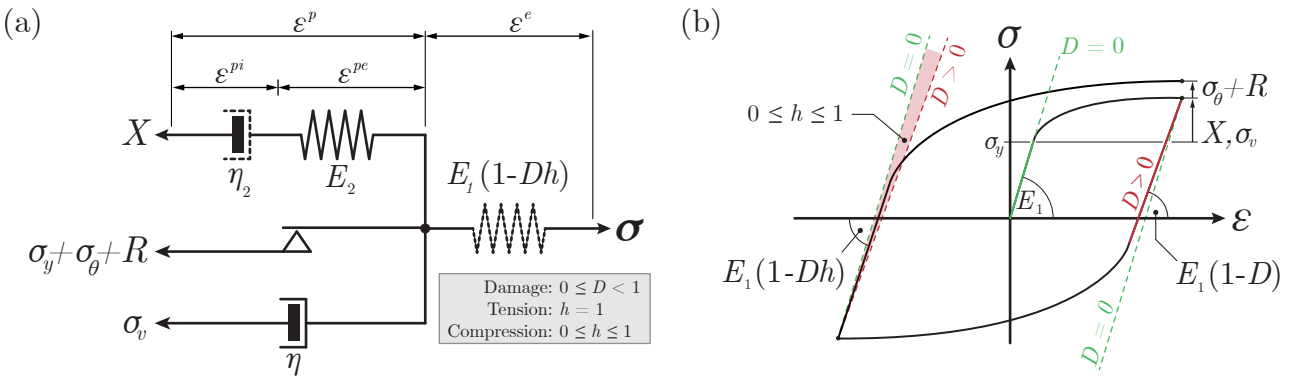

Figure 3.2: Extended one-dimensional rheological model for viscoplasticity coupled with isotropic damage D, microdefect closure effect h and thermal ageing σ_θ (a) and schematic stress-strain hysteresis of a typical cyclic loading case (b).

Figs. 3.2a and b depict the rheological model of the viscoplastic damage model in the small strain regime and the corresponding stress-strain hysteresis of a cyclic loading with a strain ratio of $R_\varepsilon = -1$, respectively. This model represents an extension of the rheological model with nonlinear ARMSTRONG-FREDERICK hardening (so-called BAUSCHINGER effect) [93, 94] basing

on the formulation of LION [95]. In contrary to the kinematic hardening models of CHABOCHE [97,98], LION initially introduced a multiplicative decomposition of both, the mechanical strain ε into its elastic ε^e and plastic ε^p parts, and the plastic strain ε^p into its reversible ε^{pe} (plastic elastic) and irreversible ε^{pi} (plastic inelastic) parts

$$\varepsilon = \varepsilon^e + \varepsilon^p = +\varepsilon^e + \varepsilon^{pe} + \varepsilon^{pi} \tag{3.22}$$

On the one hand, reversible plastic strains are assumed to be a function of the back stress X and can be interpreted as local elastic deformation caused by dislocations

$$X = E_2 \varepsilon^{pe} \tag{3.23}$$

where E_2 is a material parameter representing the stiffness of the elastic spring. On the other hand, irreversible plastic strains are determined by an additional evolution law and can be interpreted as irreversible slip processes on the microscale [99]. As depicted in Fig. 3.2a, the elastic spring is serially connected with a rate-independent dashpot (η_2) to consider nonlinear kinematic hardening effects on the basis of the PRAGER [100] rule

$$\eta_2 = \frac{E_2}{\dot{\lambda} b_{\text{kin}}} \tag{3.24}$$

which leads with Eq. 3.23 to

$$\dot{X} = E_2 \dot{\varepsilon}^{pe} - \dot{\lambda} b_{\text{kin}} X \tag{3.25}$$

where $\dot{\lambda}$ is the plastic multiplier, and b_{kin} a material parameter. Using PERZYNA [101] formulation, the plastic multiplier is given in the simplest case by

$$\dot{\lambda} = \frac{\langle \Phi_{\text{Mises}} \rangle}{\eta} \tag{3.26}$$

where Φ_{Mises} is the VON MISES' yield function, and η is a material parameter related to the rate-dependent viscous dashpot. As shown in Fig. 3.2a, the viscous dashpot represents the viscous overstress $\sigma_v = \eta \dot{\varepsilon}^p$. The VON MISES' yield function $\Phi = |\sigma - X| - (\sigma_y + \sigma_\theta + R)$ includes uniaxial stress σ, back stress X, initial yield stress σ_y, stress reduced by thermal ageing σ_θ and combined isotropic hardening and softening (with R denoting the drag stress). In the rheological model, a friction slip is used for the stress resulting from the yield stress, drag stress and the decreased stress due to thermal ageing. In this case, the yield stress σ_y corresponds to the stress limit where irreversible deformation is initiated. The drag stress R is characterized by the change of the VON MISES' yield surface and depends on either the dissipated plastic work or the accumulated plastic strain with respect to the loading history [102]. The thermal ageing stress σ_θ denotes the phenomenological decreased stress-strain behavior depending on both the ageing time and the temperature. The symbol $\langle \cdot \rangle$ defines the MACAULAY brackets

$$\langle x \rangle = \begin{cases} 0 & \text{if } x < 0, \\ x & \text{if } x \geq 0. \end{cases} \tag{3.27}$$

Furthermore, uniaxial stress σ corresponds to an elastic spring with the material parameter E_1 that represents the initial spring constant or the elastic modulus of the undamaged material, respectively. Basing on the damage theory of KACHANOV [103, 104] and taking into account the concept of effective stress by RABOTNOV [105, 106] and the principle of strain equivalence

by Lemaitre and Chaboche [107], the elastic modulus of the damaged material is defined by

$$\tilde{E}_1 = E_1(1 - D) \tag{3.28}$$

where $\tilde{E}$ is the effective elastic modulus and $0 \leq D < 1$ is the scalar damage variable. Then, the stress-strain relationship for isotropic elasticity with isotropic damage is given by

$$\sigma = E_1 \left(1 - D\right) \varepsilon^e = \tilde{E}_1 \varepsilon^e \tag{3.29}$$

Within the unified framework of isotropic damage, the effective elastic modulus in tension is assumed to be similar to the elastic modulus in compression. However, defects and cavities in the structure on the microscale are supposed to open under tensile loading and to close under compressive loading. This leads to a variation of the stiffness in uniaxial compressive direction [108–110]

$$\tilde{E_1}^{-} = E_1(1 - hD) \tag{3.30}$$

where $0 \leq h \leq 1$ is the microdefect closure parameter, and $(^-)$ defines the loading direction towards the compressive domain. Note that Eq. 3.28 is used in case of uniaxial tensile loading.

3.2.2 Continuum Mechanical Approach

On the basis of the extended one-dimensional rheological model and the principle of strain equivalence, the constitutive equations for viscoplasticity and isotropic damage with microdefect-closure effect are generalized in three dimensions. In the small strain regime, we assume that the second-order mechanical strain tensor is divided into the sum of the elastic strain tensor and the plastic strain tensor with its reversible and irreversible parts (cf. Eq. 3.22)

$$\dot{\boldsymbol{\varepsilon}} = \dot{\boldsymbol{\varepsilon}}^e + \dot{\boldsymbol{\varepsilon}}^p = \dot{\boldsymbol{\varepsilon}}^e + \dot{\boldsymbol{\varepsilon}}^{pe} + \dot{\boldsymbol{\varepsilon}}^{pi} \tag{3.31}$$

According to the second principle of thermodynamics, the differential form of the Clausius-Duhem inequality can be expressed as

$$\boldsymbol{\sigma} \colon \dot{\boldsymbol{\varepsilon}} - \rho \left(\dot{\psi} + \dot{\theta} s \right) - \boldsymbol{q} \cdot \frac{\nabla \theta}{\theta} \geq 0 \tag{3.32}$$

where ρ is the density, s is the entropy, ψ is the Helmholtz free energy function, θ is the absolute temperature, and q is the heat flux vector associated to the temperature gradient $\nabla\theta$. Note that the Clausius-Duhem inequality has to be satisfied for all processes to ensure validity of the material model. The Helmholtz free energy function is a thermodynamic potential of a solid material that is affected by irreversible processes of the inner structure due to the development of inelastic strains and microvoids [111]. Therefore, the Helmholtz free energy function is dependent on elastic strain, temperature, and internal state variables

$$\psi \left(\boldsymbol{\varepsilon}^e, \boldsymbol{\varepsilon}^{pe}, D, p_\alpha \right) \tag{3.33}$$

Regarding the rheological model in Fig. 3.2a, the Helmholtz free energy function can be composed into three parts

$$\psi = \psi^e \left(\boldsymbol{\varepsilon}^e, D \right) + \psi^{\mathrm{kin}} \left(\boldsymbol{\varepsilon}^{pe} \right) + \psi^{\mathrm{iso}} \left(p_\alpha \right) \tag{3.34}$$

where ψ^e describes the reversible material properties, ψ^{kin} refers to the elastic energy stored in dislocation fields, and ψ^{iso} represents the additional amount of stored energy due to isotropic

hardening [95, 99, 112]. According to Fassin [113], the elastic part of the Helmholtz free energy function can be expressed as

$$\begin{aligned}\rho\psi^e = &\frac{E_1\,(1-D)}{2\,(1+\nu_1)}\;\hat{\boldsymbol{\varepsilon}}^+\colon\hat{\boldsymbol{\varepsilon}}^+ + \frac{E_1\nu_1\,(1-D)}{2\,(1+\nu_1)\,(1-2\nu_1)}\left(\mathrm{tr}^+(\hat{\boldsymbol{\varepsilon}})\right)^2\\ &+\frac{E_1\,(1-Dh)}{2\,(1+\nu_1)}\;\hat{\boldsymbol{\varepsilon}}^-\colon\hat{\boldsymbol{\varepsilon}}^- + \frac{E_1\nu_1\,(1-Dh)}{2\,(1+\nu_1)\,(1-2\nu_1)}\left(\mathrm{tr}^-(\hat{\boldsymbol{\varepsilon}})\right)^2\end{aligned} \tag{3.35}$$

with split of the strain tensor's positive and negative principal values

$$\hat{\boldsymbol{\varepsilon}}^+ = \sum_{i=1}^{3}\hat{\varepsilon}_i^+\boldsymbol{n}_i\otimes\boldsymbol{n}_i\;,\quad \hat{\varepsilon}_i^+ = \langle\hat{\varepsilon}_i\rangle \tag{3.36}$$

$$\hat{\boldsymbol{\varepsilon}}^- = \sum_{i=1}^{3}\hat{\varepsilon}_i^-\boldsymbol{n}_i\otimes\boldsymbol{n}_i\;,\quad \hat{\varepsilon}_i^+ = -\langle-\hat{\varepsilon}_i\rangle \tag{3.37}$$

where $\hat{\varepsilon}_i^+$ and $\hat{\varepsilon}_i^-$ are the positive and negative eigenvalues of the second-order mechanical strain tensor with their associated eigenvectors $\boldsymbol{n}_i$. The kinematic hardening part and isotropic hardening part of the Helmholtz free energy function is given as follows

$$\rho\psi^{\mathrm{kin}} = \frac{1}{2}\,\boldsymbol{\mathcal{C}}_2\;\boldsymbol{\varepsilon}^{pe}\colon\boldsymbol{\varepsilon}^{pe} \tag{3.38}$$

$$\rho\psi^{\mathrm{iso}} = \frac{Q_0}{2}p_\alpha^2 + Q_1p_\alpha + \frac{Q_1}{b_1}e^{-b_1p_\alpha} + Q_2p_\alpha + \frac{Q_2}{b_2}e^{-b_2p_\alpha} \tag{3.39}$$

Therefore, the Helmholtz free energy function can be expressed as

$$\begin{aligned}\rho\psi = &\frac{E_1\,(1-D)}{2\,(1+\nu_1)}\;\hat{\boldsymbol{\varepsilon}}^+\colon\hat{\boldsymbol{\varepsilon}}^+ + \frac{E_1\nu_1\,(1-D)}{2\,(1+\nu_1)\,(1-2\nu_1)}\left(\mathrm{tr}^+(\hat{\boldsymbol{\varepsilon}})\right)^2\\ &+\frac{E_1\,(1-Dh)}{2\,(1+\nu_1)}\;\hat{\boldsymbol{\varepsilon}}^-\colon\hat{\boldsymbol{\varepsilon}}^- + \frac{E_1\nu_1\,(1-Dh)}{2\,(1+\nu_1)\,(1-2\nu_1)}\left(\mathrm{tr}^-(\hat{\boldsymbol{\varepsilon}})\right)^2\\ &+\frac{1}{2}\,\boldsymbol{\mathcal{C}}_2\;\boldsymbol{\varepsilon}^{pe}\colon\boldsymbol{\varepsilon}^{pe} + \frac{Q_0}{2}p_\alpha^2 + Q_1p_\alpha + \frac{Q_1}{b_1}e^{-b_1p_\alpha} + Q_2p_\alpha + \frac{Q_2}{b_2}e^{-b_2p_\alpha}\end{aligned} \tag{3.40}$$

The time derivative of the Helmholtz free energy function (see Eq. 3.33) leads to

$$\rho\dot{\psi} = \rho\frac{\partial\psi}{\partial\boldsymbol{\varepsilon}^e}:\dot{\boldsymbol{\varepsilon}}^e + \rho\frac{\partial\psi}{\partial\boldsymbol{\varepsilon}^{pe}}:\dot{\boldsymbol{\varepsilon}}^{pe} + \rho\frac{\partial\psi}{\partial D}\dot{D} + \rho\frac{\partial\psi}{\partial p_\alpha}\dot{p}_\alpha \tag{3.41}$$

with the additive composition of the plastic strain tensor and the total mechanical strain tensor (see Eq. 3.31)

$$\rho\dot{\psi} = \rho\frac{\partial\psi}{\partial\boldsymbol{\varepsilon}}:\dot{\boldsymbol{\varepsilon}} - \rho\frac{\partial\psi}{\partial\boldsymbol{\varepsilon}^{pi}}:\dot{\boldsymbol{\varepsilon}}^{pi} + \rho\frac{\partial\psi}{\partial D}\dot{D} + \rho\frac{\partial\psi}{\partial p_\alpha}\dot{p}_\alpha \tag{3.42}$$

The second-order Cauchy stress tensor is obtained by differentiating the Helmholtz free energy function (see Eq. 3.40) with respect to the strain

$$\begin{aligned}\boldsymbol{\sigma} = \rho\frac{\partial\psi}{\partial\boldsymbol{\varepsilon}} = &\frac{E_1\,(1-D)}{2\,(1+\nu_1)}\;\hat{\boldsymbol{\varepsilon}}^+\colon\hat{\boldsymbol{\varepsilon}}^+ + \frac{E_1\nu_1\,(1-D)}{2\,(1+\nu_1)\,(1-2\nu_1)}\left(\mathrm{tr}^+(\hat{\boldsymbol{\varepsilon}})\right)^2\\ &+\frac{E_1\,(1-Dh)}{2\,(1+\nu_1)}\;\hat{\boldsymbol{\varepsilon}}^-\colon\hat{\boldsymbol{\varepsilon}}^- + \frac{E_1\nu_1\,(1-Dh)}{2\,(1+\nu_1)\,(1-2\nu_1)}\left(\mathrm{tr}^-(\hat{\boldsymbol{\varepsilon}})\right)^2\end{aligned} \tag{3.43}$$

Taking into account the LAMÉ parameters $\lambda_{\mathrm{L}} = E\nu((1+\nu)(1-2\nu))^{-1}$ and $\mu_{\mathrm{L}} = E(2(1+\nu))^{-1}$, the principal stress tensor $\hat{\boldsymbol{\sigma}}$ can be formulated in terms of the fourth-order elasticity tensor $\boldsymbol{\mathcal{C}}_1$ that depends on the material parameters E_1 and ν_1 by

$$\hat{\boldsymbol{\sigma}} = \boldsymbol{\mathcal{C}}_1 (1-D)\, \hat{\boldsymbol{\varepsilon}}^{+} + \boldsymbol{\mathcal{C}}_1 (1-Dh)\, \hat{\boldsymbol{\varepsilon}}^{-} \qquad \text{with} \qquad \boldsymbol{\mathcal{C}}_1 = 2\mu_{\mathrm{L},1} \boldsymbol{\mathcal{I}}^{\mathrm{Sym}} + \lambda_{\mathrm{L},1} \mathbf{1} \otimes \mathbf{1} \tag{3.44}$$

and

$$\hat{\boldsymbol{\sigma}} = (1-D)\, \hat{\tilde{\boldsymbol{\sigma}}}^{+} + (1-Dh)\, \hat{\tilde{\boldsymbol{\sigma}}}^{-} \qquad \text{with} \qquad \hat{\tilde{\boldsymbol{\sigma}}} = \boldsymbol{\mathcal{C}}_1 \hat{\boldsymbol{\varepsilon}}^{e} = \sum_{i=1}^{3} \hat{\tilde{\sigma}}_i \boldsymbol{n}_i \otimes \boldsymbol{n}_i \tag{3.45}$$

where $\hat{\tilde{\boldsymbol{\sigma}}}$ is the second-order principal effective stress tensor decomposed into its positive and negative parts (cf. LEMAITRE [108]), $\boldsymbol{\mathcal{I}}^{\mathrm{Sym}}$ is the symmetric fourth-order unity tensor, and $\mathbf{1}$ is the second-order unity tensor. Retransformation of the principal effective stress tensor with its eigenvectors $\boldsymbol{n}_i$ results in the CAUCHY stress tensor considering the microdefect closure effect.

The second-order back stress tensor $\boldsymbol{X}$ that bases on the ARMSTRONG-FREDERICK kinematic hardening rule is obtained by

$$\boldsymbol{X} = \rho \frac{\partial \psi}{\partial \boldsymbol{\varepsilon}^{pe}} = \boldsymbol{\mathcal{C}}_2 \boldsymbol{\varepsilon}^{pe} \tag{3.46}$$

where $\boldsymbol{\mathcal{C}}_2$ is the fourth-order elasticity tensor depending on the material parameters E_2 and ν_2. In this case, we assume incompressibility of the material by setting $\nu_2 = 0.5$; so the volume remains constant [114].

The scalar drag stress R is derived by the accumulated plastic strain p_α to

$$R = \rho \frac{\partial \psi}{\partial p_\alpha} = Q_0 p_\alpha + Q_1 \left(1 - e^{-b_1 p_\alpha}\right) + Q_2 \left(1 - e^{-b_2 p_\alpha}\right) \tag{3.47}$$

where $Q_{0,1,2}$ and $b_{1,2}$ are material parameters for isotropic hardening (and softening).

With reference to LEMAITRE [108, 109] and DESMORAT [110], a transformation of the HELMHOLTZ free energy $\psi(\boldsymbol{\varepsilon})$ into the GIBBS free enthalpy $\psi^*(\boldsymbol{\sigma})$ is needed to obtain the damage driving force Y incorporating the microdefect closure parameter h

$$\begin{aligned} Y = \rho \frac{\partial \psi}{\partial D} \overset{!}{=} \rho \frac{\partial \psi^{*e}}{\partial D} = & \frac{1+\nu_1}{2E_1} \left(\frac{\hat{\boldsymbol{\sigma}}^{+} \colon \hat{\boldsymbol{\sigma}}^{+}}{(1-D)^2} + \frac{h\, \hat{\boldsymbol{\sigma}}^{-} \colon \hat{\boldsymbol{\sigma}}^{-}}{(1-Dh)^2} \right) \\ & - \frac{\nu_1}{2E_1} \left(\frac{\left(\mathrm{tr}^{+}(\hat{\boldsymbol{\sigma}})\right)^2}{(1-D)^2} + \frac{h \left(\mathrm{tr}^{-}(\hat{\boldsymbol{\sigma}})\right)^2}{(1-Dh)^2} \right) \end{aligned} \tag{3.48}$$

with the GIBBS free enthalpy function

$$\begin{aligned} \rho\psi^{*e}(\hat{\boldsymbol{\sigma}}, D) = & \frac{1}{2} \left(\frac{1+\nu_1}{E_1 (1-D)} \hat{\boldsymbol{\sigma}}^{+} \colon \hat{\boldsymbol{\sigma}}^{+} - \frac{\nu_1}{E_1 (1-D)} \left(\mathrm{tr}^{+}(\hat{\boldsymbol{\sigma}})\right)^2 \right) \\ & + \frac{1}{2} \left(\frac{1+\nu_1}{E_1 (1-Dh)} \hat{\boldsymbol{\sigma}}^{-} \colon \hat{\boldsymbol{\sigma}}^{-} - \frac{\nu_1}{E_1 (1-Dh)} \left(\mathrm{tr}^{-}(\hat{\boldsymbol{\sigma}})\right)^2 \right) \end{aligned} \tag{3.49}$$

Finally, we can write the CLAUSIUS-DUHEM inequality as follows (cf. TINI [22])

$$(\boldsymbol{\sigma} - \boldsymbol{X}) \colon \dot{\boldsymbol{\varepsilon}}^{p} + \boldsymbol{X} \colon \dot{\boldsymbol{\varepsilon}}^{pi} + Y\dot{D} - R\dot{p}_\alpha - \rho\dot{\theta}s - \boldsymbol{q} \cdot \frac{\nabla\theta}{\theta} \geq 0 \tag{3.50}$$

The VON MISES' yield criterion Φ_{Mises} corresponds to the J_2 flow theory that is assumed to be appropriate for modeling the plastic flow in ductile materials [96, 108]

$$\Phi_{\text{Mises}} = \left|\left|\tilde{\boldsymbol{\sigma}}^D - \boldsymbol{X}^D\right|\right| - \sqrt{\tfrac{2}{3}}\left(\sigma_y + \sigma_\theta + R\right) \tag{3.51}$$

with the evolution equations

$$\dot{\boldsymbol{\varepsilon}}^p = \dot{\lambda}\frac{\partial \Phi_{\text{Mises}}}{\partial\left(\boldsymbol{\sigma} - \boldsymbol{X}\right)} = \frac{\dot{\lambda}}{1-D}\left(\frac{\tilde{\boldsymbol{\sigma}}^D - \boldsymbol{X}^D}{||\tilde{\boldsymbol{\sigma}}^D - \boldsymbol{X}^D||}\right) \tag{3.52}$$

$$\dot{\boldsymbol{\varepsilon}}^{pi} = \dot{\lambda} b_{\text{kin}} \dot{\boldsymbol{\varepsilon}}^{pe,D} = \dot{\lambda} b_{\text{kin}} \frac{1+\nu_2}{E_2}\boldsymbol{X}^D \quad \text{with} \quad \boldsymbol{X}^D = \boldsymbol{\mathcal{C}}_2 \boldsymbol{\varepsilon}^{pe,D} \tag{3.53}$$

$$\dot{D} = \frac{\dot{\lambda}}{(1-D)}\sqrt{\tfrac{2}{3}}\left(\frac{Y}{S_D}\right)^{k_D}\left\langle p_\alpha - p_D\right\rangle \tag{3.54}$$

$$\dot{p}_\alpha = -\dot{\lambda}\frac{\partial \Phi_{\text{Mises}}}{\partial R} = \sqrt{\tfrac{2}{3}}\dot{\lambda} \tag{3.55}$$

and the plastic multiplier $\dot{\lambda}$ using PERZYNA formulation [101]

$$\dot{\lambda} = \frac{\left\langle \bar{\Phi}_{\text{Mises}}{}^{m_\eta}\right\rangle}{\eta} \tag{3.56}$$

where m_η and η are the viscous material parameters, $||\cdot||$ defines the tensor norm and $(\cdot)^D$ denotes the deviatoric part of the tensor. Because of numerical stability reasons, a normalized VON MISES' yield criterion is used

$$\bar{\Phi}_{\text{Mises}} = \frac{\left|\left|\tilde{\boldsymbol{\sigma}}^D - \boldsymbol{X}^D\right|\right|}{\sqrt{\tfrac{2}{3}}\left(\sigma_y + \sigma_\theta + R\right)} - 1 \tag{3.57}$$

Note that KUHN-TUCKER loading-and-unloading conditions must be satisfied for the constitutive equations of this model [111, 115]

$$\Phi_{\text{Mises}} \leq 0\ , \quad \dot{\lambda} \geq 0\ , \quad \dot{\lambda}\Phi_{\text{Mises}} = 0 \tag{3.58}$$

Due to changes in the microstructure of the copper-base alloy at high temperatures, the phenomenological stress-strain behavior is affected with respect to time [20]. In this model, the thermal ageing stress σ_θ leads to a decrease of the yield stress σ_y over heating time t_θ by

$$\sigma_\theta\left(\theta, t_\theta\right) = \left(\frac{\alpha_{\theta i}}{\beta_{\theta i} + t_\theta}\right) + \gamma_{\theta i} \tag{3.59}$$

where $\alpha_{\theta,i}, \beta_{\theta,i}$ and $\gamma_{\theta,i}$ are material parameters for thermal ageing at the temperature level i [116, 117]. Experiments with test samples made of CuCrZr showed that the influence of thermal ageing can be observed for temperatures larger than 700 K [28].

3.3 Solution Approach

One-way coupling of the fluid flow field and the thermal field with the structural displacement field is conducted. The steady state thermal field $\theta(\boldsymbol{x})$ of the solid domain results from

both the steady state fluid flow throughout the cooling channel domains and the steady state laser heating onto the TMF panel surface by taking into account radiation to ambience. In the fluid domain, the NAVIER-STOKES equations (see Eqs. 3.1, 3.2 and 3.5) are solved by using a coupled pressure-based CFX-solver. The continuum and linear momentum equations are solved simultaneously on the basis of the inlet temperature, the outlet pressure and the mass flow in each cooling channel domain (Eq. 3.7). For initialization purpose, a fluid flow velocity is employed. Because of supercritical pressure and supercritical temperature conditions of the coolant during a TMF panel test, the fluid is modeled as single-phase compressible gaseous nitrogen. The exchange of heat along the cooling channel walls is conducted on interfaces where the wall heat flux is interpolated between fluid and solid mesh (see Eq. 3.12). In combination with the heat flux generated by the laser $\boldsymbol{q}(\boldsymbol{x}, \theta)$ onto the TMF panel's surface, a steady state temperature field $\theta(\boldsymbol{x})$ of the TMF panel's solid domain is obtained (see Eq. 3.16). In the follow-on quasi-static structural analysis, the temperature field is interpolated and applied as a nodal body force. The temperature dependent nodal body forces lead to thermal strains $\boldsymbol{\varepsilon}_\theta(\boldsymbol{x}, \theta)$ that are applied on the discretized structural domain. To obtain a displacement field $\boldsymbol{u}(\boldsymbol{x}, \theta)$ of the solid domain, the nonlinear balance of momentum (see Eq. 3.20) is solved. Within the small strain regime, the strain-displacement relationship (see Eq. 3.21) leads to the strain tensor $\boldsymbol{\varepsilon}(\boldsymbol{x}, \boldsymbol{u}, \theta)$ that is applied in the displacement-based FE-solver. Then, the stress is computed using the stress-strain relationship (see Eq. 3.43) basing on the concept of effective stress and the principle of strain equivalence. In case of viscoplasticity ($\Phi_{\text{Mises}}(\boldsymbol{\sigma}, \boldsymbol{\alpha}, \theta) > 0$), the NEWTON-RAPHSON iteration scheme is applied to solve the nonlinear set of residual equations (e.g. plastic strain tensor $\boldsymbol{\varepsilon}^p(\boldsymbol{x}, \boldsymbol{u}, \theta)$, plastic-inelastic strain tensor $\boldsymbol{\varepsilon}^{pi}(\boldsymbol{x}, \boldsymbol{u}, \theta)$, isotropic damage variable $D(\boldsymbol{x}, \boldsymbol{u}, \theta)$ and accumulated plastic strain $p_\alpha(\boldsymbol{x}, \boldsymbol{u}, \theta)$) iteratively for every load step. The evolution of the internal variables (see Eqs. 3.52, 3.53, 3.54 and 3.55) is computed by using the implicit backward EULER scheme. In case of convergence of the local material tangent, the global material tangent (so-called JACOBIAN matrix) is computed numerically by using a finite difference method together with a small strain increment of $\Delta\varepsilon = 10^{-8}$. Depending on the global material tangent, the resulting stress $\boldsymbol{\sigma}(\boldsymbol{x}, \theta, \boldsymbol{\varepsilon}, \boldsymbol{\alpha})$ is computed in ANSYS for each integration point of the three-dimensional solid element. Further documentation of the mentioned methods can be found in SCHLICHTING [83], CEBECI [118], BATHE [92], BELYTSCHKO [119], HUGHES [120] and ZIENKIEWICZ [85].

4 Material Parameter Identification

4.1 Thermophysical Properties

The thermal loading history of a rocket engine during a hot run affects mainly the structural behavior of the rocket combustion chamber wall. The heat generated by the hot gas is induced into the combustion chamber's hot gas wall and transferred to the coolant. This leads to a high temperature gradient (≈ 200 K mm^{-1}) and, consequently, to a high thermal strain distribution with respect to the applied thermophysical material properties. Because microscopic crystalline and electronic structure as well as temperature dependent atomic vibrations are different for each material, the thermophysical properties are determined by the means of additional experimental measurements [121]. With regard to the TMF panel experiment, thermal expansion, specific heat, density, thermal diffusivity, and thermal conductivity of the copper-base alloy CuCrZr are analyzed from ambient temperature up to 1000 K by the Fraunhofer Institute for Mechanics of Materials (IWM). Note that the thermophysical material parameters of CuCrZr could not be determined at cryogenic temperature; although, the TMF panel's inlet temperature is approximately $\theta_{\text{in}} = 160$ K. A solution would be to follow the work of Oschwald [122]. The authors performed measurements of thermal conductivity, specific heat and thermal expansion of the copper-base alloy CuCrZr at low temperatures by using liquid helium ($\theta_{\text{He}} = 4$ K). But this approach is still a demanding task. To follow the determination process of the thermophysical properties, specific test samples are needed for each type of test. Taking into account anisotropic effects of the raw material, the test samples are taken from two directions out of the cold worked plate: One test sample from longitudinal direction and the other test sample from thickness direction. The experimental test setup and the analysis results of the thermophysical parameter determination are described in the following sections.

4.1.1 Thermal Expansion

Thermal expansion is important for any structural material that experiences a temperature gradient. Due to vibrations of the atoms, this temperature gradient affects mainly the internal structure of the material by thermal expansion. Furthermore, the presence of grain boundaries, microcracks, macrocracks, and voids also affect thermal expansion and need to be considered [121].

As most solid materials, the copper-base alloy CuCrZr also expands upon heating and contracts when cooling. With regard to a possible application of CuCrZr in a rocket engine, the temperature dependent geometric change of the applied material leads to inelastic deformation during the hot run and shut down. A thermomechanical analysis (TMA) is carried out with a Netzsch TMA 402 F3 Hyperion [123] to measure the variation of a test sample's uniaxial length under a predefined mechanical load. The linear change of length $\mathrm{d}LL_0^{-1}$ during heating

and cooling corresponds to the linear thermal expansion coefficient α. For determining the linear thermal expansion coefficient, the uniaxial elongation $\mathrm{d}L$ of the test sample and the temperature difference between operating θ and reference temperature θ_{Ref} have been taken into account by

$$\alpha = \frac{1}{L_0} \left(\frac{\mathrm{d}L(\theta) - \mathrm{d}L(\theta_{\mathrm{Ref}})}{\theta - \theta_{\mathrm{Ref}}} \right) \tag{4.1}$$

where L_0 is the initial length of the test sample. The accuracy of the thermal expansion coefficient is better than $\Delta\alpha = 0.5 \cdot 10^{-6}$ K^{-1}. A furnace made of silicon carbide (SiC) heats each test sample from ambient temperature up to $\theta_{\mathrm{Furnace}} = 1000$ K. A thermocouple Type S measures the temperature in the furnace with a standard accuracy of ± 1.5 K (or 0.5 %) up to 1873.15 K; however, the accuracy according to the calibration report is ± 0.3 K. Within the furnace, a push rod connects directly the sample carrier made of aluminum oxide (Al_2O_3) with an inductive displacement transducer (LVDT). The digital resolution of the LVDT is 0.125 nm and the accuracy is +1 µm (taken from a calibration report with a 1 mm gauge block) and +20 µm (taken from a calibration report with a 20 mm gauge block). In addition, a force sensor with a digital resolution of lower than 0.01 mN continuously measures and adjusts the push rod's force. To account for phase changes, sintering steps or softening of the material, the temperature dependent density is measured at ambient temperature with a micrometer caliper (accuracy of ± 1 µm) and a precision balance (accuracy of better than 0.1 g). This leads to an accuracy of better than ± 8.97 % for determination of the density at ambient temperature. Although the density's accuracy seems very high, comparison with the data sheet shows a deviation of only 1 % [31]. The temperature dependent density is calculated by using

$$\rho = \rho_0 \left(1 + \frac{\mathrm{d}L}{L_0} \right)^{-3} \tag{4.2}$$

where ρ_0 is the density determined at ambient temperature. Furthermore, a calibration of the measurement device is performed before each series of testing with a standard calibration target made of platinum.

The temperature dependent experimental results of density and thermal expansion for two test samples with different material orientation are depicted in Fig. 4.1. A density of $\rho_0 = 8814$ kg m^{-3} is measured at ambient temperature and decreases almost linearly with increasing temperature. By performing a regression, the resulting polynomial fit ($R^2 = 1$) for the density [kg m^{-3}] as a function of temperature [K] is

$$\rho = -5.89726 \cdot 10^{-5}\ \theta^2 - 0.40565\ \theta + 8938.867 \tag{4.3}$$

This result agrees with measurements of the linear length change parameter $\mathrm{d}LL_0^{-1}$ (see Fig. 4.1b). By using Eq. 4.1, the thermal expansion coefficient can be determined depending on the temperature. As depicted in Fig. 4.1b, the thermal expansion coefficient increases with increasing temperature. However, the calculated values of the thermal expansion coefficient need to be averaged because of an unsteady heating rate until 400 K (A). A polynomial regression is conducted by using averaged data of both measurements from 300 to 1000 K. The resulting polynomial fit ($R^2 = 0.99$) for the thermal expansion coefficient [10^{-6} K^{-1}] as a function of temperature [K] is

$$\alpha = -2.13853 \cdot 10^{-9}\ \theta^3 + 5.81797 \cdot 10^{-6}\ \theta^2 - 0.00195\ \theta + 16.93485 \tag{4.4}$$

Note that deviation of $\Delta\alpha = 7.86 \cdot 10^{-8}$ K^{-1} at 1000 K between both measurements is within the measurement accuracy of $\pm\ 0.5 \cdot 10^{-6}$ K^{-1} ($\pm$ 3 %). So, it can be concluded that no anisotropic behavior of the two test samples with different material orientation could be observed by using TMA.

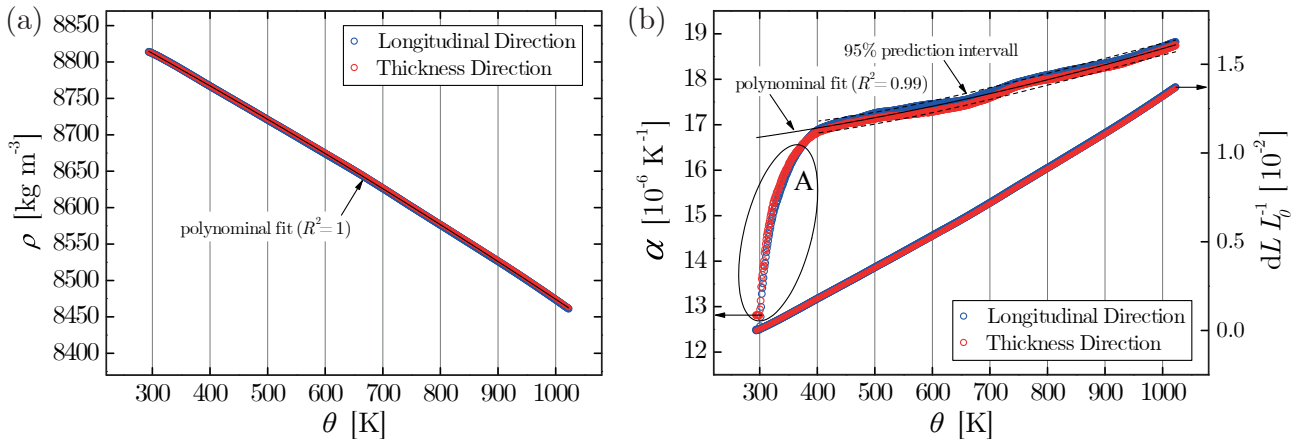

Figure 4.1: Temperature dependent density (a) and thermal expansion coefficient (b) at a reference temperature of $\theta_{\text{Ref}} = 293.15$ K (20 °C) of CuCrZr test samples with different material orientation.

4.1.2 Specific Heat

The specific heat of a material is one of the most important thermodynamic properties indicating the structure's heat retention or loss ability. The main factors that contribute to the specific heat of solids are oscillations of atoms and movement of electrons. With specific heat measurements, physical changes (such as melting, vaporization, and sublimation) and chemical changes (such as chemical reaction, dissolution, adsorption, and dilution) of a material can be investigated [121]. A differential scanning calorimetry (DSC) method is carried out to determine the temperature dependent specific heat capacity at a constant pressure of the copper-base alloy CuCrZr. Two test samples are analyzed with a Netzsch DSC 404/C/6/G Pegasus [124] from ambient temperature to 1000 K. Note that anisotropy has no influence on the specific heat capacity determination. The test sample is mounted with two micrometer screws in a crucible made of platinum with aluminum oxide (Al_2O_3) liner and a lid. Together with an empty crucible, the two crucibles are placed on a sample carrier in the center of a furnace made of silicon carbide (SiC). To avoid oxidizing of the test sample's surface, the test samples are exposed to purge argon atmosphere at a flow rate of 0.04 l min^{-1}. The furnace heats and cools at constant rates of $\Delta\dot{\theta} = 10$ K min^{-1}. A thermocouple type S (Rhodium/Platinum) with a standard accuracy of $\pm$ 1.5 K (or $\pm$ 0.5 %) up to 1873.15 K (or $\pm$ 0.5 K) is used to measure the temperature difference ($\Delta\theta_{\text{Cruc}}$) between the crucible with a test sample and the crucible without a test sample. According to the calibration report, the measured accuracy of the thermocouple at 473.15, 773.15, 1273.15 and 1873.15 K is $-0.2, +0.2, -0.5$ and -0.3 °C, respectively.

According to Blumm [125], a baseline measurement is conducted with two empty crucibles at the beginning. The measured signal can be described as follows

$$V_{\text{Baseline}} = K_C K_A \tag{4.5}$$

where V_{Baseline} is the measured voltage difference of the thermocouple between sample and the reference, K_C is a correlation factor including heating rate and sensor sensitivity, and K_A depicts the influence of the crucibles. Then, a second measurement is performed with a standard sapphire baseline, i.e. a monocrystalline standard material with known specific heat ($c_{p,\text{Sapphire}}$). The measured voltage of this calibration run is calculated by using Eq. 4.5

$$V_{\text{Sapphire}} = K_C K_A + m_{\text{Sapphire}}\ c_{p,\text{Sapphire}} \tag{4.6}$$

where m_{Sapphire} is the mass of the sapphire calibration sample. To obtain the specific heat capacity of the test sample ($c_{p,\text{CuCrZr}}$), the thermocouple's voltage (V_{CuCrZr}) is measured between both the crucible with a test sample and the crucible without a test sample. The resulting DSC signal can be described by using Eq. 4.5 as follows

$$V_{\text{CuCrZr}} = K_C K_A + m_{\text{CuCrZr}}\ c_{p,\text{CuCrZr}} \tag{4.7}$$

where m_{CuCrZr} is the known mass of the test sample made of CuCrZr. By using Eqs. 4.5, 4.6 and 4.7, the specific heat capacity can be determined by

$$c_{p,\text{CuCrZr}} = \frac{m_{\text{Sapphire}}}{m_{\text{CuCrZr}}}\ \frac{(V_{\text{CuCrZr}} - V_{\text{Baseline}})}{(V_{\text{Sapphire}} - V_{\text{Baseline}})}\ c_{p,\text{Sapphire}} \tag{4.8}$$

The accuracy of the specific heat capacity is ± 2.5 % from ambient temperature to 1673.15 K. To account for phase transition effects, separation effects, melting effects and crystallization effects, the transition enthalpy is determined from DSC measurements with an accuracy between ± 1 to ± 3 %.

The temperature dependent DSC measurements for heating and cooling of two test samples are shown in Fig. 4.2a. No endothermal and no exothermal peaks occurred that could indicate any previously mentioned enthalpy related effects or unsteady test conditions. The DSC measurements of the heating phase show a rapid endothermal incline at the beginning of the heating phase until $\theta = 373.15$ K due to unsteady heating rates (A). The maximum DCP-values are 0.02767 µm mg^{-1} at 581 K and 0.02779 µm mg^{-1} at 590 K. The maximum deviation between the two measurements related to the maximum DCP signal value during heating is $\Delta\text{DCP}_{\text{Heating}} = 0.0015$ µm mg^{-1} (5.37 %) at 1000 K. Correspondingly, a rapid exothermal incline occurred at the beginning of the cooling phase at 1000 K (B) and a slight endothermal incline at the end of the cooling phase below 423.15 K due to unsteady cooling rates. The minimum DCP signal values are −0.02441 µm mg^{-1} at 581 K and −0.02533 µm mg^{-1} at 631 K of the two test samples. The maximum deviation between both measurements during cooling is $\Delta\text{DCP}_{\text{Cooling}} = 0.0034$ µm mg^{-1} (13.56 %) from 920 to 750 K. The deviation related to the minimum DCP signal value at 581 K is approximately 0.0009 (3.50 %). Figure 4.2b depicts the specific heat capacity results of the two test samples during heating and cooling that have been determined by using Eq. 4.8. Similar to the thermal expansion results, data points below 373.15 K need to be averaged due to unsteady heating and cooling rates. For temperatures up to 673.15 K, the determined specific heat capacity is within the measurement accuracy of ± 2.5 % (± 11.6 J kg^{-1} K^{-1}). For higher temperatures up to 1000 K, the deviation of the heat capacity between heating and cooling phases increases to approximately 25 % because of unsteady cooling rate. The resulting linear regression for the specific heat capacity [J kg^{-1} K^{-1}] as a function of temperature [K] can be expressed as ($R^2 = 0.14$, cooling)

$$c_p = -2.753 \cdot 10^{-2}\ \theta + 432.561 \tag{4.9}$$

Note that the results obtained from the heating period are omitted because of the high deviation between both measurements at high temperatures. Furthermore, the raw data of the heat capacity is used for calculating the thermal conductivity (see Sec. 4.1.4).

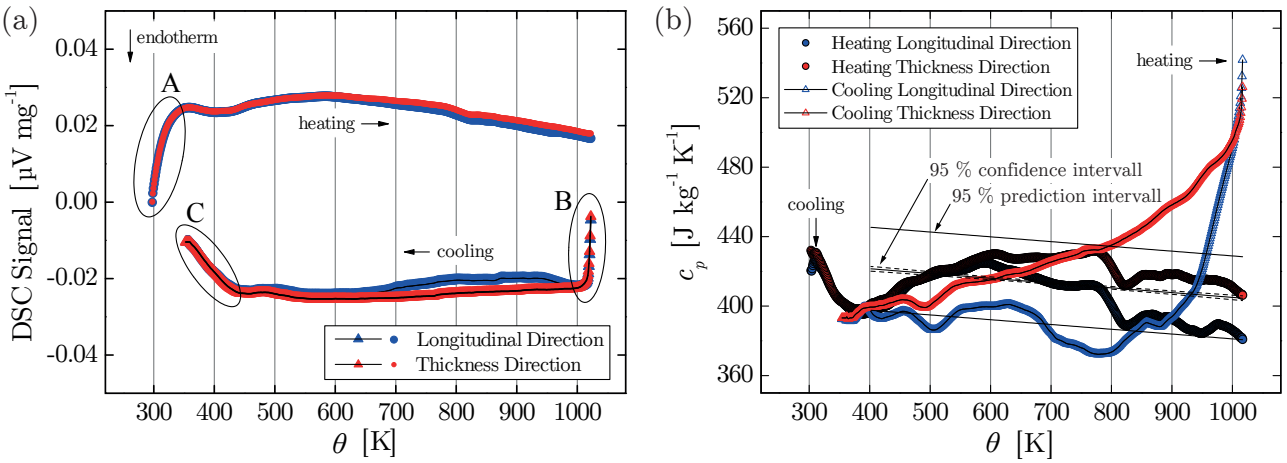

Figure 4.2: Differential-Scanning-Calorimetry (DSC) measurement curve (a) and specific heat capacity (b) of CuCrZr test samples with different material orientation.

4.1.3 Thermal Diffusivity

The principle of the laser flash calorimetry bases on a test sample that is heated by a laser pulse and the resulting temperature difference is measured precisely with an infrared (IR) detector [121]. Therefore, a laser flash analysis (LFA) is conducted with a NETZSCH LFA 427 [126] to determine the thermal diffusivity of the copper-base alloy CuCrZr. The thermal diffusivity is needed to calculate the thermal conductivity (see Sec. 4.1.4). The NETZSCH LFA 427 consists of a measuring unit, a controlling unit, a laser system that is connected with fiber optics, and a data acquisition system. Within the measurement unit, a furnace heats up the test sample with a thin graphite layer coating on both sides. The test sample is mounted on a carrier made of graphite. A thermocouple type S measures the absolute temperature of the test sample. Similar to the TMA, the two test samples are taken from different material orientation out of the raw material to investigate the influence of anisotropy. A purge argon atmosphere at a flow rate of 0.15 l min^{-1} is applied to a furnace to avoid oxidation of the test sample's surfaces. Oxidation would decrease the thermal conductivity significantly. An IR detector made of InSb (Indium-Antimonite) and cooled with liquid nitrogen is mounted on the top of the furnace. This IR detector measures the time dependent temperature increase on the rear face of the test sample after a short laser pulse. A lens made of Ge (Germanium) between the test sample and the IR detector filters the laser light to avoid distorted temperature measurements. The laser systems consists of a Nd:YAG diode laser with an operating voltage of $U_{\text{Nd:YAG}} = 550$ V, a pulse length of $t_{\text{Nd:YAG}} = 0.8$ ms and a wave length of $\lambda_{\text{Nd:YAG}} = 1064$ nm [126]. To increase the accuracy of the tests, three laser pulses are applied at sixteen temperature levels from ambient temperature to 1000 K at an increment of 50 K. Determination of the temperature dependent

thermal diffusivity at adiabatic conditions is then given by

$$a = -\frac{\ln(1/4)}{\pi^2}\frac{l^2}{t_{1/2}} \tag{4.10}$$

where l is the test sample's thickness, and $t_{1/2}(\theta)$ is the time at 50 % of the temperature increase. The accuracy given by the manufacturer is $\Delta a = \pm 3$ %. A comparison between averaged results of measurements in 2015 and 2017 with a pure iron standard showed a maximum deviation of $\Delta a = 0.1$ %.

The thermal diffusivity measurement results are shown in Fig. 4.3. As mentioned previously, three measurements are conducted at each temperature level for two test samples with different material orientation. The thermal diffusivity decreases with increasing temperature. A polynomial regression of the thermal diffusivity [mm s^{-1}] with respect to temperature [K] of the test sample in longitudinal direction ($R^2 = 0.91$) is

$$a_{\text{Long}} = -3.91018 \cdot 10^{-14}\ \theta^3 + 5.99390 \cdot 10^{-11}\ \theta^2 - 3.63299 \cdot 10^{-8}\ \theta + 9.10562 \cdot 10^{-5} \tag{4.11}$$

and of the test sample in thickness direction ($R^2 = 0.93$) is

$$a_{\text{Thick}} = -1.48944 \cdot 10^{-14}\ \theta^3 + 2.94112 \cdot 10^{-11}\ \theta^2 + 1.81974 \cdot 10^{-8}\ \theta + 3.47735 \cdot 10^{-6} \tag{4.12}$$

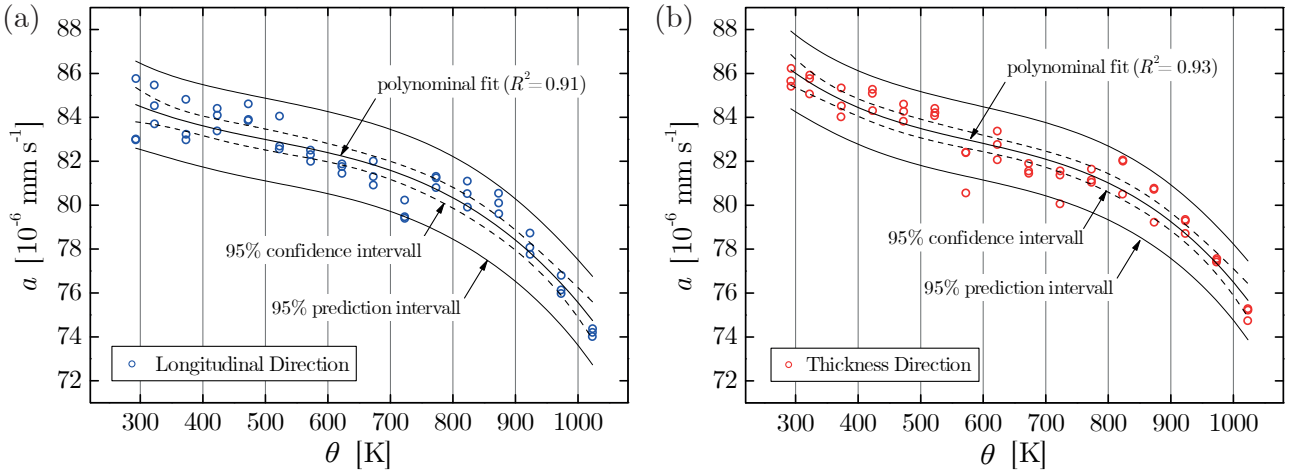

Figure 4.3: Thermal diffusivity measurements with a laser flash analysis (LFA) of CuCrZr test samples in longitudinal (a) and in thickness (b) material orientation.

4.1.4 Thermal Conductivity

Copper alloys of rocket combustion chambers are characterized by high thermal conductivity and high temperature strength [20]. The heat generated by the combustion gas is carried to the coolant in the cooling channels by the conduction electrons. Due to the fact that the heat flux induced into the inner liner of a combustion chamber can be assumed to be constant during operation, the thermal conductivity of the copper alloy influences directly the thermal gradient between the hot gas wall and the cooling channel wall according to FOURIER's law (see Sec. 3.1.3) [127]. To determine the temperature dependent thermal conductivity of the copper-base

alloy CuCrZr, experimental measurement results of density (Fig. 4.1a), specific heat capacity (see Fig. 4.2b) and thermal diffusivity (see Fig. 4.3) are taken into account by

$$\lambda = \rho \; c_p \; a \tag{4.13}$$

Because thermal conductivity cannot be measured directly, polynomial regression data (see Eqs. 4.3, 4.9 and 4.11) is used in combination with Eq. 4.13 instead. The propagation of the calculated thermal conductivity uncertainty correlates with the uncertainty of specific heat (± 2.5 %), thermal diffusivity (± 3 %), density (± 1 %), and thermal expansion coefficient[3] (± 3). In other words, the uncertainty of the calculated thermal conductivity is expected to be $\Delta\lambda \pm 9.5$ % (i.e. ±28.6 W m^{-1} K^{-1} at $\theta = 300$ K).

Figure 4.4 shows the results of the calculated thermal conductivity of the copper-base alloy CuCrZr. The maximum thermal conductivity at $\theta = 300$ K for the test sample in longitudinal direction is $\lambda_{\text{Long}} = 316.99$ W m^{-1} K^{-1} and for the test sample in thickness direction is $\lambda_{\text{Thick}} = 320.14$ W m^{-1} K^{-1} . The thermal conductivity decreases nonlinearly with increasing temperature. The minimum values are 241.72 W m^{-1} K^{-1} and 257.87 W m^{-1} K^{-1} at $\theta = 1016$ K, respectively. Note that the specific heat capacity coefficient from ambient temperature to $\theta = 400$ K contains a large deviation because of an unsteady heating rate at the beginning of the DSC analyses. Therefore, a combined polynomial regression ($R^2 = 0.81$) is performed for thermal conductivity [W m^{-1} K^{-1}] as a function of temperature [K]

$$\lambda = -2.11769 \cdot 10^{-7} \; \theta^3 + 2.35704 \cdot 10^{-4} \; \theta^2 - 0.08291 \; \theta + 310.3419 \tag{4.14}$$

Regarding the polynomial regression of the thermal conductivity, the maximum value is $\lambda_{\text{Fit,max}}$ = 302.24 W m^{-1} K^{-1} at $\theta = 160$ K and the minimum value is $\lambda_{\text{Fit,min}}$ = 251.37 W m^{-1} K^{-1} at $\theta = 1000$ K. The 95-%-prediction-limit of the polynomial fit agrees with an expected total uncertainty (without density) of $\Delta\lambda = 5.5$ % at ambient temperature (i.e. ±16.6 W m^{-1} K^{-1} at 300 K).

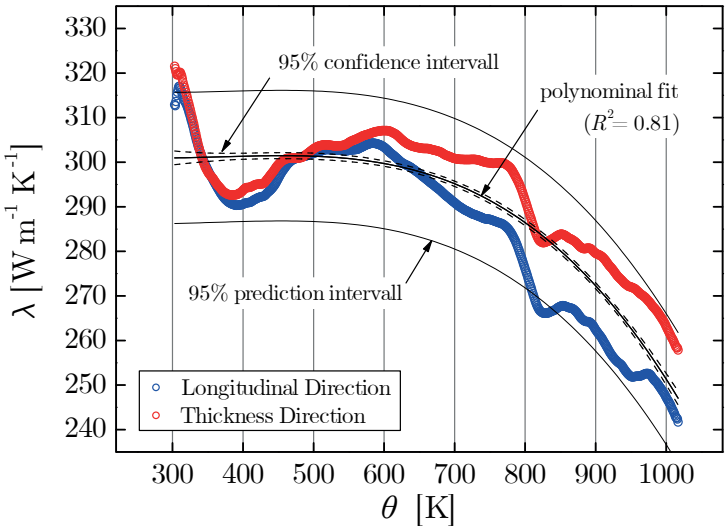

Figure 4.4: Determined thermal conductivity results of CuCrZr tests samples in longitudinal and thickness material orientation.

[3]Accuracy of thermal expansion corresponds to the accuracy of the density above ambient temperature.

Table 4.1: Experimentally determined thermophysical material parameters of CuCrZr.

$\boldsymbol{\theta}$ [K]	$\boldsymbol{\rho}$ [kg m^{-3}]	$\boldsymbol{\alpha}$ 10^{-6} [K^{-1}]	$\boldsymbol{c_p}$ [J kg^{-1} K^{-1}]	$\boldsymbol{\lambda}$ [W m^{-1} K^{-1}]
0	8938.87	16.7000	432.56	302.24[4]
160	8872.45	16.7630	428.16	302.24
300	8811.86	16.8157	424.30	300.96
500	8721.30	17.1470	418.80	301.34
600	8674.25	17.3974	416.04	299.71
700	8626.02	17.6871	413.29	295.16
800	8576.60	18.0034	410.54	286.44
900	8526.01	18.3334	407.78	272.26
1000	8474.24	18.6643	405.03	251.37
1300	8311.86	19.5339	396.77	135.64

4.1.5 Thermal Material Parameter Set

Table 4.1 depicts the temperature dependent density (ρ), thermal expansion coefficient (α), specific heat capacity (c_p), and thermal conductivity (λ) of the copper-base alloy CuCrZr based on Eqs. 4.4, 4.9, 4.11 and 4.14, respectively. Temperature dependent thermal conductivity is used in the coupled steady state fluid thermal analysis in Ansys CFX. The specific heat capacity is used in a separate transient thermal analysis of the solid structure with fitted heat transfer coefficients to determine the laser loading period in the follow-on structural analysis. Note that the transient thermal analysis is not described in this thesis. In addition, the temperature dependent thermal expansion coefficient as well the density are taken into account in the quasi-static structural analysis in Ansys Mechanical (see Fig. 3.1).

4.2 Uniaxial Mechanical Properties

Cyclic laser heating leads to thermomechanical fatigue failure of the actively cooled TMF panel structure. To model the structural response of the employed copper-base alloy CuCrZr with the previously described material model (see Sec. 3.2), required material parameters have to be determined. Uniaxial tensile tests (TT), low-cycle fatigue tests (LCF), multiple hardening stress relaxation tests (SRT) and dwell tests (DT) are performed at different temperatures to obtain the material parameters for elasticity, nonlinear kinematic hardening, combined isotropic hardening and isotropic softening, isotropic ductile damage, microdefect closure effect, and thermal ageing. In this section, the test setup and the material parameter identification approach are described.

4.2.1 Test Setup

Experimental data is acquired by both, uniaxial strain-controlled tests with cylindrical test samples and extensometer measurement (MPA, see Fig. 4.5a), and uniaxial displacement-controlled tests with hourglass-shaped test samples and optical strain measurement (ILK, see

[4]Manually set constant.

Fig. 4.5b). The test samples are heated inductively up to $\theta_{\mathrm{MPA}} = 300, 500, 700$ and 900 K (furnace heating) and $\theta_{\mathrm{ILK}} = 600, 800$ and 1000 K (surrounding heating coil), respectively. The displacement-controlled tests are used to capture the local strain distribution in the necking area of the hourglass-shaped test samples during tensile loading [117]. Note that these tests are only used to complete the temperature range up to 1000 K of the material parameter set determined with strain-controlled tests.

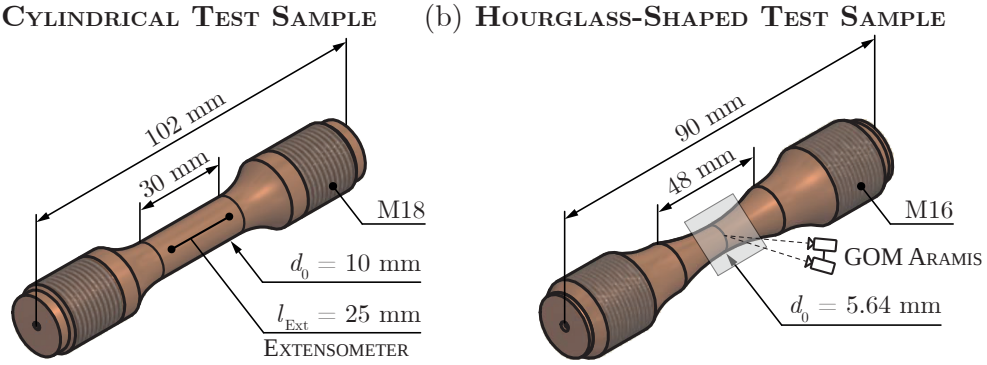

Figure 4.5: Test sample geometry of the strain-controlled (a) and displacement-controlled (b) material characterization test.

The experimental setup of the strain-controlled tests (MPA) is already described by Bouajila [128, 129], Masuoka [130] and Thiede [28, 131, 132]. The setup consists of a cylindrical test sample made of CuCrZr with a minimum diameter of $d_0 = 10$ mm ($\pm$ 0.1 mm), an extensometer with a length of $l_{\mathrm{Ext}} = 25$ mm, and a servo-hydraulic testing machine (Maytec Machine 50) with an accuracy of $\Delta F_{\mathrm{Maytec}} = 0.25$ kN at a maximum load cell loading of $\hat{F}_{\mathrm{Maytec}} = 50$ kN (class 0.5). Combining the absolute accuracy of diameter measurement and load cell, it leads to a stress uncertainty of $\Delta\sigma_{\mathrm{MPA}} = 4$ % for the strain-controlled tests. The accuracy of the extensometer is $\Delta u = 0.5{\cdot}10^{-4}$ mm (class 0.5). The extensometer is attached on the test sample's surface to adjust the servo-hydraulic testing machine's traverse displacement. The accuracy of temperature measurement within the furnace is $\Delta\theta_{\mathrm{MPA}} = \pm$ 3 K.

The experimental setup of the displacement-controlled tests (ILK) is already described by Thiede [117]. The test setup comprises of an hourglass-shaped test sample, a spiral-shaped inductive coil heater, a high speed pyrometer (Sensortherm Metis HI16), an IR camera (InfraTec VarioCAM), and an optical deformation measurement system (GOM Aramis 5M) with two light spots. The hourglass-shaped test samples are made of CuCrZr with a minimal diameter of $d_0 = 5.64$ mm that accords to DIN EN 6072 (see Fig. 4.5b) [133]. To measure the local engineering strains on the test sample's surface, a three layer PVD-coating system (similar to the TMF panel coating described in Sec. 2.1.4) with a random speckle pattern made of aluminum oxide (Al_2O_3) is used. Two high-resolution cameras are mounted together with 75 mm objectives at an angle of 24.1° in direction to the sample's center. A calibration is performed with a calibration plate before each test under test conditions. The resulting calibration deviation is determined to approximately 0.052 px at 2448 x 2050 px. The displacement-controlled tensile tests are carried out on a servo-hydraulic testing system (Schenck PC63M with Instron 8800 control unit) with a maximum load of $F_{\mathrm{Schenck}} = 40$ kN. The servo-hydraulic testing machine measures the force with a load cell and the traverse displacement. Unfortunately, the servo-hydraulic traverse movement could not be adjusted by the GOM Aramis 5M system directly. Scattering of optical determined strain data (measurement noise) could lead to instable movement of the traverse and, consequently, to damage of the testing machine.

However, application of an extensometer on the sample's surface to strain-control the servo-hydraulic testing machine was not possible due to insufficient space of the test setup [117]. As previously mentioned, we used induction heating to heat up the test sample to the targeted test temperature. The temperature on the test sample's surface is measured with a high speed pyrometer (SENSORTHERM METIS HI16) and an IR camera (INFRATEC VARIOCAM). The pyrometer adjusts the inductive heater directly at a spectral range from 1.45 to 1.8 µm and at a temperature range from 673.15 to 1473.15 K (high resolution). The IR camera is used to measure the temperature distribution on the entire surface of the test sample. The emissivity coefficient of the pyrometer and the IR camera is set to $\varepsilon_\alpha = 1$. Therefore, a coated dummy sample with a thermocouple mounted in the inside of the sample is used to calibrate the pyrometer and the IR camera together at the three different temperature levels $\theta_{\mathrm{ILK}} = 600, 800$ and 1000 K.

4.2.2 Approach and Results

Figure 4.6 depicts the material parameter identification approach that is used in this work. This approach consists of four steps: Set initial values for each temperature level obtained from literature, optimize the viscoplastic parameters on the basis of experimental test data, adjust all parameters manually with respect to numerical stability at high temperature gradients, and validate the final parameter set.

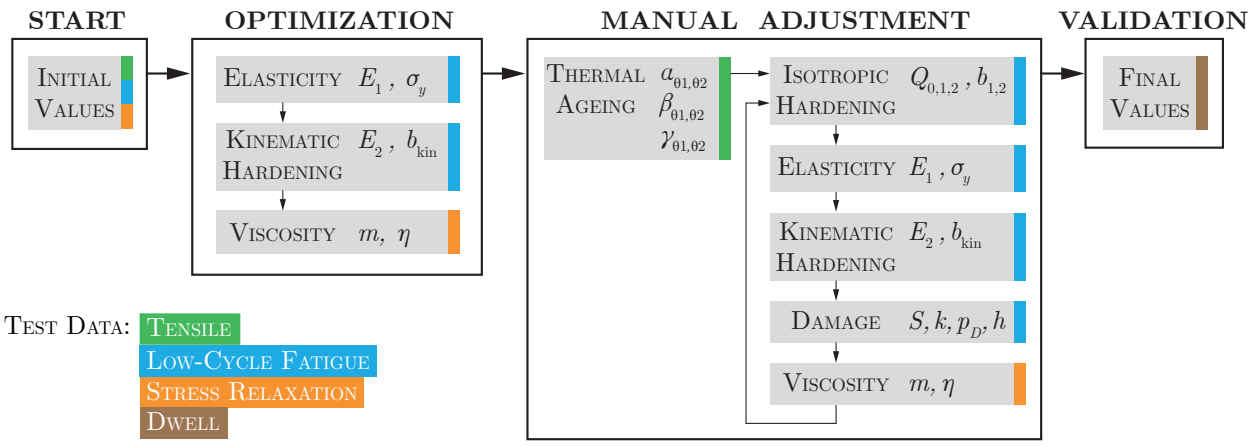

Figure 4.6: Overview of the material parameter fitting approach.

First, initial values for elasticity, nonlinear kinematic hardening, combined isotropic hardening and isotropic softening, viscosity and isotropic ductile damage are taken from THIEDE [132] and initial values for thermal ageing are taken from THIEDE [116, 117]. Neglecting all constant values, 21 material parameters have to be fitted entirely. Note that further effects are implemented in the model, but omitted due to numerical stabilization reasons. Examples are decrease of rupture strain depending on ageing time by variation of the damage material parameter S (see Eq. 4.17), and static recovery of nonlinear kinematic hardening A_x (see Eq. 4.19).

Hence, the second step is to optimize the viscoplastic material parameters by using the method of conjugated gradients in ANSYS. This method minimizes the object function $f(x)$ as follows

$$\min\left(f(x)=\frac{1}{2}\sum_{i=1}^{N}\left(\sigma_{\text{true,EXP}}(\varepsilon,t,\theta)-\sigma_{\text{true,FEM}}(\varepsilon,t,\theta)\right)^2\right) \tag{4.15}$$

where $\sigma_{\text{true,EXP}}$ is the true (logarithmic) uniaxial stress obtained from experimental data and $\sigma_{\text{true,FEM}}$ is the true (logarithmic) uniaxial stress computed in Ansys. Note that only a unity cell is employed, i.e. a second-order one-element model with an edge length of $l_0 = 1$ m each. Due to the fact that the SI-unit system (m, kg, K, s, W) is applied in the simulation, the unity cell's nodal displacements Δu correspond to the engineering strain obtained from experimental data

$$\varepsilon_{\text{eng}}=\frac{\Delta u}{l_0}=e^{\varepsilon_{\text{true}}}-1 \quad \text{and} \quad \sigma_{\text{true}}=\sigma_{\text{eng}}\left(1+\varepsilon_{\text{eng}}\right) \tag{4.16}$$

where Δu is the uniaxial elongation in loading direction with respect to the initial length. Note that the displacement applied on the unity cell depends on the loading time t and the uniform temperature θ. The linear elasticity parameters and nonlinear kinematic hardening parameters at $\theta_{\text{MPA}} = 300, 500, 700$ and 900 K are optimized on the basis of the initial strain-controlled LCF cycle at a strain range of $\Delta\varepsilon = \pm\ 1$ % and at a strain rate of $\dot{\varepsilon} = 0.002\ \text{s}^{-1}$ (see Fig. 4.6). The viscosity parameters are then optimized based on multiple hardening stress relaxation tests at 700 and 900 K. Thermal ageing is omitted in the optimization procedure because of the short time periods ($t_{\text{SRT}} < 1$ h).

According to the material parameter fitting approach presented in Fig. 4.6, the third step consists of a manual adjustment of all contained material parameters at all temperature levels. At first, thermal ageing parameters are fitted with tensile loaded test samples that have been carried out in a furnace for $t_\theta = 0, 10$ and 20 h before testing. The displacement controlled tensile tests with strain measurement by the means of DIC are performed until rupture of the specimens, but only a strain range up to 1 % at $\theta_{\text{ILK}} = 800$ and 1000 K is used to model the stress shift σ_θ with reference to ageing time and temperature. As depicted in Fig. 4.7, the experimental determined stress decrease due to thermal ageing between $t_\theta = 0$ to 10 h is $\sigma_{\theta,0\to10\text{h}} = 46.19$ MPa and between $t_\theta = 10$ to 20 h is $\Delta\sigma_{\theta,10\to20\text{h}} = 18.01$ MPa at 800 K. In the same way, the stress decrease at 1000 K is $\sigma_{\theta,0\to10\text{h}} = 14.73$ MPa and $\sigma_{\theta,10\to20\text{h}} = 3.68$ MPa, respectively. The deviation between experimental and numerical results at a mechanical strain of $\varepsilon_{\text{mech}} = 1$ % is $\Delta\sigma_{\theta,0\to10\text{h}} = 1.28$ MPa and $\Delta\sigma_{\theta,10\to20\text{h}} = 4.16$ MPa at 800 K as well as $\Delta\sigma_{\theta,0\to10\text{h}} = 5.94$ MPa and $\Delta\sigma_{\theta,10\to20\text{h}} = 2.04$ MPa at 1000 K, respectively. It can be concluded that thermal ageing affects the material three times more between the ageing periods 0 and 10 h than between 10 and 20 h. A total stress decrease of 24.54 and 26.50 % is observed at 800 and 1000 K, respectively. Note that the experimental data of 20-h-aged CuCrZr test samples at 700 K showed a stress decrease less than 2 %; therefore, it remains within the measurement uncertainty limit and is omitted below this temperature [28, 116, 117].

Besides the modeling of thermal ageing with respect to the decrease of yield stress limit depicted in Fig. 4.7, the rupture strain is also affected by thermal ageing. As shown in the work of Thiede [116, 117], the rupture strain decreases with significantly increasing ageing periods at high temperatures. A linear decrease of the damage parameter S (see Eq. 3.54) by thermal ageing is considered in this model as follows

$$\bar{S}=S+S\left(S_\vartheta-1\right)\frac{t_\theta}{t_\vartheta} \tag{4.17}$$

where $0 \geq S_\vartheta \geq 1$ and t_ϑ are material parameters, and t_θ is the current ageing time stored

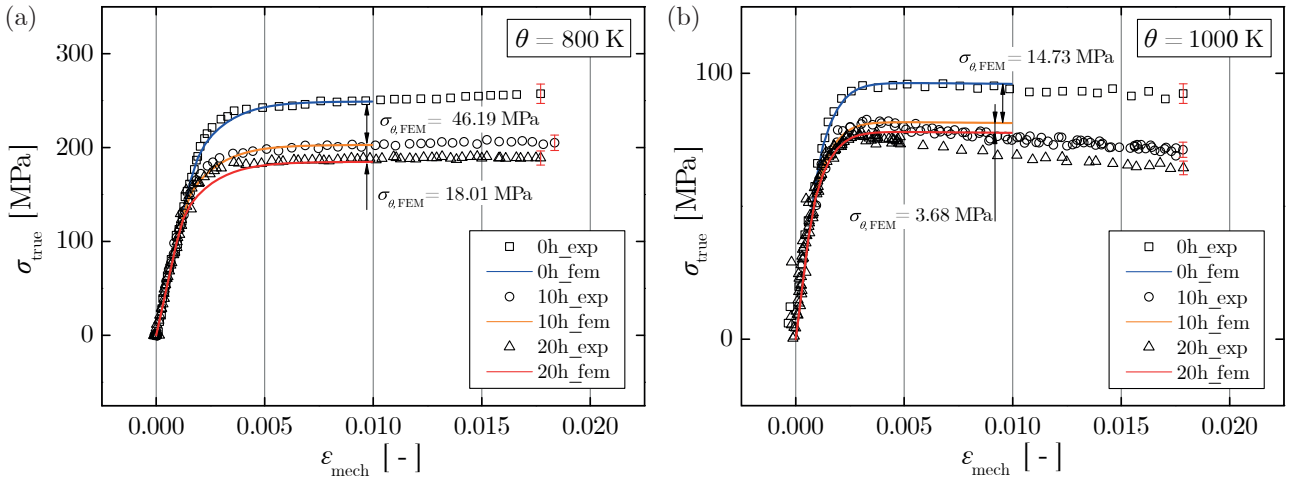

Figure 4.7: Comparison of experimental and numerical stress-strain results of aged test samples under tensile loading at $\theta_{\mathrm{ILK}} = 800$ K (a) and 1000 K (b).

as an internal state variable. However, this effect is needed to be examined carefully and, consequently, omitted in this work.

After having fitted the thermal ageing parameters, the parameters for combined isotropic hardening and isotropic softening, elasticity, kinematic hardening and isotropic damage with crack closure effect are adjusted manually on the basis of LCF tests (see Fig. 4.6). As mentioned previously, the LCF tests at $\theta_{\mathrm{MPA}} = 300, 500, 700$ and 900 K are conducted strain-controlled with a strain range of $\Delta\varepsilon = \pm\ 1\ \%$ and a strain rate of $\dot{\varepsilon} = 0.002\ \mathrm{s}^{-1}$ (linear loading). The LCF tests at $\theta_{\mathrm{ILK}} = 600, 800$ and 1000 K are performed displacement-controlled with an envisaged strain range of $\Delta\varepsilon = \pm 1\ \%$ at the same strain rate (sinusoidal loading). The strain ratio of the LCF tests is $R_\varepsilon = -1$. Figure 4.8 depicts the experimental and numerical uniaxial stress depending on the accumulated plastic strain over all cycles until failure. One the one hand, isotropic softening mainly governs the evolution of the stress at elevated temperatures as a consequence of the cyclic change of the yield surface. As depicted in Fig. 4.8a, isotropic hardening is only observed for low values of accumulated plastic strain up to $p_\alpha = 0.3$ and 0.19 at $\theta_{\mathrm{MPA}} = 300$ and 500 K, respectively. Pure linear isotropic softening appears at temperatures higher than 700 K. Cyclic softening is modeled by fitting the parameter Q_0. The parameter Q_0 describes the linear softening (or linear hardening) behavior at large values of accumulated plastic strain. The parameters $Q_{1,2}$ and $b_{1,2}$ are used to model the cyclic hardening and softening at low values of accumulated plastic strain. Note that accumulated plastic strain is calculated from experimental data by using

$$p_\alpha \approx 2\Delta\varepsilon^p n_{\mathrm{Cyc}} \tag{4.18}$$

where $\Delta\varepsilon^p$ is the cyclic plastic strain range, and n_{Cyc} is the cycle number [134]. According to Lemaitre [109], the cyclic plastic strain range can be easily calculated from strain-controlled LCF tests (see Fig. 4.8a). However, it is difficult to identify $\Delta\varepsilon^p$ on the basis of displacement-controlled tests (see Fig. 4.8b). By comparing Figs. 4.8a and b, one can see that the maximum value of accumulated plastic strain decreases from 10.84 to 4.7 depending on the temperature from 300 to 800 K, respectively. For temperature levels at 900 and 1000 K, the maximum accumulated plastic strain value increases continuously instead. Consequently, ductility of the CuCrZr material increases with increasing temperature over 800 K. A reason could be that chromium is more and more solved in the copper matrix and could no longer prevent the grains

from growing extensively [33, 34].

Furthermore, the damage threshold value p_D activates evolving of ductile isotropic damage that decreases elastic stiffness continuously until failure (see Eq. 3.54). In case of either structural failure or development of a macro crack, the damage state variable D reaches the critical damage value D_c. This parameter limits the phenomenological material model and a follow-on model basing on fracture mechanics needs to be applied to consider further crack growth. In addition, the LCF tests could not always be conducted until clear failure of the test samples (fully cracked) to prevent the testing machine from damage. Therefore, the isotropic damage parameters are fitted with respect to existing data. Regarding the strain-controlled tests depicted in Fig. 4.8a, a good accordance with experimental data is obtained. However, fitting of the damage parameters S and k on the basis of cyclic displacement-controlled tests is difficult due to numerical instabilities. These instabilities occurred primarily at small stress ranges ($\Delta\sigma_{\text{true}} \approx \pm$ 30 MPa) in combination with large values of accumulated plastic strain ($p_\alpha \approx 8$) at high temperatures ($\theta_{\text{ILK}} = 1000$ K) (see Fig. 4.8b). In addition, the stress range at 600 K (see Fig. 4.8b) does not fit entirely to experimental data obtained by strain-controlled tests at $\theta_{\text{MPA}} = 300$ and 500 K (see Fig. 4.8a); therefore, the parameter set at $\theta_{\text{ILK}} = 600$ K would lead to numerical instabilities in FE analyses at high thermal gradients and should be neglected in the TMF panel fatigue analysis. The microdefect closure parameter is fitted depending on the cyclic stress change while damage is active. Lemaitre [108] suggests a microdefect closure parameter of $h = 0.2$ for copper materials, but this would lead to a much steeper decrease of the stress in the compressive domain. As shown in Figs. 4.8a and b, a temperature independent value of $h = 0.8$ shows a good accordance to experimental data with test samples made of the copper-base alloy CuCrZr.

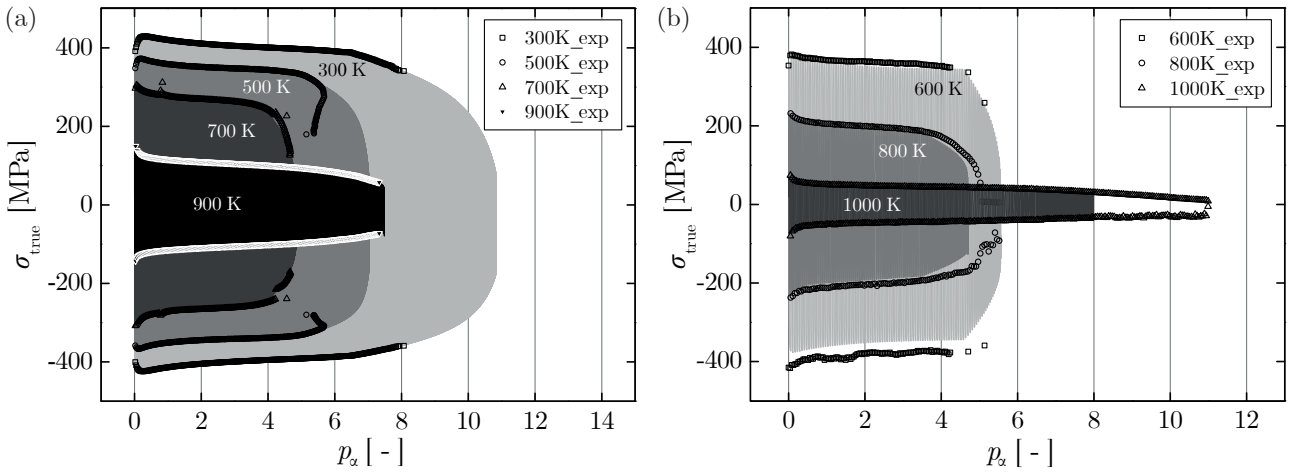

Figure 4.8: Development of the stress depending on accumulated plastic strain over all cycles at different temperatures of strain-controlled LCF tests (a) and displacement-controlled LCF tests (b).

Figure 4.9 shows the numerical results at $\theta = 800, 900$ and 1000 K with and without thermal ageing. Deactivation of thermal ageing decreases the stress level by $\sigma_\theta = 10.1, 6.6$ and 6.5 MPa with respect to ageing time and leads to a failure at an earlier stage depending on decreased values of accumulated plastic strain by $p_\alpha = 0.27, 0.81$ and 0.73, respectively. Therefore, thermal ageing needs to be considered in the fitting procedure of both, the isotropic hardening parameters, and the isotropic damage parameters.

Figure 4.10 depicts the stress-strain hysteresis of the very first LCF cycle from $\theta = 300$ to

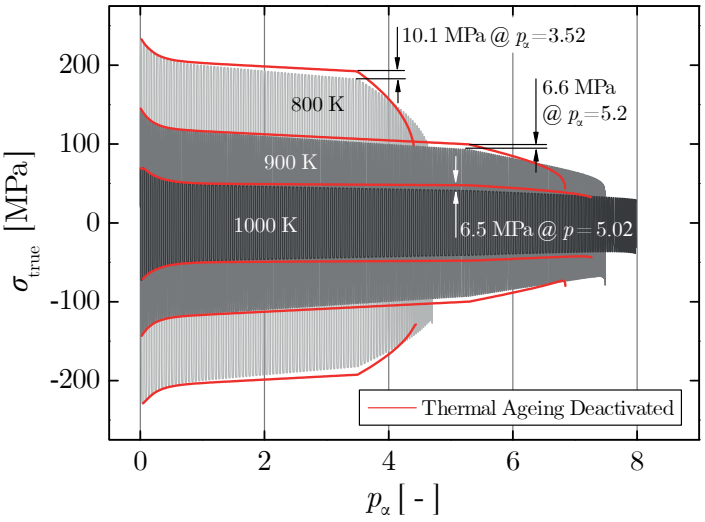

Figure 4.9: Influence of thermal ageing on the stress and damage behavior over all cycles at different temperatures.

1000 K. Because of lack of data, the YOUNG's modulus and the yield stress at temperatures of $\theta = 160$ and 1300 K are extrapolated by $\pm$ 20 %. It is strongly recommended to conduct material tests at the envisaged TMF panel cooling temperature (e.g. $\theta_{in} = 160$ K) at least. On the basis of strain-controlled tests, the numerical results computed with a unity cell accords with experimental data (see Fig. 4.10a). Only the stress hysteresis during initial loading is underrepresented. Expanding the kinematic hardening formulation by using either a second parallel-connected spring-damper element or including a static or a dynamic recovery factor (see SCHWARZ [21] and BOUAJILA [129]) could lead to a better accordance of numerical fitted data to experimental data at initial loading. Figure 4.10b shows the stress-strain hysteresis from displacement-controlled tests. Despite this, the displacement is set to an initial optical measured strain of $\Delta\varepsilon = \pm$ 1 % before each test manually, the LCF strain range still differs from the initial strain range due to the influence of temperature onto the test sample's structure.

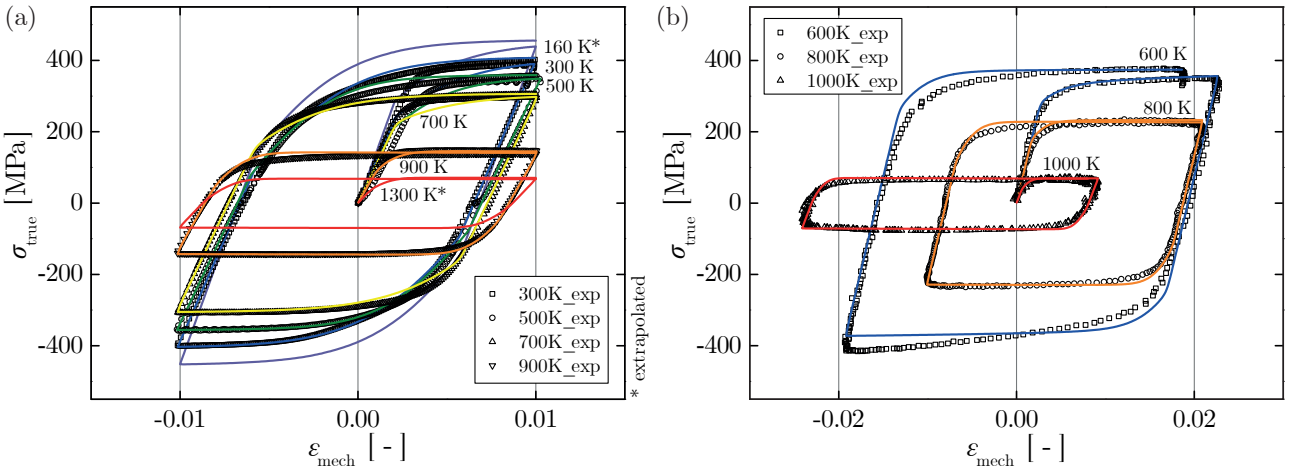

Figure 4.10: Stress-strain hysteresis of the first LCF cycle at different temperatures with experimental data from strain-controlled LCF tests (a) and displacement-controlled LCF tests (b). The symbol (*) depicts the numerical computed results with extrapolated material parameter set.

The rate-dependent behavior of the applied material model is demonstrated by multiple hardening stress relaxation tests at $\theta_{\mathrm{MPA}} = 700$ and 900 K with holding periods of $t = 600$ s (10 min) and a strain increment of $\Delta\varepsilon_{\mathrm{Loading}} = +1$ % (see Fig. 4.11b). The holding period corresponds to a common rocket engine's hot-firing cycle. Figure 4.11a shows the numerical obtained results compared to experimental data. A good accordance is observed at 700 K. At a temperature of 900 K, the difference between peak stress and decreased stress (so-called viscous stress) as well as the linear slope of the stress during holding period deviates to experimental data. To increase the viscous stress, the yield stress σ_y should be reduced and then compensated with the kinematic hardening parameters E_2 and b_{kin}. Another approach is to implement a static recovery effect of kinematic hardening into the present material model. According to Chaboche [134], such a time recovery factor would lead to a partial loss of the hardening effect by the vanishing of dislocations and redistribution of internal stresses in metals at high temperatures. Therefore, the static recovery factor A_x for kinematic hardening is implemented in the material model by

$$\boldsymbol{\varepsilon}^{pi} = \boldsymbol{\varepsilon}^{pe,D}\dot{\lambda}\; b_{\mathrm{kin}} + \boldsymbol{\varepsilon}^{pe,D} A_x \tag{4.19}$$

The difference of the stress relaxation with and without static recovery factor is depicted in Fig. 4.11a. A good accordance with experimental data at $\theta_{\mathrm{MPA}} = 900$ K can be observed. Application of the static recovery factor to the TMF panel analysis leads to numerical instabilities caused by the linear interpolation between the different temperature levels with regard to the large temperature gradient. Therefore, the presented static recovery factor is omitted in the TMF panel analysis ($A_x = 0$). The difference of the decreased stress without static recovery to experimental data at a constant strain of $\varepsilon = 1$ % at the holding periods of $t = 200$ s and 600 s is $\Delta\sigma = 7.8$ MPa (5.9 %) and 15.3 MPa (11.6 %), respectively. Note that for consistency reasons of isotropic softening and viscous stress, the yield stress parameter is decreased by $\Delta\sigma_y = 5.5$ MPa (13.1 %) for the stress relaxation test at 900 K. Viscosity is also neglected for temperatures lower than 500 K and set constant for temperatures higher than 900 K.

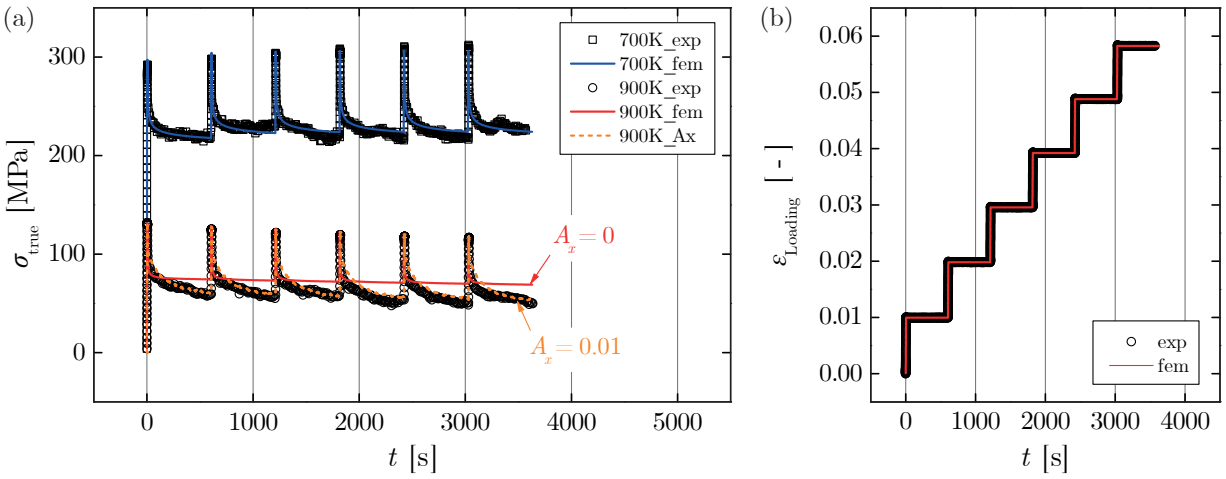

Figure 4.11: Schematics of multiple hardening stress relaxation tests with holding periods of 600 s at 700 and 900 K with and without static recovery (a) and loading history (b).

In addition to performed low-cycle fatigue and stress relaxation tests, uniaxial dwell tests at $\theta_{\mathrm{MPA}} = 700$ and 900 K with a similar holding period of $t = 600$ s in tension and compression are carried out to validate the assessed material parameter set at elevated temperatures. The experimental and numerical results from the 1$^{\mathrm{st}}$ to the 5$^{\mathrm{th}}$ cycle and their corresponding loading

history are depicted in Figs. 4.12a and b. Comparison of the numerical results show a good accordance with experimental data at 700 K. A slight increase of isotropic hardening is observed for low values of accumulated plastic strain that accords with stress relaxation test results depicted in Fig. 4.11a. As shown in Fig. 4.12a, modeling of the stress relaxation at 900 K is more accurate by taking into account the static recovery of kinematic hardening ($A_x = 0.01$). As soon as the parameter A_x needs to be neglected for numerical stability reasons, the viscous stress is underrepresented by 7.7 MPa (5.6 %) and 16.5 MPa (15.1 %) at the end of the 1$^{\text{st}}$ (10 min) and 5$^{\text{th}}$ (60 min) cycle under tensile loading, respectively. Note that the viscous parameters at 1000 K are similar to the viscous parameters at 900 K.

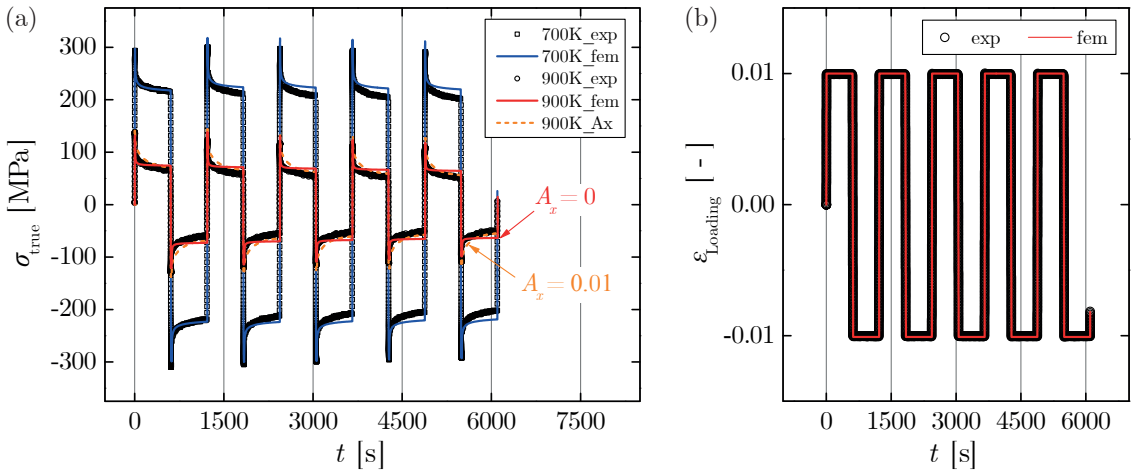

Figure 4.12: Schematics of dwell tests with holding periods of $t = 600$ s at $\theta_{\text{MPA}} = 700$ and 900 K with and without static recovery (a) and loading history (b).

Figure 4.13 shows the numerical and experimental results of the dwell tests with a strain range of $\pm$ 1 % at $\theta_{\text{MPA}} = 700$ and 900 K over all loading cycles. Regarding the experimental acquired data, only the first 10 cycles and every further 5$^{\text{th}}$ cycle is plotted. The total number of strain-controlled cycles is $\hat{n}_{\text{Cyc,700K}} = 132$ ($\hat{t}_{700\text{K}} = 44$ h) at 700 K and $\hat{n}_{\text{Cyc,900K}} = 147$ ($\hat{t}_{900\text{K}} = 49$ h) at 900 K. A good accordance between numerical results and experimental data at 700 K is observed. Similar to the LCF tests, the dwell tests are stopped early to prevent the testing machine from damage. At a temperature of 900 K, the numerical results agree with experimental data at low values of accumulated plastic strain ($t_\theta \approx 5$ h). Then, thermal ageing leads to linear decrease of the maximum stress until failure at 20 h. In case of deactivating thermal ageing in the model, the stress is increased by $\Delta\sigma_{900K,20h} = 23.95$ MPa (63.9 %) at $t_\theta = 20$ h. Due to the fact that the thermal ageing parameters are fitted on the basis of tensile tests at temperatures of $\theta_{\text{ILK}} = 800$ and 1000 K, the stress decrease within this range is linear interpolated (e.g. for 900 K). Due to the fact that the run-time of the TMF panel tests is expected to be lower than $t = 20$ h and the predefined hot-wall temperature of the TMF panel experiment is $\hat{\theta} = 1000$ K, the thermal ageing parameters are fitted to $\theta_{\text{ILK}} = 1000$ K. Although, it is strongly recommended to perform strain-controlled dwell tests at 1000 K to obtain better accordance to reality.

4.2.3 Structural Material Parameter Set

Table 4.2 depicts the entire structural material parameter set for a temperature range of $\theta = 160$ to 1300 K. This set accords to the material parameter fitting results showed in pre-

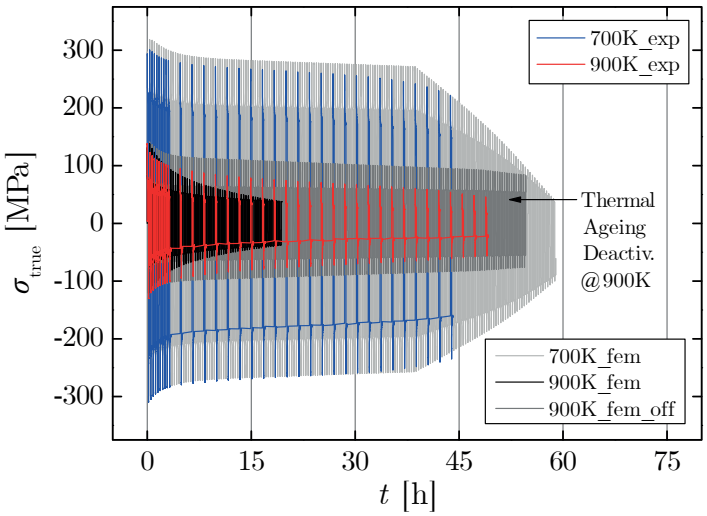

Figure 4.13: Comparison of experimental and numerical obtained results of dwell tests performed until failure of the test samples.

vious Sec. 4.2.2. Due to lack of data at 160 and 1300 K, the elastic parameters E_1 and σ_y as well as the damage parameter S are extrapolated by ± 20 % (see Tab. 4.2). The Poisson's ratio is set constant to $\nu = 0.3$. Viscosity of the copper-base alloy CuCrZr is assumed to be negligible for temperatures lower than 500 K; therefore, the viscosity parameter is set to almost zero ($\eta = 10^{-5}$). In case of setting the viscosity parameter $\eta = 0$, numerical instabilities would appear leading to an increase of iteration steps and the computation time. In addition, the microdefect closure parameter ($h = 0.8$) is assumed to be temperature independent. As mentioned previously, the temperature levels 600 and 800 K are neglected in the material parameter set prepared for the finite element analysis of the TMF panel; so that $\theta = 160, 300, 500, 700, 900, 1000$ and 1300 K are used instead.

To complete the material parameter set, Tab. 4.3 depicts the applied thermal ageing parameters at $\theta_{\text{ILK}} = 800$ and 1000 K that accord with experimental data showed in Fig. 4.7. Thermal ageing is enabled at temperatures higher than 700 K and linear interpolated between 800 and 1000 K. For temperatures higher than 1000 K, the thermal ageing parameters are set constant. Therefore, the parameters are not extrapolated and the stress decrease remains constant at temperatures higher than 1000 K.

The proposed material model contains of further effects that are omitted in this work. Examples are the static recovery factor of kinematic hardening A_x (see Eq. 4.19) and a damage scaling factor S_ϑ at a predefined ageing temperature t_ϑ (see Eq. 4.17). As mentioned previously, application of the static recovery factor leads to a more accurate stress relaxation slope at high temperatures under constant strain [132]. A decrease of the damage parameter S causes an increase of damage with respect to ageing time t_θ. Consequently, the rupture strain decreases with increasing ageing time at elevated temperatures [116, 117].

[5]Extrapolated by ± 20 % to closest value.

Table 4.2: Structural material parameters of CuCrZr.

$\boldsymbol{\theta}$ [K]	$\boldsymbol{E_1}$ 10^9 [Pa]	$\boldsymbol{\sigma_y}$ 10^6 [Pa]	$\boldsymbol{E_2}$ 10^9 [Pa]	$\boldsymbol{b}_{\text{kin}}$ [-]	$\boldsymbol{Q_1}$ 10^6 [Pa]	$\boldsymbol{b_1}$ [-]	$\boldsymbol{Q_2}$ 10^6 [Pa]	$\boldsymbol{b_2}$ [-]	$\boldsymbol{Q_0}$ 10^6 [Pa]
160	138 [5]	271.2 [5]	64.991	337.467	−40	0.5	37	10	0
300	115	226	64.991	337.467	−40	0.5	37	10	0
500	105	198	75.698	447.330	−31	0.7	24	16	0
600	105	175	23.000	381.000	−23	0.7	30	32	0
700	105	130	27.073	315.585	−22	4.0	10	32	−2.5
800	105	107	48.438	781.537	−18	5.0	5	32	−2.5
900	87.5	42	57.826	1261.900	−10	5.5	0	32	−1.5
1000	65	22	58.000	1825.840	−11	3.9	0	32	−0.2
1300	52 [5]	17.6 [5]	58.000	1825.840	−11	3.9	0	32	−0.2

$\boldsymbol{\theta}$ [K]	$\boldsymbol{\eta}$ [Pa s]	$\boldsymbol{m_\eta}$ [-]	$\boldsymbol{S_D}$ 10^6 [Pa]	$\boldsymbol{k_D}$ [-]	$\boldsymbol{p_D}$ [-]	$\boldsymbol{h}$ [-]
160	10^{-5}	6.4	2.100	2.0	6.0	0.8
300	10^{-5}	6.4	1.750	2.0	6.0	0.8
500	10^{-5}	6.4	1.110	2.0	4.7	0.8
600	38	6.4	0.740	2.0	4.6	0.8
700	76	6.4	0.400	2.0	3.7	0.8
800	76	6.4	0.255	2.0	3.5	0.8
900	1800	3.2	0.105	2.0	5.3	0.8
1000	1800	3.2	0.095	1.0	5.3	0.8
1300	1800	3.2	0.076	1.0	5.3	0.8

Table 4.3: Thermal ageing parameters of CuCrZr.

$\boldsymbol{\theta}$ [K]	$\boldsymbol{\alpha_\theta}$ 10^9 [Pa s]	$\boldsymbol{\beta_\theta}$ 10^3 [s]	$\boldsymbol{\gamma_\theta}$ 10^6 [Pa]
800	2741	46	158.40
1000	333.1	24	72.22

4.3 Scanning Electron Microscopy of Test Samples

According to Sec. 2.1.2, scanning electron microscopy (SEM) of the fracture surface from selected test samples after tensile and fatigue loading is conducted. The SEM images captured with detection of secondary electrons are used to draw conclusions about the TMF panel's failure mode [135]. To do so, the fracture surface of the TMF panel crack is compared to the fracture surface of ruptured test samples. Figure 4.14 depicts both the ductile fracture surface of tensile loaded non-aged test samples at $\theta_{\mathrm{ILK}} = 600, 800$ and 1000 K (upper-side) and the fracture surface of cyclically loaded non-aged test samples at $\theta_{\mathrm{ILK}} = 600, 800$ and 1000 K (lower-side).

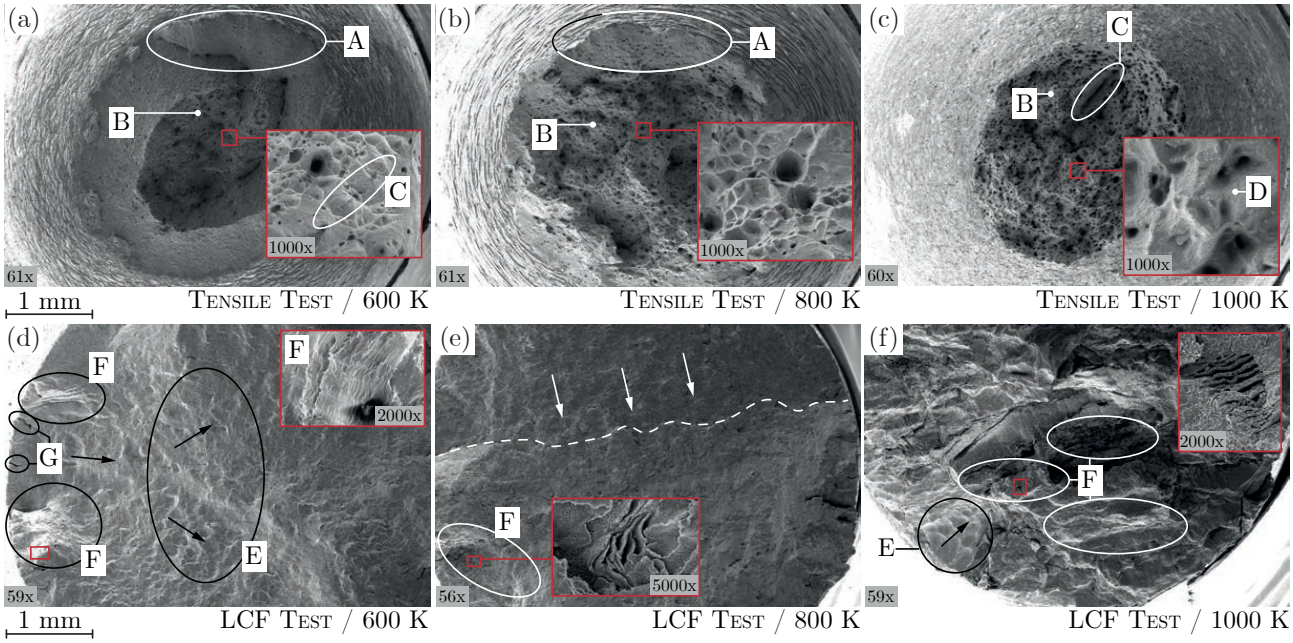

Figure 4.14: SEM images of a test sample's fracture surface after tensile loading (upper-side) and fatigue loading (lower-side) at different temperatures without pre-aged test samples.

Regarding the tensile ruptured test samples, a shear fracture (A) with necking at the outsides and a ductile fracture (B) in the center of the test sample are observed at $\theta_{\mathrm{ILK}} = 600$ and 800 K. At 1000 K, only a ductile fracture surface (B) after necking is observed. The shear fracture can be interpreted as a cup-and-cone fracture that typically occurs at an angle of 45° around the fracture surface. The shear lip of the tensile loaded test sample at 600 K is smoother and larger compared to the tested test sample at 800 K. A dimple structure indicates ductile fracture as a result of micro void growth and coalescence [81]. One can see that increasing the temperature leads to an increase of the dimple structure size. This causes higher ductility and stronger necking of the copper alloy CuCrZr at elevated temperatures (see upper-side of Fig. 4.14). In addition, large magnification of the fracture surfaces shows a lamellar structure that is caused by oxidation of the fractured copper surface after testing (D). Another important fact is that material defects could lead to a decreased rupture strain during testing. The upper-left side of Fig. 4.14 depicts a crack that is detected in the ductile fracture surface of the tensile loaded test sample caused by a material defect (C) [135].

The lower-side of Fig. 4.14 depicts the fracture surfaces of cyclically loaded test samples at $\theta_{\mathrm{ILK}} = 600, 800$ and 1000 K. Due to the fact that the LCF tests are not conducted until

clear failure of the test samples, the test samples are torn apart into two pieces after the test to get prepared for SEM. This leads partially to a ductile fracture surface that does not belong to the fatigue failure mode. The fatigue fracture surfaces of test samples made of CuCrZr are mainly characterized by beach marks, fatigue striations and cracks. According to BÜRGEL [81], beach marks denote macroscopic visible positioning marks representing the crack propagation direction. Fatigue striations are similar to beach marks, but they characterize the crack growth per cycle at a microscopic scale. As depicted in Fig. 4.14, beach marks (E) and striations (F) are observed at all test samples. In particular, wave-shaped beach marks are located in the center of test sample at 600 K. It seems that the crack grow evolved from the left side of the test sample where macro cracks are depicted (G). The cracks are initiated from the outside by sharp notches. Several microcracks surround the two macroscopic cracks (G). Striations are also detected in this region perpendicular to the crack growth direction. The fracture surface at 600 K is smooth; similar to the fracture face of the test sample LCF-tested at 800 K. Following the results at 800 K, the crack grow evolved from the upper side of the test sample to the dotted line (see lower-center side of Fig. 4.14). The area below the dotted line is the residual fracture face that indicates a clear tension-pressure-loading under high nominal stress (similar to the LCF test at 600 K) [136]. A few fatigue striations could be observed as well on the left-hand side of the test sample (F) and almost invisible in the crack growth area. In contrary to the fracture surfaces of the LCF test samples tested at 600 and 800 K, the fracture surface of the 1000-K-LCF-test-sample is very rough and irregular. It is also composed of many fatigue striations in the center (F). The lamella-shape of these striations is observed only at high temperatures. It is noticeable that line-shaped concentrations of chromium are detected by EDX mapping within these lamellae. A few beach marks are also observed at the outside of the test sample from where the crack could have been initiated (E). The rupture cycle number of the displacement-controlled LCF tests are 121 cycles at 600 K ($\Delta\varepsilon_{1^{\text{st}},600\text{K}} \approx 4$ %), 100 cycles at 800 K ($\Delta\varepsilon_{1^{\text{st}},800\text{K}} \approx 3$ %), and 161 cycles at 1000 K ($\Delta\varepsilon_{1^{\text{st}},1000\text{K}} \approx 3.5$ %)

The influence of thermal ageing onto test samples that have been carried out in a furnace before testing at different periods of time is depicted in Fig. 4.15. The upper-side of Fig. 4.15 shows the necked fracture surface of tensile loaded test samples. Depending on the ageing time of $t_\theta = 0, 10$ to 20 h at $\theta_{\text{ILK}} = 1000$ K, the half-maximum and half-minimum length of the ductile fracture surface (assumed to be appropriate to a semi major and semi minor axis of an ellipse) decreases from $1.344, 0.601$ to 0.484 mm and from $1.344, 0.387$ to 0.259 mm, respectively. Taking into account the ruptured ellipse area A_R and the initial circle area A_0 with initial diameter $d_0 = 5.64$ mm, the obtained necking factors $Z = (A_0 - A_R)A_0^{-1}$ are $0.81, 0.97$ and 0.98 for the $0, 10$ and 20 h aged tests samples tests at 1000 K (see Fig. 4.15). Assuming a fully incompressible deformation ($\nu = 0.5$) during tensile loading, the rupture strain $\varepsilon_{\text{true,R}} = 1 - \sqrt{1 - Z}$ is determined to $56.6, 82.9$ and 87.5 %, respectively. It can be concluded that the ductility of CuCrZr increases significantly with respect to ageing time.

On the lower-side of Fig. 4.15, the fracture surfaces of aged test samples after cyclic loading until rupture at $\theta_{\text{ILK}} = 1000$ K are shown. At elevated temperatures, it is very difficult to identify the failure mode clearly due to strong oxidation of the regarded fracture surfaces (108 cycles corresponds to 3 h testing time). Magnification of the 0-h-aged-test-sample focuses on the typical fatigue striations with a cavity width of approximately 2 µm in the center of the test sample. As already discussed, this lamella-type striation structure develops widely only at elevated temperatures. Although the fatigue failure mode cannot be identified clearly, the crack is probably initiated at the lower-left edge of the test sample (see Fig. 4.14). The 10-h-aged test sample is depicted in the lower-center of Fig. 4.15, a ductile fracture surface (dimple structure)

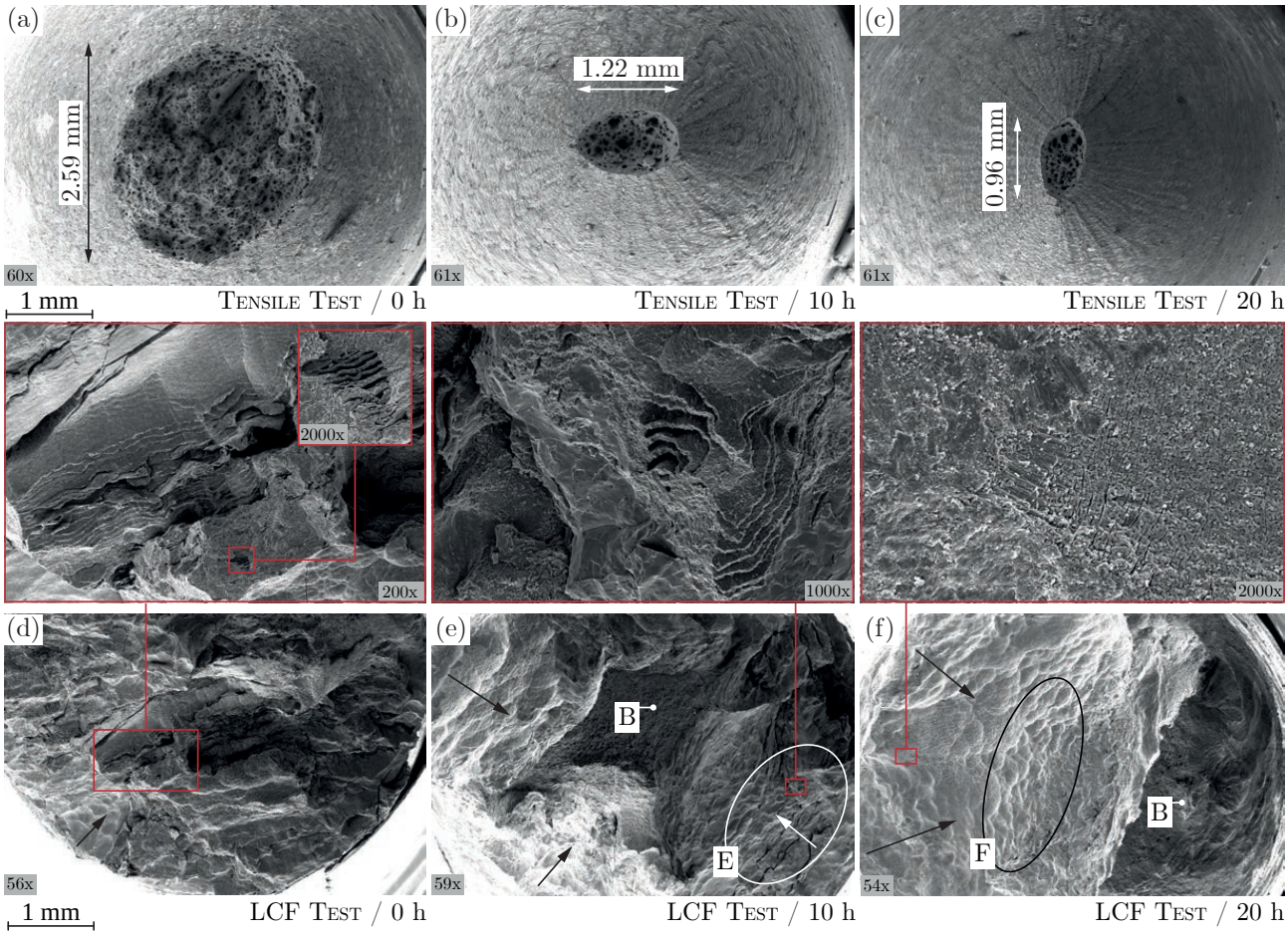

Figure 4.15: SEM images of a test sample's fracture surface after tensile loading (upper-side) and fatigue loading (lower-side) at 1000 K and taking into account thermal ageing of the test samples.

is identified in the center of the test sample being a result of the final forced rupture (B). Around the center, concentric beach marks and striations are observed. In contrary to a typical tension-pressure-loading failure, a multiaxial fatigue bending failure of the test sample with high stress concentrations related to the notch effect is observed [136, 137]. The cracks developed cyclically from several points at the outside to the center. These areas are characterized by a lamella-type striation structure that refers to fatigue failure. Indeed, LCF tests at high strain ranges with test samples made of CuCrZr lead often to an unsymmetrical stress-strain-hysteresis during long-term cyclic loading with a loading ratio of $R_\varepsilon = -1$; especially, in the compressive domain. A reason could be that an evolving macro crack at the outside of the test sample affects the test sample's bending stability; therefore, buckling occurs at a certain crack length under compression. The fracture surface of the 20-h-aged test sample is shown on the lower-right side of Fig. 4.15. The fatigue fracture surface is smooth with wave-shaped beach marks indicating the crack growth direction (F). The rough surface is composed of a dimple structure that indicates the final forced rupture (B). Because of that, a bending failure without notching effect at relatively low nominal stress can be concluded [136, 137]. Due to strong oxidation after the tests, fatigue striations could not be detected clearly. Only cracks in the oxidation layer are observed (see magnified detail on the lower-right-hand side of Fig. 4.15). Finally, the number of rupture cycles of the displacement-controlled LCF tests at 1000 K

are $\hat{n}_{\mathrm{Cyc,0h}} = 121$ cycles with 0-h-aged-tests samples ($\Delta\varepsilon_{10^{\mathrm{th}}} \approx 4$ % at $R_\varepsilon \approx +1$), $\hat{n}_{\mathrm{Cyc,10h}} = 271$ cycles at with 10-h-aged-tests samples ($\Delta\varepsilon_{10^{\mathrm{th}}} \approx 4.9$ % at $R_\varepsilon \approx -1$), and $\hat{n}_{\mathrm{Cyc,20h}} = 251$ cycles at 1000 K ($\Delta\varepsilon_{10^{\mathrm{th}}} \approx 5.47$ % at $R_\varepsilon \approx -1$).

5 Fatigue Life Analyses of the TMF Panel Experiment

5.1 Mesh

A three-dimensional mesh is used for both the thermal-fluid analysis in Ansys CFX and the structural analysis in Ansys Mechanical. To generate a structured mesh of the TMF panel with its cooling channels, the entire geometry is imported in Ansys DesignModeler as a STEP file that has been exported from CAD software. Due to symmetry reasons in flow direction, the imported geometry contains only one half of the entire structural domain (Ω_{CuCrZr}). This symmetry condition reduces the mesh size by the factor of two. Drill holes, radii, cooling channel sealings and connection tubes are omitted in the imported geometry. The half part of the homogeneous structural part is then partitioned into multiple parts basing on the cooling channel geometry, the external TMF panel geometry, and the length of the laser loaded area to be prepared for a structured mesh with hexahedrons in Ansys. To create the fluid domains, solid bodies are extruded along the cooling channel length. Note that only three and one half cooling channel domains are modeled due to symmetry reasons. The half cooling channel in the center of the TMF panel represents the reference cooling channel of a common rocket combustion chamber's cooling channel. To finish the preparation process, the partitioned solid bodies (2G: 78x and 3G: 318x) are associated to one single solid part and the fluid domains (2G: 12x and 3G: 54x) are associated to their fluid parts (i.e. each cooling channel domain). This leads to one sliced solid part and four sliced fluid parts that are prepared in Ansys DesignModeler for generation of the mesh. In the following sections, the mesh of the fluid domains (basing on the finite volumes method) and the mesh of structural domain (basing on the finite element method) are described in detail.

5.1.1 Finite Volume Fluid Mesh

Regarding to Ansys CFX [82], an element-based finite volume method (FVM) is used to discretize the fluid domains of the cooling channels. The mass, momentum and energy equations are solved and conserved in these finite volumes. The applied three-dimensional mesh consists of hexahedral elements with 8 nodes and 8 tri-linear shape functions. According to Weintritt [138,139], a structured mesh is employed in the center of the fluid domain with a mesh resolution of 64 elements in width direction (1.3 mm) and 448 elements in height direction (9 mm). As depicted in Fig. 5.1, the structured mesh is related to the x-y-cross-section of the TMF panel's cooling channel (A). The applied mesh resolution is determined on the basis of a mesh convergence study. The maximum temperature in the fluid flow and the maximum temperature on the laser loaded surface of the TMF panel structure are investigated depending

Table 5.1: Composition of the fluid mesh.

	Elements	Nodes
2G Model	$29.7 \cdot 10^6$	$30.3 \cdot 10^6$
3G Model	$22.6 \cdot 10^6$	$23.1 \cdot 10^6$

on the number of elements in width direction of the cooling channel. To obtain comparable results, 16 inflation layers with a first prism layer factor of 0.8 (1.37 µm) are used for all meshes in this study. Figure 5.1a depicts the results of the element number variation study. One can see that a remarkable deviation of the fluid and structural temperature is apparent until a mesh density of 32 elements per cooling channel width (1.3 mm), i.e. $\Delta\theta_{\text{Structure}} = 20.83$ K and $\Delta\theta_{\text{Fluid}} = 24.8$ K. To increase the accuracy of the heat transfer within the viscous sublayer of the turbulent flow profile, 19 inflation layers are applied with a first prism layer factor of 0.4. By using a growth rate of 1.2, the first prism layer height is then 0.6 µm with a total prism layer thickness of 108 µm (B). Investigation of the boundary layer's influence onto the fluid temperature is also performed by Weintritt [138,139]. Figure 5.1b depicts the variation of the first prism layer factor depending on the fluid temperature at a constant dimensional distance of $y^+ = 1$ (see Eq. 3.14). Weintritt showed that the lower the thickness of the rectangular cooling channel's first prism layer, the better the convergence behavior of the fluid temperature until it converges at 712 K for the present simulation.

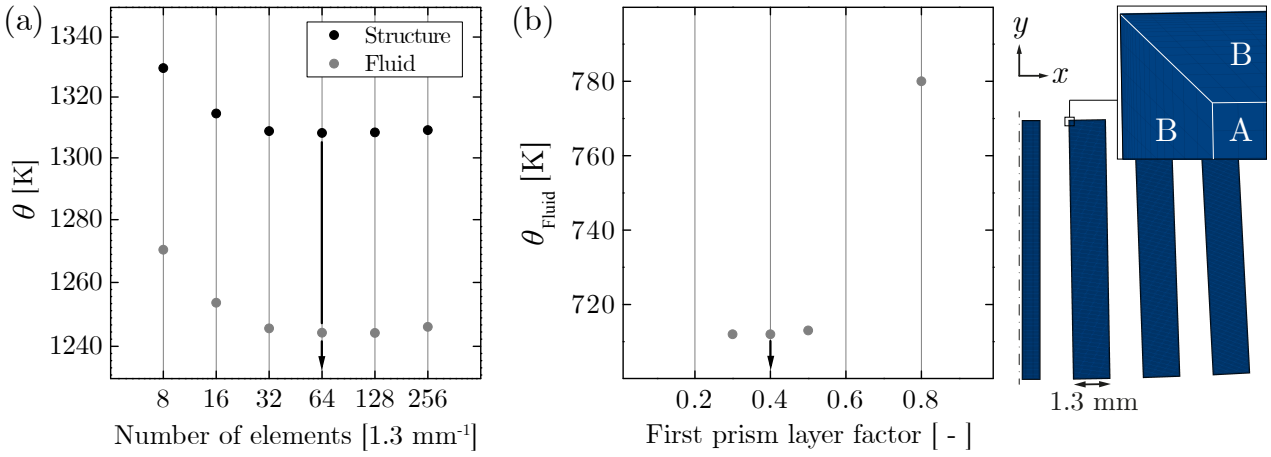

Figure 5.1: Convergence study of the fluid mesh with variation of the number of elements per cooling channel width (a) and variation of the first prism layer factor (b).

In flow direction (z-direction), hexahedral elements are elongated with a mesh resolution of 0.5 elements per mm at the inlet and the outlet of the TMF panel model. In the laser loaded region, the mesh is refined by a factor of 4; so that a mesh resolution of 2 elements per mm is applied there. Finally, the total number of elements of the 2G's and 3G's fluid domains is depicted in Tab. 5.1.

5.1.2 Finite Element Structural Mesh

Regarding to Ansys Mechanical [140], a displacement-based finite element method (FEM) is used to discretize the structural domains of the TMF panel geometry. Three-dimensional continuum solid elements with either linear shape functions (8 node hexahedral SOLID185) or

quadratic shape functions (20 node hexahedral SOLID186) are applied. To account for both large plastic deformation within the laser loaded area and bending outwards of the TMF panel's laser loaded wall, uniform reduced integration is used for linear elements as well as for quadratic elements. This option overcomes volumetric locking effects and shear locking effects. In case of volumetric locking, the structural stress response becomes too stiff in nearly incompressible cases (plasticity) [141, 142]. In case of shear locking (so-called hourglassing), the bending phenomena is underrepresented by parasitic shear stresses that lead to an overstiff stress response. Especially by using linear elements with reduced integration, stresses and strains are computed at only one integration (Gauss) point and zero shear strain energy modes can occur [141, 143]. Note that the hourglass scaling factor is set to the default value of HGSF = 1 in the TMF panel analyses; therefore, any additional artificial energy term is thereby omitted (see Flanagan and Belytschko [144] and Ansys APDL Theory Manual [140]). However, the results computed with under-integrated linear elements have to be checked carefully with respect to shear locking.

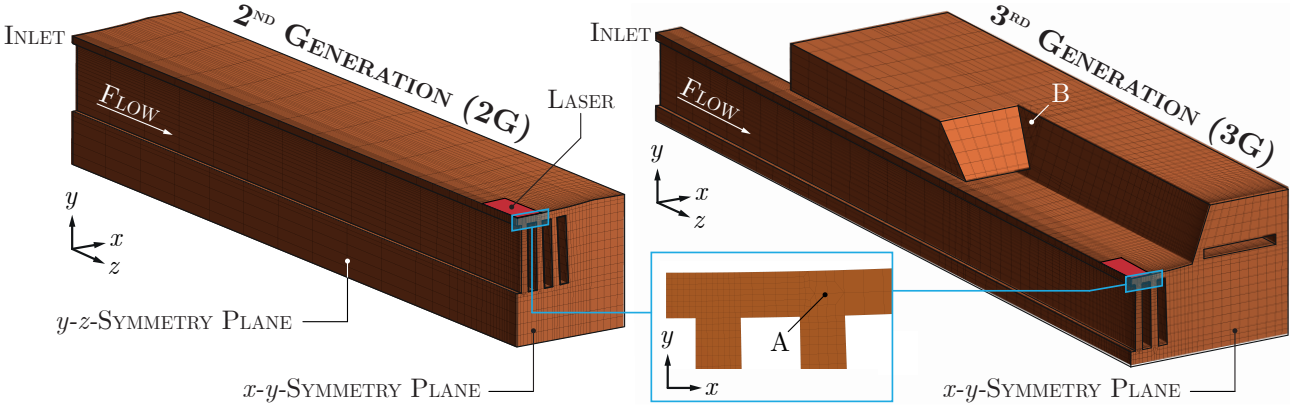

Figure 5.2: Quarter mesh of the 2nd and 3rd generation TMF panel model.

Figure 5.2 depicts each half of the 2G and 3G TMF panel's structural model. One can see that a mesh density of 8 elements per mm is applied in the cross-section of the laser loaded TMF panel wall. To reduce computational time, the number of elements decreases with increasing distance to the laser area. In other words, a coarse mesh is applied at the outer regions where the temperature gradient is lower than the gradient in laser loaded area. As depicted in Fig. 5.2, transition from fine to coarse mesh is conducted in defined volume parts to maintain a structured mesh composed of hexahedral elements (A). One reason is that the application of tetrahedral elements (instead of hexahedral elements) would increase the overall mesh size and decrease of accuracy of this bending problem with first-order elements. To decrease the mesh size any further, the element size is controlled by using bias type at the edges. This option adjusts the spacing ratio of nodes on edges and it is applied along the cooling channel's height edges ($-y$-direction) as well as along the TMF panel's length edges ($\pm$ z-direction) in the laser loaded area. Note that tetrahedral elements are only applied in the corner of the pit to ensure accurate mesh generation (B). Due to the distance from the coarse mesh to the laser field and the cooling channels, the influence on the laser loaded area is assumed to be neglected. Table 5.2 depicts the total number of elements for the regarded solid domains.

Another important fact is that the applied structural mesh should be able to reproduce the envisaged thinning and bending phenomena (similar to the doghouse deformation in common rocket chambers) of the TMF panel's reference cooling channel wall ligament. Therefore, the applied mesh density bases on results computed with a simple beam model (see Fig. 5.3). This

Table 5.2: Composition of the structural mesh.

	Elements	Nodes
2G Model	$56.1 \cdot 10^3$	$65.0 \cdot 10^3$ (lin.)
		$251.0 \cdot 10^3$ (quad.)
3G Model	$103.3 \cdot 10^3$	$117.9 \cdot 10^3$ (lin.)
		$457.1 \cdot 10^3$ (quad.)

simplified beam model represents the wall between cooling channel and laser loaded surface (1 x 1.3 mm). Note that the length of the three-dimensional beam model is 1 mm in z-direction. In this convergence study, the number of elements varies in x- and y-direction. A factor of 1.3 is used in combination with integer format of the number of elements along the cooling channel width. For example, 64 elements per 1 mm leads to 83 elements per 1.3 mm. A constant pressure of 55 bar is applied as a surface load onto the bottom surface (1 x 1 mm). The applied pressure corresponds to the outlet pressure that is measured during laser heating. From the mechanical point of view, the beam model is over-determined because of the two ending's displacement is fixed in space ($u_{x,y,z} = 0$). Figure 5.3 shows the displacement u_y (a) and the strain ε_y (b) at two center nodes of the beam model (P_1 and P_2). It can be concluded that a mesh density of 8 elements per 1 mm is sufficient to reproduce the bending displacement in the center of the simple beam model (within ± 1 %). However, convergence of the strain could not be clearly obtained with first-order elements (SOLID185) until a mesh density of 128 elements per 1 mm. This is also important with respect to the damage computation that bases mainly on the accumulated plastic strain value (see Eq. 3.54). Thiede [28] showed that the used damage model is mesh dependent up to 32 elements per 1 mm. This could be also explained by the convergence behavior of the strain depicted in Fig. 5.3b. Because of limitation of computational resources, a mesh density of only 8 elements per 1 mm is carried out for the finite element mesh in the laser loaded area of the TMF panel (see Fig. 5.2). The deviation of the strain is in this simple beam model +23.09 % (P_1) and +4.53 % (P_2) for linear elements (SOLID185) and −13.85 % (P_1) and −2.66 % (P_2) for quadratic elements (SOLID186).

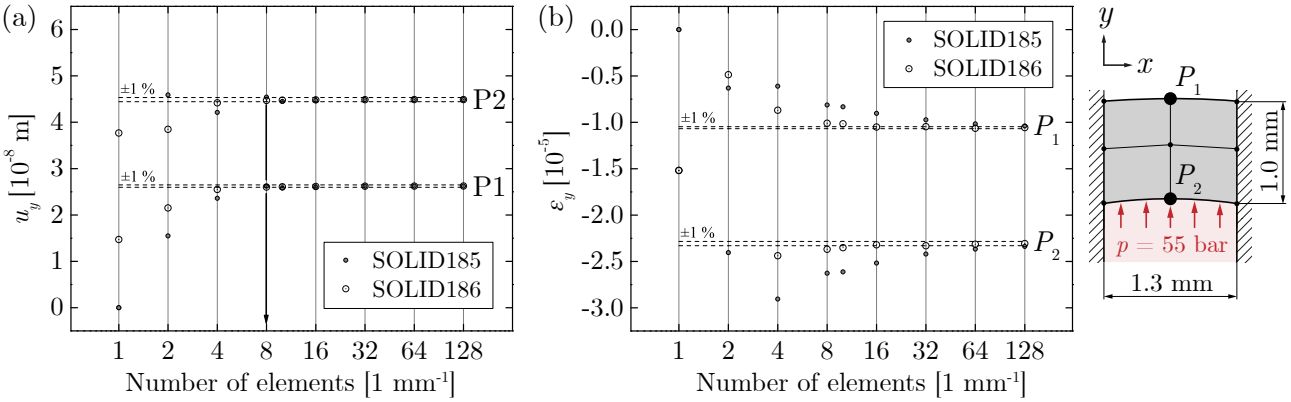

Figure 5.3: Convergence study of bending displacement (a) and strain (b) at two points of a simple beam problem depending on the number of elements.

The applied mesh density accords with the work of Schwarz [21]. The author applied approximately 8 elements per 1 mm on a three-dimensional full model of a nozzle extension-type TMF panel. By regarding models that consists of only a half cooling channel geometry

from a common rocket combustion chamber, 20 elements per 1.3 mm and 16 elements per 1.3 mm as well as approximately 12 elements per 1 mm are applied by Kuhl [15], Tini [22,26] and Schwarz [21], respectively. Note that these kinds of models allow much larger mesh densities that would lead to more accurate reproduction of the cooling channel's bending phenomena.

5.2 Boundary Conditions

Different boundary conditions are applied in the stationary thermal-fluid analysis as well as in the follow-on quasi-static structural analysis to take into account experimental test conditions as realistic as possible. The employed boundary conditions are described in the following sections.

5.2.1 Thermal-Fluid Model

A stationary thermal-fluid analysis is performed in Ansys CFX to compute the temperature distribution within the TMF panel and the pressure distribution along the rectangular cooling channel walls. In this model, the temperature distribution is mainly affected by the heat flux generated by a laser, the heat transfer from the TMF panel structure to the cooling channels, and the radiation from the TMF panel surfaces to ambience (testing area).

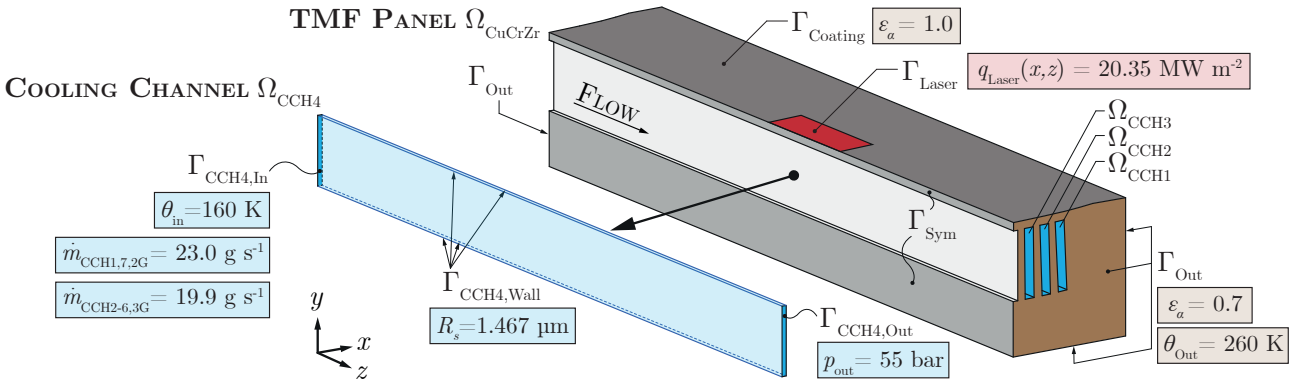

Figure 5.4: Schematics of the boundary conditions used for the thermal-fluid analysis in Ansys CFX.

To model the laser loading in this thermal-fluid analysis, the two-dimensional laser beam intensity distribution is applied on the coated TMF panel surface (Γ_{Laser}) without any reflections; therefore, the emissivity coefficient is $\varepsilon_\alpha = 1.0$ (see Fig. 5.4). The two-dimensional laser beam intensity distribution bases on measurements conducted with a beam profiler that is tipped up to 5° from its vertical position. To apply this heat flux data onto the surface of the TMF panel model in Ansys CFX, the measurement data is exported as table data with a resolution of 128 x 256 px. A user program is employed to normalize each heat flux value with respect to the maximum value, to scale the coordinate axes from pixel unit into length unit, and to transform the coordinate system according the coordinate system in the TMF panel analysis by translation of the origin and rotation around the axes. Then, the normalized laser beam intensity distribution ($0 \leq \bar{q} \leq 1$) is exported and imported as a CCL function in Ansys CFX. By multiplying the maximum heat flux value with the normalized laser beam distribution, the

resulting heat flux distribution is obtained

$$q_{\text{Laser}}(x,z) = \hat{q}\,\bar{q}(x,z) \tag{5.1}$$

where the maximum heat flux value $\hat{q} = 20.35 \cdot 10^6$ W m^{-2} is fitted with respect to a maximum temperature of $\hat{\theta} = 1000$ K on the 2G TMF panel surface. Note that this measured heat flux distribution is carried out for both the 2G and the 3G TMF panel analysis.

Temperature dependent density, thermal conductivity, and specific heat capacity are used as thermophysical material parameter data for CuCrZr to compute the thermal field of the solid domain (Ω_{CCH}) depending on the fluid flow in the cooling channel domains ($\Omega_{\text{CCH},i}$). As shown on the left-hand side of Fig. 5.4, an inlet temperature of $\theta_{\text{in}} = 160$ K and a mass flow of $\dot{m}_{\text{CCH,2G}} = 23.0$ g s^{-1} are defined at the inlet surface of each cooling channel domain ($\Gamma_{\text{CCH,In}}$) as well as an outlet pressure of $p_{\text{out}} = 55 \cdot 10^5$ Pa (55 bar) at the outlet surface of each cooling channel domain ($\Gamma_{\text{CCH,Out}}$) to compute the coolant flow. The mass flow rate of the 3G's cooling channels (except 1$^{\text{st}}$ and 7$^{\text{th}}$ cooling channel) is decreased by $\Delta\dot{m}_{\text{CCH}} = 3.1$ g s^{-1} to $\dot{m}_{\text{CCH,3G}} = 19.9$ g s^{-1}. Adjusting of the 3G TMF panel's cooling channel mass flow is needed to obtain a maximum surface temperature of $\hat{\theta} = 1000$ K on the 3G TMF panel surface with regard to a similar applied heat flux distribution that is also used for the 2G TMF panel analysis. Note that the coolant's flow velocity is kept constant in all cooling channels; so that the mass flow of the two outer cooling channels (1$^{\text{st}}$ and 7$^{\text{th}}$) of the 3G TMF panel is increased by a factor of $1.\bar{2}$ depending on the ratio of their areas 1.3 x 9 mm and 1.3 x 11 mm. A high intensity turbulence of 10 % is applied at the inlet surface to take into account any inflow deflection from the test bench's feeding lines (e.g. rectangular angle). With regard to compressible flow conditions, the real gas properties of single-phase supercritical nitrogen are considered by temperature dependent and pressure dependent fluid table data (such as density and specific heat capacity) that is generated with NIST REFPROP V9.1. To compute the coolant's turbulent velocity profile along the rectangular cooling channels, the shear stress turbulence (SST) model with a turbulent PRANDTL number of $\text{Pr}_t = 0.9$ is employed (default). Variation of the turbulent PRANDTL number needs to be verified very accurately. The lower Pr_t, the better the heat transfer into the fluid domains and, consequently, the higher the applied heat flux on the TMF panel surface. The cooling channel walls ($\Gamma_{\text{CCH,Wall},i}$) are treated as rough walls taking into account a sand-grain roughness of $R_s = 1.467$ µm (see Eq. 3.11). The coolant's turbulent velocity profile in flow direction and the cooling channel's surface roughness are also used to compute the heat transfer from the solid structure to the compressible fluid flow that is characterized by a wall heat transfer coefficient. By using the conservative heat flux option (see Eq. 3.12), the heat transfer coefficient is computed at the interfaces along the cooling channel walls with respect to the laser heat flux. Therefore, the heat transfer coefficient at the cooling channel walls varies significantly in flow direction. Symmetry boundary condition in y-z-direction is applied at the reference cooling channel's center because only half of the center cooling channel is modeled.

In addition, the temperature distribution within the TMF panel solid domain (Ω_{CuCrZr}) is also affected by thermal radiation from the solid surfaces to the testing area. As depicted on the right-hand side of Fig. 5.4, the testing area's ambient temperature is set to $\theta_{\text{Out}} = 260$ K with an assumed emissivity coefficient of $\varepsilon_\alpha = 0.7$ for non-polished copper surfaces (Γ_{Out}). Thermal radiation of the coated surface (Γ_{Coating}) is neglected; so that the heat flux generated by the laser is fully induced into the TMF panel structure without any radiation (see Equ. 3.19). Note that the heat flow from the TMF panel to the surrounding holding system and connector tubes is also neglected in this thermal-fluid analysis.

5.2.2 Structural Model

In the quasi-static structural analyses, the boundary conditions are divided into displacement, pressure, and thermal conditions. First, symmetry displacement conditions are applied onto the y-z-symmetry plane (Γ_{Sym}) of the half TMF panel model ($u_x = 0$). As shown in Fig. 5.5, the displacements of a single node (A) are constrained in all directions ($u_{x,y,z} = 0$) and the displacement of another single node (B) is constrained only in height direction ($u_y = 0$). These boundary conditions are needed to obtain statically determinate support. But according to the TMF panel mounting system that is depicted in Fig. 2.11, all nodes belonging to the inlet surface are displacement-fixed in longitudinal direction ($u_z = 0$) of the TMF panel. Free movement of the 2G and the 3G TMF panel's outlet surfaces in longitudinal direction ($u_z \neq 0$) is allowed to account for thermal contraction and thermal expansion during steady-state cooling and cyclic laser heating, respectively. However, the rotational degrees of freedom (DOF's) of the coupled nodes on the 2G's outlet surface are constrained in all directions ($\varphi_{x,y,z} = 0$) by using deformable remote displacement. This boundary condition comes from the mounting system where the inlet and outlet tubes are arranged circular around the inlet and the outlet surface. This configuration suppresses their in-plane rotation. The rotational DOF's of the coupled nodes on the 3G's outlet surface are constrained only in height and longitudinal direction ($\varphi_{y,z} = 0$). The lateral rotational DOF is free ($\varphi_x \neq 0$) due to the fact that ball bearings have been used at the back of the holding system to allow possible bending of the TMF panel (see Sec. 2.2.6). However, application of these boundary conditions leads to statically overdetermined TMF panel models, but they are set as close as possible to the experimental test. Note that all displacement-based boundary conditions depicted in Fig. 5.5 are applied in the analyses directly from the beginning at all load steps.

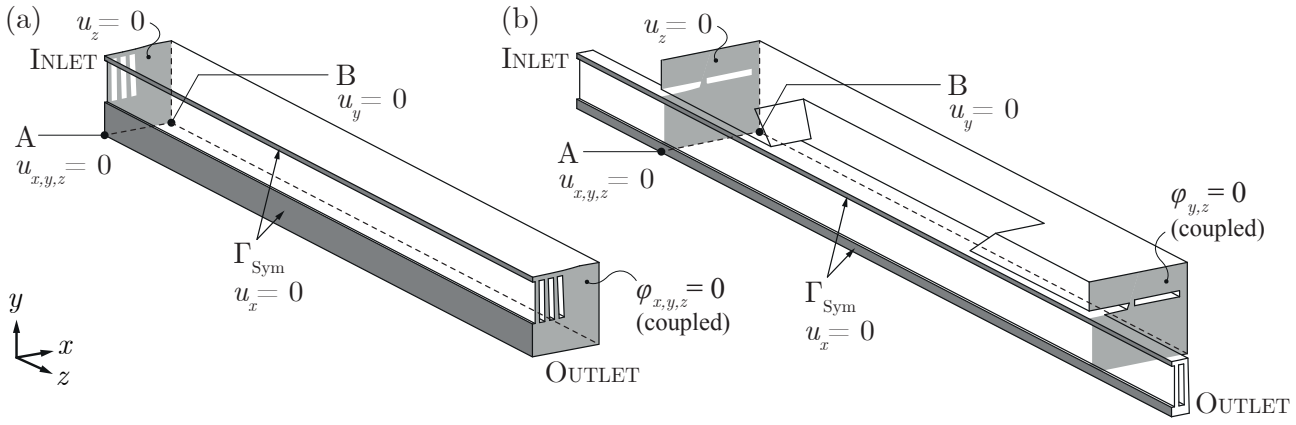

Figure 5.5: Schematics of the displacement-based boundary conditions used for the structural analysis of the 2nd (a) and 3rd (b) generation TMF panel in ANSYS MECHANICAL.

A constant pressure loading of $p = 55 \cdot 10^5$ Pa (55 bar) is applied perpendicular to each cooling channel wall. The pressure corresponds to the steady state outlet pressure (p_{out}) that has been measured experimentally during laser heating; although, the pressure is adjusted to $50 \cdot 10^5$ Pa (50 bar) during cooling before each laser heating phase. The pressure drop along the cooling channels due to surface roughness is relatively small and, therefore, omitted in the analyses. Similar to the displacement-based boundary conditions, the constant pressure loading is applied as a surface load normal to the cooling channel walls from the beginning of all load steps.

Finally, the temperature distribution from the steady-state thermal-fluid analysis is imported into the quasi-static structural analysis and applied as a nodal body force on each node separately. In case of mismatching meshes between thermal and structural analysis, the temperature is linearly interpolated between the nodes. In FE analyses, nodal temperature loading is similar to nodal displacement loading that depends on the thermal expansion coefficient [92]. Therefore, temperature dependent thermal expansion coefficients are used in combination with the material model's parameters to compute the stress response of the solid domain (Ω_{CuCrZr}) affected by thermal and mechanical strains. To initialize the fatigue analyses of the TMF panel, a constant outlet pressure (p_{out}) is applied as a surface load onto the cooling channel walls at an ambient temperature of 300 K ($t_{\mathrm{Ini,Pressurize}} = 1$ s) with all displacement-based boundary conditions activated (see Fig. 5.6). Then, a uniform temperature distribution of 160 K is applied as nodal body force ($t_{\mathrm{Ini,Precooling}} = 1$ s). This temperature represents the fluid inlet temperature during the experimental TMF test. After the initialization process, the temperature field representing laser loading is applied cyclically by the means of APDL commands (see Attmt. A.3). To assess the period of time that the instantaneously switch-on laser needs to heat up the entire TMF panel structure with respect to the structure's specific heat capacity, a transient thermal analysis is employed. Basing on the results computed with a transient thermal analysis incorporating a fitted constant heat transfer coefficient along the cooling channel walls, entire heating of the 2G and 3G TMF panel model lasts approximately $t_{\mathrm{On}} = 2$ s and 10 s, respectively. As depicted in Fig. 5.6, these heating periods are carried out to the quasi-static structural analyses where the nodal temperature distribution from the steady-state thermal-fluid analysis is linearly applied (t_{On}). After a steady laser-on holding period of $t_{\mathrm{Hold}} = 200$ s, the temperature distribution is decreased linearly from a maximum solid temperature of $\hat{\theta} = 1000$ K to a uniform temperature of $\theta_{\mathrm{in}} = 160$ K within $t_{\mathrm{Off}} = 10$ s. This accords with linear decreasing of the laser's voltage at the end of each cycle. To finish the cycle in the analyses, steady state cooling with a uniform temperature distribution of 160 K is applied until $t_{\mathrm{Cyc}} = 250$ s is reached.

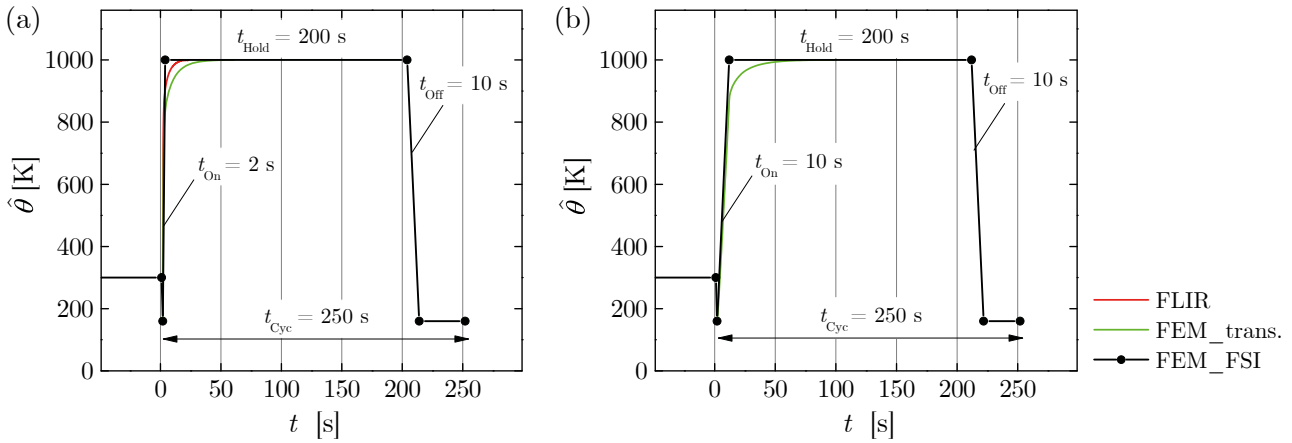

Figure 5.6: Temperature loading history for one cycle up to $\hat{\theta} = 1000$ K including initialization of the 2G's (a) and 3G's (b) TMF panel analysis.

Regarding the temperature loading history depicted in Fig. 5.6, one can see that the linear applied temperature of the FSI analysis is overestimated with respect to experimentally acquired temperature slope during laser heating (t_{On}). In contrary, the temperature slope obtained from a transient FE analysis with simplified laser heat flux and fitted heat transfer coefficients along the cooling channel walls is obviously underrepresented. Therefore, it is assumed that simplified

linear temperature loading is appropriate with respect to the high thermal conductivity of the employed copper-base alloy. Note that the transient temperature slope during shut down of the laser ($t_{\mathrm{Off}} = 10$ s) is similar to an assumed linear decrease.

5.3 Analysis Options

Regarding the solution options for thermal-fluid analysis in Ansys CFX, high resolution advection scheme and high resolution turbulence numerics are applied. Because of the analysis' steady state type, the fluid timescale control is set to $\Delta t_{\mathrm{Fluid}} = 0.0117$ s and the solid timescale factor is set to 1 (default). A root mean square (RMS) residual is computed for each cooling channel fluid domain and it is obtained by taking all of the residuals throughout the domains, squaring them, taking the mean, and then taking the square root of the mean. To obtain a reasonably converged solution within the fluid domains, a residual of $\mathrm{RMS}_{\mathrm{Ansys}} = 5 \cdot 10^{-5}$ is recommended by Ansys [82]. In the thermal-fluid analyses, a residual of $\mathrm{RMS} = 1 \cdot 10^{-5}$ is carried out; that is five times lower than the recommendation. Besides the RMS residuals, convergence of the maximum temperature in the solid domain (Ω_{CuCrZr}) as well as the maximum temperature and the mass flow averaged outlet pressure in the center cooling channel domain (Ω_{CCH4}) are assessed. In addition, the accuracy of the numerical results is increased by using double-precision executables. Note that for solving the 3G model, a topology estimate factor zif = 1.2 (default: 1.0) is applied to increase the initial memory usage by 20 % [82].

Regarding the solution options for the quasi-static structural analysis in Ansys Mechanical, direct (SPARSE) solver with shared memory parallelization (SMP) is employed. It accounts for performance with respect to robust computation. Distributed memory parallelization (DMP) is usually preferred to obtain faster solution time; but the assembling of large residual files after calculation is highly time-consuming on large volume hard disks as well as necessary restart procedures. By activating solution control (SOLCONTROL,ON) in the solution processor, a set of commands applicable to nonlinear options is activated. Examples are large deformation (NLGEOM,ON), full Newton-Raphson iteration scheme (NROPT,FULL), line search (LNSRCH,ON), and ramped loading (KBC,0). The convergence check uses L2-norm of force with a tolerance of $\Delta F = 5$ % and an infinite norm check of displacement with a tolerance of $\Delta u = 0.5$ % [140]. Note that any nonlinear stabilization techniques are deactivated in both analyses. As depicted in Fig. 5.6, the main laser cycle of a TMF panel test contains four load steps. Therefore, the applied initial and minimal substep numbers for each load step have a strong influence on the result due to accumulation of numerical uncertainties per cycle. In Thiede [116], minimal substep numbers are evaluated to obtain a converged tangential stress solution with an uncertainty lower than 1 % on the laser loaded side of the TMF panel's center cooling channel. In fact, 16, 16, and 32 minimal substeps are recommended for the heating-up period ($t_{\mathrm{On}} = \{2\ \mathrm{s}, 10\ \mathrm{s}\}$, ramped slope), the steady state hot run ($t_{\mathrm{Hold}} = 200$ s) and the laser shut down period ($t_{\mathrm{Off}} = 10$ s, ramped slope), respectively. In our structural analyses, 32, 16, and 32 minimal substeps are applied. Note that the initial substep number of the steady state hot run period is set to 512 to account for large time-dependent stress relaxation at the beginning of the holding period. The initial and minimal substep number for pressure application ($t_{\mathrm{Ini,Pressure}} = 1$ s), pre-cooling ($t_{\mathrm{Ini,Pre\text{-}Cooling}} = 1$ s), and post-cooling ($t_{\mathrm{Post\text{-}Cooling}} = \{38\ \mathrm{s}, 30\ \mathrm{s}\}$) are set to 4.

5.4 Numerical Results

In this section, a selection of results that has been computed by the stationary thermal-fluid analysis and the follow-on quasi-static structural analysis of the second generation (2G) and the third generation (3G) TMF panel are presented. As mentioned previously, the thermal-fluid analysis is used to compute the temperature distribution within the solid domain depending on the laser loading, the pressurized coolant flow in the cooling channels, and the thermophysical properties of the applied copper-base alloy CuCrZr. The resulted temperature distribution is then applied cyclically as a body force in the structural analysis together with constant pressure at the cooling channel walls under realistic mounting conditions. Taking into account the presented material model and its corresponding temperature dependent material parameters, the fatigue life of the 2G and 3G TMF panel model is examined.

5.4.1 Thermal-Fluid Analysis

Figure 5.7 shows the numerically applied heat flux distribution that is assumed to be generated by laser radiation during the experiment. The two dimensional heat flux distribution ($\bar{q}(x, y)$) bases on exported and normalized laser intensity distribution data from measurements that has been performed with a PRIMES BM 100 beam profiler at a tilt angle of $\delta = 5°$ before the TMF test. The tilt angle of the beam profiler corresponds to the mounting angle of the TMF panel during the experiment. The normalized intensity distribution is then multiplied with a maximum heat flux of $\hat{q} = 20.35 \cdot 10^6$ W m^{-2} to be applied without radiation effects ($\varepsilon_\alpha = 1.0$) onto the laser loaded surface of the 2G and 3G TMF panel models. Another possibility would be to model the laser loading as pure radiation that induces the heat into the TMF panel wall by using the STEFAN-BOLTZMANN law [145]. However, this approach of radiative heat exchange is not considered in this work and convection due to application of an experimental measured heat flux distribution is preferred instead.

To characterize the flow in the center cooling channel, the differential pressure (Δp_{CCH4}), the dimensionless wall distance parameter (y^+_{CCH4}), and the heat transfer coefficient ($h_{c,\mathrm{CCH4}}$) are depicted in Figs. 5.7a-c. Basing on an outlet pressure of $p_{\mathrm{out}} = 55$ bar during laser loading, the mass flow averaged differential pressure along the 2G and 3G TMF panel model's center cooling channel is $\Delta p_{\mathrm{2G,CCH4}} = 319.23$ mbar and $\Delta p_{\mathrm{3G,CCH4}} = 263.86$ mbar, respectively (see Fig. 5.7a). One can see that the differential pressure in the 3G's center cooling channel is approximately 17.34 % lower; although, the 3G's center cooling channel length is 30 mm longer with similar surface roughness and channel geometry. The reason for this could be that the mass flow rate is fitted in each analysis separately to obtain a maximum temperature of $\hat{\theta} = 1000$ K on the TMF panel's surface under similar heating and cooling conditions. As a result, the mass flow in the 3G's center cooling channel ($\dot{m}_{\mathrm{3G,CCH4}} = 19.9$ g s^{-1}) is 13.48 % lower compared to the mass flow in the center cooling channel of the 2G TMF panel model ($\dot{m}_{\mathrm{2G,CCH4}} = 23.0$ g s^{-1}). According to the VENTURI effect that bases on BERNOULLI's principle, the pressure drop for a steady state incompressible flow through a duct is given by [146]

$$\Delta p = \frac{\rho}{2} \Delta(v)^2 \tag{5.2}$$

The mass flow difference leads to a variation of the temperature distribution that affects the coolant's density within the cooling channels; so that the lower differential pressure within the 3G's center cooling channel seems to be reasonable.

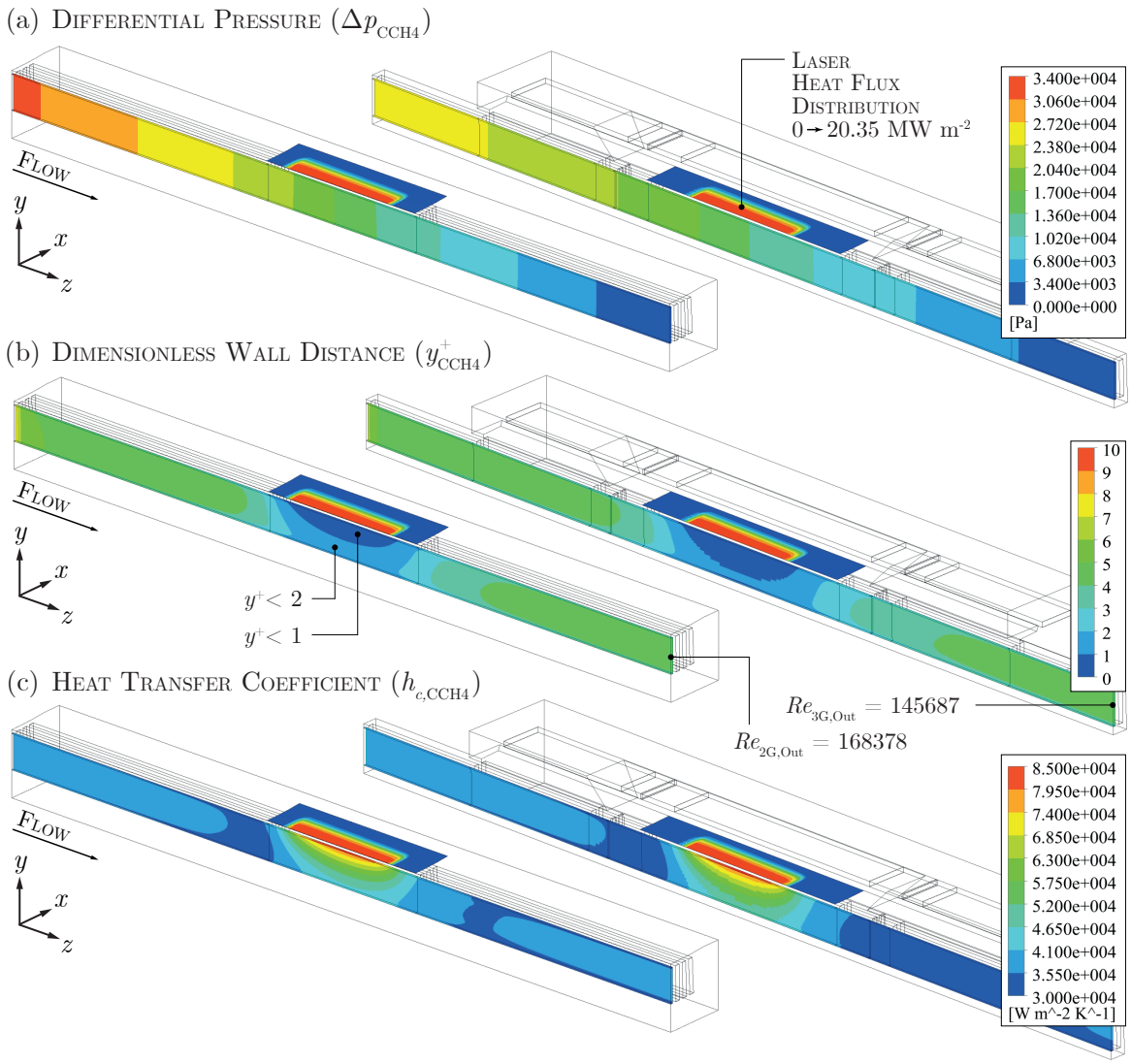

Figure 5.7: Distributions of differential pressure (a), dimensionless wall distance (b) and heat transfer coefficient (c) along the center cooling channel wall of the 2G and 3G TMF panel models with applied laser heat flux distribution.

The dimensionless wall distance along the center cooling channel wall ($y^+_{CCH4}(y,z)$) is shown in Fig. 5.7b. The y^+-value characterizes the viscous sublayer and the logarithmic profile of the turbulent flow. This viscous sublayer plays an important role with regard to the heat transfer along the cooling channel walls from the solid domain into the fluid domains. According to White [147], a Reynolds number larger than $Re > 10^4$ indicates fully turbulent flow in closed ducts. In particular, the Reynolds number for a rectangular cooling channel is defined as

$$Re = \frac{\rho \, u_z \, d_\mathrm{H}}{\mu} \tag{5.3}$$

where ρ is the density, u_z is the velocity in flow direction, d_H is the hydraulic diameter, and μ is the dynamic viscosity of the fluid. By using mass flow averaged values, the Reynolds number at the outlet of the 2G's and of the 3G's center cooling channel is $Re_{2G,Out} = 168378$ and $Re_{3G,Out} = 145687$, respectively. These results state that the coolant's flow within center cooling channel domains is fully turbulent. By regarding the heat transfer within the turbulent

flow, a dimensionless wall distance value of $y^+ \rightarrow 1$ implies that viscosity is more dominant than turbulent advection near the wall [148]. In other words, the lower the y^+-value, the better the heat transfer prediction within the applied fluid mesh that is attached near to the wall when using two-equation turbulence models (e.g. SST model). As depicted in Fig. 5.7b, the dimensionless wall distance of the 2G and 3G models is $y^+ \leq 1$ within the region where the laser heat flux is applied. Because of that, the applied fluid mesh near the wall seems to be appropriate for a good prediction of the heat transfer from the solid domain to the fluid domains.

As shown in Fig. 5.7c, the heat transfer coefficient at the 2G's and 3G's center cooling channel walls varies in flow direction with respect to the induced heat flux and the resulting temperature gradient through the laser loaded wall. Maximum heat transfer coefficients of $\hat{h}_{c,2G} = 85937.8$ and $\hat{h}_{c,3G} = 86136.7$ W m^{-2} K^{-1} are obtained along the center cooling channel walls. The heat transfer coefficient along the inflow and outflow walls is almost constant and remains below 35000 W m^{-2} K^{-1} (see Attmt. A.4).

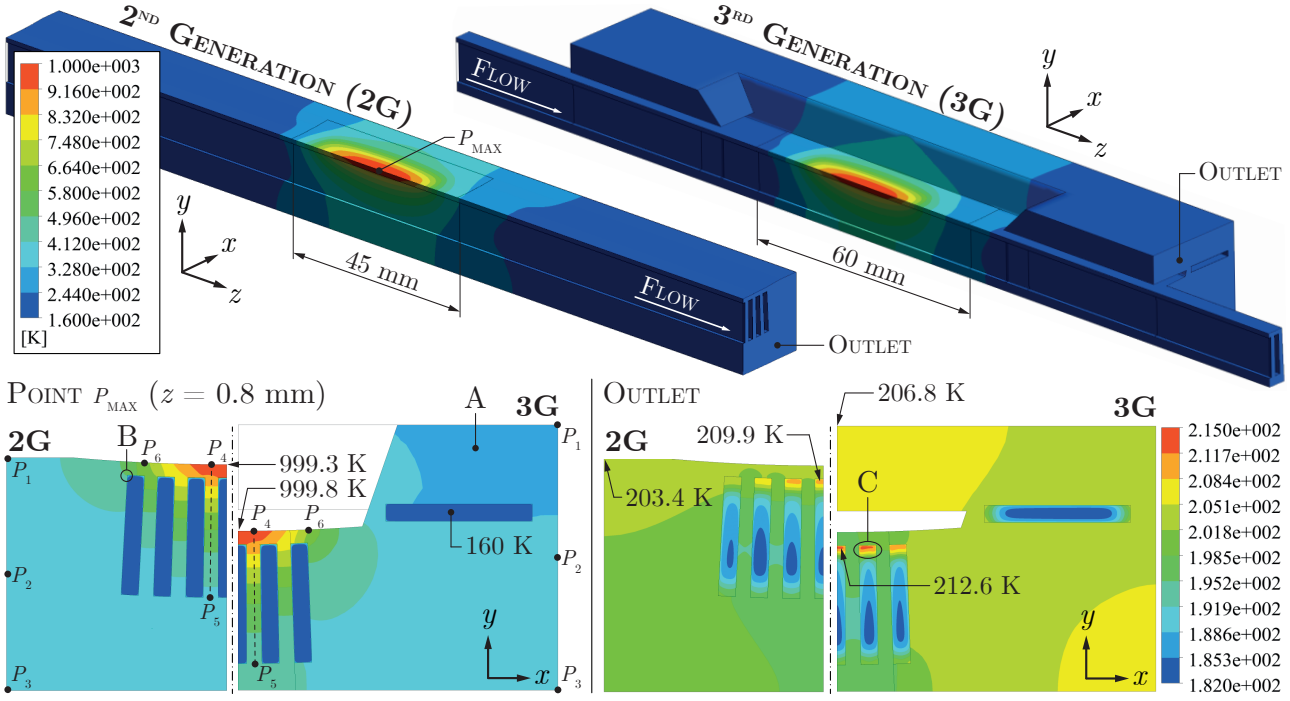

Figure 5.8: Temperature distribution of the solid domain (a) and in the x-y-cross-section at (P_{MAX}) and at the outlet (b) of the 2G and 3G TMF panel models.

Figure 5.8 depicts the resulting temperature distribution of each solid domain that is transferred to the structural analysis. A maximum temperature of $\hat{\theta}_{2G} = 999.3$ (2G) and $\hat{\theta}_{3G} = 999.8$ K (3G) is obtained on the laser loaded surface. The maximum temperature is fitted by adjusting the coolant's mass flow rate in the cooling channels for each analysis separately. The maximum solid temperature at the inlet and at the outlet is approximately $\theta_{\mathrm{in,Solid}} = 170.1$ and $\theta_{\mathrm{out,Solid}} = 203.4$ K for the 2G model and $\theta_{\mathrm{in,Solid}} = 171.1$ and $\theta_{\mathrm{out,Solid}} = 206.8$ K for the 3G model, respectively. One can see that the thermal field is elongated in z-direction due to the coolant's flow velocity; so that a heat transfer in longitudinal direction is taken into account. The point P_{MAX} is located at the z-coordinate where the maximum temperature occurs. The outer wall temperature is evaluated at the three points P_1, P_2, and P_3 in the center x-y-cross-section ($z = 0$ mm) of each TMF panel model. The outer wall temperatures are $\theta_{P_1,2G} = 362.7$,

$\theta_{P_2,2G} = 376.9$, and $\theta_{P_3,2G} = 400.2$ K for the 2G model and $\theta_{P_1,3G} = 351.1$, $\theta_{P_2,3G} = 340.7$, and $\theta_{P_3,3G} = 316.8$ K for the 3G model. Comparison of these selective temperature results implies that the 3G's outer wall temperature is approximately 20 % lower than the outer wall temperature of the 2G TMF solid domain (A). The development to the 3G TMF panel design (modifications by adding extra material at the outsides of the 2G TMF panel and moving the 1st and 7th cooling channel towards the extra material) leads to hoop stress induced into the laser loaded wall area of the 3G TMF panel. This effect is similar to the compressive effect of a common combustion chamber's cryogenically cooled nickel jacket that suppresses thermal expansion of the inner liner made of a copper-base alloy. Furthermore, the temperature difference in y-direction along the cooling channel's ligament ($\overline{P_4P_5}$) is $\Delta\theta_{y,2G} = 580.2$ and $\Delta\theta_{y,3G} = 534.8$ K; so that the 3G's temperature gradient is approximately 7.83 % smaller at a length of 10 mm. In contrary, the 3G's temperature difference in x-direction from the symmetry axis ($x = 0$ mm) to P_6 ($x \approx 5.13$ mm) is 15.4 % higher ($\Delta\theta_{x,3G} = 321.59$ K) compared to the temperature difference of the 2G model ($\Delta\theta_{x,2G} = 272.07$ K).

Regarding the flow in the cooling channels, heat transfer from the solid domain to each fluid domain can be observed with the applied mesh resolution at the center of the TMF panel models (B). The maximum fluid temperature at the wall of the 2G's and 3G's center cooling channel is $\hat{\theta}_{2G,Fluid} = 938.3$ and $\hat{\theta}_{3G,Fluid} = 941.4$ K, respectively. Due to the high mass flow rate and the local heating, thermal stratification of the fluid is obtained at the outlet (C) [149]. The maximum fluid temperature within the thermal stratification at the depicted outlet is $\theta_{out,Fluid} = 209.9$ (2G) and $\theta_{out,Fluid} = 212.6$ K (3G). By using a mass flow average outlet temperature with respect to a constant inlet temperature of $\theta_{in} = 160$ K, a temperature difference between inlet and outlet of the center cooling channel of $\Delta\theta_{2G,CCH4} = 30.38$ and $\Delta\theta_{3G,CCH4} = 30.11$ K is achieved. A reason could be that the secondary flow is much lower compared to the primary flow; so that the high mass flow rate suppresses developing of vortices in cross-sectional direction encouraging mixing of the fluid. Further details of this effect for cooling channel application are described by Torres [150] and Pizzarelli [151].

5.4.2 Structural Analysis

The following structural results are evaluated from quasi-static analyses with following mechanical loading conditions: Cyclic nodal temperature loading from 160 K during cooling to approximately 1000 K during hot run leading to high thermal strains basing on the related thermal expansion coefficients of CuCrZr, constant surface pressure loading of 55 bar normal to the cooling channel walls, and suppressed nodal displacement to account for realistic mounting of the TMF panel (see Sec. 5.2.2). Instead of importing the surface pressure computed by the thermal-fluid analysis in Ansys CFX, a constant pressure is used in Ansys Mechanical. The reason for this is the relatively low pressure difference between inlet and outlet of the center cooling channel ($\Delta p_{2G,CCH4} \approx 350$ mbar).

Figure 5.9 depicts a two-dimensional cut-out of the temperature loading in the center x-y-cross-section ($z = 0$ mm) of the 2G and 3G TMF panel models that is transferred from the thermal-fluid analysis to the structural analysis. This imported three-dimensional temperature field is then applied cyclically as a nodal body force load onto the structural mesh. Because the solid mesh's density of the thermal-fluid analysis is higher than the solid mesh's density of the structural analysis (except the center cooling channel's laser loaded wall segment), the temperature is mapped and linear interpolated by Ansys automatically. The maximum local temperature in the center cross-section ($z = 0$ mm) on the laser loaded surface of the 2G

and 3G model is $\hat{\theta}_{2G} = 998.77$ and $\hat{\theta}_{3G} = 999.39$ K (A); however, the maximum global solid temperature for each model is 999.23 K and 999.79 K at $z = 0.8$ mm, respectively (cf. Fig. 5.8). With regard to the isothermal lines illustrated in Fig. 5.9, a smooth temperature distribution is obtained in regions with fine mesh (B1, B2) and coarse mesh (C1, C2); although, structural elements with linear displacement function are used. As mentioned already in Sec. 5.4.1, the 3G model's temperature gradient during laser loading is higher in transversal direction (x) and lower in height direction (y) compared to the temperature gradients of the 2G solid domain.

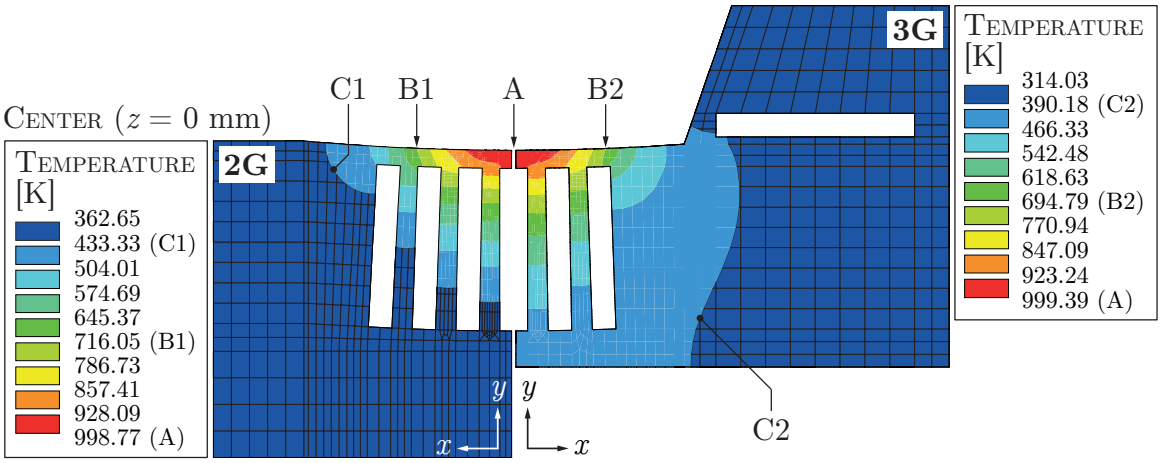

Figure 5.9: Comparison of the applied nodal temperature loading in the center x-y-cross-section ($z = 0$ mm) of the 2G's and the 3G's structural analysis.

Figure 5.10 depicts the transversal stress-strain hysteresis for all loading cycles at three evaluation points P_1, P_2, and P_3 in the center x-y-cross-section ($z = 0$ mm) of the two models. The points are located around the center cooling channel's wall. P_1 is on the laser loaded side of the center wall ligament, P_2 is on the laser loaded side in the y-z-symmetry plane, and P_3 is on the cooling channel side of the laser loaded wall in the y-z-symmetry plane. The nodal temperatures at these points are approximately $\theta_{P_1} = 981.6$, $\theta_{P_2} = 999.3$ and $\theta_{P_3} = 950.7$ K (2G) and $\theta_{P_1} = 978.3$, $\theta_{P_2} = 999.8$ and $\theta_{P_3} = 952.2$ K (3G), respectively. Note that analysis' solution data is only saved at the end of each load step; except for cycles 1 to 10 and each 50^{th} cycle where solution data is saved at every substep.

The first cycle is composed of the following steps: Uniform cooling down from ambient conditions to 160 K ($\Delta t_{\text{Ini,Pre-Cooling}} = 1$ s), applying a constant pressure of $55 \cdot 10^5$ Pa (55 bar) onto the cooling channel walls ($\Delta t_{\text{Ini,Pressure}} = 1$ s), using the imported high temperature field ($\hat{\theta} = 1000$ K) with respect to experimental laser-on time ($\Delta t_{\text{On,2G}} = 2$ s, $\Delta t_{\text{On,3G}} = 10$ s), holding period at high temperature ($\Delta t_{\text{Hold}} = 200$ s), uniform cooling down to 160 K ($\Delta t_{\text{Off}} = 10$ s) and holding period until end of first cycle ($\Delta t_{\text{Post-Cooling,2G}} = 38$ s, $\Delta t_{\text{Post-Cooling,3G}} = 30$ s). Then, the next cycle starts by applying the imported high temperature field again ($t_{\text{Cyc}} = 250$ s). According to these analyses, initial cooling leads to an elastic response at P_2 in transversal direction up to $\sigma_x = 285.44$ MPa at $\varepsilon_{x,\text{mech}} = 0.0228$ % (2G) and $\sigma_x = 272.14$ MPa at $\varepsilon_{x,\text{mech}} = 0.0217$ % (3G) into the tensile domain. Application of a constant pressure at the cooling channel walls decreases the tensile strain in transversal direction at P_2 by $\Delta\varepsilon_{x,\text{mech}} = 0.0038$ % (2G) and $\Delta\varepsilon_{x,\text{mech}} = 0.0036$ % (3G) at almost constant stress. When the laser is switched on during the first cycle, a transversal mechanical strain of -0.338 % (2G) and -1.105 % (3G) is obtained at P_2 as well as -1.013 % (2G) and -3.584 % (3G) is obtained at P_3 at the end of this quasi-static load step where the maximum temperature field is employed. During the laser

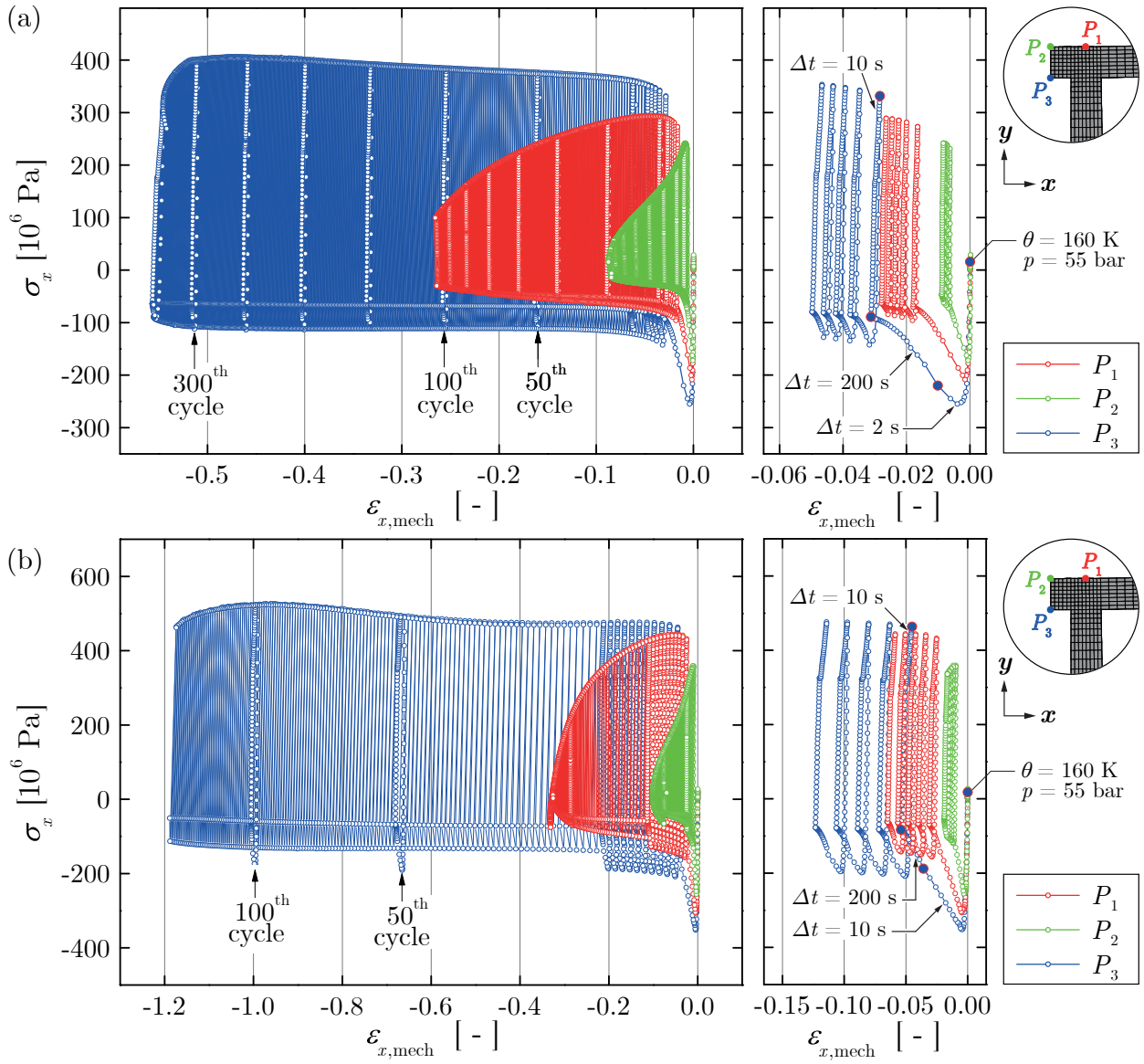

Figure 5.10: Stress-strain response in transversal direction (x) at the points P_1, P_2 and P_3 in the center of the 2G (a) and 3G (b) TMF panel's cross-section ($z = 0$ mm).

heating ramp, the transversal stress at P_3 reaches a minimum peak of $\sigma_{x,\min} = -255.17$ MPa at $t = 3.75$ s (2G) and $\sigma_{x,\min} = -351.68$ MPa at $t = 8.25$ s (3G) closely followed by short stress relaxation until the end of the ramped temperature loading (see Figs. 5.10a and b). Then, stress relaxation continues during laser holding period of 200 s. It is interesting to note that the inelastic deformation processes in a very short period of time; for example, 33.18 % within 2 s (2G) and 67.21 % within 10 s (3G) at point P_3. At the end of the laser holding period, transversal mechanical strain at P_2 decreases to $\varepsilon_{x,\text{mech}} = -0.683$ % at $\sigma_x = -58.14$ MPa (2G) and $\varepsilon_{x,\text{mech}} = -1.295$ % at $\sigma_x = -55.22$ MPa (3G) as well as at P_3 to $\varepsilon_{x,\text{mech}} = -3.121$ % at $\sigma_x = -89.35$ MPa (2G) and $\varepsilon_{x,\text{mech}} = -5.367$ % at $\sigma_x = -85.31$ MPa (3G). Next, a uniform temperature of 160 K is applied onto all nodes as ramped loading. One can see that the transversal stress-strain response from high temperature to 160 K is purely elastic and only affected by the temperature dependent material properties for elasticity (see Tab. 4.2). Therefore, the stress state at all points turns from compression into tension but it still remains

in the compressive strain domain at the end of the first cycle leading to compressive strain ratcheting. The transversal stress-strain response for the 2G model is then $\Delta\sigma_x = 289.67$ at $\Delta\varepsilon_{x,\text{mech}} = 0.019$ % at point P_2 and $\Delta\sigma_x = 420.85$ MPa at $\Delta\varepsilon_{x,\text{mech}} = 0.017$ % at point P_3 (see Fig. 5.10a) as well as for the 3G model $\Delta\sigma_x = 414.37.67$ at $\Delta\varepsilon_{x,\text{mech}} = 0.012$ % at point P_2 and $\Delta\sigma_x = 548.14$ MPa at $\Delta\varepsilon_{x,\text{mech}} = 0.009$ % at point P_3 (see Fig. 5.10b). In comparison to structural analysis' results of a common rocket combustion chamber made of a generic copper-base alloy that has been performed by SCHWARZ [21], tensile strain ratcheting of the hot wall ligament occurs due to overcompensation of inelastic compressive strains after shut down of the engine.

To sum up the first cycle, a transversal mechanical strain range of $\Delta\varepsilon_{x,\text{mech}} = 0.650$ % (2G) and $\Delta\varepsilon_{x,\text{mech}} = 0.975$ % (3G) are obtained at P_2 and $\Delta\varepsilon_{x,\text{mech}} = 2.850$ % (2G) and $\Delta\varepsilon_{x,\text{mech}} = 4.521$ % (3G) are obtained at P_3. The transversal stress ranges are $\Delta\sigma_x = 165.85$ MPa at P_2 and $\Delta\sigma_x = 200.12$ MPa at P_3 (2G) as well as $\Delta\sigma_x = 238.92$ MPa at P_2 and $\Delta\sigma_x = 261.66$ MPa at P_3 (3G), respectively. So, the 3G model's maximum transversal strain range is $\Delta\hat{\varepsilon}_{x,P_3} = 78.43$ % higher and it's transversal stress range is $\Delta\hat{\sigma}_{x,P_3} = 23.52$ % higher compared to the strain and stress ranges of the 2G model at P_3 for the first cycle. As shown in Figs. 5.10a and b, the strain range from the first to the second cycle decreases by 86.62 % at P_2 and 77.65 % at P_3 (2G) and 78.67 % at P_2 and 60.23 % at P_3 (3G). The 2G's strain range and stress range values are $\Delta\varepsilon_{x,\text{mech}} = 0.087$ % at P_2 and $\Delta\varepsilon_{x,\text{mech}} = 0.637$ % at P_3 as well as for the 3G model $\Delta\varepsilon_{x,\text{mech}} = 0.208$ % at P_2 and $\Delta\varepsilon_{x,\text{mech}} = 1.798$ % at P_3. As mentioned previously, compressive strain ratcheting with accumulation of plastic strain in the compressive domain is observed for both models by comparing the stress-strain hysteresis loops of the first and second cycle. In addition, the strain range within the 2G's hot wall decreases cyclically. A reason could be that an additional nickel layer at the bottom of the TMF panel is omitted for the two TMF panel designs. However, the strain range of the 3G model's second cycle is $\Delta\varepsilon_{2^{\text{nd}},P_2} = 58.17$ % higher at P_2 and $\Delta\varepsilon_{2^{\text{nd}},P_3} = 64.57$ % higher at P_3 compared to the 2G model. This is because of the contraction effect caused by hoop stresses induced from the relatively cold extra material at the outsides of the 3G TMF panel into the laser loaded wall. For example, the 2G's strain ranges at P_3 are 2.850 (1^{st}), 0.637 (2^{nd}), 0.453 (3^{rd}), 0.385 (4^{th}), 0.214 (10^{th}) and 0.104 % (300^{th} cycle) as well as the 3G's strain ranges at P_3 are 4.521 (1^{st}), 1.798 (2^{nd}), 1.708 (3^{rd}), 1.724 (4^{th}), 0.878 (10^{th}) and 0.489 % (100^{th} cycle). One can see that the strain range of the 2G model decreases more per cycle than the 3G's strain range. The transversal strain range at the penultimate cycle of the 3G model is three times higher compared the 2G model (see Figs. 5.10a and b). It seems that the cyclic decrease of the strain range within the 2G hot wall can be associated with an almost elastic shakedown behavior that would usually lead to high cycle fatigue. However, isotropic softening and thermal ageing at high temperatures leads to a cyclic decrease in the transversal stress range. By comparing the cyclic transversal stress range at the points P_2 and P_3, the stress at P_2 is more affected by softening effects due to higher temperature ($\theta_{P_2} \approx 1000$ K, $\theta_{P_3} \approx 950$ K). This leads to a numerically predicted life time of 356 (2G) and 144 (3G) cycles that accounts for a low cycle fatigue failure.

The results of the damage analysis at point P_3 of the 2G model and the 3G model are given in Fig. 5.11. With respect to the temperature dependent damage threshold material parameter, damage starts to evolve at $p_{D,\text{2G}} = 3.53$ during cooling at 202^{nd} cycle and at $p_{D,\text{3G}} = 3.76$ during cooling at 89^{th} cycle, respectively (see Fig. 5.11a). Although equal material parameters are used for both analyses, variation of the temperature gradient in y-direction leads to different damage threshold parameters that linear interpolated by ANSYS between the predefined temperature levels. The crack initiation point of the 2G model is located in the center on the cooling

channel side of the laser loaded wall (A). The maximum damage at point P_3 of the 2G model is $\hat{D}_{P_3} = 0.69$ at 160 K (356$^{\text{th}}$ cycle). On the contrary, the 3G's elemental damage distribution indicates that the main damage initiation point is on the upper left corner of the adjacent cooling channel (B). The maximum damage at B and P_3 is $\hat{D}_B = 0.49$ and $\hat{D}_{P_3} = 0.32$ at 160 K (144$^{\text{th}}$ cycle), respectively. Note that $\hat{D}_{P_3}$ at B is obtained at the 141$^{\text{th}}$ cycle; so that damage increases by $\Delta D_{\text{B}} \approx 0.36$ during the last 3.84 cycles until numerical divergence of the analysis occurred. On the one hand, the mesh density in x-direction is decreased by a factor of 2 and further investigations of Thiede [28] showed that the number of predicted cycles increases with decreased mesh density. Therefore, it is assumed that damage would start to evolve earlier when similar mesh density is applied in this region. On the other hand, damage at initiation point B could be a numerical fragment that is affected by a singularity due to massive deformation of the cooling channel's upper edge [152]. Figure 5.12 depicts the inelastic deformation at the edge where a sharp angle develops (A). In other words, a crack with a stress field singularity at the tip is formed due to large inelastic deformation [153]. This could lead to overstress affecting mechanical strain and isotropic damage. We assume that failure of the 3G TMF panel experiment will be similar to the 2G model and located at the point P_3 (instead at B).

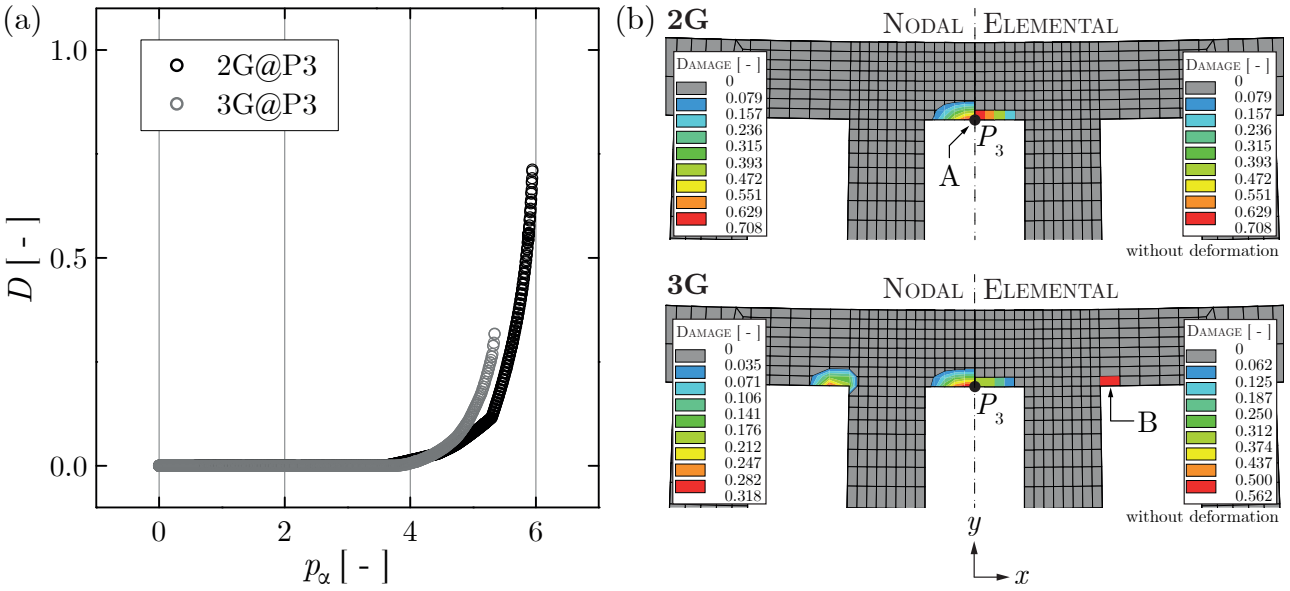

Figure 5.11: Damage evolution at point P_3 (a) and two-dimensional damage distribution (nodal and elemental solution without deformation) in the center of the 2G and 3G TMF panel's cross section ($z = 0$ mm).

Figure 5.12 shows a comparison of several cut-outs from the 2G's and 3G's hot wall deformation (non-scaled) with a two-dimensional distribution of accumulated plastic strain until failure. One can see that irreversible strains accumulating most at point P_3 in the y-z-symmetry-plane on the cooling channel side of the center cooling channel's wall segment. According to this result at the 10$^{\text{th}}$ cycle, the maximum accumulated plastic strain value of the 3G model ($p_\alpha = 2.245$) is approximately 60.36 % higher compared to the 2G model ($p_\alpha = 0.890$) because of the higher transversal strain range per cycle (see Fig. 5.10). The maximum deformation in y-direction of point P_2 at the y-z-symmetry-plane of the 3G model ($\hat{u}_y = 0.342$ mm) is approximately 84.96 % higher than the out-of-plane displacement of the 2G's hot wall ($\hat{u}_y = 0.051$ mm). With increasing numbers of cycles, the hot wall thickness of the 3G's center cooling channel increases

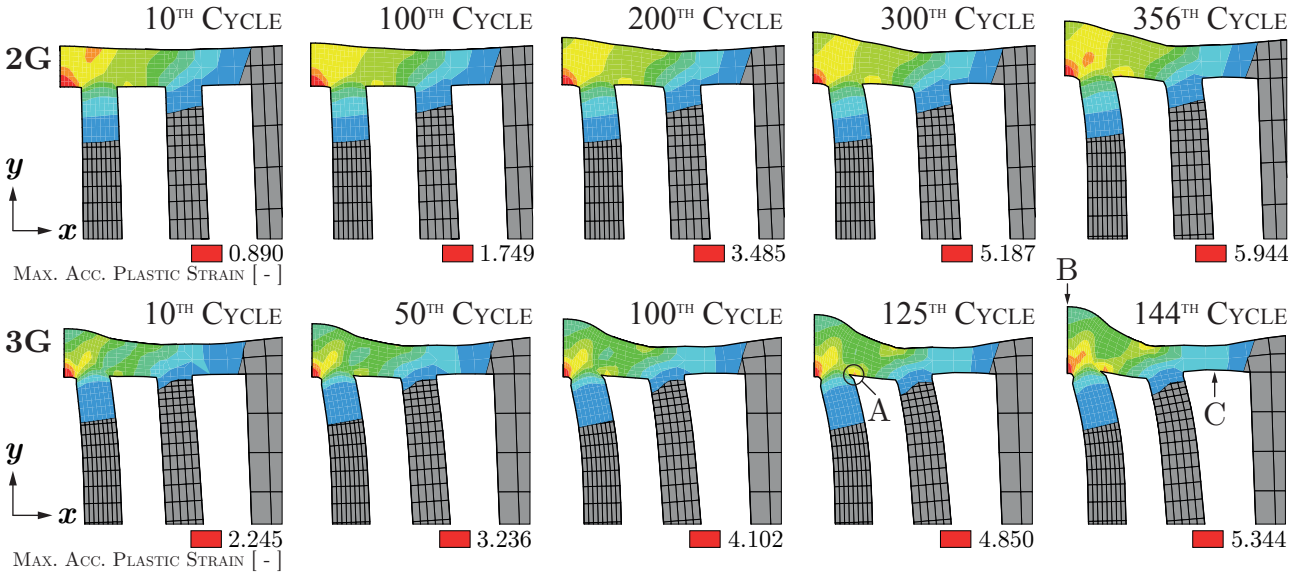

Figure 5.12: Cyclical development of inelastic deformation at the end of each cycle under cooling conditions (160 K) for 2G (a) and 3G (b) TMF panel cut-outs.

(B) and the wall thickness of the adjacent cooling channel decreases significantly (C).

5.5 Comparison to Experimental Results

Comparison between experimental results (see Sec. 2.3) and numerical results (see Sec. 5.4) for validating the fatigue life analysis of the 2G TMF panel experiment is described in the following section. Particular focus has been given to the temperature distribution on the TMF panel's surface, the fatigue life of the TMF panel structure, and the remaining plastic deformation of the TMF panel's laser loaded wall ligament. Because laser loading is one of the most important thermal boundary conditions in the coupled FSI analysis of the TMF panel, the experimental obtained laser intensity distribution measured with a PRIMES BM 100 beam profiler is compared to the numerically applied heat flux distribution (see Fig. 5.13). In this case the experimental measurement bases on a maximum laser output voltage of $\hat{U} = 6.4$ V that leads to a maximum laser intensity of $\hat{q} = 28.5$ MW m^{-2} $\pm$ 5 % at a tilt angle of 5° $\pm$ 1° (see Sec. 2.2.1). However, significant variation of the laser intensity distribution between 2 and 6 V could not be observed. With regard to Fig. 5.13, no noticeable difference between the experimental measured laser intensity distribution and the numerically applied heat flux distribution with a maximum heat flux value of 20.35 MW m^{-2} can be identified. That's because experimental data points are used directly as a normalized heat flux distribution in the thermal-fluid analysis (see Sec. 5.2.1).

Experimentally measured and numerically determined plots of the two-dimensional temperature field are given in Fig. 5.14. The plots are related to temperature values along the x- and y-axis on the TMF panel's laser loaded surface. An IR camera combined with several optical filters is used to measure the temperature distribution in-situ during laser loading on the TMF panel's surface. With regard to the coating's reflection properties, an emissivity coefficient of $\varepsilon_\alpha = 0.92$ is employed. To avoid effects on the temperature distribution within the hot wall coming from internal structural change due to high temperatures (cf. Fig. 2.12), an IR result at steady state conditions during laser loading at an envisaged maximum surface temperature

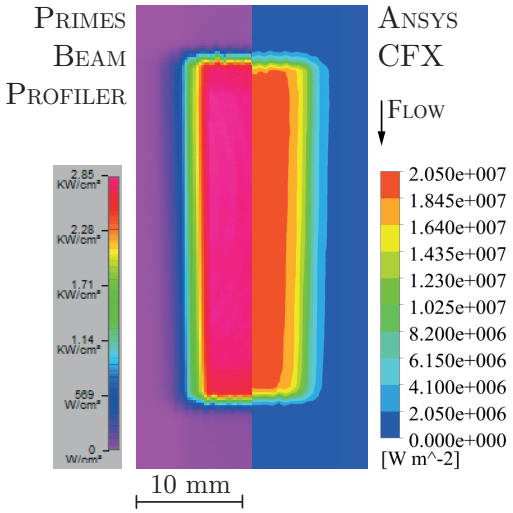

Figure 5.13: Measured laser intensity and numerically applied heat flux distribution.

of $\hat{\theta}_{\mathrm{IR}} = 1000$ K is used. The numerically determined temperature field bases on the stationary thermal-fluid analysis that is applied cyclically in the one-way coupled quasi-static structural analysis. In Figs. 5.14a and b, the temperature slopes in longitudinal (x) and transversal (y) direction are compared to each other. Four temperature ranges with different integration times are used as follows: $t_{\mathrm{IR1}} = 294.8$ µs (573.2 to 747.4 K), $t_{\mathrm{IR2}} = 152.8$ µs (695.9 to 873.3 K), $t_{\mathrm{IR3}} = 85.8$ µs (792.0 to 1020.3 K) and $t_{\mathrm{IR4}} = 66.4$ µs (842.5 to 1101.6 K). Note that t_{IR3} is employed for evaluation to avoid a temperature cut-off at high temperatures (A). Although the heat flux distribution between experiment and numerical analysis is almost equal, the temperature gradient of the numerical result (CFD) is much lower in longitudinal direction than the temperature gradient measured with the IR camera. This leads to an increased temperature profile range of the CFD analysis by 33.60 % at 600 K ($\Delta x_{\mathrm{CFD}} = 31.91$ mm) compared to the IR camera's temperature profile range ($\Delta x_{\mathrm{IR}} = 21.19$ mm) in flow direction (see Fig. 5.14a). In contrary, the experimental measured and numerically determined temperature gradients in transversal direction show a very good agreement (see Fig. 5.14b). Only a small deviation of the transversal CFD temperature is observed at temperatures lower than 450 K (B and C); but the temperature is lower than the IR camera's confidence limit (573.2 to 1773.2 K). In the end, the temperature gradient in transversal direction is 39.97 % higher than in longitudinal direction at $\theta = 600$ K (dotted line). Due to the fact that the temperature gradient in transversal direction is more important than in longitudinal direction, it is well reproduced by the stationary thermal-fluid analysis. To increase the accordance of the temperature gradient in longitudinal direction, the mesh density of the fluid domains should be constant in flow direction within the laser loaded area; instead of using biased meshing. Another factor could be the idealized geometry that is used for the mesh. Measurements of a non-damaged cross-sectional cut-out of the 2G TMF panel with a digital microscope showed that real values of the laser loaded wall's thickness ($\bar{l}_{\mathrm{Wall}} = 0.94$ mm) and the center cooling channel's width ($\bar{l}_{\mathrm{Width}} = 1.28$ mm) and height ($\bar{l}_{\mathrm{Height}} = 8.73$ mm) are approximately 6.0, 1.5, and 3.0 % lower compared to corresponding idealized geometry, respectively (see Sec. 2.3.4). Omitting of radii ($\bar{R} = 0.22$ mm) at the cooling channel edges could also affect the heat transfer from the solid domain to the fluid domains. With regard to the thermophysical properties of the copper-base alloy CuCrZr, temperature dependent thermal conductivity is determined from density, specific heat capacity, and thermal diffusivity measurements (see Sec. 4.1.4); so that a maximum

uncertainty of $\Delta\lambda \pm 9.5$ % can be expected (± 5.5 % is assumed to be appropriate).

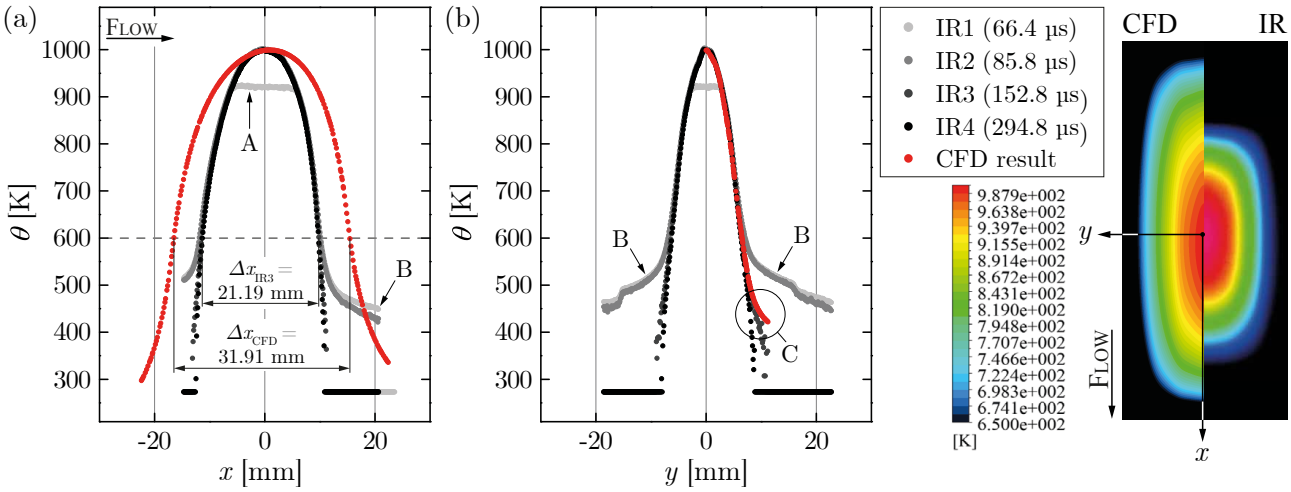

Figure 5.14: Two-dimensional temperature distribution measured during experiment with an infrared camera at different integration times compared to numerically determined temperature slopes.

Furthermore, the experimentally obtained and numerically determined cycles to structural failure of the 2G TMF panel are $\hat{n}_{\mathrm{Cyc,EXP}} = 369$ and $\hat{n}_{\mathrm{Cyc,FEM}} = 356$, respectively. The one-way coupled FSI underestimates the fatigue life by only 3.52 % which ends up very well in accordance with the experiment. Figure 5.15 depicts the cyclic deformation that has been computed numerically for the 2G and the 3G TMF panel as well as the maximum out-of-plane deformation correlated by the means of DIC. Correlation is performed at each test day before precooling under ambient temperature and ambient pressure (see Sec. 2.3.3). One can see that the remaining maximum out-of-plane displacement of the 3G's hot wall ($\hat{u}_{y,3\mathrm{G}} = 0.832$ mm) is 4.3x higher compared the displacement of the 2G's hot wall ($\hat{u}_{y,2\mathrm{G}} = 0.193$ mm) at the end of the 144$^{\mathrm{th}}$ cycle under cryogenic conditions. Final deformation just before rupture is approximately 1.7x higher ($\hat{u}_{y,2\mathrm{G}} = 0.484$ mm), respectively. With regard to the 2G TMF panel, a linear regression of the DIC values is employed starting from the 95$^{\mathrm{th}}$ cycle and the computed values between 100$^{\mathrm{th}}$ and 300$^{\mathrm{th}}$ cycle under ambient conditions. As depicted in Fig. 5.15, a remaining deformation difference of $\Delta u_{y,100^{\mathrm{th}}} = 0.065$ mm and $\Delta u_{y,300^{\mathrm{th}}} = 0.046$ mm is observed at the 100$^{\mathrm{th}}$ and 300$^{\mathrm{th}}$ cycle. Although the displacement gradient of the numerical solution is approximately 6 % higher, the remaining deformation is 8.82 % lower compared to the correlated value ($\hat{z}_{\mathrm{DIC}} = 0.522$ mm according to Eq. 2.5, $R^2 = 0.99$) at the 300$^{\mathrm{th}}$ cycle of the 2G TMF panel experiment. To conclude the deformation results of the 2G TMF panel's laser loaded wall ligament, cyclic accumulation of permanent deformation as a result of the structural analysis seems to be appropriate to the experimental result. However, the numerically determined maximum out-of-plane deflection is less than the displacement evaluated by the means of DIC. In other words, bulging of the laser loaded wall is slightly underrepresented by the numerical analysis. As mentioned previously, a digital microscope is used to measure the laser loaded wall's thickness. An actual thickness of $\bar{l}_{\mathrm{Wall}} = 0.94$ mm is determined that is 6 % lower than the idealized wall thickness of 1.0 mm. This would lead to a decreased cross-sectional area moment of inertia I_x (assuming a fixed beam type with uniform continuous distributed load) and, consequently, to a larger deflection of the wall's center.

Figure 5.16 depicts the comparison of the final deformation results between experiment (left-hand side) and one-way coupled FSI analysis (right-hand side) in the center cross-section of the

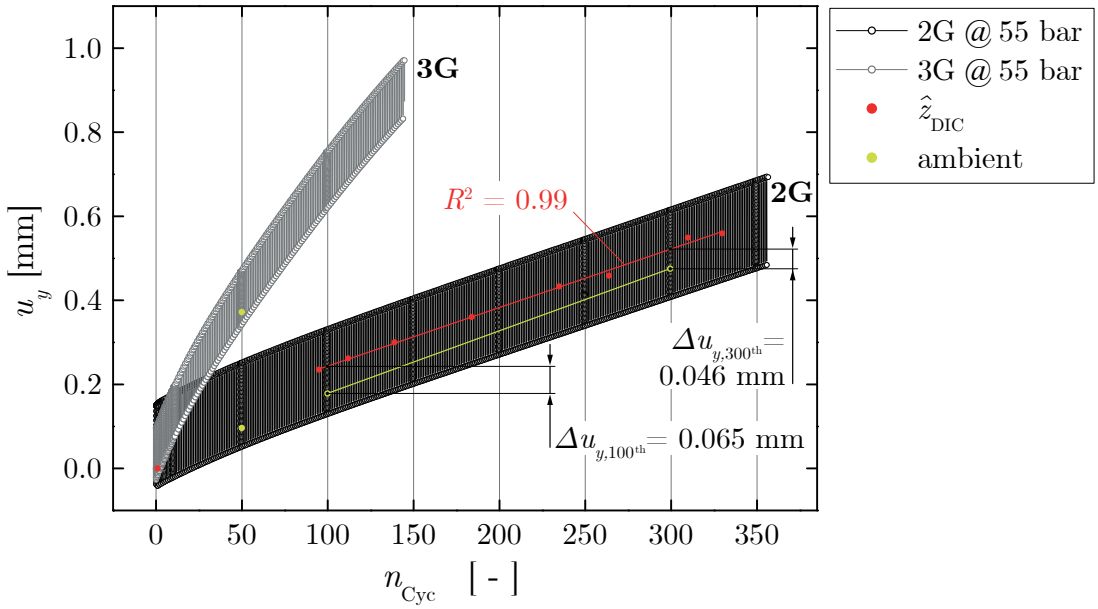

Figure 5.15: Comparison and linear regression plots of the 2G TMF panel's surface deformation computed numerically and correlated by the means of DIC.

2G TMF panel. To highlight the areas that are affected by plastic deformation, accumulated plastic strain distribution is plotted as elemental solution. Here, elemental solution is more suitable because elements with linear displacement function are employed in the structural analysis. The location of the crack growth initiation point at the symmetry axis (A) and the width of the damage area (B) are well reproduced by the analysis. Due to the fact that a phenomenological damage model is applied, simulation of the cyclic crack growth process including a mesh adaptation due to element deletion could not be realized. However, application of a crack propagation model related to fracture mechanics could improve the cyclic deformation results. In contrary to correlated deflection that is larger than the computed deformation (see Fig. 5.15), the ruptured laser loaded wall segment is probably affected by spring back phenomena after the EDM cut at the crack's starting point (C). This could have led to the final shape with a decreased maximum out-of-plane deformation of the cross-sectional cut-out (cf. Fig. 5.16). Nevertheless, the numerically determined increase of the reference cooling channel's laser loaded wall agrees with experimental results. Regarding the adjacent cooling channels (no. 3 and 5), high values of accumulated plastic strain indicate the initiation point of the asymmetric doghouse deformation mode that has caused bulging and thinning of the second wall ligament (D). Unfortunately, doghouse deformation of the adjacent wall ligament could not be reproduced correctly. On the one hand, deformation in transversal direction is overrepresented by the numerical analysis. Examples are the second fin that is deformed towards the center (E) and its wall ligament thickness that is decreased significantly (F). So, the material moves from the outside areas towards the center due to temperature dependent thermal expansion in transversal direction. On the other hand, deformation of the laser loaded wall is underrepresented in height direction (D). A reason could be the usage of a rolled cold-worked plate as a raw material basis for manufacturing the TMF panels as well as the material characterization test samples (cf. Fig. 2.5). For this case, anisotropic material properties could have a significant influence on the deformation mode in the plate's thickness direction. Application of an anisotropic damage model could help to improve this deformation mode.

Note that the thickness of the procured plate is limited; so that the material properties could not be investigated in this direction.

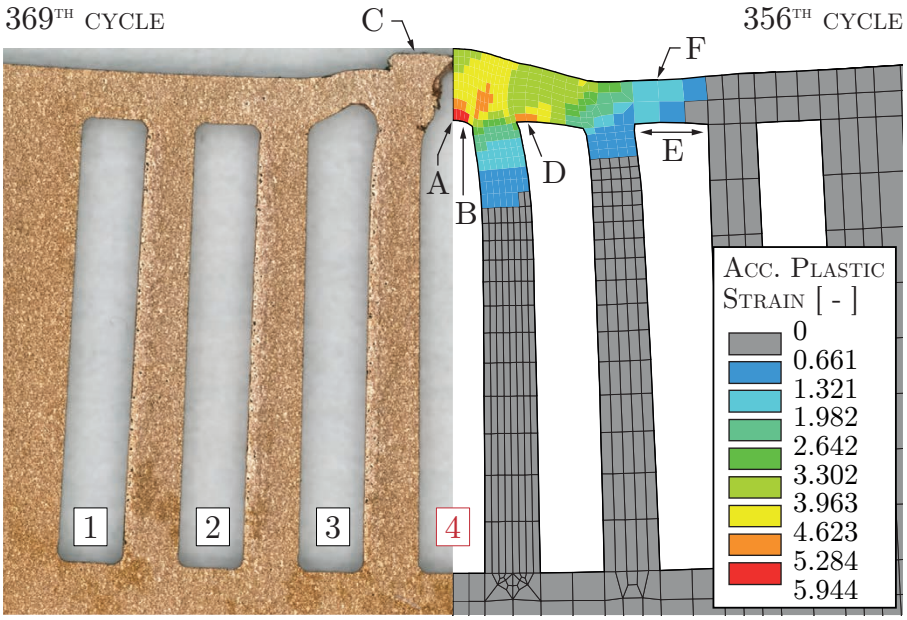

Figure 5.16: Experimental and numerical deformation results with accumulated plastic strain distribution (as an elemental solution) in the center cross-section of the 2G TMF panel.

A summary of the comparison between experimental and computational results is given in Tab. 5.3. Note that these results only refer the center cooling channel. Because the experimental values are measured with electronic devices, the determination of uncertainties is required. We assume both, the heat generated by the laser is absorbed entirely by the coolant and the heat flow into the holding system is neglected. According to Eqs. 2.2 and 2.3, the laser's heat flux and its uncertainty can be calculated reversely by taking into account the enthalpy difference of the coolant in each cooling channel at steady state laser loading, constant mass flow rate, and geometry of the applied laser area (the so-called caloric method) (see Attmt. A.2). To obtain the enthalpy difference $\mathrm{d}H_{\mathrm{N2},i}$ for each cooling channel, pressure and temperature values at the inlet and the outlet have to be determined. Hence, the uncertainty of pressure bases on measurement from absolute pressure sensor at the outlet tube ($\Delta p_{\mathrm{out}} = 106.3$ mbar) and a differential pressure sensor between inlet and outlet tubes ($\Delta p_{\mathrm{diff}} = 15.3$ mbar). The temperature is measured in all inlet tubes and all outlet tubes with thermocouples; so that the uncertainty of two thermocouples needs to be taken into account ($\Delta\hat{\theta} = 2 + 2 = 4$ K). A heat flux uncertainty of $\Delta q_{\mathrm{Laser}} = 19.29\ ^{+4.44}_{-3.72}$ MW m^{-2} $\left(^{+23.02\%}_{-19.27\%}\right)$ is then calculated considering a total mass flow uncertainty of $\Delta\dot{m}_{\mathrm{total}} = 0.158$ g s^{-1} (relative error of $7 \cdot 0.1$ %) and a laser area uncertainty of $\Delta A_{\mathrm{Laser}} = 48.3$ mm^2 (absolute error of 5 % per length and width). This leads to a temperature inaccuracy of $\Delta\hat{\theta} = 63.4$ K with an emissivity coefficient of $\varepsilon_\alpha = 0.74$ ($\Delta\varepsilon_\alpha = -0.18$). Neglecting the laser area's uncertainty, a resulting heat flux and a resulting maximum surface temperature uncertainty of ± 2.12 MW m^{-2} (± 11 %) and ± 35 K (± 3.5 %) with a emissivity coefficient deviation of approximately 10 % is obtained, respectively. Note that determination the local heat flux and its measurement error is still a difficult task. Regarding to the work of Suslov [154], a measurement error of ≈ 14 % would accord to heat flux values around $20 \cdot 10^6$ W m^{-2}. To decrease uncertainty of the maximum surface temperature, the coating could also affect the temperature difference between the laser loaded surface and

Table 5.3: Comparison of experimental and numerical results with uncertainties.

	$\boldsymbol{\Delta p}_{\text{Fluid}}$ [mbar]	$\boldsymbol{\Delta \theta}_{\text{Fluid}}$ [K]	$\boldsymbol{q}_{\text{Laser}}$ [MW m^{-2}]	$\hat{\boldsymbol{\theta}}$ [K]	$\hat{\boldsymbol{n}}_{\text{Cyc}}$ [-]	$\hat{\boldsymbol{u}}_{\boldsymbol{y}}$ [mm]
2G experiment	350[6] ±15.3	33.99[7] ±4	$19\,29\,^{+4.44}_{-3.72}$[8]	1000 ± 63.4[8]	369	0.559 ± 0.06 %[9]
2G FSI analysis	319.2[10]	30.4[10]	20.35[11]	999.3	356	0.484
3G FSI analysis	263.9[10]	30.1[10]	20.35[11]	999.8	144	0.832

cooling channel wall by acting as a thermal barrier coating (TBC). The total thickness of the coating is approximately 8.1 µm which includes a 0.1 µm Ti-layer on the TMF panel surface, a 2 µm Ni/Cr-layer and a 6 µm high-emissivity layer on the top of the coating system. Assuming one-dimensional heat flow, a thermal conductivity of $\lambda_{\text{Ti}} = 20$ W m^{-1} K^{-1} (corresponds to titan at ambient conditions) and a heat flux of 18.72 MW m^{-2} (including $\varepsilon_\alpha = 0.92$), a temperature difference of $\Delta\theta_{\text{TBC}} = 7.58$ K between the TBC's top and bottom is obtained. In other words, the temperature on the TMF panel's laser loaded copper surface is 7.58 K lower than the temperature measured on the top of the coating acting as a TBC.

[6] Pressure values measured in the cylindrical inlet and outlet tubes.
[7] Selectively averaged from cycles $10, 100, 200, 300$ and 369.
[8] Enthalpy differences are determined by the means of the caloric method.
[9] Correlated at cycle 330 with DIC under ambient conditions.
[10] Mass flow averaged values are used.
[11] A emissivity coefficient of $\varepsilon_\alpha = 1$ is used on the laser loaded surface.

6 Application to a Rocket Chamber Segment

6.1 Finite Element Modeling

In the following sections, the presented damage model is employed to a representative combustion chamber segment with an inner liner made of CuCrZr and a cooling channel geometry proposed by KUHL [15]. A transient thermal analysis is carried out to a quasi-static structural analysis to model hot firing cycles until structural failure. Two different sets of material parameters are used. Finally, the results are presented and discussed with respect to the fatigue life time and deformation behavior of these configurations.

Figure 6.1 depicts the two-dimensional geometry of a half cooling channel segment in the cross-section of the combustion chamber's throat. Only a half model is needed because of rotational symmetry. The angle of the half segment is 0.5° at a given throat radius of $R = 130$ mm. The segment's thickness in z-direction corresponds to the minimal length of an equidistant element within the hot wall ligament ($l_z = 0.1$ mm). According to KUHL [15], the hot wall ligament's thickness and the cooling channel's width and height are $l_{\mathrm{CCH,Wall}} = 1$ mm, $l_{\mathrm{CCH,Width}} = 1.3$ mm and $l_{\mathrm{CCH,Height}} = 9$ mm, respectively. These dimensions accord with dimensions of the 2G and 3G TMF panel's center cooling channels. A nickel layer with a height of $l_{\mathrm{Ni}} = 8$ mm is attached directly on the inner liner that is made of CuCrZr.

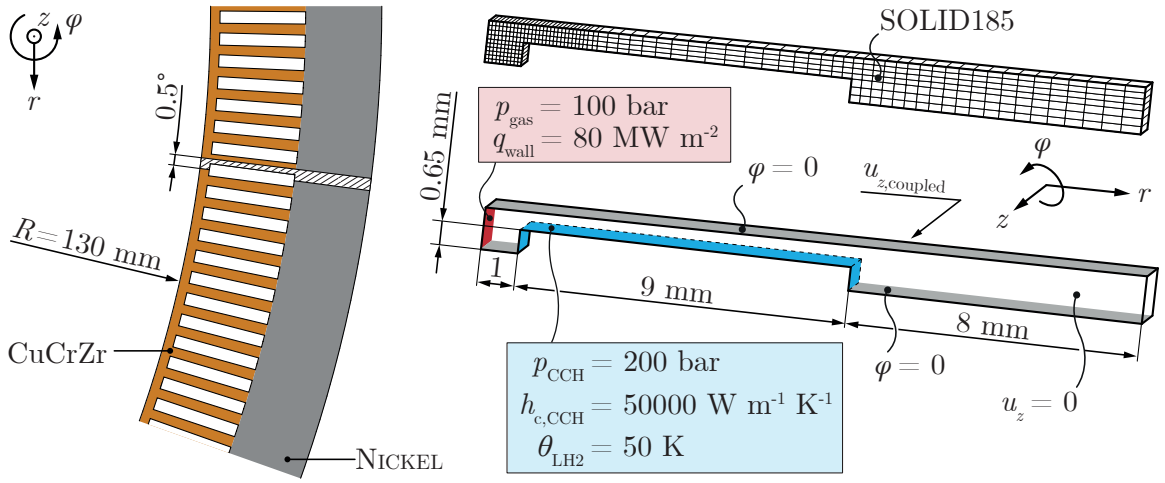

Figure 6.1: Illustration of the half cooling channel model with structural and thermal boundary conditions.

To be comparable with TMF panel analyses, the FE mesh of the rocket chamber segment consists of three-dimensional solid elements with linear displacement function and reduced

Table 6.1: Cyclic thermal and structural boundary conditions of the combustion chamber model.

t_{Cyc} [s]	q_{wall} [MW m^{-2}]	$h_{c,\mathrm{CCH}}$ [kW m^{-1} K^{-1}]	θ_{LH2} [K]	p_{gas} [MPa]	p_{CCH} [MPa]
0	0	50	50	0	20
10	0	50	50	0	20
10.1	80	50	50	10	20
11	80	50	50	10	20
610	80	50	50	10	20
612	0	50	50	0	20
614	0	0.15	293	0	0
1000	0	0.15	293	0	0

integration; so that only one integration point is used for each solid element. One can see that a mapped fine mesh with equidistant elements is applied at inner liner regions where large temperature gradients are expected. A coarse mesh with biased elements is used at the inner liner where the temperature gradients are relatively small. In the same way, a coarse mesh is also used for the nickel part that is cryogenically cooled and assumed to behave with linear elasticity. This leads to an entire mesh size of only 321 elements and 802 nodes and decreases computational time significantly.

A representative operating cycle of a common combustion chamber can be divided in the following stages: Pre-cooling, hot-run, post-cooling, and return to ambient conditions. During pre-cooling, the regeneratively cooling system is activated and pressurized liquid hydrogen (LH2) flows through the cooling channels ($t_{\mathrm{Pre\text{-}Cooling}} = 10$ s). Convection is determined by the heat transfer coefficient $h_{c,\mathrm{CCH}}$ and the coolant's bulk temperature θ_{LH2}. It is applied onto the cooling channel walls. Hot firing starts with igniting oxidizer (LOX) and fuel (LH2 acting as coolant) in the chamber ($t_{\mathrm{On}} = 0.1$ s); followed by a holding time representing the operational time ($t_{\mathrm{Hold}} = 600$ s). The temperature and the pressure of the hot gas increase rapidly. A heat flux (q_{wall}) is applied on the hot gas wall and enforces convection at the cooling channel walls. Taking into account the hot gas pressure that acts as a surface load on the hot gas wall area, the pressure difference in the hot gas wall ligament decreases to a half of the initial channel pressure ($\Delta p = 100$ bar). Post-cooling is characterized by shutting down the engine (deactivation of heat flux and hot gas pressure) while the regenerative cooling system is still activated ($t_{\mathrm{Off}} = 2$ s). Then, the cooling system is shut down (deactivation of channel pressure and decreasing the heat transfer coefficient to almost zero) and the combustion chamber structure returns back to ambient conditions ($t_{\mathrm{Cyc}} = 1000$ s). Table 6.1 gives an overview of the structural and thermal boundary conditions that have been applied in the transient thermal analysis and in the quasi-static structural analysis of the combustion chamber segment during an operational cycle.

To allow expansion and contraction of the combustion chamber in radial direction, rotational symmetry ($\varphi = 0$) is used at the two r-z-symmetry-planes of the half chamber segment's (see Fig. 6.1). The displacement of the top is fixed in thickness direction ($u_z = 0$) while the opposite side is coupled in the z-direction ($u_{z,\mathrm{coupled}}$). Coupling is needed to take into account generalized-plane-strain conditions; although, three-dimensional solid elements are employed [155]. Note that these boundary conditions are used to demonstrate the applicability of the

proposed material model to a generic rocket combustion chamber.

The pseudo two-dimensional transient thermal analysis is carried out to compute the thermal field during a loading cycle within 1709 time steps. The transient thermal field is then transferred to a pseudo two-dimensional quasi-static structural analysis and applied cyclically as a time dependent nodal body force by using APDL commands. The mesh of the transient thermal analysis and the follow-on quasi-static structural analysis is identical; so that no interpolation is performed by ANSYS. Static pressure, convection and heat flux are applied as surface loads on the related areas. Following options are activated during solution: Large-deflection effects, nonlinear solution control for optimized defaults, and full NEWTON-RAPHSON method with unsymmetrical element matrices combined with line search [140]. Similar to the TMF panel analyses, a direct solver and no stabilization techniques are used. The cyclic structural analysis is finished when damage reaches the critical value or solution diverges; even though the sub step number has been increased significantly.

6.2 Numerical Results

Figure 6.2 depicts the temperature history results computed by the pseudo two-dimensional transient thermal analysis. This analysis bases on thermophysical material parameters that have been determined for both the inner liner made of CuCrZr (see Tab. 4.1) and the nickel jacket taken from RICCIUS [156]. Due to the fact that the nickel jacket is constantly cooled in this analysis at $\theta_{\min} = 55.95$ K, isothermal density $\rho_{\mathrm{Ni}} = 8910$ kg m^{-3}, isothermal specific heat capacity $c_{p,\mathrm{Ni}} = 444$ J kg^{-1} K^{-1}, and isothermal thermal conductivity $\lambda_{\mathrm{Ni}} = 75$ W m^{-1} K^{-1} are employed [19, 156]. As shown in Fig. 6.2b, a maximum temperature of $\hat{\theta} = 1097.7$ K is obtained on the hot gas side of the wall ligament. The temperature gradient along the center wall ligament is $\mathrm{d}\theta/\mathrm{d}l_{\mathrm{CCH,wall}} = 211.68$ K mm^{-1} and, therefore, 4.4x higher compared to the temperature gradient along the symmetry plane of the 2G TMF panel's wall ($\mathrm{d}\theta/\mathrm{d}l_{\mathrm{2G,wall}} = 47.91$ K mm^{-1}). During the transient cyclic loading, heating (t_{On}) and cooling (t_{Off}) correlate to a linear temperature gradient because of the high thermal conductivity of the copper-base alloy (see Fig. 6.2a). Transient behavior is only observed at the beginning of each cycle while cooling down from ambient to cryogenic temperature as well as at the end of each cycle while returning back from cryogenic to ambient temperature. Note that the transient thermal analysis is performed for one loading cycle. The resulting temperature distribution is then imported and applied cyclically as a nodal body force in the follow-on structural analysis (see Fig. 6.2b).

In the pseudo two-dimensional quasi-static structural analysis, the phenomenological damage model with microdefect closure effect and thermal ageing is employed for the inner liner. In contrary to common combustion chambers, CuCrZr is used here as an inner liner material. Isotropic elasticity ($E_{\mathrm{Ni}} = 193 \cdot 10^9$ Pa, $\nu_{\mathrm{Ni}} = 0.3$) and an isothermal thermal expansion ($\alpha_{\mathrm{Ni}} = 12.2 \cdot 10^{-6}$ K^{-1}) are assumed for the nickel layer instead [19, 156]. With regard to the material properties of CuCrZr, similar material parameters that have been taken for the TMF panel analyses are used (see Tabs. 4.1 and 4.2). Only the temperature dependent damage threshold parameter is fitted to account for ductile failure and fatigue failure together [20], i.e. $p_D = 0, 0, 0, 0, 1.5, 2.25$ and 4.5 at the temperature points $\theta = 160, 300, 500, 700, 900, 1000$ and 1300 K, respectively. Figure 6.3 depicts the deformation behavior and the accumulated plastic strain distribution for several cycles at ambient conditions. The number of predicted failure cycles is $\hat{n}_{\mathrm{Cyc}} = 36$. It is 2.8x higher than the predicted life with the similar material model taking into account only ductile damage (13 cycles) [117]. It is also approximately 1.8x

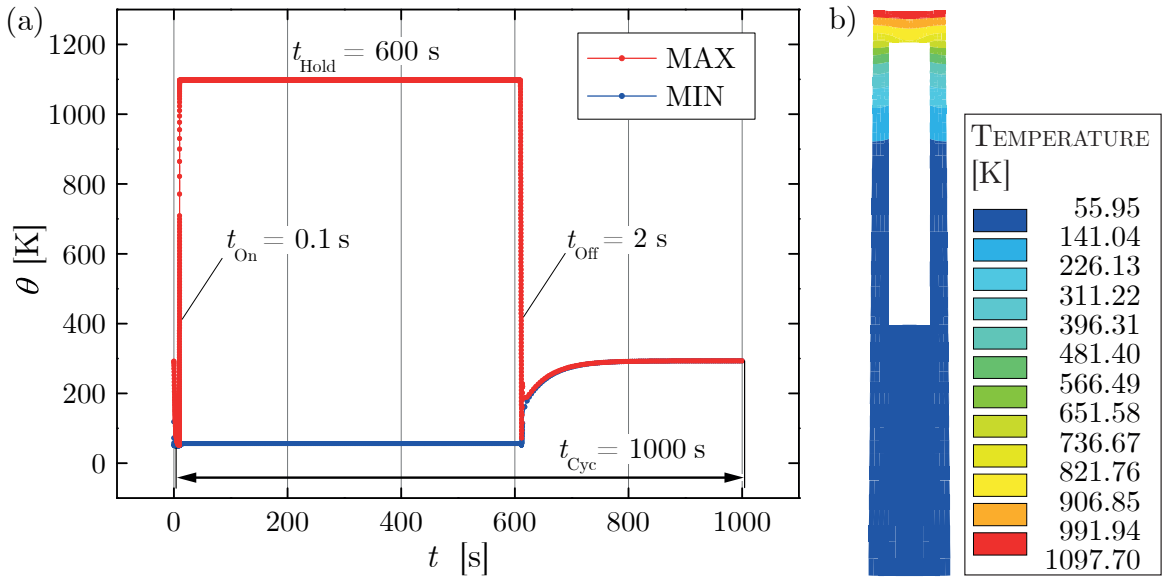

Figure 6.2: Maximum and minimum temperature plots (a) and cross-sectional temperature distribution during hot run (b) of the transient thermal analysis.

higher compared to the expected life a common single-used rocket engine (20 cycles) [23, 76] and approximately 1.53x lower than the service time of a reused SSME's RS-25 engine (55 cycles) [157]. Neglecting modification of the damage threshold parameter $p_D(\theta) = 0$ would decrease the life by nearly 22 % ($\Delta\hat{n}_{\mathrm{Cyc}} = 8$ cycles); however, maximum damage would appear then on the wall's surface at the center of the cooling channel fin (C). Regarding the structural analysis results, bulging and necking of the hot wall ligament is observed that lead to final rupture. This accords with results presented by Schwarz [21] who used a different phenomenological material model, a different channel geometry, and a different inner liner material (generic copper alloy). With regard to Fig. 6.3, damage starts to evolve from the very first cycle ($t = 8.76$ s). Final rupture is then reached at a maximum accumulated plastic strain value of approximately $\hat{p}_\alpha = 145$ % with a maximum damage value of $\hat{D} = 82.3$ % during the hot-run of the 37$^{\mathrm{th}}$ cycle. The damage difference at the last cycle is $\Delta D \approx 20$ % that indicates extensive damage growth. Due to the fact that the applied material parameters for CuCrZr are fitted to predict a fatigue failure within a temperature range of 300 to 1000 K, we assume that the engine's life would decrease in case of fitting the model's material parameters up to a temperature of 1100 K. In addition, Frölich proposed that a hot wall temperature increase of only 40 K would lead to a fatigue life decrease by 50 % [158]. In the end, a temperature difference of $\Delta\theta \approx 100$ K would lead to a significant decrease of the predicted fatigue life of the regarded chamber segment.

On the basis of the previously discussed material parameter set, a cross-sectional distribution for mechanical hoop strain, accumulated plastic strain, and damage are depicted in Fig. 6.4a. These structural results are placed at ambient conditions of the last cycle before rupture (36$^{\mathrm{th}}$ cycle). The mechanical strain range per cycle in hoop direction is $\Delta\varepsilon_{\varphi,A} = 1.48$ % (tensile domain) on the hot gas side (A) and $\varepsilon_{\varphi,B} = 0.67$ % (compressive domain) on the cooling channel side (B). One can see that cyclic tensile strain range is approximately 2.2x larger in the tensile domain. Coupling of tensile strains on the top and compressive strains at the bottom in the symmetry plane lead to shear strains from the cooling channel edges to the center of the hot wall ligament. In combination with a steadily applied static pressure difference of $\Delta p = 100$

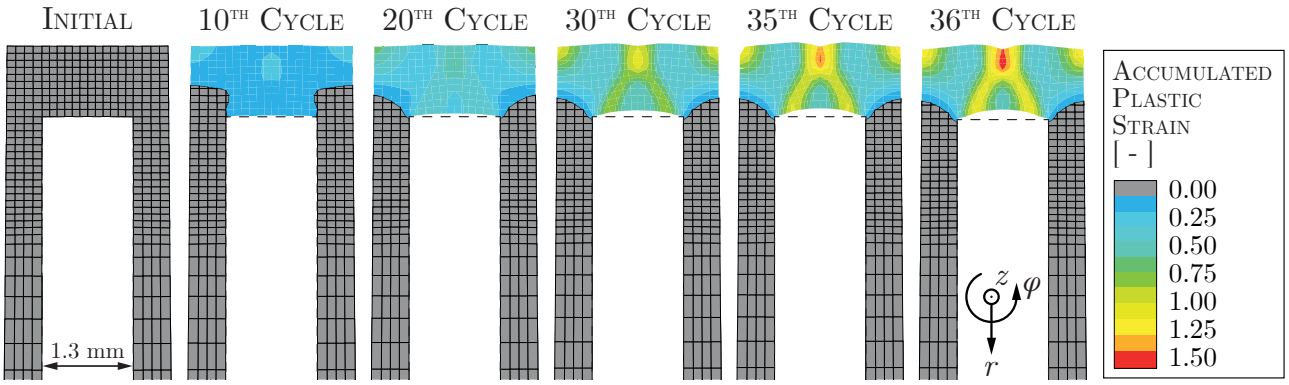

Figure 6.3: Accumulated plastic strain distribution with cyclic deformation of the hot wall ligament.

bar on the cooling channel wall, cyclic process of necking in tension and bulging in compression leads to a doghouse failure. By using this material parameter set for CuCrZr, the doghouse deformation mode of the hot wall ligament is underrepresented compared to observations of already tested full-scale combustion chambers made of NARloy-Z [23]. With regard to Fig. 6.4a, a localization of plastic strains is also observed on the hot gas side in the center of the cooing channel fin (C). Without fitting the damage threshold parameter p_D in this numerical analysis, ductile failure would occur there at an earlier stage.

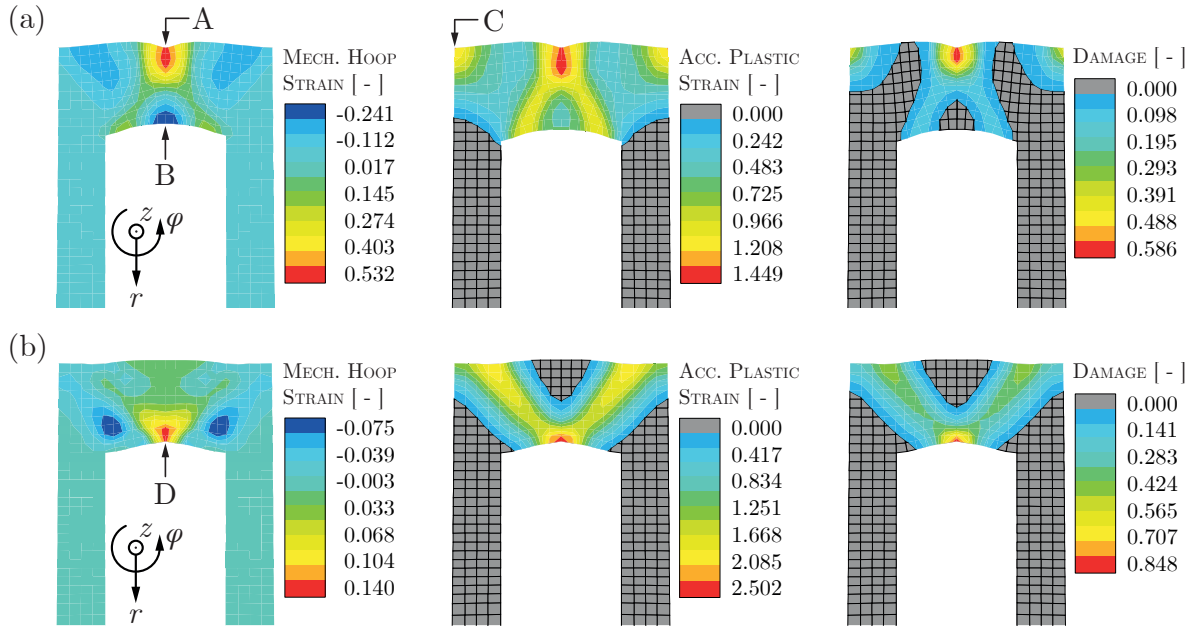

Figure 6.4: Comparison of mechanical hoop strain, accumulated plastic strain, and damage distribution of a material parameter set related to the TMF panel model with fitted damage threshold (a) and a simplified material parameter set without isotropic softening, thermal ageing and temperature dependent viscosity and damage parameters (b) at ambient conditions.

According to Schwarz [21], thermal load level of the engine's hot gas wall and viscosity behavior of the material model affect location of the neck as well as the mechanical loading state. Therefore, a second material parameter set of a generic copper alloy is carried out to the pseudo two-dimensional structural analysis of the combustion chamber segment (see Tab. 6.2). The

Table 6.2: Simplified structural material parameters of a generic copper alloy [19, 22, 156].

$\boldsymbol{\theta}$	$\boldsymbol{E_1}$	$\boldsymbol{\nu}$	$\boldsymbol{\sigma_y}$	$\boldsymbol{E_2}$	$\boldsymbol{b}_{\text{kin}}$	$\boldsymbol{\eta}$	$\boldsymbol{m_\eta}$	$\boldsymbol{S_D}$	$\boldsymbol{k_D}$	$\boldsymbol{p_D}$	$\boldsymbol{h}$
[K]	[MPa]	[-]	[MPa]	[MPa]	[-]	[MPa s]	[-]	[MPa]	[-]	[-]	[-]
0	148000	0.34	232	3133	16.33	0.1	1	2	0.5	0	0.2
800	90000	0.34	121	260	16.33	0.1	1	2	0.5	0	0.2
900	82000	0.34	108	52	16.33	0.1	1	2	0.5	0	0.2
1300	53000	0.34	53	52	16.33	0.1	1	2	0.5	0	0.2

structural material parameters for linear elasticity, nonlinear kinematic hardening, viscosity, isotropic ductile damage, and microdefect closure are taken from Riccius [156], Schwarz [19] and Tini [22]. The parameters for viscosity, damage, and microdefect closure are temperature independent and remain constant. Note that isotropic softening, static recovery of kinematic hardening, and thermal ageing effects are omitted in this analysis. The structural results computed with the simplified material parameter set of a generic copper alloy are depicted in Fig. 6.4b. In contrary to the preceding results, mechanical hoop strains in the tensile domain occur in the center of the hot wall along the entire z-r-symmetry plane. The maximum tensile strain range per cycle is $\Delta\varepsilon_{\varphi,D} = 0.28$ % that is 5.3x smaller compared to the maximal tensile strain range on the hot gas side (A) computed with the preceding material parameter set (see Fig. 6.4a). Although, the predicted life is 1.4x larger ($\hat{n}_{\text{Cyc}} = 50$ cycles) with a 1.7x larger maximum accumulated plastic strain value ($\hat{p}_\alpha = 250.2$ %). Smaller deformation is caused by higher viscosity (σ_v) that leads to higher stresses and an increased stiffness behavior of the wall ligament [22]. The maximum mechanical tensile strain in hoop direction is located on the cooling channel side of the hot wall's center where the tip of the doghouse deformation shape is expected (D).

With respect to the depicted results in Fig. 6.4b, a macro-crack would have been initiated at the tip of the doghouse and would develop cyclically through the hot wall towards the hot gas side. This would accord with investigations from the tested 2G TMF panel where fatigue striations are observed on the fracture surface (see Sec. 2.3.5). However, SEM images of a hot wall's crack surface from a tested common chamber shows irregular porous ductile fracture surfaces; so that Schwarz [20] concluded a tensile rupture failure there. In other words, necking of the hot wall seems to be more appropriate as a numerically predicted failure mechanism. Temperature dependent isotropic softening, thermal ageing, viscosity, and isotropic damage need to be taken into account to obtain realistic results with the proposed material model with respect to a rocket combustion chamber segment.

7 Conclusions and Outlook

The present thesis combines experimental work simultaneous with numerical work to validate a fatigue life analysis for actively cooled wall structures under thermomechanical loading conditions. A thermomechanical test campaign is performed with a 2G combustion-chamber-type TMF panel. The TMF panel is made of the copper-base alloy CuCrZr that is typically used for research combustion chambers at the DLR in Lampoldshausen. We also assume that CuCrZr is a potential material candidate for inner liners of future rocket engines with respect to costs and reusability specifications. During the test, the TMF panel is cooled with a mixture of liquid and gaseous nitrogen at cryogenic temperature of $\theta_{\text{in}} = 160$ K while the TMF panel's surface is cyclically loaded with a diode laser. The mass flow in each cooling channel as well as the laser power are controlled to obtain a maximum surface temperature of $\hat{\theta} = 1000$ K that is in-situ measured with an infrared camera using a constant coating's emissivity coefficient of $\varepsilon_\alpha = 0.92$. The experimental test is performed successfully because the center cooling channel failed, i.e. a crack occurred on the TMF panel's surface and outflowing coolant could be observed. The 2G TMF panel's fatigue life is determined to $\hat{n}_{\text{Cyc,EXP}} = 369$ cycles. Basing on SEM investigation of the crack surface, fatigue striations could be observed that indicates a cyclic crack growth with an averaged distance of 5 µm. A one-way coupled FSI analysis is carried out to compute the multiple physical phenomena of the 2G as well as the 3G TMF panel model whose design is modified to increase the cyclic strain range on the laser loaded surface; but still not tested yet. The thermal field of each TMF panel model during laser loading is computed on the basis of both, a steady-state fluid flow analysis with boundary conditions similar to the experiment, and determined thermophysical material properties for CuCrZr. The thermal field is then imported into a quasi-static structural analysis and applied cyclically with a constant pressure of $p_{\text{out}} = 55$ bar on the cooling channel walls. The displacement boundary conditions are set as close as possible to the TMF panel's mounting. To compute the damage evolution and the fatigue life of the TMF panel models, a viscoplastic damage model programmed by Tini [22, 24] is implemented in Ansys. The constitutive equations for viscosity [101], ductile isotropic damage [108], kinematic and isotropic hardening [95,134,159] are extended by the following effects: Combined isotropic hardening and isotropic softening [131,159], microdefect closure effect [108,110], and thermal ageing [117]. Static recovery of kinematic hardening [21,129] as well as a nonlocal damage approach are implemented indeed, but unfortunately not considered in this thesis because of numerical instabilities during the TMF panel computation. To link numerical modeling with reality, structural material parameters of test samples made of CuCrZr from the same material batch are fitted on the basis of uniaxial tensile, low-cycle fatigue, stress relaxation, and dwell tests at elevated temperatures up to 1000 K. To validate this fatigue life analysis with the proposed viscoplastic damage model, the numerical results are then compared to the experimentally obtained results. The fatigue life of the 2G TMF panel is predicted to be $\hat{n}_{\text{Cyc,FEM}} = 356$ cycles; so that the life is underestimated by only 3.5 %. The origin of the rupture crack is also predicted correctly on the center cooling channel's

upper side. However, deformation of the TMF panel is overrepresented regarding the maximum out-of-plane displacement of the TMF panel surface in height direction as well as the movement of the cooling channels towards the center. Then, the proposed material model with the fitted material parameters for CuCrZr are carried out to a simplified rocket combustion chamber analysis. On the one hand bulging and necking of the hot gas wall ligament could be reproduced very well; similar to the results obtained with a phenomenological damage model by Schwarz [19–21]. Although the predicted life time of 36 cycles seems relatively high compared to the expected life time of common single-used rocket engines [23, 76].

An important aspect of the TMF panel experiment is to draw conclusions from the experimental level to the development of full-scale rocket engines. Depending on the heat flux that is generated by the laser, this experiment allows examination of the structural behavior of both, combustion chambers of upper-stage engines, and nozzle extensions of main engines. To achieve comparability with a main engine's combustion chamber, a 4x-higher heat flux needs to be applied on the combustion-chamber-type TMF panel's surface, at least to increase the temperature gradient up to $\mathrm{d}\theta/\mathrm{d}y \approx 200$ K mm^{-1} along the laser loaded wall ligament. Furthermore, the TMF panel's surface temperature should be increased by $\Delta\theta = 100$ K. It is assumed that a maximum wall temperature of $\hat{\theta} = 1100$ K that would accord better to reality; although, the wall temperature in the throat of a rocket engine cannot be measured directly. This would further decrease the strength of the applied copper-base alloy and ductility becomes more important. As a result of the temperature increase, the fatigue life of the TMF panel would decrease significantly because it is still too high compared to a real rocket engine's life time. Regarding the design of the 2G and 3G TMF panels, the galvanically deposited nickel layer is omitted due to manufacturing reasons. However, application of the nickel layer once more would ensure almost constant cyclic strain ranges on the laser loaded surface without a tendency towards elastic shakedown. It could also lead to inelastic deformation of the hot wall ligament during the cooling process; so that damage would accumulate in tensile direction similar to the stress-strain-behavior of a rocket engine's hot gas wall [21]. Concerning the damage accumulation on the laser loaded surface of the two current TMF panels, it is still directed towards the compressive domain. Using alternative high-conductivity materials with decreased strength could help to address this issue. For example, a TMF panel made of pure copper would lead to inelastic deformation while cooling down from high temperatures to cryogenic temperatures because of the decreased yield stress limit at elevated temperatures. Another idea of improving the experimental setup by applying an adequate force constraint onto the TMF panel structure that represents the thrust force generated by a rocket engine seems unrealistic with respect to possible thrust values of $F_{\text{RS-25}} \approx 1.86$ MN (at sea level) [160] as well as the experimental setup. From the mechanical point of view, the TMF panel's holding system should ensure less constraints instead.

Regarding the numerical approach, performing a two-way coupled FSI analysis for computing the TMF panel experiment as well as the combustion chamber segment is strongly recommended when computational resources are sufficient. The influence of the cooling channel deformation process onto the fluid flow and the heat transfer along the cooling channel walls is assumed to be an important factor. Cyclic thinning of the wall ligament influences the thermal gradient within the wall ligament and, consequently, the surface temperature directly. In order to reproduce the doghouse deformation shape even better, elements incorporating finite strain theory should be used to model the massive structural deformation of the hot wall ligament. The higher the applied mesh density, the larger is the displacement of the nodes which is usually limited by FE software to avoid numerical instabilities. But such a finite strain approach

needs to be implemented at least on elemental level. In the same way, a nonlocal damage approach could be also implemented in a user-defined element to account for mesh dependency of the applied damage model [22, 28]. Although a convergence study is performed in this work with respect to the bending displacement of a simple beam problem (that is assumed to be appropriate to the wall ligament), damage evolves exactly where strain localizes. Note that a nonlocal damage approach is implemented into the material model indeed, but needs further validation yet. In the end, application of a nonlocal damage model would increase validity of the numerical results.

In displacement-based FE formulation, the stress tensor and the consistent material tangent (the so-called JACOBIAN matrix) are computed for a given strain increment. So, the applied structural material parameter set affects directly the computation of the stress tensor. In order to obtain reliable structural results, the material parameter identification procedures plays an important role. In this thesis, the material parameters are mainly fitted on the basis of uniaxial low-cycle fatigue and stress relaxation tests which ends up in a very good accordance by using a unity cell model. But as mentioned previously, the cooling channels move together towards the center of the TMF panel that indicates overestimation of creep effects in the structural analysis. Due to numerical instabilities, viscosity ($\eta = 10^{-5}$) could not be omitted entirely at low temperatures ($\leq$ 500 K); so that a slight stress decrease is still present. With regard to the numerical results, it is assumed that viscosity should be also neglected up to a temperature of approximately 800 K; although, stress relaxation at $\theta_{\mathrm{MPA}} = 700$ K within $t_{\mathrm{Hold}} = 600$ s could be determined experimentally. Further improvement of the applied material parameter set would be additional strain-controlled material tests at the TMF panel's cooling temperature $\theta_{\mathrm{in}} = 160$ K as well at the TMF panels' maximum surface temperature $\hat{\theta} = 1000$ K or even higher. In this work, strain-controlled material tests are performed only up to $\theta_{\mathrm{MPA}} = 900$ K and the material parameter sets at $\theta_{\mathrm{ILK}} = 1000$ and 1300 K are based on displacement-controlled tests conducted by the means of DIC and on extrapolation, respectively. Unlike the structural material parameters at low temperatures (< 300 K), the thermophysical properties are extrapolated by using regressions. According to the work of OSCHWALD [122], thermal expansion as well as thermal conductivity of CuCrZr at cryogenic temperatures should be determined with respect to the TMF panel's cooling conditions. With regard to structural behavior of the TMF panel's hot wall surface, accumulation of transversal strains towards the compressive domain is observed. However, the presented low-cycle fatigue tests are conducted with a strain ratio of $R_\varepsilon = -1$ and initial loading into tensile domain. The low-cycle fatigue test campaign should consider possible loading conditions of the TMF panel surface; so that initial loading would be into the compressive domain and the strain amplitude would vary between a given compressive strain value $\varepsilon_{\mathrm{mech}} = -\Delta\varepsilon$ and 0 ($R_\varepsilon = -\infty$). On the basis of such low-cycle fatigue tests, the damage parameters could have been fitted closer to the test conditions of the present TMF panel experiment. Another important fact is that the TMF panels are taken out of a rolled cold-worked plate; so that anisotropic material properties exist. Due to the fact that the raw material plate's thickness is limited, material parameters could not have been determined in this direction; especially under compressive loading. In combination with an anisotropic damage model, the structural behavior as well as the fatigue life prediction of the TMF panel experiment and the rocket combustion chamber could be modeled even more precisely.

By comparing thermal fluid flow results to experimental results, a very good accordance of the laser's heat flux distribution on the TMF panel's surface is obtained. In combination with the coolant flow in the cooling channels, the transversal temperature gradient in the center

cross-section of the TMF panel structure is reproduced very well by the stationary thermal fluid flow analysis. However, the computed temperature gradient in flow direction deviates from steady state data acquired with an IR camera during laser loading. On the one hand, the mesh density is biased along the flow direction to decrease computational efforts. Using an equidistant mesh within the laser loaded area would increase accuracy of the temperature result there. On the other hand, effects of local heating, wall roughness, and mesh density within the viscous sublayer onto the heat transfer from the solid domain to the fluid domain along the cooling channel walls should be investigated in more detail. Gernoth [54] concluded on the basis of nozzle-extension-type TMF panel experiments that application of the SST turbulence model is appropriate to model both, pressure difference in rectangular cooling channels, and the heat transfer from solid structure to fluid flow depending on a high temperature gradient. Due to the fact that the computed mass-flow averaged pressure difference in the center cooling channel is approximately 30 mbar lower compared to measurements, the applied sand-grain roughness could be increased. This would also increase the heat transfer and, consequently, decrease the surface temperature.

As mentioned previously, the fatigue life of the 2G TMF panel shows a very good agreement with experimental data. The origin of the crack is also predicted correctly. Basing on SEM investigation of the crack surface after test, application of crack-growth model by the means of fracture mechanics could help to improve cyclic crack growth prediction. Also, transversal mechanical strain range at the first loading cycle accords to computed the strain range of a common combustion chamber's hot wall surface [21]; however, cyclic decreasing of the TMF panel's strain range needs to be addressed. Again, application of a nickel layer would ensure a steady accumulation of plastic strains during the hot run of each cycle.

According to numerical obtained results on the basis of a simplified rocket chamber segment analysis, bulging and necking of the hot gas wall ligament is reproduced very well by applying the proposed damage model with the determined material parameters for CuCrZr. However, the predicted life and the computed deformation is assumed to be overestimated and underestimated, respectively. Following the conclusions of Schwarz [20], the main failure mechanism of a hot gas wall made of NARloy-Z is more related to tensile rupture than to fatigue; therefore, the material model's damage parameters should to be fitted on the basis of tensile tests by using a full-scale model of a test sample. This would decrease the fatigue life of the simplified rocket chamber segment significantly [117]. Similar to Schwarz [21] and Masuoka [130], the combination of ductile damage with fatigue and creep damage within the framework of continuum damage mechanics would improve damage modeling. In addition, reactive chemicals during combustion causes roughening of the inner liner's surface (the so-called 'blanching'); so that heat flux increases highly at local spots leading to an unsymmetrical temperature distribution in hoop direction. Riccius [161] showed that the fatigue life of a half channel model is approximately 2.7 times higher compared to the fatigue life of a three-channel model with a varied temperature distribution by $\Delta\theta = 20$ K. In addition, hydrogen embrittlement needs also to be addressed while conducting a fatigue analysis of the rocket chamber. The inner liner surface becomes brittle and cracks are induced by corrosion effects. Note that these effects are neglected in the present simplified fatigue analysis of a rocket chamber segment.

A Appendencies

A.1 EDX Analyses of CuCrZr

Ambient Temperature without Ageing (L3)

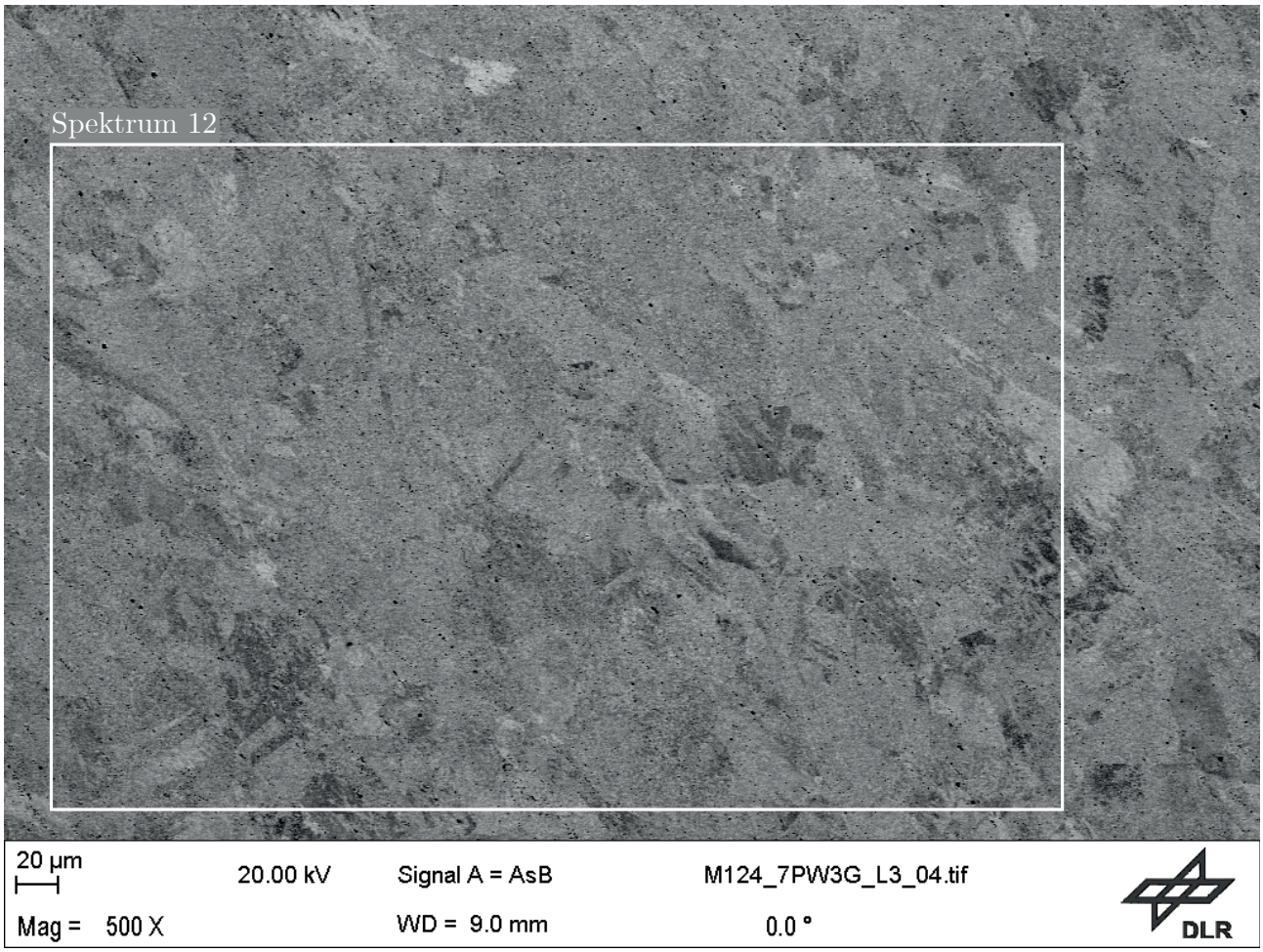

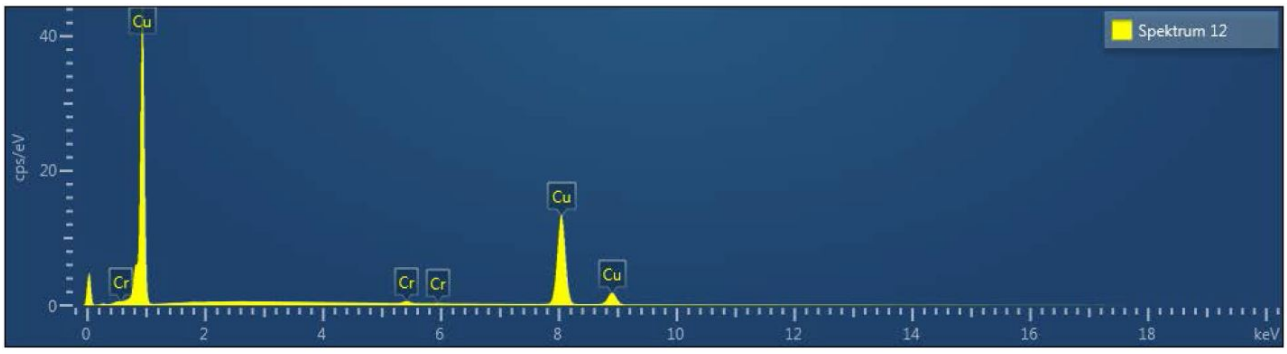

Spektrum	Cu [wt.%]	Cr [wt.%]	Zr [wt.%]
12	99.17	0.83	-

Spektrum	Cu [at.%]	Cr [at.%]	Zr [at.%]
12	98.99	1.01	-

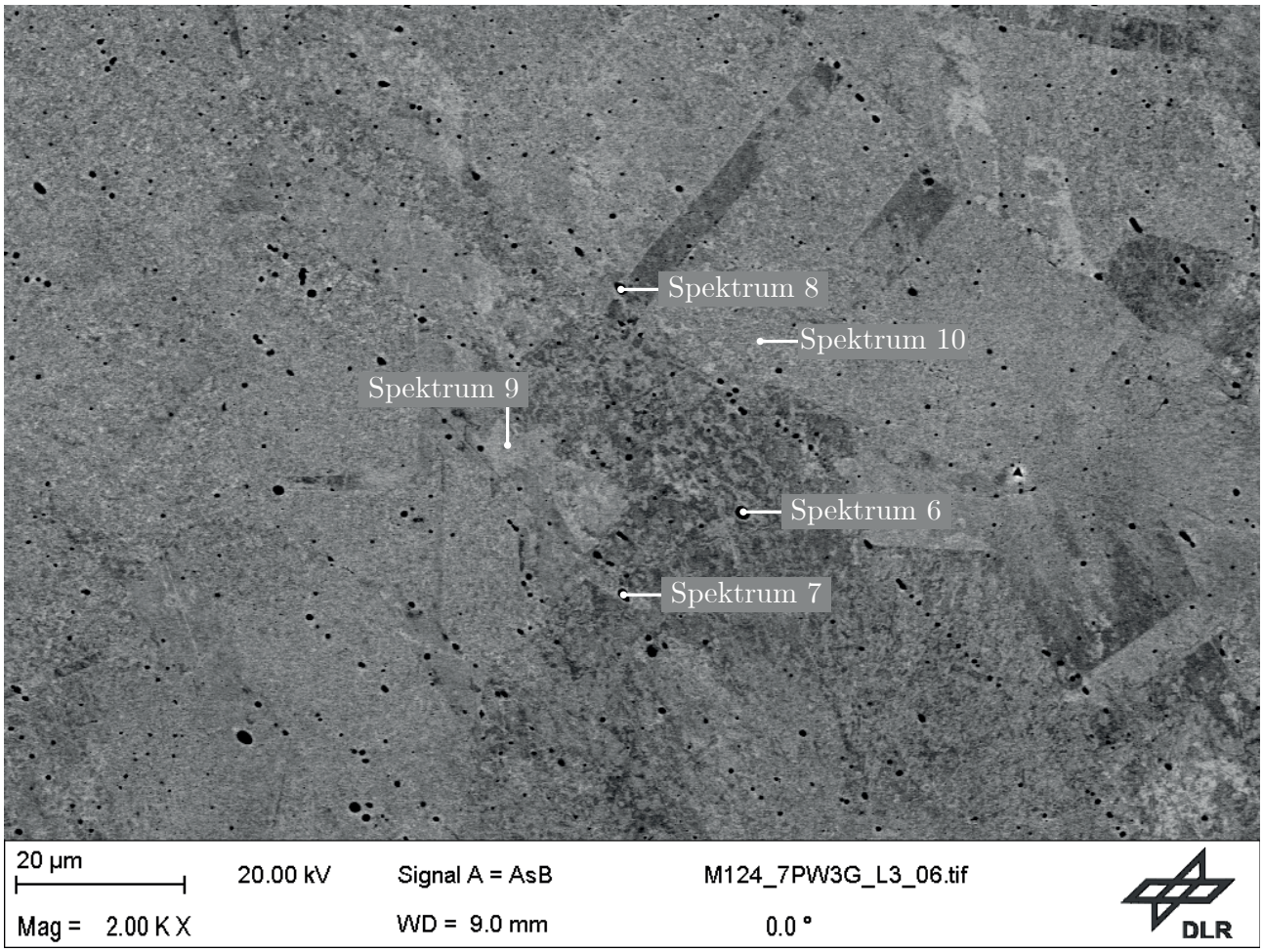
Spektrum 8
Spektrum 10
Spektrum 9
Spektrum 6
Spektrum 7
20 µm
20.00 kV
Signal A = AsB
M124_7PW3G_L3_06.tif
Mag = 2.00 K X
WD = 9.0 mm
0.0 °
DLR

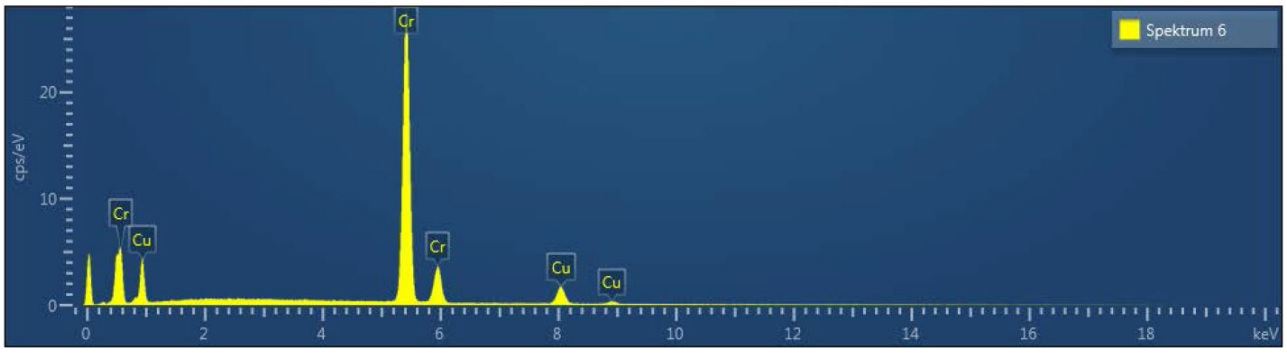
Spektrum 6
cps/eV
Cr
Cu
keV

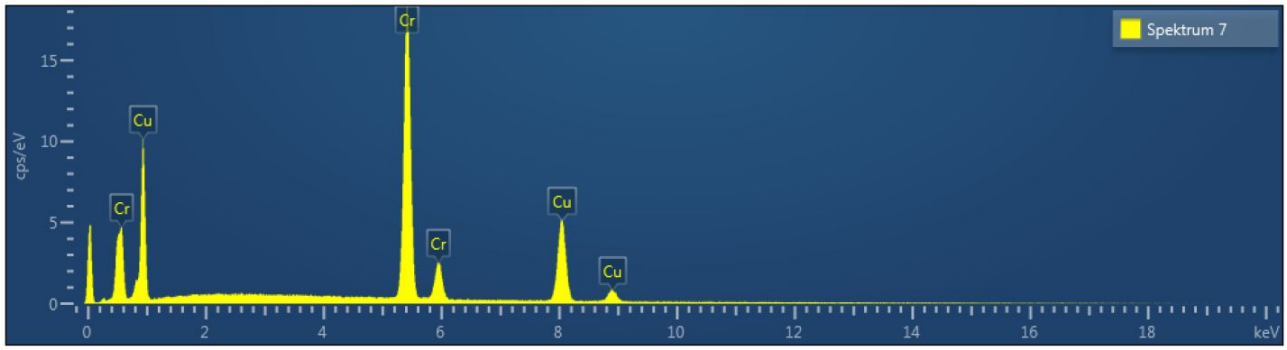
Spektrum 7
cps/eV
Cr
Cu
keV

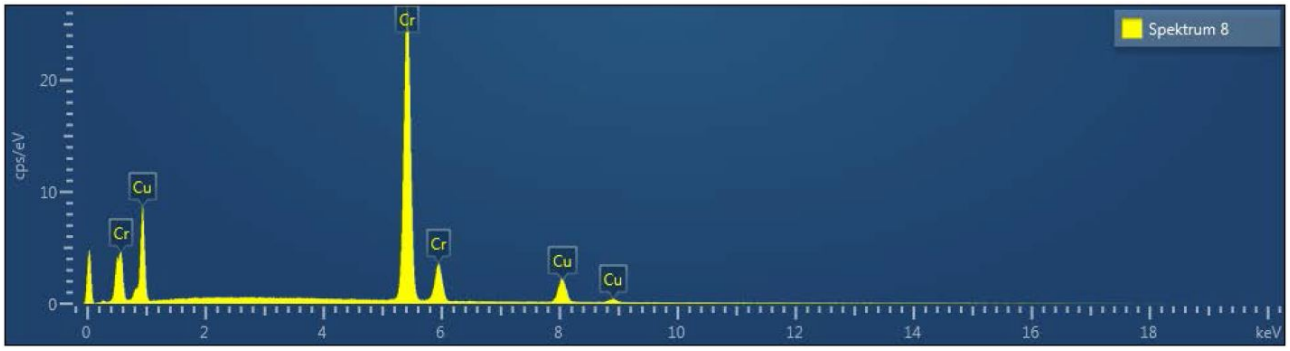

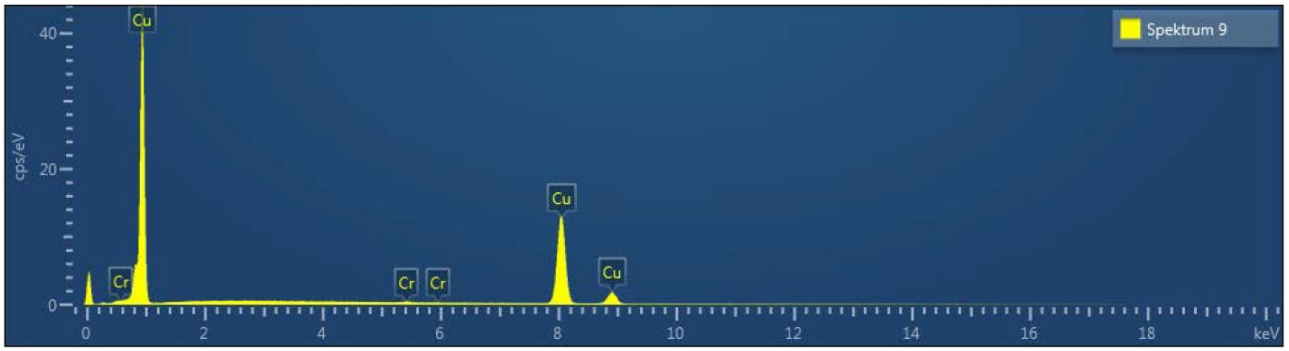

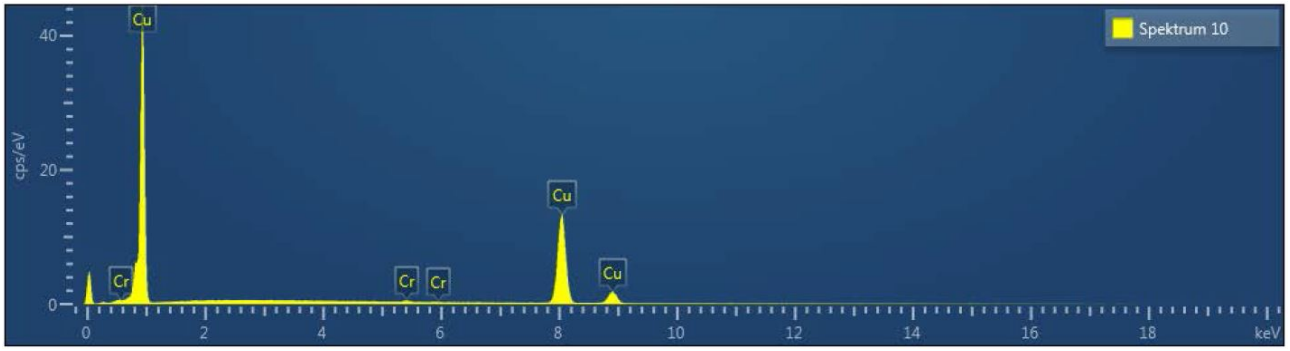

Spektrum	Cu [wt.%]	Cr [wt.%]	Zr [wt.%]
6	14.11	85.89	-
7	44.04	55.96	-
8	18.55	81.45	-
9	99.61	0.39	-
10	99.48	0.52	-

Spektrum	Cu [at.%]	Cr [at.%]	Zr [at.%]
6	11.85	88.15	-
7	39.17	60.83	-
8	15.71	84.29	-
9	99.52	0.48	-
10	99.36	0.64	-

Temperature of 1000 K with Ageing of 10 h (Q11)

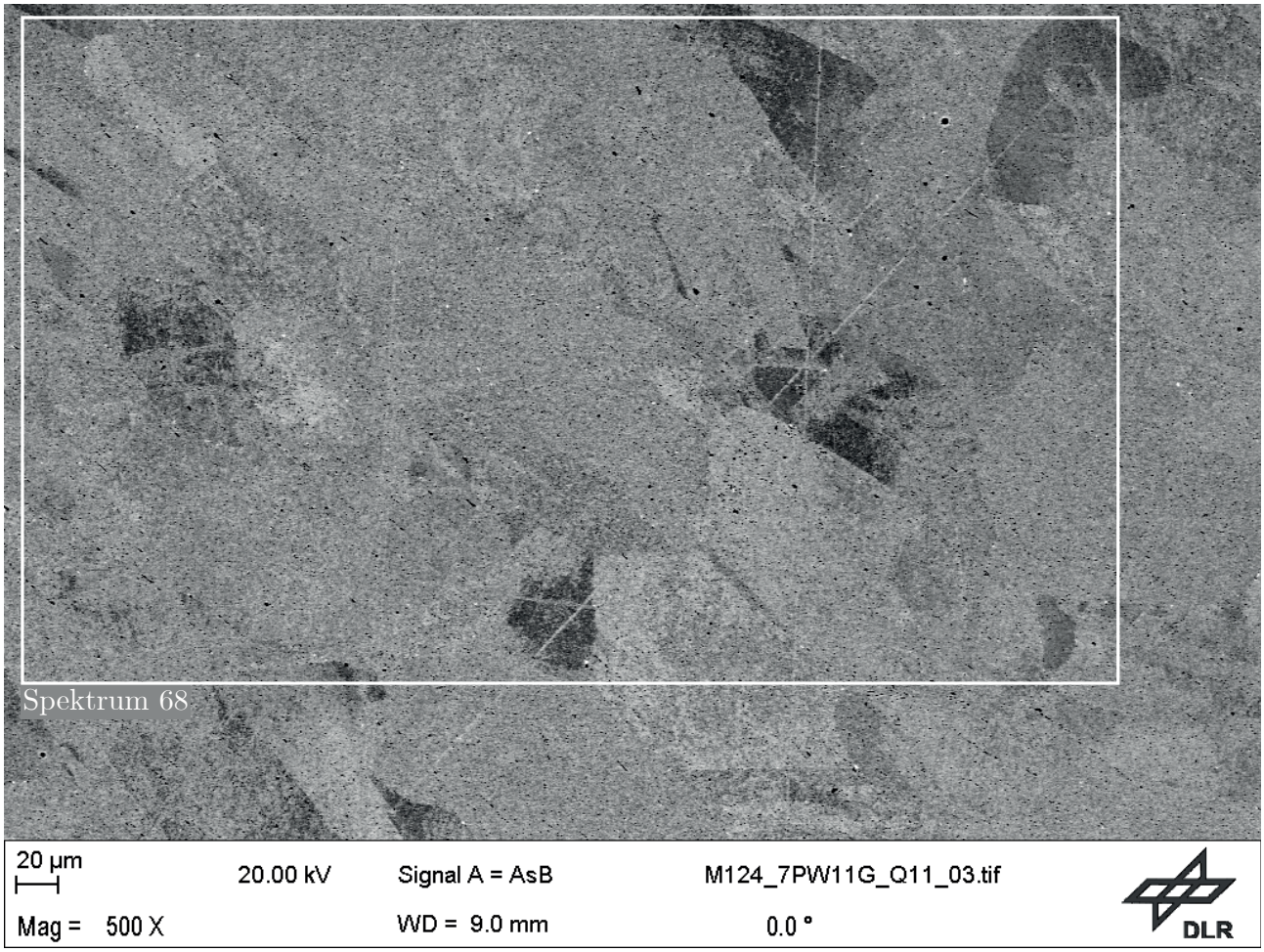

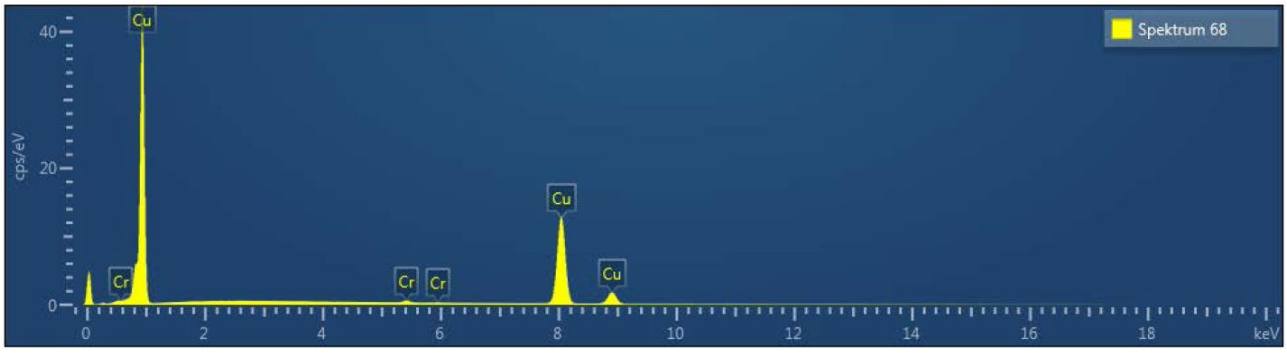

Spektrum	Cu [wt.%]	Cr [wt.%]	Zr [wt.%]
68	99.16	0.84	-

Spektrum	Cu [at.%]	Cr [at.%]	Zr [at.%]
68	98.98	1.02	-

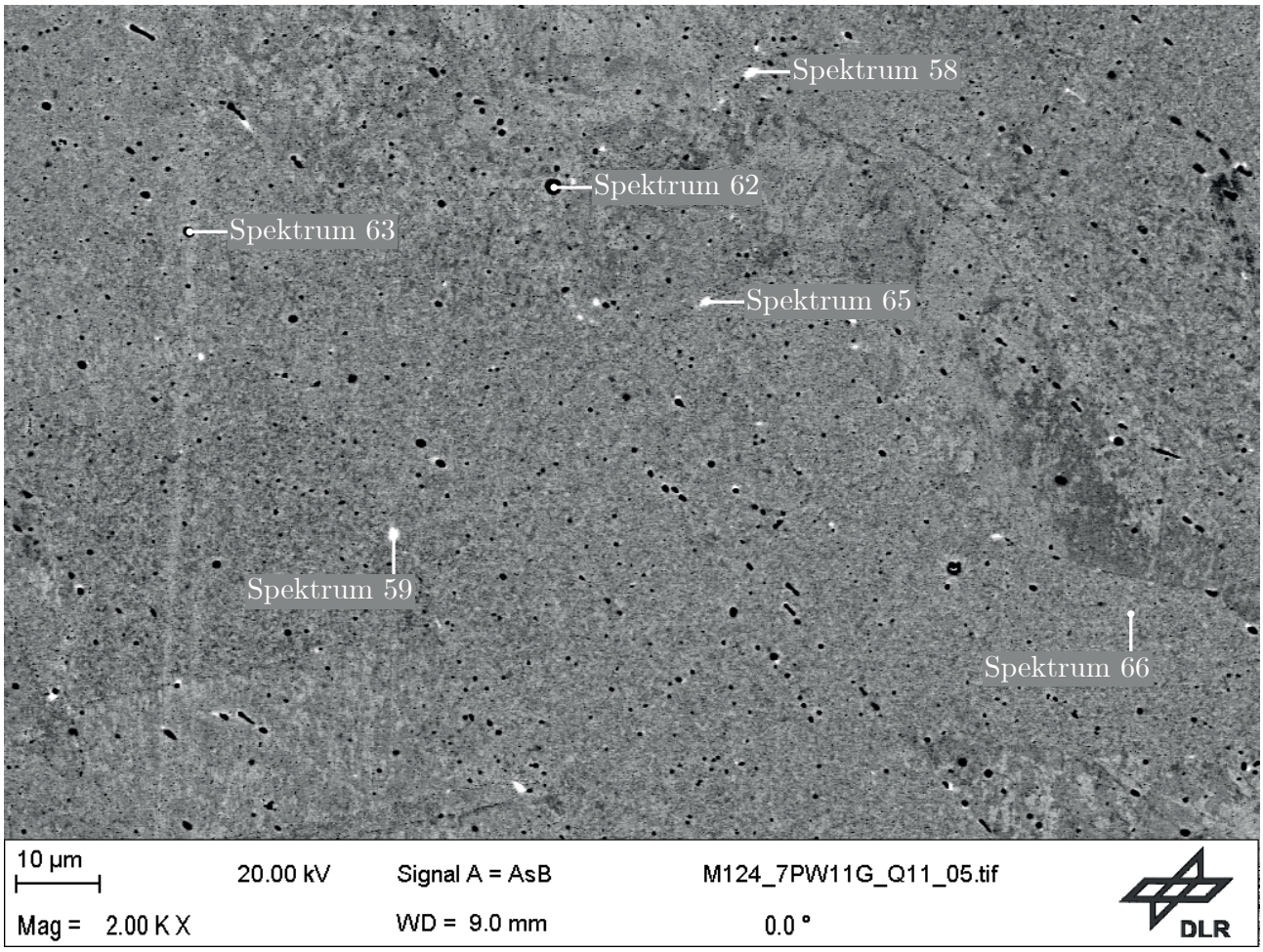
Spektrum 58
Spektrum 62
Spektrum 63
Spektrum 65
Spektrum 59
Spektrum 66
10 µm
20.00 kV
Signal A = AsB
M124_7PW11G_Q11_05.tif
Mag = 2.00 K X
WD = 9.0 mm
0.0 °
DLR

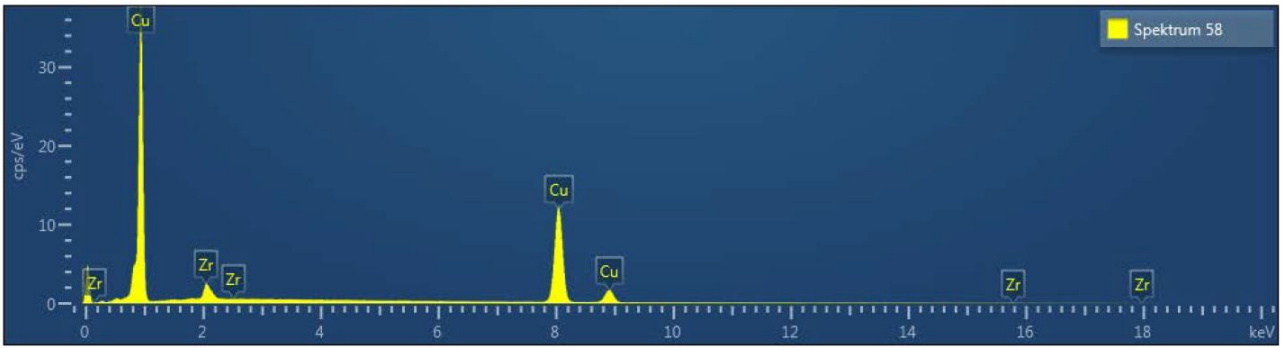
Spektrum 58
cps/eV
Cu
Zr
keV

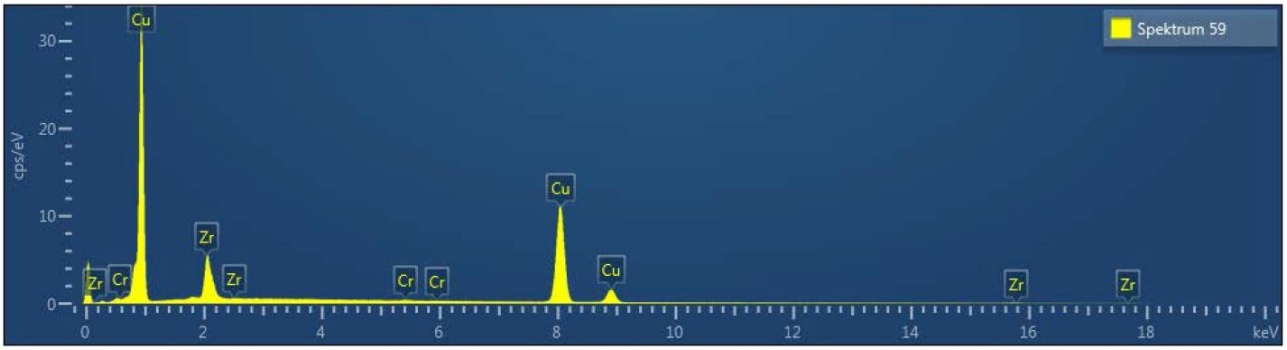
Spektrum 59
cps/eV
Cu
Zr
Cr
keV

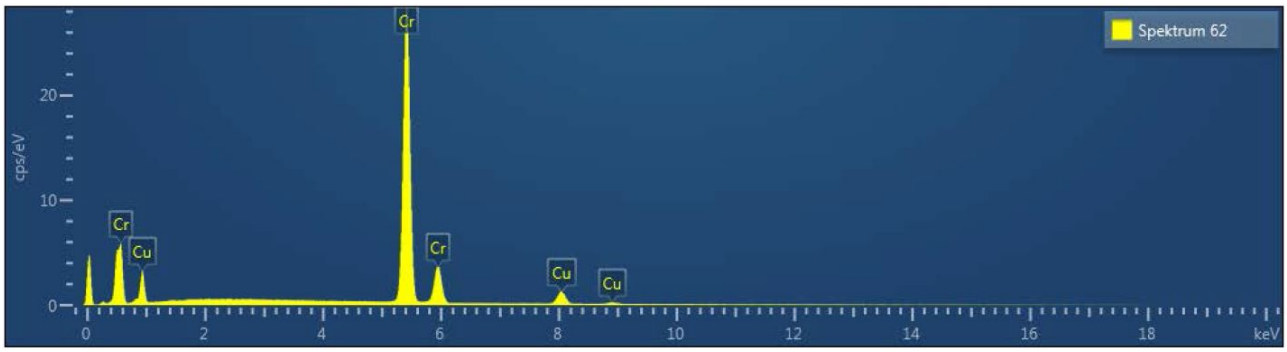
Spektrum 62
cps/eV
keV
Cr
Cu

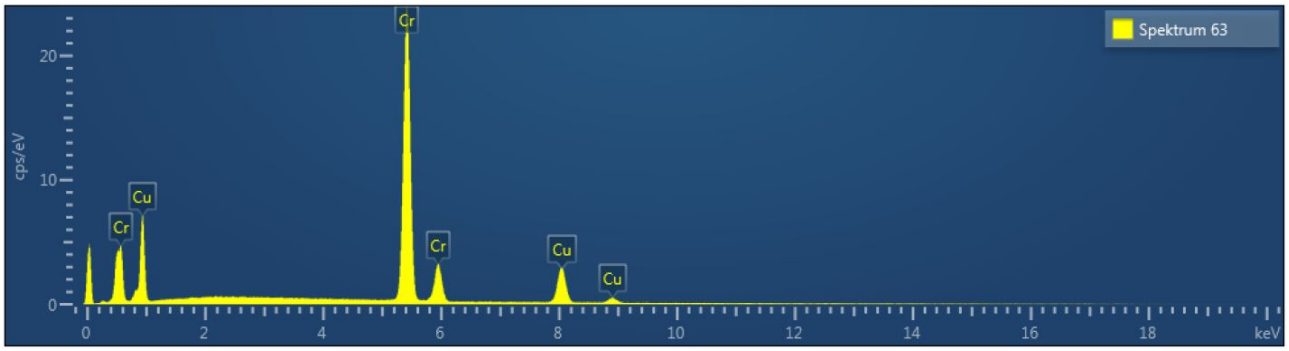
Spektrum 63
cps/eV
keV
Cr
Cu

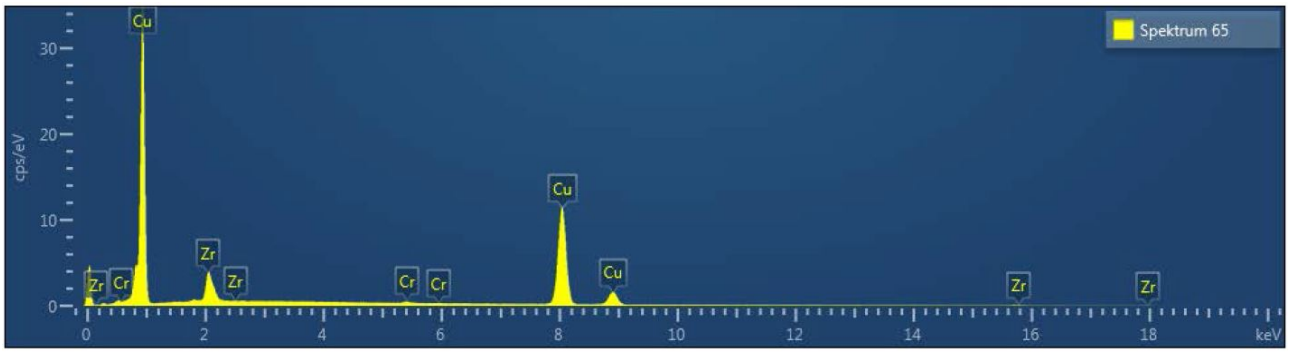
Spektrum 65
cps/eV
keV
Cu
Zr
Cr

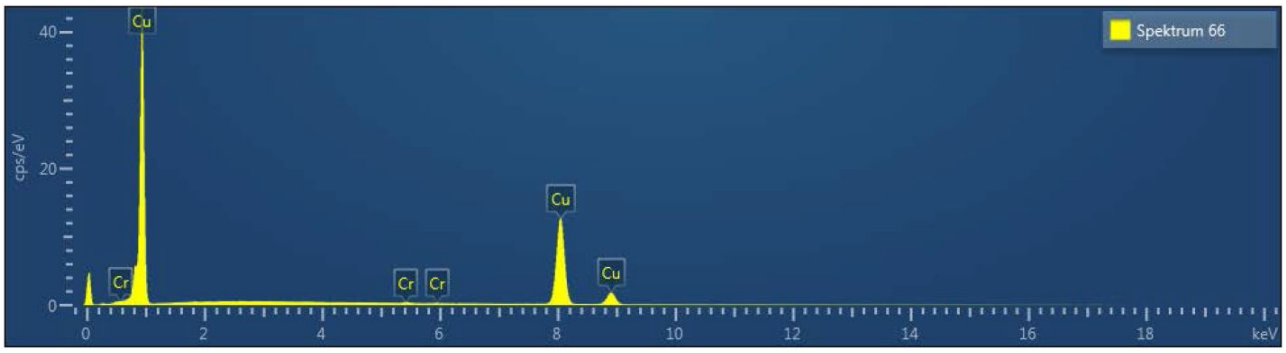
Spektrum 66
cps/eV
keV
Cu
Cr

Spektrum	**Cu** [wt.%]	**Cr** [wt.%]	**Zr** [wt.%]
58	93.27	-	6.73
59	83.78	0.19	16.04
62	10.49	89.51	-
63	25.57	74.43	-
65	87.87	0.44	11.69
66	99.60	0.40	-

Spektrum	**Cu** [at.%]	**Cr** [at.%]	**Zr** [at.%]
58	95.22	-	4.78
59	88.02	0.24	11.74
62	8.75	91.25	-
63	21.94	78.06	-
65	91.01	0.56	8.43
66	99.51	0.49	-

A.2 Calculation of Experimental Measurement Errors

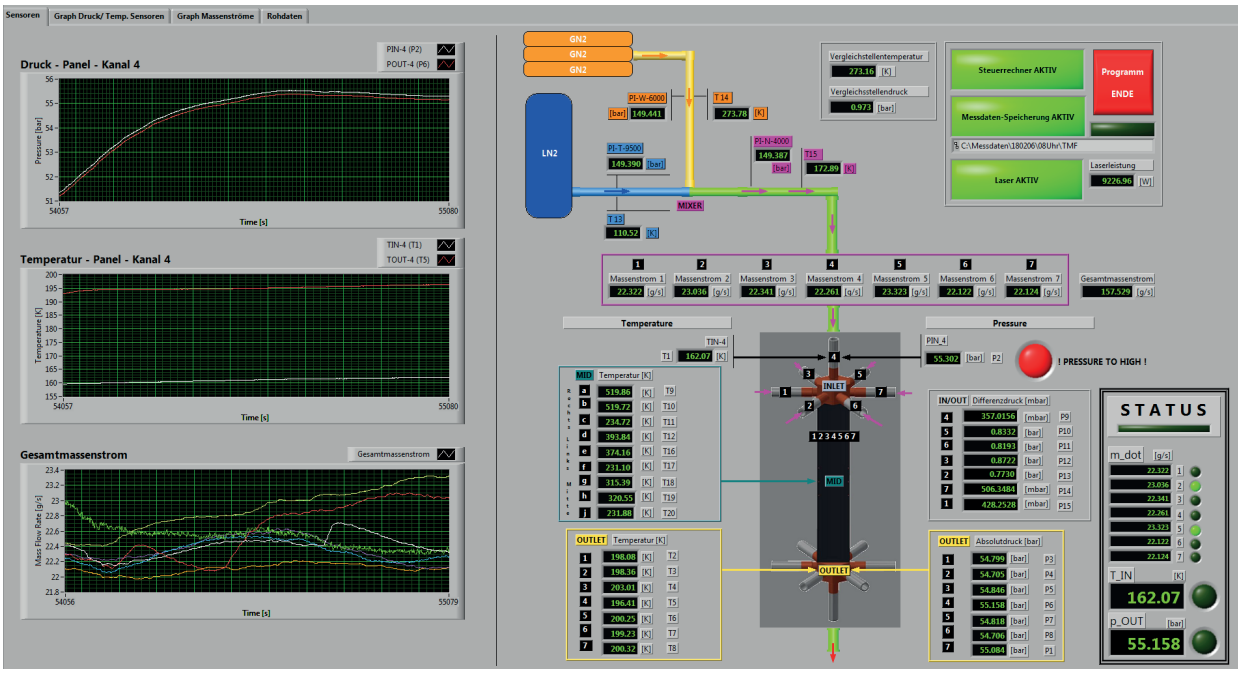

Temperature: Thermocouple Type K ($T_{1,\mathrm{IN}}, T_{i,\mathrm{OUT}}$)

Sensor	Value [K]	Accuracy [K]	Minimum [K]	Maximum [K]
$T_{1,\mathrm{IN}}$	162.07	±2.0	160.07	164.07
$T_{1,\mathrm{OUT}}$	198.08	±2.0	196.08	200.08
$T_{2,\mathrm{OUT}}$	198.36	±2.0	196.36	200.36
$T_{3,\mathrm{OUT}}$	203.01	±2.0	201.01	205.01
$T_{4,\mathrm{OUT}}$	196.41	±2.0	194.41	198.41
$T_{5,\mathrm{OUT}}$	200.25	±2.0	198.25	202.25
$T_{6,\mathrm{OUT}}$	199.23	±2.0	197.23	201.23
$T_{7,\mathrm{OUT}}$	200.32	±2.0	198.32	202.32

Temperature Difference: 2x Thermocouples Type K ($T_{i\mathrm{OUT}} - T_{1,\mathrm{IN}}$)

Sensor	Value [K]	Accuracy [K]	Minimum [K]	Maximum [K]
ΔT_1	36.01	±4.0	32.06	40.01
ΔT_2	36.29	±4.0	32.29	40.29
ΔT_3	40.94	±4.0	36.94	44.94
ΔT_4	34.34	±4.0	30.34	38.34
ΔT_5	38.18	±4.0	34.18	42.18
ΔT_6	37.16	±4.0	33.16	41.16
ΔT_7	38.25	±4.0	34.25	42.25

Outlet Pressure: Absolute Pressure Sensors ($p_{i,\mathbf{OUT}}$)

Sensor	Name	Value [bar]	Accuracy [bar]	Minimum [bar]	Maximum [bar]
$p_{1,\mathrm{OUT}}$	PI-N-5002	54.799	±0.0425 @60bar	54.757	54.842
$p_{2,\mathrm{OUT}}$	PI-N-4204	54.705	±0.0367 @60bar	54.668	54.742
$p_{3,\mathrm{OUT}}$	PI-N-5000	54.846	±0.0423 @60bar	54.804	54.889
$p_{4,\mathrm{OUT}}$	PI-N-4202	55.158	±0.1063 @60bar	55.052	55.264
$p_{5,\mathrm{OUT}}$	PI-N-4201	54.818	±0.0916 @60bar	54.726	54.910
$p_{6,\mathrm{OUT}}$	PI-N-4203	54.706	±0.0224 @60bar	54.684	54.728
$p_{7,\mathrm{OUT}}$	PI-N-4200	55.084	±0.0404 @60bar	55.044	55.124

Pressure Difference: Differential Pressure Sensors ($\mathrm{d}p_i$)

Sensor	Name	Value [mbar]	Accuracy [mbar]	Minimum [mbar]	Maximum [mbar]
$\mathrm{d}p_1$	DDPI-N-4105	357.02	±0.156 @0.4bar	356.86	357.17
$\mathrm{d}p_2$	DDPI-N-4206	833.20	±2.856 @2.0bar	830.344	836.056
$\mathrm{d}p_3$	DDPI-N-4207	819.30	±3.008 @2.0bar	816.292	822.308
$\mathrm{d}p_4$	DDPI-N-4107	872.20	±0.519 @0.4bar	871.681	872.719
$\mathrm{d}p_5$	DDPI-N-4208	773.00	±15.291 @2.0bar	757.709	788.291
$\mathrm{d}p_6$	DDPI-N-4205	506.35	±3.089 @2.0bar	503.260	509.437
$\mathrm{d}p_7$	DDPI-N-4109	428.25	±0.460 @0.4bar	427.793	428.713

Inlet Pressure: 2x Pressure Sensors ($p_{\mathrm{i},\mathbf{OUT}} - \mathrm{d}p_i$)

Sensor	Value [bar]	Accuracy [bar]	Minimum [bar]	Maximum [bar]
$p_{1,\mathrm{IN}}$	55.16	±0.043	55.11	55.20
$p_{2,\mathrm{IN}}$	55.54	±0.040	55.50	55.58
$p_{3,\mathrm{IN}}$	55.67	±0.045	55.62	55.71
$p_{4,\mathrm{IN}}$	56.03	±0.107	55.92	55.14
$p_{5,\mathrm{IN}}$	55.59	±0.107	55.48	55.70
$p_{6,\mathrm{IN}}$	55.21	±0.026	55.19	55.24
$p_{7,\mathrm{IN}}$	55.51	±0.041	55.47	55.55

Enthalpy from REFPROP Database for Nitrogen (ΔH_i)

Channel	T_{IN} [K]	p_{IN} [bar]	T_{OUT} [K]	p_{OUT} [bar]	H_{IN} [kJ kg^{-1}]	H_{OUT} [kJ kg^{-1}]	ΔH [kJ kg^{-1}]
1	162.07	55.16	198.08	54.80	68.01	125.31	57.30
2	162.07	55.54	198.36	54.71	68.26	125.70	57.45
3	162.07	55.67	203.01	54.85	68.34	133.02	64.68
4	162.07	56.03	196.41	55.16	68.58	122.89	54.31
5	162.07	55.59	200.25	54.82	68.29	128.71	60.42
6	162.07	55.21	199.23	54.71	68.04	127.06	59.02
7	162.07	55.51	200.32	55.08	68.24	128.96	60.72

Channel	$T_{min,IN}$ [K]	$p_{min,IN}$ [bar]	$T_{min,OUT}$ [K]	$p_{min,OUT}$ [bar]	$H_{min,IN}$ [kJ kg^{-1}]	$H_{min,OUT}$ [kJ kg^{-1}]	ΔH_{min} [kJ kg^{-1}]
1	160.07	55.11	196.08	54.76	64.71	122.16	50.87
2	160.07	55.50	196.36	54.67	64.96	122.55	51.01
3	160.07	55.62	201.01	54.80	65.04	139.89	58.27
4	160.07	55.92	194.41	55.05	65.25	119.70	47.80
5	160.07	55.57	198.25	54.71	64.95	125.53	53.91
6	160.07	55.19	197.23	54.68	64.76	123.92	52.60
7	160.07	55.47	198.32	55.04	64.95	125.82	54.14

Channel	$T_{max,IN}$ [K]	$p_{max,IN}$ [bar]	$T_{max,OUT}$ [K]	$p_{max,OUT}$ [bar]	$H_{max,IN}$ [kJ kg^{-1}]	$H_{max,OUT}$ [kJ kg^{-1}]	ΔH_{max} [kJ kg^{-1}]
1	164.07	55.20	200.08	54.84	71.29	128.46	63.75
2	164.07	55.58	200.36	54.74	71.54	128.84	63.88
3	164.07	55.71	205.01	54.89	71.62	136.14	71.10
4	164.07	56.14	198.41	55.26	71.90	126.08	60.84
5	164.07	55.71	202.25	54.92	71.63	131.88	66.94
6	164.07	55.24	201.23	54.73	71.32	130.19	65.43
7	164.07	55.55	202.32	55.12	71.52	132.09	67.14

Mass Flow ($\dot{m}_{i,\mathbf{IN}}$)

Sensor	**Value** [g s^{-1}]	**Accuracy** [%]	**Minimum** [g s^{-1}]	**Maximum** [g s^{-1}]
$\dot{m}_{1,IN}$	22.322	±0.1	22.300	22.344
$\dot{m}_{2,IN}$	23.036	±0.1	23.013	23.059
$\dot{m}_{3,IN}$	22.341	±0.1	22.319	22.363
$\dot{m}_{4,IN}$	22.261	±0.1	22.239	22.283
$\dot{m}_{5,IN}$	23.323	±0.1	23.300	23.346
$\dot{m}_{6,IN}$	22.122	±0.1	22.100	22.144
$\dot{m}_{7,IN}$	22.124	±0.1	22.102	22.146

Laser Area ($A_{\mathbf{Laser}} = l_{\mathbf{Width}} \cdot l_{\mathbf{Height}}$)

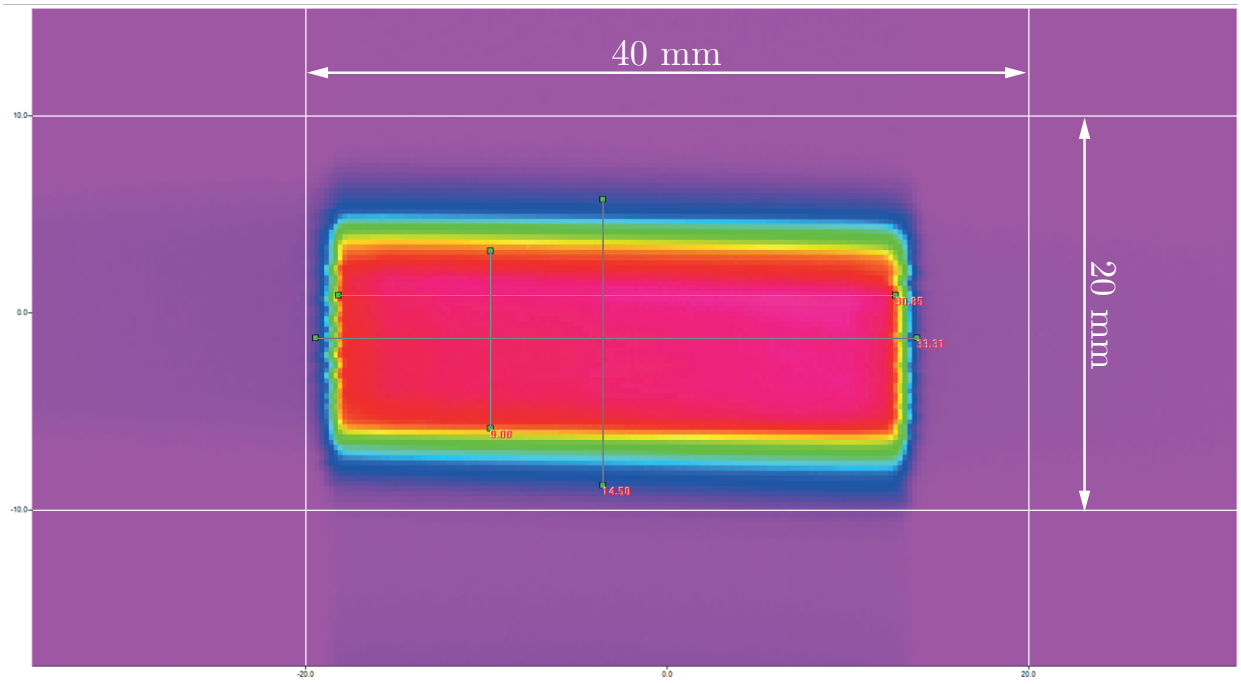

Unit	Value [mm]	Accuracy [%]	Minimum [mm]	Maximum [mm]
l_{Width}	33.31	±5.0	31.645	34.976
l_{Height}	14.50	±5.0	13.775	15.225

Unit	Value [mm^2]	Accuracy [%]	Minimum [mm^2]	Maximum [mm^2]
A_{Laser}	482.995	±10.0	435.903	532.502

Heat Flux ($q_i = Q_i \cdot A_{\mathbf{Laser}}^{-1} = \dot{m}_{i,\mathbf{IN}} \cdot \Delta H_i \cdot A_{\mathbf{Laser}}^{-1}$)

Channel	$\boldsymbol{Q_i}$ [W]	$\boldsymbol{q_i}$ [MW m^{-2}]	$\boldsymbol{Q_{i,\min}}$ [MW m^{-2}]	$\boldsymbol{Q_{i,\max}}$ [MW m^{-2}]	$\boldsymbol{\Delta Q_i}$ [MW m^{-2}]
1	1279.140	2.648	1134.340	1424.428	145.044
2	1323.303	2.740	1173.960	1472.919	149.489
3	1445.061	2.992	1300.441	1589.944	144.751
4	1209.062	2.503	1063.012	1355.602	146.295
5	1409.199	2.918	1255.969	1562.686	153.359
6	1305.596	2.703	1162.498	1448.912	143.207
7	1343.414	2.781	1200.110	1486.979	143.435
$\sum$	9314.774	**19.285**			

Channel	$\boldsymbol{Q_{i,\min}A_{\min}^{-1}}$ [MW m^{-2}]	$\boldsymbol{Q_{i,\min}A_{\max}^{-1}}$ [MW m^{-2}]	$\boldsymbol{Q_{i,\max}A_{\min}^{-1}}$ [MW m^{-2}]	$\boldsymbol{Q_{i,\max}A_{\max}^{-1}}$ [MW m^{-2}]
1	2.602	2.130	3.268	2.675
2	2.693	2.205	3.379	2.766
3	2.983	2.442	3.647	2.986
4	2.439	2.996	3.110	2.546
5	2.881	2.359	3.585	2.935
6	2.667	2.183	3.324	2.721
7	2.753	2.254	3.411	2.792
$\sum$	19.019	15.569	23.724 s	19.421
$\mathrm{TOL_{REF}}$		(**−3.717**)	(**+4.439**)	

Emissivity Coefficient

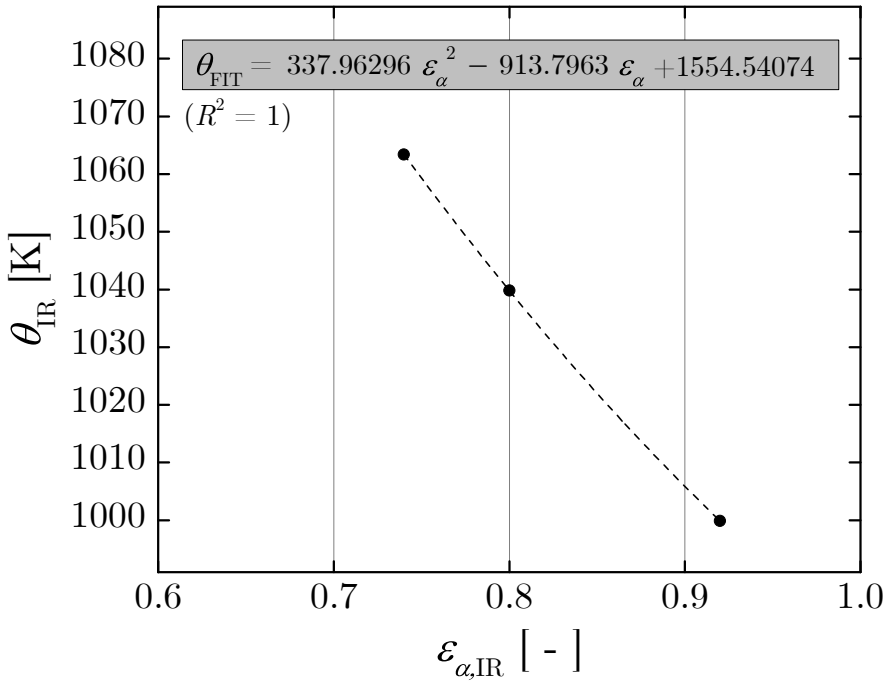

A.3 APDL Commands in ANSYS Mechanical

General Settings (Execution: All Steps)

```
!
! Commands inserted into this file will be executed just prior to the ANSYS SOLVE command.
! These commands may supersede command settings set by Workbench.
! Active UNIT system in Workbench when this object was created: Metric (m, kg, N, s, V, A)
! NOTE: Any data that requires units (such as mass) is assumed to be in the consistent solver unit system.
! See Solving Units in the help system for more information.
!
BCSOPTION,,INCORE
OUTRES,SVAR,ALL
OUTRES,ALL,ALL ! LAST
NEQIT,30
NLGEOM,ON
SOLCONTROL,ON,OFF
NROPT,UNSYM
LNSRCH,ON
!
```

2G TMF Panel (Execution: Last Step)

```
!
SOLVe
!
/com,
/com,*************************************************
/com,*********** FINISHED SOLVE FOR LS 3 ************
/com,*************************************************
/com,
/com,
/com,************* SOLVE FOR LS 4 OF i ************** [APDL SNIPPET]
/com,

SOLCONTROL,ON,OFF

 strt_cycle = 1
  end_cycle = 500
   time_ini = 2
 time_cycle = 250
   sub_fact = 2

*DO,i_cycle,strt_cycle,end_cycle,1

  /com, * ---------------------------------*
  /com, * CYCLE *
  output_cycle = i_cycle
  /com, * ---------------------------------*

  *IF,i_cycle,GE,100,THEN
    sub_fact = 2
  *ENDIF

  OUTRES,SVAR,ALL
  OUTRES,ALL,LAST
  !
  *IF,i_cycle,LE,5,THEN
    OUTRES,ALL,ALL
  *ELSEIF,i_cycle,EQ,10,OR,i_cycle,EQ,50,THEN
    OUTRES,ALL,ALL
  *ELSEIF,i_cycle,EQ,100,OR,i_cycle,EQ,150,THEN
    OUTRES,ALL,ALL
  *ELSEIF,i_cycle,EQ,200,OR,i_cycle,EQ,250,THEN
    OUTRES,ALL,ALL
  *ELSEIF,i_cycle,EQ,300,OR,i_cycle,EQ,350,THEN
    OUTRES,ALL,ALL
  *ELSEIF,i_cycle,EQ,400,OR,i_cycle,EQ,450,THEN
    OUTRES,ALL,ALL
  *ENDIF

  ALLSEL,ALL
  BFDELE,ALL,TEMP

  /NOPR

  BF, 1,TEMP,-69.499
  BF, 2,TEMP,-69.394
  [...]
  BF, 64960,TEMP,-45.9

  /GOPR

  TIME,time_ini+time_cycle*(i_cycle-1)+2
```

```
  NSUBST,8*sub_fact,10000,8*sub_fact
  SOLVE

  /NOPR

  BF, 1,TEMP,-69.499
  BF, 2,TEMP,-69.394
  [...]
  BF, 64960,TEMP,-45.9

  /GOPR

  TIME,time_ini+time_cycle*(i_cycle-1)+202
  NSUBST,256*sub_fact,10000,8*sub_fact
  SOLVE

  ALLSEL,ALL
  BFDELE,ALL,TEMP
  TUNIF,-113.15 ! T = 160 K
  TIME,time_ini+time_cycle*(i_cycle-1)+212
  NSUBST,32*sub_fact,10000,32*sub_fact
  SOLVE

  ALLSEL,ALL
  TUNIF,-113.15 ! T = 160 K
  TIME,time_ini+time_cycle+time_cycle*(i_cycle-1)
  NSUBST,4,10000,4
  SOLVE

*ENDDO

/com,
/com,************* FINISHED SOLVE i ************** [APDL SNIPPET]
/com,

FINIsh
!
```

3G TMF Panel (Execution: Last Step)

```
!
SOLVe
!
/com,
/com, ************************************************
/com, ************* FINISHED SOLVE FOR LS 3 **************
/com, ************************************************
/com,
/com, ************** SOLVE FOR LS 4 of i ***************** [APDL Snippet]
/com,

SOLCONTROL,ON,OFF

 strt_cycle = 1
  end_cycle = 500
   time_ini = 2
 time_cycle = 220
   sub_fact = 2

*DO,i_cycle,strt_cycle,end_cycle,1

  /com,
  /com, *-------------------------*
  /com, * CYCLE *
  output_cycle = i_cycle
  /com, *-------------------------*
  /com,

  *IF,i_cycle,GE,100,THEN
    sub_fact = 2
  *ENDIF

  OUTRES,ALL,LAST
  OUTRES,SVAR,ALL
  !
  *IF,i_cycle,LE,11,THEN
    OUTRES,ALL,ALL
  *ELSEIF,i_cycle,EQ,50,OR,i_cycle,EQ,100,THEN
    OUTRES,ALL,ALL
  *ELSEIF,i_cycle,EQ,150,OR,i_cycle,EQ,200,THEN
    OUTRES,ALL,ALL
  *ELSEIF,i_cycle,EQ,250,OR,i_cycle,EQ,300,THEN
    OUTRES,ALL,ALL
  *ELSEIF,i_cycle,EQ,350,OR,i_cycle,EQ,400,THEN
    OUTRES,ALL,ALL
  *ELSEIF,i_cycle,EQ,450,OR,i_cycle,EQ,500,THEN
    OUTRES,ALL,ALL
  *ENDIF

  ALLSEL,ALL
```

```
  BFDELE,ALL,TEMP

  /NOPR

  BF, 1,TEMP,-53.989189
  BF, 2,TEMP,-54.123436

  [...]
  BF, 117861,TEMP,-108.80004

  /GOPR

  TIME,time_ini+time_cycle*(i_cycle-1)+10
  NSUBST,16*sub_fact,10000,16*sub_fact
  SOLVE

  /NOPR

  BF, 1,TEMP,-53.989189
  BF, 2,TEMP,-54.123436
  [...]
  BF, 117861,TEMP,-108.80004

  /GOPR

  TIME,time_ini+time_cycle*(i_cycle-1)+209.9
  NSUBST,256*sub_fact,10000,8*sub_fact
  SOLVE

  ALLSEL,ALL
  BFDELE,ALL,TEMP
  TUNIF,-113.15 ! T = 160 K
  TIME,time_ini+time_cycle*(i_cycle-1)+219.9
  NSUBST,32*sub_fact,10000,16*sub_fact
  SOLVE

  ALLSEL,ALL
  TUNIF,-113.15 ! T = 160 K
  TIME,time_ini+time_cycle*(i_cycle-1)+time_cycle
  NSUBST,4,10000,4
  SOLVE

*ENDDO

/com,
/com, ************************************************
/com, ************ FINISHED SOLVE FOR LS i ************
/com, ************************************************ [APDL Snippet]
/com,

FINIsh
!
```

Rocket Chamber Segment (Execution: Last Step)

```
!
!================================!
! !
! Import Transient Thermal Field !
! ~~~~~~~~~~~~~~~~~~~~~~~~~~~~~~ !
! !
! via Imported Body Temperature: !
! "_lv_138__0" !
! "_lv_138__SELECTION" !
! !
!================================!

!------------!
! Parameters !
!------------!

 end_cycle = 500
time_steps = 1709 ! see transient thermal analysis
   n_steps = 2

   time_p1 = 10
   time_p2 = 10.1
   time_p3 = 11
   time_p4 = 610
   time_p5 = 612
   time_p6 = 614
time_cycle = 1000
load_steps = 7

!-------------------------!
! Get Value from Database !
!-------------------------!

*GET, nr_node, node, 0, NUM, MAX ! Max. Nr. of Nodes

```

```
!------------------!
! Dimension Arrays !
!------------------!

*DIM, temp_array, TABLE, time_steps, nr_node, , TIME, NODE ! t updated array for cycling
*DIM, time_array, ARRAY, time_steps, 1 ! manually stored for cycling
!
*DIM, pres_array_hot, TABLE, load_steps + 1,1,1,TIME,
*DIM, pres_array_cold, TABLE, load_steps + 1,1,1,TIME,

!--------------------------------------!
! Store Pressure !
!--------------------------------------!

 pres_array_hot(1,1,1) = 0 ! Units: Pa
 pres_array_hot(2,1,1) = 0
 pres_array_hot(3,1,1) = 10e6
 pres_array_hot(4,1,1) = 10e6
 pres_array_hot(5,1,1) = 10e6
 pres_array_hot(6,1,1) = 0
 pres_array_hot(7,1,1) = 0
 pres_array_hot(8,1,1) = 0
 !
 pres_array_cold(1,1,1) = 20e6 ! Units: Pa
 pres_array_cold(2,1,1) = 20e6
 pres_array_cold(3,1,1) = 20e6
 pres_array_cold(4,1,1) = 20e6
 pres_array_cold(5,1,1) = 20e6
 pres_array_cold(6,1,1) = 20e6
 pres_array_cold(7,1,1) = 0
 pres_array_cold(8,1,1) = 0

!--------------------------------------!
! Store Time Steps Manually For Cycles !
!--------------------------------------!

 time_array( 1) = 0.0000000000000000
 time_array( 2) = 0.1000000000000000
 [...]
 time_array(1709) = 1000.000000000000000

!-----------------------------------------!
! Copy Tables of Imported Body Temperature !
!-----------------------------------------!

*TOPER,temp_array,_lv_138__0,ADD,_lv_138__0,1,0,0


!------------!
! COUPLED BC ! <----- IMPORTANT
!------------!

CSYS,0
ASEL,ALL
NSEL,ALL
ASEL,S,LOC,Z,0.1
NSLA,S,1
CP,1,UZ,ALL
NSEL,ALL
ASEL,ALL


!------------------!
! Cycles - DO LOOP !
!------------------!

*DO,i_cyc,1,end_cycle,1
  !
  !----------------------------!
  ! Update Time (row, col = 0) !
  !----------------------------!
  !
  *DO,i_row,1,time_steps,1
    temp_array(i_row,0,1)= time_array(i_row)+time_cycle*(i_cyc-1)
  *ENDDO
  !
  pres_array_hot(1,0,1) = 0 + time_cycle*(i_cyc-1)
  pres_array_hot(2,0,1) = time_p1 + time_cycle*(i_cyc-1)
  pres_array_hot(3,0,1) = time_p2 + time_cycle*(i_cyc-1)
  pres_array_hot(4,0,1) = time_p3 + time_cycle*(i_cyc-1)
  pres_array_hot(5,0,1) = time_p4 + time_cycle*(i_cyc-1)
  pres_array_hot(6,0,1) = time_p5 + time_cycle*(i_cyc-1)
  pres_array_hot(7,0,1) = time_p6 + time_cycle*(i_cyc-1)
  pres_array_hot(8,0,1) = time_cycle + time_cycle*(i_cyc-1)
  !
  pres_array_cold(1,0,1) = 0 + time_cycle*(i_cyc-1)
  pres_array_cold(2,0,1) = time_p1 + time_cycle*(i_cyc-1)
  pres_array_cold(3,0,1) = time_p2 + time_cycle*(i_cyc-1)
  pres_array_cold(4,0,1) = time_p3 + time_cycle*(i_cyc-1)
  pres_array_cold(5,0,1) = time_p4 + time_cycle*(i_cyc-1)
  pres_array_cold(6,0,1) = time_p5 + time_cycle*(i_cyc-1)
  pres_array_cold(7,0,1) = time_p5 + time_cycle*(i_cyc-1)
  pres_array_cold(8,0,1) = time_cycle + time_cycle*(i_cyc-1)
  !
  BF,_lv_138__SELECTION,TEMP,%temp_array% ! "_LV_39__SELECTION" generated by "Imported Body Load" / Block of all nodes
  !BFDELE,ALL,TEMP
  !
```

```
  ESEL,S,TYPE,,8
  NSLE
  SF,ALL,PRES,%pres_array_hot%
  ESEL,S,TYPE,,9
  NSLE
  SF,ALL,PRES,%pres_array_cold%
  ESEL,S,TYPE,,10
  NSLE
  SF,ALL,PRES,%pres_array_cold%
  ESEL,S,TYPE,,11
  NSLE
  SF,ALL,PRES,%pres_array_cold%
  NSEL,ALL
  ESEL,ALL
  !
  SBCTRAN
  !
  ! -------
  ! SOLVING
  ! -------
  !
  TIME,time_cycle*(i_cyc-1)+time_p1
  NSUBST,100*n_steps,10000,100
  SOLVe
  !
  TIME,time_cycle*(i_cyc-1)+time_p2
  NSUBST,100*n_steps,10000,100
  SOLVe
  !
  TIME,time_cycle*(i_cyc-1)+time_p3
  NSUBST,200*n_steps,10000,100
  SOLVe
  !
  TIME,time_cycle*(i_cyc-1)+time_p4
  NSUBST,100*n_steps,10000,10
  SOLVe
  !
  TIME,time_cycle*(i_cyc-1)+time_p5
  NSUBST,100*n_steps,10000,100
  SOLVe
  !
  TIME,time_cycle*(i_cyc-1)+time_p6
  NSUBST,100*n_steps,10000,100
  SOLVe
  !
  TIME,time_cycle*(i_cyc-1)+time_cycle
  NSUBST,100*n_steps,10000,10
  SOLVe
  !
*ENDDO

FINIsh

/POST1
COMBINE,RST ! while using distributed solution with i-cores
FINIsh
!
```

A.4 Heat Transfer Along Center Cooling Channel Wall

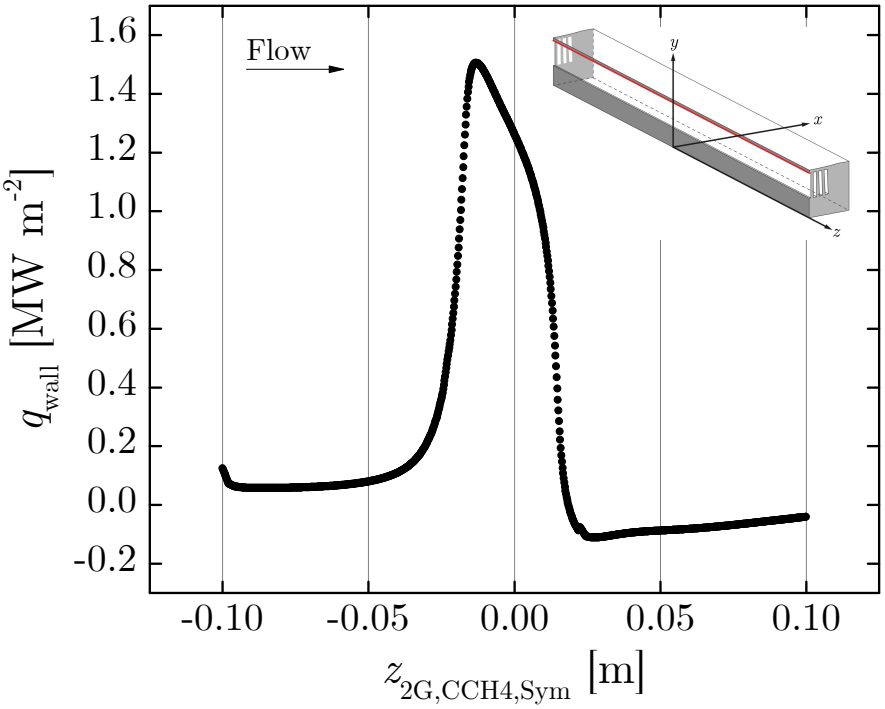

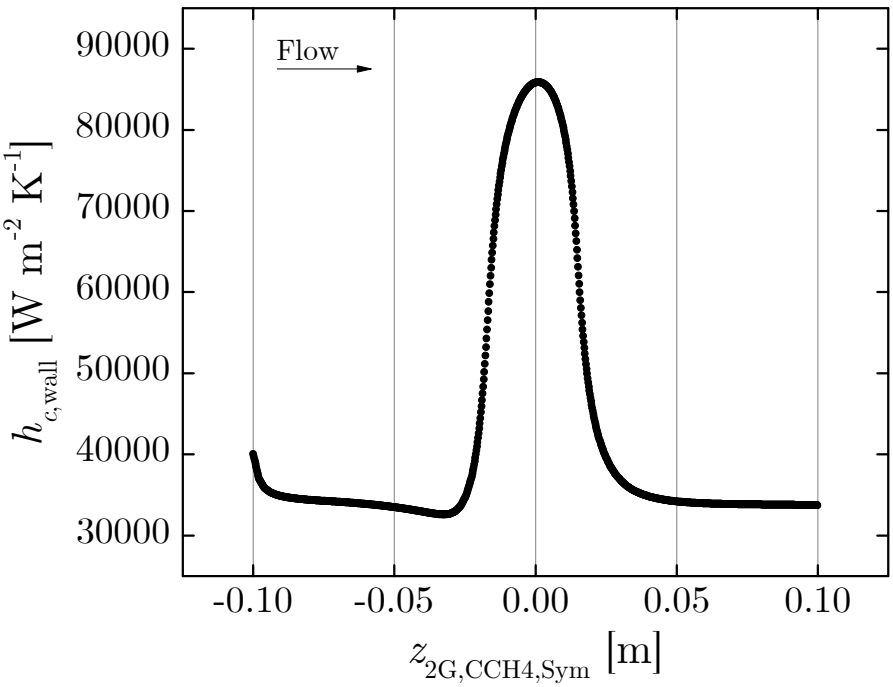

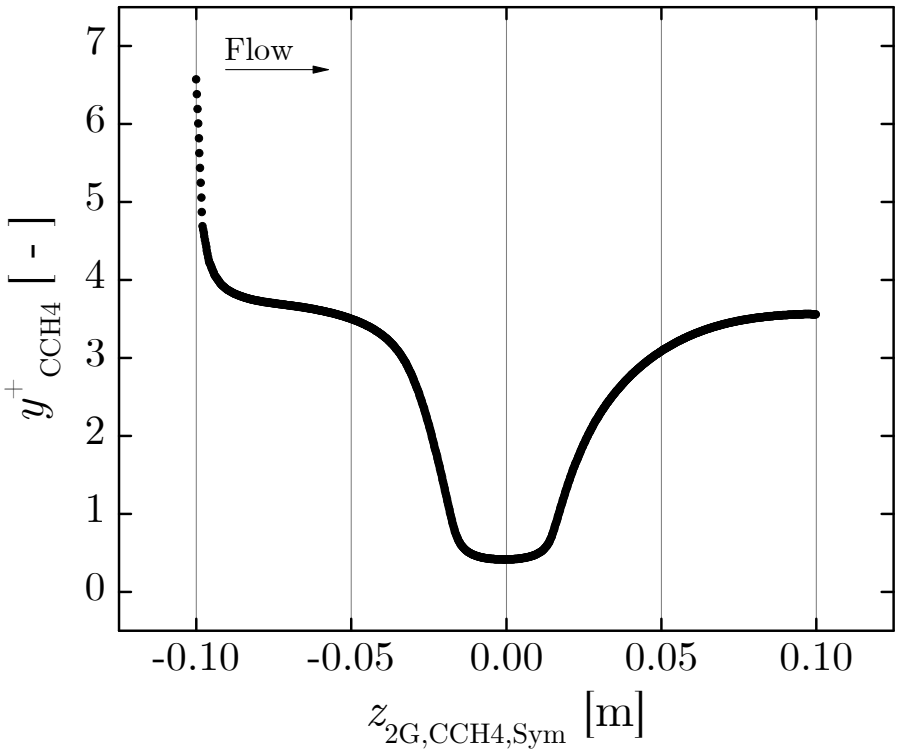
Flow
7
6
5
4
3
2
1
0
-0.10
-0.05
0.00
0.05
0.10
y^+_{CCH4} [-]
$z_{2G,CCH4,Sym}$ [m]

Bibliography

[1] Carden, A. E., Harman, D. G., and Franco-Ferreira, E. A., "Thermal fatigue analysis of a cryogenically cooled rocket nozzle," Tech. rep., Oak Ridge National Labaratory, 1966.

[2] Miller, R. W., "Cyclic fatigue analysis of rocket thrust chambers: Volume 1: OFHC copper chamber low cycle fatigue," Tech. rep., NASA-CR-134641-VOL-1, NASA Lewis Research Center, 1974.

[3] Kasper, H. J., "Graphical method for predicting life of a rocket thrust chamber with half-hard zirconium-copper liner and electroformed nickel closeout," Tech. rep., NASA-TM-X-3499, NASA Lewis Research Center, 1977.

[4] Esposito, J. J. and Zabora, R. F., "Thrust chamber life prediction. Volume 1: Mechanical and physical properties of high performance rocket," Tech. rep., NASA-CR-134806, NASA Lewis Research Center, 1975.

[5] Armstrong, W. H. and Brogren, E. W., "Thrust chamber life prediction. Volume 2: Plug nozzle centerbody and cylinder life analysis," Tech. rep., NASA-CR-134822, NASA Lewis Research Center, 1975.

[6] Armstrong, W. H. and Brogren, E. W., "Three dimensional thrust chamber life prediction," Tech. rep., NASA-CR-134979, NASA Lewis Research Center, 1976.

[7] Quentmeyer, R. J., "Experimental fatigue life investigation of cylindrical thrust chambers," Tech. rep., NASA-TM-X-13665, NASA Lewis Research Center, 1977.

[8] Hannum, N. P. and Price, R. G., "Some effects of thermal-cycle-induced deformation in rocket thrust chambers," Tech. rep., NASA-TP-1834, NASA Lewis Research Center, 1981.

[9] Armstrong, W. H. and Brogren, E. W., "Structural analysis of cylindrical thrust chambers. Volume 1," Tech. rep., NASA-CR-159522, NASA Lewis Research Center, 1979.

[10] Badlani, M. L., Porowski, J. S., Odonnell, W. J., and Peterson, D. B., "Development of a simplified procedure for rocket engine thrust chamber life prediction with creep," Tech. rep., NASA-CR-168261, NASA Lewis Research Center, 1984.

[11] Dai, X. and Ray, A., "Life prediction of the thrust chamber wall of a reusable rocket engine," *Journal of Propulsion and Power*, Vol. 11, No. 6, 1995, pp. 1279–1287.

[12] Butler, D. T. and Pindera, M.-J., "Analysis of factors affecting the performance of RLV thrust cell liners," Tech. rep., NAG3-2359, NASA Glenn Research Center, 2004.

[13] Robinson, D. N. and Swindeman, R. W., "Unified creep-plasticity constitutive equations for 2-1/4 Cr-1 Mo steel at elevated temperature," Tech. rep., Oak Ridge National Laboratory, 1982.

[14] Norton, F. H., *The Creep of Steel at High Temperatures*, McGraw-Hill Book Company, 1929.

[15] Kuhl, D., Riccius, J. R., and Haidn, O. J., "Thermomechanical analysis and optimization of cryogenic liquid rocket engines," *Journal of Propulsion and Power*, Vol. 18, No. 4, 2002, pp. 835–846.

[16] Quentmeyer, R. J., "Rocket combustion chamber life-enhancing design concepts," *AIAA Paper 90-2116*, 1990.

[17] Popp, M. and Schmidt, G., "Rocket engine combustion chamber design concepts for enhanced life," *AIAA Paper 96-3303*, 1996.

[18] Riccius, J. R., Zametaev, E. B., and Haidn, O. J., "Comparison of 2d and 3d structural FE-analyses of LRE combustion chamber walls," *AIAA Paper 2006-4365*, 2006, p. 4365.

[19] Schwarz, W., Wiedmann, D., Schwub, S., Höppel, H., and Göken, M., "Assessment of different continuum damage models for life-time prediction of high-thrust cryogenic combustion chambers," *European Conference for Aeronautics and Space Sciences (EUCASS)*, 2011.

[20] Schwarz, W., Schwub, S., Quering, K., Wiedmann, D., Höppel, H., and Göken, M., "Life prediction of thermally highly loaded components: modelling the damage process of a rocket combustion chamber hot wall," *Council of European Aerospace Societies (CEAS) Space Journal*, Vol. 1, No. 1–4, 2011, pp. 83–97.

[21] Schwarz, W., *Modelling of Viscoplasticity, Ageing and Damage for Life Prediction of Rocket Combustion Chambers*, Ph.D. thesis, Friedrich-Alexander-Universität Erlangen-Nürnberg, 2013.

[22] Tini, V., *Lifetime Prediction of a Typical Rocket Combustion Chamber by means of Viscoplastic Damage Modeling*, Ph.D. thesis, RWTH Aachen, 2014.

[23] Schwub, S., *Mikrostruktur, mechanische Eigenschaften und Schädigungsmechanismen von Kupfer-Silber-Zirkonium Legierungen für Hochtemperaturanwendungen*, Ph.D. thesis, Friedrich-Alexander-Universität Erlangen-Nürnberg, 2012.

[24] Tini, V., Vladimirov, I. N., and Reese, S., "Lifetime prediction of rocket combustion chamber wall by means of viscoplasticity coupled with ductile isotropic damage," *ASME Conference on Engineering Systems Design and Analysis*, American Society of Mechanical Engineers, 2012, pp. 497–502.

[25] Tini, V., Vladimirov, I. N., and Reese, S., "Influence of anisotropic damage on the lifetime prediction of regeneratively cooled nozzle structure," *Space Propulsion Conference*, 3AF (Association Aéronautique et Astronautique de France) Paper 2012-2359070, 2012, pp. 1–8.

[26] Kowollik, D., Tini, V., Reese, S., and Haupt, M., "3D fluid-structure interaction analysis of a typical liquid rocket engine cycle based on a novel viscoplastic damage model," *International Journal for Numerical Methods in Engineering*, Vol. 94, No. 13, 2013, pp. 1165–1190.

[27] Riccius, J. R., Bouajila, W., and Zametaev, E. B., "Comparison of finite element analysis and experimental results of a combustion chamber type TMF panel test," *AIAA Paper 2013-3846*, 2013.

[28] Thiede, R. G., Riccius, J. R., and Reese, S., "Life prediction of rocket combustion-chamber-type thermomechanical fatigue panels," *Journal of Propulsion and Power*, Vol. 33, No. 6, 2017, pp. 1529–1542.

[29] KEYENCE Corporation, *User Manual: Digital Microscope VHX-5000*, April 2014, Doc.-No. 96M13026.

[30] KEYENCE Corporation, *Data Sheet: High-Resolution Zoom Lens VH-Z500R*, June 2018.

[31] KME Germany GmbH & Co. KG, *Data Sheet: ELBRODUR-Alloys*, 2015, Doc.-No. 0315.000.0100.

[32] Ellis, D. L., Keller, D. J., and Nathal, M., "Thermophysical properties of GRCop-84," Tech. rep., NASA-CR-2000-210055, NASA Glenn Research Center, 2000.

[33] Dies, K., *Kupfer und Kupferlegierungen in der Technik*, Springer, 1967.

[34] de Groh III, H. C., Ellis, D. L., and Loewenthal, W. S., "Comparison of GRCop-84 to other Cu alloys with high thermal conductivities," *Journal of Materials Engineering and Performance*, Vol. 17, No. 4, 2008, pp. 594–606.

[35] Watanabe, C., Monzen, R., and Tazaki, K., "Mechanical properties of Cu–Cr system alloys with and without Zr and Ag," *Journal of Materials Science*, Vol. 43, No. 3, 2008, pp. 813–819.

[36] Shangina, D. V., Bochvar, N. R., Gorshenkov, M. V., Yanar, H., Purcek, G., and Dobatkin, S. V., "Influence of microalloying with zirconium on the structure and properties of Cu–Cr alloy after high pressure torsion," *Materials Science and Engineering: A*, Vol. 650, 2016, pp. 63–66.

[37] Bochvar, N. R., "Cr-Cu-Zr (Chromium-Copper-Zirconium): Datasheet from Landolt-Börnstein - Group IV Physical Chemistry, Volume 11C2: Non-Ferrous Metal Systems, Part 2," 2007, Copyright 2007 Springer.

[38] Davis, J. R., *Copper and Copper Alloys*, ASM international, 2001.

[39] Holzwarth, U. and Stamm, H., "The precipitation behaviour of ITER-grade Cu–Cr–Zr alloy after simulating the thermal cycle of hot isostatic pressing," *Journal of Nuclear Materials*, Vol. 279, No. 1, 2000, pp. 31–45.

[40] Zeng, K. J., Hämäläinen, M., and Lilius, K., "Phase relationships in Cu-rich corner of the Cu-Cr-Zr phase diagram," *Scripta Metallurgica et Materialia*, Vol. 32, No. 12, 1995, pp. 2009–2014.

[41] Ellis, D. L., "Observations of a cast Cu-Cr-Zr alloy," Tech. rep., NASA-TM-2006-213968, NASA Glenn Research Center, 2006.

[42] Kanaya, K. and Okayama, S., "Penetration and energy–loss theory of electrons in solid targets," *Journal of Physics D: Applied Physics*, Vol. 5, No. 1, 1972, pp. 43.

[43] Goldstein, J. I., Newbury, D. E., Michael, J. R., Ritchie, N. W. M., Scott, J. H. J., and Joy, D. C., *Scanning Electron Microscopy and X-ray Microanalysis*, Springer, 4th ed., 2017.

[44] Zeng, K. J. and Hämäläinen, M., "A theoretical study of the phase equilibria in the Cu–Cr–Zr system," *Journal of Alloys and Compounds*, Vol. 220, No. 1-2, 1995, pp. 53–61.

[45] Schultrich, B. and Zimmer, O., *Jahrbuch Oberflächentechnik*, chap. Vakuumbogenabscheidung dünner Schichten, Leuze Verlag, 1st ed., 2009, pp. 118–140.

[46] Anders, A., *Cathodic Arcs: From Fractal Spots to Energetic Condensation*, Springer, 2008.

[47] Mesyats, G. A., *Cathode Phenomena in a Vacuum Discharge: The Breakdown, the Spark, and the Arc*, Nauka, Moscow (Russia), 2000.

[48] Ferrandon, O., James, P., Girard, P., Terhardt, M., Blasi, R., Johnsson, R., and Damgaard, T., "Vulcain 2 nozzle extension: Integrated European team and advanced computational model to the service of nozzle design," *AIAA Paper 2005-4535*, 2005, p. 4535.

[49] Riccius, J. R., Gernoth, A., Suslova, E., Böhm, C., Zametaev, E. B., Haidn, O. J., Brummer, L., Mewes, B., Knab, O., Terhardt, M., and Hagemann, G., "TMF: Laser application for a close-to-reality simulation of thermo-mechanical fatigue processes in rocket engines," *European Conference for Aeronautics and Space Sciences (EUCASS)*, 2007, pp. 1–5.

[50] Calvo, J. B. and Hannemann, K., "Numerical Simulation of Liquid Rocket Engine Cooling Channels," *AIAA Paper 2009-5302*, 2009.

[51] Gernoth, A., Riccius, J. R., Haidn, O. J., Brummer, L., Mewes, B., and Quering, K., "TMF panel tests: close-to-reality simulation of thermomechanical fatigue processes in heat-loaded walls," *AIAA Paper 2008-5237*, 2008.

[52] Gernoth, A., Wurdak, M., Riccius, J. R., Schlechtriem, S., Wiedmann, D., Schwarz, W., and Brummer, L., "TMF test based validation of numerical methods for the analysis of heat-loaded walls," *AIAA Paper 2010-6887*, 2010.

[53] Gernoth, A., Riccius, J. R., and Schlechtriem, S., "Optical heating, thermography and deformation measurement of nozzle wall structures," *AIAA Paper 2011-1264*, 2011.

[54] Gernoth, A., *Untersuchung der Turbulenzmodellierung von rauen Rechteckkanalströmungen mit Berücksichtigung der Oberflächenverformung im Hinblick auf die Anwendung in Raketenmotoren*, Ph.D. thesis, Universität Stuttgart, 2013.

[55] Köhler, B., Noeske, A., Kindervater, T., Wessollek, A., Brand, T., and Biesenbach, J., "11-kW direct diode laser system with homogenized 55 x 20 mm^2 Top-Hat intensity distribution," *Proc. SPIE, High-Power Diode Laser Technology and Applications V*, Vol. 6456, 2007, pp. 1–12.

[56] DILAS Diodenlaser GmbH, *User Manual: DILAS Diodenlaser-Gerät DL 100*, Dec. 2006.

[57] PRIMES GmbH, *Data Sheet: PRIMES PowerMonitor PM*, Rev. 6.0.

[58] PRIMES GmbH, *Data Sheet: PRIMES CompactPowerMonitor CPM*, Rev. 6.0.

[59] PRIMES GmbH, *Data Sheet: PRIMES BeamMonitor BM 100*, Feb. 2014, Rev. 02/2014 DE.

[60] PRIMES GmbH, *User Manual: PRIMES BeamMonitor BM 100*, Rev. 6.0.

[61] KRYTEM GmbH, *Data Sheet: Reciprocating Pump*, Jan. 2004.

[62] KRYTEM GmbH, *User Manual: Reciprocating Pump*, March 2009, Ver. 1.3.

[63] Emerson Process Management GmbH & Co OHG, *Data Sheet: Emerson Micro Motion ELITE*, March 2007, Doc.-No. PS-00447, Rev. G.

[64] FLIR Systems, Inc., *Data Sheet: FLIR SC7000 Series*, Oct. 2014.

[65] Spectrogon AB, *Data Sheet: Spectrogon Optical Filter LP-2500 nm*, May 2015.

[66] Allied Vision, *Data Sheet: Prosilica GE 4900*, Ver. 3.2.0.

[67] Semiconductor Components Industries, *Data Sheet: Onsemi KAI-16000*, Feb. 2016, Rev. 6.0.

[68] Dantec Dynamics GmbH, *User Manual: ISTRA 4D Q-400 System*, Aug. 2014, Ver. 2.6.2.

[69] Herbst, C., Splitthof, K., and Ettemeyer, A., "New features in digital image correlation techniques," Tech. rep., SAE Technical Paper, 2005.

[70] Peters, W. H. and Ranson, W. F., "Digital imaging techniques in experimental stress analysis," *Optical Engineering*, Vol. 21, No. 3, 1982, pp. 427–431.

[71] Sutton, M. A., Wolters, W. J., Peters, W. H., Ranson, W. F., and McNeill, S. R., "Determination of displacements using an improved digital correlation method," *Image and Vision Computing*, Vol. 1, No. 3, 1983, pp. 133–139.

[72] Isothermal Technology Limited, *Data Sheet: TRUrac Model 847*.

[73] Horn, H., *User Manual: Messverstärkereinschub AS4*, Deutsches Zentrum für Luft- und Raumfahrt e.V., Nov. 2008.

[74] Simeoni, G. G., Bryk, T., Gorelli, F. A., Krisch, M., Ruocco, G., Santoro, M., and Scopigno, T., "The Widom line as the crossover between liquid-like and gas-like behaviour in supercritical fluids," *Nature Physics*, Vol. 6, No. 7, 2010, pp. 503–507.

[75] Banuti, D. T., "Crossing the Widom-line–Supercritical pseudo-boiling," *The Journal of Supercritical Fluids*, Vol. 98, 2015, pp. 12–16.

[76] Haidn, O. J., "Advanced rocket engines," *Advances on Propulsion Technology for High-Speed Aircraft*, Vol. 1, 2008, pp. 6–1 – 6–40.

[77] Preclik, D., Wiedmann, D., Oechslein, W., and Kretschmer, J., "Cryogenic rocket calorimeter chamber experiments and heat transfer simulations," *AIAA Paper 1998-3440*, 1998.

[78] Kazaroff, J. M., Jankovsky, R. S., and Pavli, A. J., "Hot fire test results of subscale tubular combustion chambers," Tech. rep., NASA-TP-3222, NASA Lewis Research Center, 1992.

[79] Donahue, R. J., Clark, H. M., Atanmo, P., Kumble, R., and McEvily, A. J., "Crack opening displacement and the rate of fatigue crack growth," *International Journal of Fracture Mechanics*, Vol. 8, No. 2, 1972, pp. 209–219.

[80] Bartsch, M., Kelm, K., and Franke, A., "Mikroskopische Untersuchungen an Kühlkanalproben aus CuCrZr-Legierungen nach thermischer Zyklierung," Tech. rep., DLR M124 Zwischenbericht 2, German Aerospace Center, Institute of Materials Research, 2018.

[81] Bürgel, R., *Festigkeitslehre und Werkstoffmechanik: Werkstoffe sicher beurteilen und richtig einsetzen*, Vieweg, 1st ed., 2005.

[82] ANSYS, Inc., *User Manual: ANSYS CFX-Solver Theory Guide*, Aug. 2017, Release: 18.2.

[83] Schlichting, H. and Gersten, K., *Grenzschicht-Theorie*, Springer, 2006.

[84] Munson, B. R., Okiishi, T. H., Huebsch, W. W., and Rothmayer, A. P., *Fundamentals of Fluid Mechanics*, John Wiley & Sons, 7th ed., 2012.

[85] Zienkiewicz, O. C., Taylor, R. L., and Zhu, J. Z., *The Finite Element Method: Its Basis and Fundamentals*, Butterworth-Heinemann, 7th ed., 2013.

[86] Arendt, W. and Warma, M., "Dirichlet and Neumann boundary conditions: What is in between?" *Journal of Evolution Equations*, Vol. 3, No. 1, 2003, pp. 119–135.

[87] Menter, F. R., "Two-equation eddy-viscosity turbulence models for engineering applications," *AIAA Journal*, Vol. 32, No. 8, 1994, pp. 1598–1605.

[88] Wilcox, D. C., "Reassessment of the scale-determining equation for advanced turbulence models," *AIAA Journal*, Vol. 26, No. 11, 1988, pp. 1299–1310.

[89] Kader, B. A., "Temperature and concentration profiles in fully turbulent boundary layers," *International Journal of Heat and Mass Transfer*, Vol. 24, No. 9, 1981, pp. 1541–1544.

[90] Adams, T., Grant, C., and Watson, H., "A simple algorithm to relate measured surface roughness to equivalent sand-grain roughness," *International Journal of Mechanical Engineering and Mechatronics*, Vol. 1, No. 1, 2012, pp. 66–71.

[91] Launder, B. E. and Spalding, D. B., "The numerical computation of turbulent flows," *Computer Methods in Applied Mechanics and Engineering*, Vol. 3, No. 2, March 1974, pp. 269–289.

[92] Bathe, K.-J., *Finite Element Procedures*, Prentice Hall, 1996.

[93] Armstrong, P. J. and Frederick, C. O., *A Mathematical Representation of the Multiaxial Bauschinger Effect*, Vol. 731, Central Electricity Generating Board & Berkeley Nuclear Laboratories, Research & Development Department Berkeley, 1966.

[94] Frederick, C. O. and Armstrong, P. J., "A mathematical representation of the multiaxial Bauschinger effect," *Materials at High Temperatures*, Vol. 24, No. 1, 2007, pp. 1–26.

[95] Lion, A., "Constitutive modelling in finite thermoviscoplasticity: A physical approach based on nonlinear rheological models," *International Journal of Plasticity*, Vol. 16, No. 5, 2000, pp. 469–494.

[96] Wriggers, P., *Nichtlineare Finite-Element-Methoden*, Springer, 2001.

[97] Chaboche, J.-L. and Rousselier, G., "On the plastic and viscoplastic constitutive equations - Part I: Rules developed with internal variable concept," *Journal of Pressure Vessel Technology*, Vol. 105, No. 2, 1983, pp. 153–158.

[98] Lemaitre, J., "A continuous damage mechanics model for ductile fracture," *Journal of Engineering Materials and Technology*, Vol. 107, No. 1, 1985, pp. 83–89.

[99] Dettmer, W. and Reese, S., "On the theoretical and numerical modelling of Armstrong–Frederick kinematic hardening in the finite strain regime," *Computer Methods in Applied Mechanics and Engineering*, Vol. 193, No. 1-2, 2004, pp. 87–116.

[100] Prager, W., "Recent developments in the mathematical theory of plasticity," *Journal of Applied Physics*, Vol. 20, No. 3, 1949, pp. 235–241.

[101] Perzyna, P., "Fundamental problems in viscoplasticity," *Advances in Applied Mechanics*, Vol. 9, No. 1, 1966, pp. 243–377.

[102] Chaboche, J. L., "Constitutive equations for cyclic plasticity and cyclic viscoplasticity," *International Journal of Plasticity*, Vol. 5, No. 3, 1989, pp. 247–302.

[103] Kachanov, L. M., "Time of the rupture process under creep conditions," *Izvestiia Akademii Nauk SSSR*, Vol. 8, No. 1, 1958, pp. 26–31.

[104] Kachanov, L. M., "Rupture time under creep conditions," *International Journal of Fracture*, Vol. 97, No. 1–4, 1999, pp. 11–18.

[105] Rabotnov, Y. N., "Creep of structural elements," 1966.

[106] Rabotnov, Y. N., "Creep problems in structural members," *North–Holland Series in Applied Mathematics and Mechanics*, 1969.

[107] Lemaitre, J. and Chaboche, J.-L., "Aspect phénoménologique de la rupture par endommagement," *Journal de Mecanique Appliquee*, Vol. 2, No. 3, 1978, pp. 317–365.

[108] Lemaitre, J., *A Course on Damage Mechanics*, Springer, 1992.

[109] Lemaitre, J. and Desmorat, R., *Engineering Damage Mechanics: Ductile, Creep, Fatigue and Brittle Failures*, Springer, 2005.

[110] Desmorat, R. and Cantournet, S., "Modeling microdefects closure effect with isotropic/anisotropic damage," *International Journal of Damage Mechanics*, Vol. 17, No. 1, 2008, pp. 65–96.

[111] Murakami, S., *Continuum Damage Mechanics: A Continuum Mechanics Approach to the Analysis of Damage and Fracture*, Vol. 185, Springer, 2012.

[112] Vladimirov, I. N., Pietryga, M. P., and Reese, S., "On the modelling of non-linear kinematic hardening at finite strains with application to springback - comparison of time integration algorithms," *International Journal for Numerical Methods in Engineering*, Vol. 75, No. 1, 2008, pp. 1–28.

[113] Fassin, M., Wulfinghoff, A., and Reese, S., "A gradient-extended elastic isotropic damage model considering crack-closure," *Proceedings of the 7th GACM Colloquium on Computational Mechanics for Young Scientists from Academia and Industry*, 2017.

[114] Zienkiewicz, O. C. and Godbole, P. N., "A penalty function approach to problems of plastic flow of metals with large surface deformations," *Journal of Strain Analysis*, Vol. 10, No. 3, 1975, pp. 180–183.

[115] Ju, J. W., "On energy-based coupled elastoplastic damage theories: constitutive modeling and computational aspects," *International Journal of Solids and Structures*, Vol. 25, No. 7, 1989, pp. 803–833.

[116] Thiede, R. G., Riccius, J. R., and Reese, S., "Parameter identification of a copper-base alloy using digital image correlation and application to a liquid rocket engine combustion chamber wall," *Joint Conference: 31st ISTS, 26th ISSFD & 8th NSAT, Matsuyama, Ehime (Japan)*, 2017.

[117] Thiede, R. G., Riccius, J. R., and Reese, S., "Parameter identification of a copper-base alloy using digital image correlation and application to a liquid rocket engine combustion chamber wall," *Transactions of the Japan Society for Aeronautical and Space Sciences, Aerospace Technology Japan*, Vol. 16, No. 5, 2018, pp. 345–352.

[118] Cebeci, T., Shao, J. P., Kafyeke, F., and Laurendeau, E., *Computational Fluid Dynamics for Engineers*, Springer, 1st ed., 2005.

[119] Belytschko, T., Liu, W. K., Moran, B., and Elkhodary, K., *Nonlinear Finite Elements for Continua and Structures*, John Wiley & Sons, 2nd ed., 2013.

[120] Hughes, T. J. R., *The Finite Element Method: Linear Static and Dynamic Finite Element Analysis*, Dover Civil and Mechanical Engineering, 2012.

[121] Chaplot, S. L., Mittal, R., and Choudhury, N., *Thermodynamic Properties of Solids: Experiment and Modeling*, John Wiley & Sons, 2010.

[122] Oschwald, M., Suslov, D., and Woschnak, A., "Temperature dependence of material properties and its influence on the thermal distribution in regeneratively cooled combustion chamber walls," *European Conference for Aeronautics and Space Sciences (EUCASS)*, 2004.

[123] NETZSCH-Gerätebau GmbH, *Data Sheet: NETZSCH TMA 402 F1/F3 Hyperion*, Doc.-No. 0917.

[124] NETZSCH-Gerätebau GmbH, *Data Sheet: NETZSCH Differential Scanning Calorimetry - DSC 404 F1/F3 Pegasus*, Doc.-No. 0416.

[125] Blumm, J. and Kaisersberger, E., "Accurate measurement of transformation energetics and specific heat by DSC in the high-temperature region," *Journal of Thermal Analysis and Calorimetry*, Vol. 64, No. 1, 2001, pp. 385–391.

[126] NETZSCH-Gerätebau GmbH, *Data Sheet: NETZSCH Laser Flash Apparatus LFA 427*, Doc.-No. 0718.

[127] Grimvall, G., *Thermophysical Properties of Materials*, Elsevier, 1st ed., 1999.

[128] Bouajila, W. and Riccius, J. R., "Identification of the unified Chaboche constitutive model's parameters for a cost efficient copper-based alloy," *Space Propulsion Conference*, 3AF (Association Aéronautique et Astronautique de France) Paper 2014-2959116, 2014.

[129] Bouajila, W. and Riccius, J. R., "Modelling of the cyclic and viscoplastic behavior of a copper-base alloy using Chaboche model," *Space Propulsion Conference*, 3AF (Association Aéronautique et Astronautique de France) Paper 2016-3124805, 2016.

[130] Masuoka, T. and Riccius, J. R., "Life evaluation of a combustion chamber by TMF panel tests based on a creep fatigue and ductile damage model," *International Journal of Damage Mechanics*, 2019.

[131] Thiede, R. G., Zametaev, E. B., Riccius, J. R., Fassin, M., and Reese, S., "Comparison of damage parameter based finite element fatigue life analysis results to combustion chamber type TMF panel test results," *AIAA Paper 2015-4070*, 2015.

[132] Thiede, R. G., Riccius, J. R., and Reese, S., "Validation of damage parameter based finite element fatigue life analysis results to combustion chamber type TMF panel test results," *AIAA Paper 2016-4583*, 2016.

[133] DIN Deutsches Institut für Normung e. V., "Aerospace series – Metallic materials – Test methods - Constant amplitude fatigue testing (DIN EN 6072)," Beuth, June 2011.

[134] Lemaitre, J. and Chaboche, J.-L., *Mechanics of Solid Materials*, Cambridge University Press, 1990.

[135] Watermeyer, P. and Kelm, K., "Mikroanalytische Untersuchung an geprüften/ermüdeten CuCrZr-Legierungen," Tech. rep., DLR M124 Zwischenbericht 1, German Aerospace Center, Institute of Materials Research, May 2017.

[136] Zimmermann, M., "Lecture Notes: Schadensanalyse - Risse und Fraktographie," Technische Universität Dresden, Oct. 2017.

[137] Richard, H. A. and Sander, M., *Ermüdungsrisse*, Springer, 3rd ed., 2012.

[138] Weintritt, S., *Modellierung und Durchführung gekoppelter Strömungs- und Strukturberechnungen (FSI) von TMF-Panel-Experimenten mit zyklischer Laserbelastung*, Master's thesis, Paderborn University, 2017.

[139] Riccius, J. R., Thiede, R. G., and Weintritt, S., "Liquid booster engine related TMF panel tests," *European Conference for Aeronautics and Space Sciences (EUCASS)*, 2017, pp. 1–7.

[140] ANSYS, Inc., *User Manual: ANSYS APDL Theory Reference*, Aug. 2017, Release: 18.2.

[141] Koschnick, F., *Geometrische Locking-Effekte bei Finiten Elementen und ein allgemeines Konzept zu ihrer Vermeidung*, Ph.D. thesis, Technical University of Munich, 2004.

[142] Doll, S., Schweizerhof, K., Hauptmann, R., and Freischläger, C., "On volumetric locking of low-order solid and solid-shell elements for finite elastoviscoplastic deformations and selective reduced integration," *Engineering Computations*, Vol. 17, No. 7, 2000, pp. 874–902.

[143] Belytschko, T., Ong, J. S.-J., Liu, W. K., and Kennedy, J. M., "Hourglass control in linear and nonlinear problems," *Computer Methods in Applied Mechanics and Engineering*, Vol. 43, No. 3, 1984, pp. 251–276.

[144] Flanagan, D. P. and Belytschko, T., "A uniform strain hexahedron and quadrilateral with orthogonal hourglass control," *International Journal for Numerical Methods in Engineering*, Vol. 17, No. 5, 1981, pp. 679–706.

[145] Crepeau, J., "A brief history of the T4 radiation law," *ASME 2009 Heat Transfer Summer Conference collocated with the InterPACK09 and 3rd Energy Sustainability Conferences*, American Society of Mechanical Engineers, 2009, pp. 59–65.

[146] Anderson Jr, J. D., *Fundamentals of Aerodynamics*, McGraw-Hill Education, 3rd ed., 2001.

[147] White, F. M., *Fluid Mechanics*, McGraw-Hill, 1998.

[148] Wilcox, D. C., *Turbulence Modeling for CFD*, Vol. 3, DCW Industries La Canada, CA, 2006.

[149] Kacynski, K. J., "Thermal stratification potential in rocket engine coolant channels," Tech. rep., NASA-TM-4378, NASA Lewis Research Center, 1992.

[150] Torres, Y., *Heat and Mass Transfers in Curved Cooling Channels of Rocket Engines*, Ph.D. thesis, L'Université de Valenciennes et du Hainaut Cambrésis, 2008.

[151] Pizzarelli, M., Nasuti, F., Paciorri, R., and Onofri, M., "Numerical analysis of three-dimensional flow of supercritical fluid in cooling channels," *AIAA Journal*, Vol. 47, No. 11, 2009, pp. 2534–2543.

[152] de Souza Neto, E. A., Perić, D., and Owen, D. R. J., *Computational Methods for Plasticity: Theory and Applications*, John Wiley & Sons, 1st ed., 2011.

[153] Fawkes, A. J., Owen, D. R. J., and Luxmoore, A. R., "An assessment of crack tip singularity models for use with isoparametric elements," *Engineering Fracture Mechanics*, Vol. 11, No. 1, 1979, pp. 143 – 159.

[154] Suslov, D., Betti, B., Aichner, T., Soller, S., Nasuti, F., and Haidn, O. J., "Experimental investigation and CFD-simulation of the film cooling in an O2/CH4 subscale combustion chamber," *Space Propulsion Conference*, 3AF (Association Aéronautique et Astronautique de France), 2012.

[155] Kamal, S. M., Dixit, U. S., Roy, A., Liu, Q., and Silberschmidt, V. V., "Comparison of plane-stress, generalized-plane-strain and 3D FEM elastic–plastic analyses of thick-walled cylinders subjected to radial thermal gradient," *International Journal of Mechanical Sciences*, Vol. 131, 2017, pp. 744–752.

[156] Riccius, J. R. and Zametaev, E. B., "Stationary and transient thermal analyses of cryogenic liquid rocket combustion chamber walls," *AIAA Paper 2002-3694*, 2002.

[157] Ballard, R. O., "SSME to RS-25: Challenges of adapting a heritage engine to a new vehicle architecture," *European Conference for Aeronautics and Space Sciences (EUCASS)*, 2015.

[158] Fröhlich, A., Popp, M., Schmidt, G., and Thelemann, D., "Heat transfer characteristics of H2/O2-combustion chambers," *AIAA Paper 93-1826*, 1993.

[159] Voce, E., "The relationship between stress and strain for homogeneous deformation," *Journal of the Institute of Metals*, Vol. 74, No. 1, 1948, pp. 537–562.

[160] "Aerojet Rocketdyne RS-25 Engine," http://www.rocket.com/rs-25-engine, Accessed: November 15, 2018.

[161] Riccius, J. R., Zametaev, E. B., Bouajila, W., and Wargnier, Q., "Inner liner temperature variation caused deformation localization effects in a multichannel model of a generic LRE wall structure," *AIAA Paper 2014-3988*, 2014, pp. 1–12.